THE APPLICATION OF POSITRON EMISSION TOMOGRAPHY IN RADIOTHERAPY TREATMENT PLANNING

A THESIS SUBMITTED TO THE UNIVERSITY OF MANCHESTER
FOR THE DEGREE OF DOCTOR OF PHILOSOPHY
IN THE FACULTY OF MEDICAL AND HUMAN SCIENCES

2010

By

Moamen M.O.M. Aly

School of Medicine

Contents

Chapter 2:
SEGMENTATION OF RADIOLOGICAL MEDICAL IMAGES ...63

Chapter 3:
DEVELOPMENT OF NEW PET/CT VOLUME SEGMENTATION TECHNIQUES.....86

Chapter 5:
THE IMPACT OF DEFINING THE MAXIMUM LESION UPTAKE 159

Chapter 6:
PRELIMINARLY INVESTIGATION IN PATIENTS 228

Word Count: 51,534

List of Figures

List of Tables

List of Abbreviations and Symbols

The reader is assumed to possess basic knowledge of measurement units and their prefixes, scientific symbols, and abbreviations in common usage. Examples pertinent to this thesis are millimetre (mm), millilitres (ml), kilo- (k), Fluorine-19 (^{18}F), Iodine-124 (^{124}I), two-dimension (2D) and three-dimension (3D). Some quantities carry non-SI units such kilo-Becquerel per millilitre (kBq/ml) for radioactivity concentration. A number of abbreviations which occur infrequently have been omitted from the following list. These are expanded at the appropriate point in the main text.

<<	Used with the p value to indicate that it is highly significant
40% or $40\%_1$	Fixed thresholding using 40% of the maximum voxel activity concentration
$40\%_{27}$	Fixed thresholding using 40% of the mean activity concentration of 27 voxels around the maximum voxel
$40\%_9$	Fixed thresholding using 40% of the mean activity concentration of 9 voxels around the maximum voxel
BGO	Bismuth Germanate scintallator
BTV	Biological target volume
CAT	Contrast adjusted thresholding method
CAT_{27}	Contrast adjusted thresholding method using the mean of 27 voxels around the maximum activity concentration voxel
CAT_{27}-60	Contrast adjusted thresholding method using the mean of 27 voxels around the maximum activity concentration voxel and 60 min single calibration curve
CAT-60 or CAT_1-60	Contrast adjusted thresholding method using 60 min single calibration curve

CAT_9	Contrast adjusted thresholding method using the mean of 9 voxels around the maximum activity concentration voxel
CAT_9-60	Contrast adjusted thresholding method using the mean of 9 voxels around the maximum activity concentration voxel and 60 min single calibration curve
CI	Conformity index
C_o	Observed contrast
CS	Crescent irregular volume
CT	Computed tomography
C_t	True contrast
CTV	Clinical Target Volume
DSC	Dice similarity coefficient
E_A	Acceptable error
EDT	Euclidean distance transformation
FBP	Filtered-backprojection reconstruction technique
FDG	^{18}F-fluoro-deoxyglucose
fMRI	functional magnetic resonance
FoV	Field of interest
FWHM	Full width at half maximum
GTV	Gross target volume
ICRU	International Commission on Radiation Units and Measurements
IMRT	Intensity modulated radiotherapy
IT	Iterative reconstruction technique
ITM	Iterative thresholding method
ITV	Internal target volume
IV	Irradiated volume
JSC	Jaccard similarity coefficient
Lmax	Maximum voxel value
$Lmax_{27}$	Mean of 27 voxels around the maximum voxel value
$Lmax_9$	Mean of 9 voxels around the maximum voxel value

LOR	Line of response
LSO	Lutetium oxyorthosilicate scintillator
MD-CRT	Multidimensional conformal radiotherapy
MLC	Multi-leaf collimator
MR	Magnetic resonance
MRI	Magnetic resonance imaging
Nal(TI)	Sodium iodide scintillator
NEMA	National electrical manufacturers association
NSCLC	non-small cell lung cancer
NTCP	Normal tissue complication probability
OAR	organs at risk
p	P-value
PET	Positron emission tomography
PMT	Photomultiplier tube
PSF	Point spread function
PTV	Planning target volume
PVE	Partial volume effect
RC	Recovery coefficient
RT	Radiotherapy
RTP	Radiotherapy treatment planning
S/B	Signal to background ratio
SD	Standard deviation
SF	Scatter fraction
SNR	Signal to noise ratio
SPECT	Single photon emission computed tomography
SUV	Standardized uptake value
SUV_{max}	Maximum standardized uptake value
t_{AC}	Acquisition time
TCP	Tumour control probability
TH	Top-hat irregular volume
TOF	Time of flight
T_{opt}	Optimum threshold
TV	Treated volume
V	True volume
VCAT	Volume and contrast adjusted thresholding

	method
$VCAT_{27}$	Volume and contrast adjusted thresholding method using the mean of 27 voxels around the maximum activity concentration voxel
$VCAT_{27}$-60	Volume and contrast adjusted thresholding method using the mean of 27 voxels around the maximum activity concentration voxel and 60 min single calibration curve
VCAT-60 or $VCAT_1$-60	Volume and contrast adjusted thresholding method using 60 min single calibration curve
$VCAT_9$	Volume and contrast adjusted thresholding method using the mean of 9 voxels around the maximum activity concentration voxel
$VCAT_9$-60	Volume and contrast adjusted thresholding method using the mean of 9 voxels around the maximum activity concentration voxel and 60 min single calibration curve
VoI	Volume of interest
χ^2	Chi-square

Abstract

THE APPLICATION OF POSITRON EMISSION TOMOGRAPHY IN RADIOTHERAPY TREATMENT PLANNING

A thesis for the degree of PhD

Moamen Mohamed Omran Moustafa Aly

The University of Manchester

October 2010

Positron emission tomography (PET) is a molecular imaging technique that provides a direct and accurate evaluation of tissue function *in vivo*. PET of the glucose analogue ^{18}F-fluoro-deoxy-glucose, is increasingly in use to aid in gross target volume delineation in radiotherapy treatment planning (RTP) where it shows reduced inter-observer variability. The aim of this thesis was to develop and investigate a new technique for delineating PET-GTV with sufficient accuracy for RTP. A new technique, volume and contrast adjusted thresholding (VCAT), has been developed to automatically determine the optimum threshold value that measures the true volume on PET images. The accuracy was investigated in spherical and irregular lesions in phantoms using both iterative and filtered back-projection reconstructions and different image noise levels. The accuracy of delineation for the irregular lesions was assessed by comparison with CT using the Dice Similarity Coefficient and Euclidean Distance Transformation. A preliminarily investigation of implementing the newly developed technique in patients was carried out. VCAT proved to determine volumes and delineate tumour boundaries on PET/CT well within the acceptable errors for radiotherapy treatment planning irrespective of lesion contrast, image noise level and reconstruction technique.

Declaration

No portion of the work referred to in the thesis has been submitted in support of an application for another degree or qualification of this or any other university or other institute of learning.

Moamen M.O.M. Aly

_____

12th October 2010

Copyright

i. The author of this thesis (including any appendices and/or schedules to this thesis) owns certain copyright or related rights in it (the "Copyright") and he has given The University of Manchester certain rights to use such Copyright, including for administrative purposes.

ii. Copies of this thesis, either in full or in extracts and whether in hard or electronic copy, may be made only in accordance with the Copyright, Designs and Patents Act 1988 (as amended) and regulations issued under it or, where appropriate, in accordance with licensing agreements which the University has from time to time. This page must form part of any such copies made.

iii. The ownership of certain Copyright, patents, designs, trade marks and other intellectual property (the "Intellectual Property") and any reproductions of copyright works in the thesis, for example graphs and tables ("Reproductions"), which may be described in this thesis, may not be owned by the author and may be owned by third parties. Such Intellectual Property and Reproductions cannot and must not be made available for use without the prior written permission of the owner(s) of the relevant Intellectual Property and/or Reproductions.

iv. Further information on the conditions under which disclosure, publication and commercialisation of this thesis, the Copyright and any Intellectual Property and/or Reproductions described in it may take place is available from the Head of School of Medicine (or the Vice-President).

To my wife,

my son, and my parents

for their love, support and encouragements

Acknowledgements

This thesis is the result of nearly four years of work at the Christie Hospital. I received the help and support from numerous people, without whom this dissertation would have never been completed.

First, I would like to sincerely thank my supervisors: Dr David Hastings, Dr Carl Rowbottom, and Dr Peter Julyan have all contributed much time to my education. They have provided a great deal of advice and guidance, and each of them has taken the time to provide comments on an initial draft of this thesis. I am especially indebted to Peter Julyan, who first introduced the fundamental concept of PET to me, and who was acting as one of my supervisors although he was not officially. I also extremely grateful to David Hastings, who was my main supervisor has provided me with continual feedback and has been supportive to the research.

I express my sincere thanks to my advisor Prof Peter Williams for the help and support I have received from him. He was the first person to get in touch with to obtain my acceptance letter from The University of Manchester.

I would like also to thank Dr Beng Yap, Dr Margaret Harris, Dr Paul Hulse, and Dr Prakash Manoharan for helping in delineation of the tumour volumes on the patients study.

I express my gratitude to Peter Carson and Thomas Hamnett for constructing the irregular lesions with a very thin wall thickness and within the available time frame. Also, I gratefully thank Mr David Ryder for providing the statistical support during my studying.

I can not forget the great help and inspiration from all the people I used to see day to day in North Western Medical Physics (NWMP). I am proud of having had the opportunity to work with you. So, thank you all.

Finally, I would like to thank all of my family and friends, for their love and great encouragement. I gratefully acknowledge the financial support I have received from the Egyptian Ministry of High Education to acquire my PhD degree.

About the Author

Moamen Aly was born during the spring of 1977, in an upper Egyptian city called Assiut. He first became interested in physics in general while studying the physics course during his secondary school, and subsequently after joining the Faculty of Science in 1994. Moamen graduated form the faculty in 1998 with the specialty in Physics and Mathematics. During that time, a new cancer institute was about to establish in the same university – Assiut University (AU). He then got a job as a medical physicist in the radiotherapy and nuclear medicine in the same graduation year. This experience opened his eyes to field of medical physics, which he found very interesting not only because he started to apply what he was learning but also because he was feeling that his role is very important in the process of treating patients. In 2000, he finished a one year medical physics diploma from AU, which allows him to expose to the basics of radiobiology, the physics of radiotherapy as well as the role of medical physics in hospitals in general. He then continued his post-graduate education to acquire a master degree in nuclear physic from AU in 2003; the thesis title was: "Radiographic Film and Ionization Chamber Dosimetric Measurements". After working 7 years as a medical physicist then lecturing in the South Egypt Cancer Institute at AU, he spent 6 months training in IMRT and Monte Carlo simulation in Nice, France late 2005.

In 2006, Moamen was awarded a scholarship from the Egyptian government to study for his PhD in medical physics from a high-ranking foreign university. He then accepted the offer form The University of Manchester to study for this degree with the great experience of the Christie Hospital and has started January 2007.

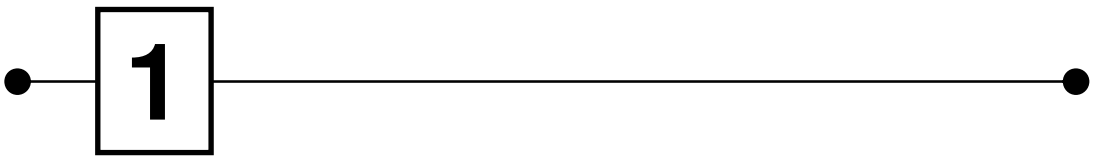

Chapter 1:

BACKGROUND

1.1. Principles of Radiotherapy

Radiotherapy (RT), or radiation therapy, is the technique that uses high-energy ionizing radiation in the form of x-rays or gamma rays, or a beam of particles such as electrons or protons to treat diseases. Radiotherapy is an interdisciplinary field which draws on medicine, physics, mathematics, computer science, radiobiology, electrical and mechanical engineering. Radiotherapy has been in use for cancer treatments since the discovery of x-rays in 1895 by Wilhelm Röntgen. However, radiotherapy has been dynamically advanced over the past 50 years in an extraordinary manner. Key milestones of this development are discussed in this section to understand how we have reached this treatment modality.

A key development was the replacement of cobalt-60 and betatron treatment machines by linear accelerators (or linacs) between 1960 and 1980. Linacs are accurate treatment machines that can deliver different energies of electron and photon beams that are higher in energy and dose rate than that obtained from cobalt machines. This higher energy improved the treatment of deep tumours as well as reducing the dose absorbed on the skin due to the skin sparing phenomena. Modern computer-controlled linacs are comparatively reliable, compact and have a high mechanical accuracy.

Another important milestone was the invention of x-ray computed tomography (CT). CT was introduced to radiotherapy at the end of the 1970's as a tool to help in the diagnoses and the treatment planning of cancer. This resulted in 3D computerized treatment planning that now is a standard tool in all radiotherapy departments. With the subsequent invention of magnetic resonance imaging (MRI), and developments to register MRI images with CT the delineation of treatment planning target volumes was enhanced even further.

The computer revolution had a tremendous impact on the development of radiotherapy. Computerised methods are now integral to each of the individual steps in the patient's pathway from the treatment simulation through immobilization and treatment planning, to the treatment itself and verification during the treatment. The treatment simulation stage has benefited from the introduction of 3D virtual simulation whereby 3D images can be acquired and manipulated in the absence of the patient to decide on the beam entrance, isocentre localization, and calculation of the dose distribution. The application of complex computer techniques allowed the introduction of 3D dose calculation algorithms as well as improving the

accuracy of the available algorithms. This computer revolution also increased the accuracy of the treatment machines which translated into developing new treatment machines that could deliver a very small field size (< 4 cm) with a very high stability and accuracy.

A more recent revolution in radiotherapy was the development of computerized multi-leaf collimators (MLCs). The MLC was first introduced to accurately tailor the treatment beams to spare the normal organs in a technique that is called 3D conformal radiotherapy. By the mid 1990s, the combination of 3D treatment planning and 3D conformal radiotherapy by MLCs led to a new technique called intensity modulated radiotherapy (IMRT). The development of the IMRT technique required a new treatment planning software, where the desired dose distribution is the input data and the output data are the beams sizes and directions. Because this treatment planning follows the opposite process of the previously established treatment planning, it was termed inverse treatment planning. The IMRT techniques improved the conformation to complex shaped tumours.

From the beginning of this millennium, another evolving concept is biologically adaptive radiotherapy. Due to the advances in the understanding of tumour biology, the hypothesis that the tumour consists of homogenous concentrations of clonogenic cells is now out-dated and has been revised with the new understanding that the tumour consists of different types of tissue which have different levels of radio-sensitivity that could lead to radiotherapy success or failure. The introduction of single photon emission computed tomography (SPECT), positron emission tomography (PET) and functional magnetic resonance (fMRI) allow for differentiating between the tumour's different cell's types. The inclusion of this functional image data with other

treatment techniques, such as IMRT, will allow for delivering different radiation doses to each different cell type in order to control tumour growth.

1.1.1. Types of Radiotherapy

The goal of radiotherapy is to deliver an accurately measured high-dose of radiation to a particular region of tissue to kill cancer cells while sparing the normal tissues. Radiotherapy can be classified into two major types based on the delivery technique: teletherapy using external radiation beams, and brachytherapy using internal radiation from radioactive sources inside the body. External-beam radiotherapy uses a radiation source external to the patient, and some form of collimation to direct the radiation field to treat deep diseases, while brachytherapy is a technique whereby a radiation source is implanted directly within the body, or swallowed, to locally irradiate the disease area. Both radiotherapy techniques are used to treat a wide variety of diseases including cancer, thyroid disorders, some blood diseases and certain types of arthritis. Radiotherapy may be used for either curative or palliative treatments.

1.1.2. Radiotherapy Treatment Planning

The aim of treatment planning is to find a particular geometry where it is possible to deliver a radiation dose to cure or control tumour growth while minimizing radiation to surrounding normal tissues in order to minimize the side effects. Tumour control probability (TCP) and normal tissue complication probability (NTCP) are biological models that predict the treatment planning outcome in terms of both tumour control and consequent complication in normal tissue. Figure 1.1 shows a favourable treatment scenario where there

is enough separation between the TCP and NTCP to define a therapeutic window which will determine the prescribed dose. The shape and relative positions of the dose-response curves vary according to the radio-sensitivity of the tissues concerned, as well as details of the treatment regime such as the fractionation scheme. Fractionation is a technique where the total radiation dose is delivered not in a single treatment setting, but in a series of smaller fractions over a period of days or weeks, and is employed to allow cell recovery in normal tissues during the periods between fractions, hence reducing the NTCP. The success of the fractionation technique depends on normal tissue recovery having a higher rate than tumour cell recovery, thereby increasing the gap between TCP and NTCP.

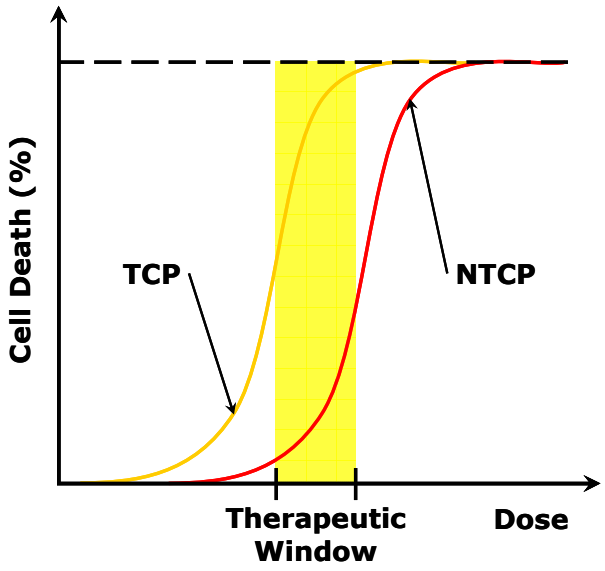

Figure 1.1: Dose response curves showing the tumour control probability (TCP) and normal tissue complication probability (NTCP) to demonstrate the therapeutical window.

The International Commission on Radiation Units and Measurement (ICRU) has issued recommendations to standardise the methodology used to prescribe, record and report doses to volumes of interest. ICRU 50 [1]

introduced concepts and the terminology to aid standard definitions of dose distributions and treatment volumes. Some years later, ICRU 62 [2] was published as a supplement to ICRU 50, refining some of the recommendations in the light of developments in techniques for accurate target volume localisation and precise treatment delivery.

Treatment planning starts by delineating the target volumes which are usually of two types: oncological and geometrical. Figure 1.2 depicts these different types of volumes. The gross tumour volume (GTV) and the clinical target volume (CTV) are purely oncological concepts independent of technology; however the internal target volume (ITV), planning target volume (PTV), treated volume (TV) and irradiated volume (IV) are geometrical concepts developed for the treatment planning process. The GTV is the volume that includes the visible or palpable malignant growth, and the CTV is the volume that contains the GTV plus subclinical microscopic malignancy. A margin that represents the physiological movements of the CTV, for example due to respiration, is added further to form the ITV. Additionally margins are added to the ITV to allow for the setup error of the treatment technique, and for the dose calculation accuracy, to form the PTV. Depending on the treatment technique, two further volumes can be identified. The TV is the volume that is enclosed by an isodose surface appropriate to achieve the purpose of treatment (radical or palliative); usually 90%. The IV is that volume which receives a significant dose to the normal tissue tolerance (i.e. 50% target dose).

In addition to these, the BTV is a volume that has been proposed by Ling et al. [3] (not the ICRU) which integrates physical and biological

conformity for the purpose of multidimensional conformal radiotherapy (MD-CRT). This concept is discussed further in section 1.3 later in this chapter.

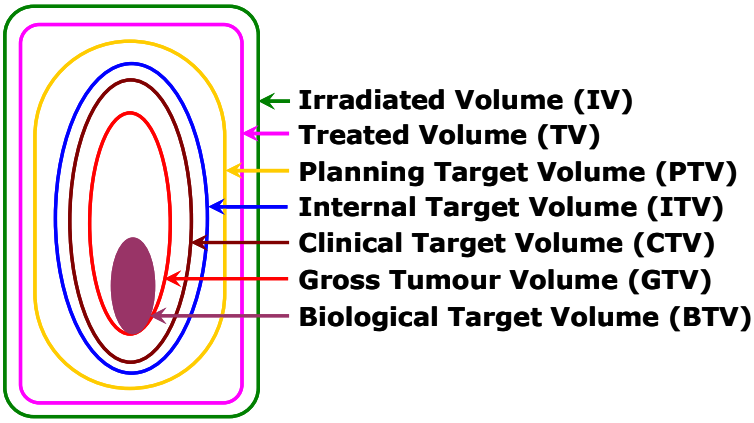

Figure 1.2: Schematic diagram showing the different target volumes recommended by the ICRU [1, 2].

1.2. Principles of PET

Positron emission tomography (PET) is a powerful medical imaging modality that provides a non-invasive tool to investigate biochemical and physiological processes in vivo. Positron emitting radionuclides decay by emitting a positron particle which has the mass of an electron but with a positive charge. These radionuclides can be incorporated into particular molecule to form a radiotracer, the molecule being chosen to investigate a specific biochemical or physiological process. The common positron emitting radionuclides used for PET have half-lives varying from 1 to 110 minutes as listed in Table 1.1.

Once the positron emitted, it travels a certain distance, called the positron range, before encountering an electron and undergoing annihilation. The positron range depends on the energy of the positron, which is specific to the nuclide. The positron range can vary from a few millimetres to over a centimetre giving rise to an uncertainty in detecting the location of the

positron emission, which results in an inherent limitation of spatial resolution in PET [4]. The positron-electron annihilation results in the emission of a pair of photons of energy 511 keV at approximately 180° to each other. These two photons are then detected by PET detectors to identify the positron decay location. This simultaneous detection of the photons is called a coincidence event of which there are several million during a typical scan. The line that connects the two detection points of the photons is called the line of response – LOR. These events are used to form a 3D representation of the activity concentration using image reconstruction techniques, as described below in section 1.2.3.

Radionuclide	**Half-Life (minutes)**
Flourine-18	110
Carbon-11	20.3
Nitrogen-13	10
Oxygen-15	2.07
Rubidium-82	1.25

Table 1.1: Half-Lives of common positron emitting radionuclides.

To acquire a PET diagnostic scan, the patient receives an intravenous injection of a radiotracer solution or inhales a radioactive gas containing particular molecules labelled with a positron emitter. The blood circulates this radiotracer and distributes it throughout the body. The most commonly used PET radiotracer is ^{18}F-fluoro-deoxyglucose (FDG) labelled with ^{18}F which has a half-life of 110 minutes. FDG is chemically similar to glucose and is therefore actively transported into the cells by glucose transporters. Inside the cell the FDG is phosphorylated and then trapped for many hours as FDG-6-phosphate, see Figure 1.3. Cancerous cells produce energy at a higher rate than most

normal cells as described by Warburg [5]. Therefore, FDG will be taken up predominantly by cancer cells according to the greater level of energy required. However, not all cancer cells get their energy from glucose as will be demonstrated in section 1.4.1 later. For a PET diagnostic scan the patient is allowed to rest for about an hour after injecting the FDG to allow for this cellular uptake process. The distribution of the FDG on the PET scan then reflects the glucose demand of the body's various tissues.

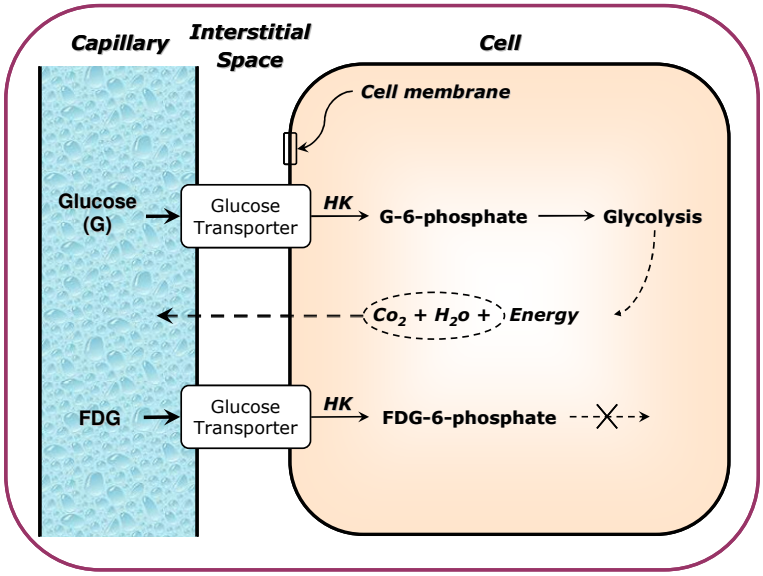

Figure 1.3: Schematic diagram illustrating glucose and FDG metabolism.

In addition to FDG, several other radiotracers have been proposed and investigated, with one of the positron emitting nuclides shown in Table 1.1 being used to label specific ligands to study specific biological targets [6]. One example that has undergone extensive clinical investigation is the thymidine analogue ^{18}F-3'-fluoro-3'-deoxy-thymidine (^{18}F-FLT) which measures cell proliferation [7]. Table 1.2 presents a list of some of the radiotracers that have been used, along with their biological targets and measured effects, in the field of oncology [8].

Tracer	Target	Measured Effect
^{18}F-flurodeoxyglucose (^{18}F-FDG)	Glucose metabolism	Glucose consumption or metabolism
^{18}F-flouro-L-dihydroxyphenylalanine (^{18}F-fluoro-L-DOPA)	Activity of aromatic L-amino acid decarboxylase	Dopaminergic system
^{11}C-choline, ^{18}F-choline	Phosphatidylcholine	Membrane function
1-^{11}C-acetate	Tricarboxylic acid cycle via acetyl coenzyme A	Lipid synthesis
^{18}F-3'-fluoro-3'-deoxy-thymidine (^{18}F-FLT)	Activity of thymidine kinase-1	DNA synthesis, tumour cells proliferation, tumour hypoxia
Fluoromisonidazol (^{18}F-FMIZO)	Androgen receptor	Tumour hypoxia, tumour androgen receptors
Fluorine-18-fluoride (^{18}F-fluoride)	Hydroxyl group in bone crystal	Bone blood flow and osteoblastic activity

Table 1.2: Different PET tracers for molecular imaging in medical oncology [8].

1.2.1. PET Scanners

PET scanners (or PET cameras) consists of a set of detectors arranged is a certain geometry and surrounding the object to be imaged. PET scanners are designed to convert the high-energy photons resulted from the positron

annihilation process into an electronic signal. This process is generally achieved by scintillation detectors and photomultiplier tubes (PMTs) where scintillation light from the scintillation crystals is detected by the PMTs. The annihilation photon of energy 511 keV interacts with the scintillator crystal either by photoelectric absorption or Compton scattering leading to cascade visible light photons. Many of these light photons are captured by the photo-cathode of a PMT ejecting photo-electrons that then get accelerated and multiplied resulting in a short electric pulse. This signal is amplified further and fed to coincidence circuitry. When two signals from opposing detectors arrive in coincidence, or within the coincidence time-window, the circuitry records it as a coincidence event. These coincidence events are usually stored in the form of a sinogram. In the sinogram, each LOR is defined by the distance r (the perpendicular distance between the LOR and the centre of the scan field) and the angle Φ (the angle between r and the vertical axis of the field).

PET scanner technology has been advanced significantly over recent decades, although the basic model of detecting the annihilation photons remains the same. The history of PET is characterised by the continuous pursuit for better sensitivity and spatial resolution. The early 1950 witnessed the birth of a primitive PET scanner that composed of two opposed sodium iodide {NaI(TI)} detectors. Despite the relatively crude nature of initial results of attempting to detect brain tumours, it encouraged further development to obtain a three-dimensional image by rotating the two opposed detectors [9].

Figure 1.4 shows a schematic diagram of the four most common PET detectors configurations for both single and block detectors as well as stationary and rotated rings.

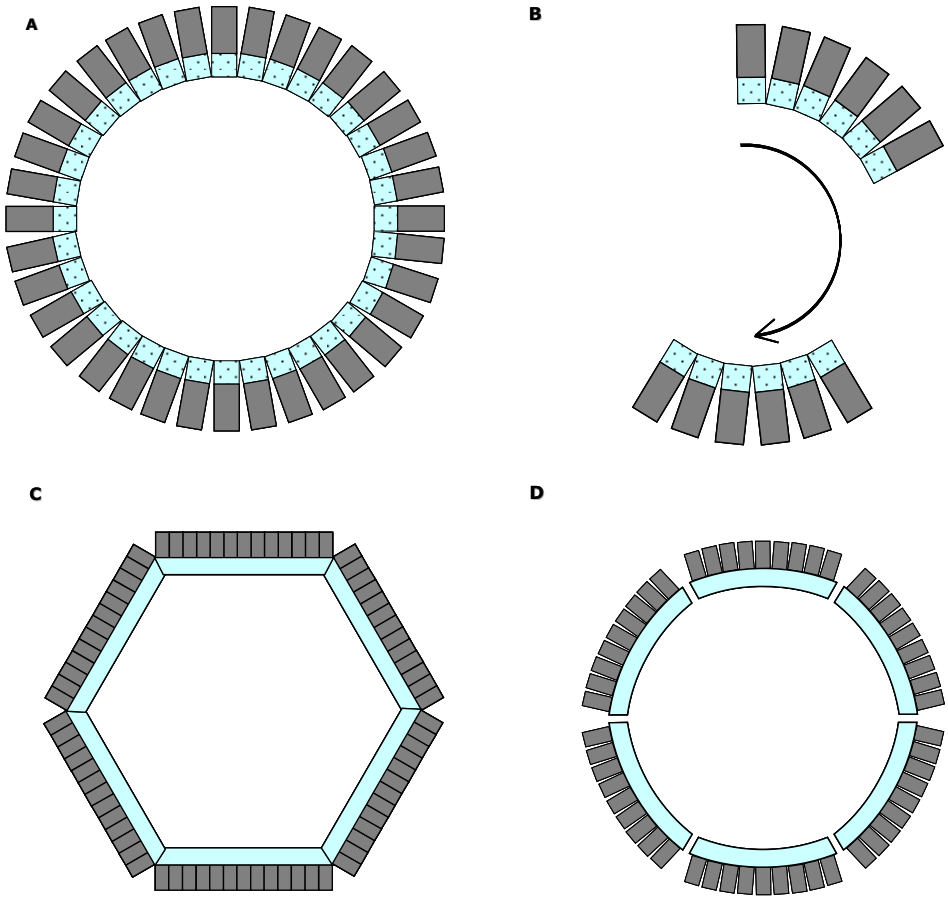

Figure 1.4: Schematic diagram illustrates the four common PET scanner configurations. A, stationary block ring system, B, rotating block ring system, C, stationary Nal(TI) system with a six flat detectors, D, stationary Nal(TI) system with a six curved continuous detectors. Adopted from [10].

It was obvious that increasing sensitivity was required at that time. Therefore, in the mid 1960's a new hybrid scanner that increased sensitivity was developed. This device was consisted of two rows of nine detectors, each in coincidence with three detectors in the opposite row. This model was used for almost a decade until it was updated at the beginning of the 1970's using 2D detectors arrays as a single hexagon of detectors (Figure 1.4C). Significant advances made in the early 1980's were achieved by using Bismuth

Germanate (BGO) scintallator as a detector and adding another hexagon of detectors next to the other one to increase the axial field of view (FoV). BGO has a higher stopping power than NaI(TI) which results in increasing sensitivity. Increasing the axial FoV also contribute to increased sensitivity. These two rings were axially collimated by lead septa to maintain simplicity in the reconstruction process and reduce the scattered and random events (described in section 1.2.2) however it reduces the total counts rate.

The next major advance in PET technology was in the mid 1980's by the development of the block detector [11], in which the scintillation crystal is cut into many elements and coupled to several PMTs, as well as, the development of position sensitive PMTs [12].

In early 1990's, the PET scanners advanced to allow for 3D data acquisition where the collimation septa were removed so high count rate was detected. Although this 3D mode increased the sensitivity, it requires reconstruction algorithms that take into consideration the correction for scatter and random coincidence events.

This millennium has witnessed developments in PET scanner mainly by introducing new scintillators such as lutetium oxyorthosilicate (LSO) that is faster and produces higher light than BGO. Also, significant improvements have made it possible to add the time-of-flight (TOF) technology to improve the PET image quality as well as to integrate other modalities with PET in a multi-modality imaging such as PET/CT and PET/MR. The image quality can be enhanced further by confining the annihilation position along LORs using the TOF information. The position can be estimated by determining the difference in the arrival times of the pair of photons in opposite detectors which will

increase the accuracy of measuring the annihilation position. This accuracy can be translated into a dose reduction or shorter imaging time [13, 14].

Today, most PET scanners are offered in tandem with a CT scanner which can be considered as an independent imaging device. The CT component provides complementary data to more accurately localize functional abnormality and to correct for attenuation. This multi-modality device enables the combination of the functional information from the PET with the anatomical information from the CT in form of fused or co-registered PET/CT images. The advantages of the multi-modality imaging lead to combine the PET scanners with magnetic resonance (MR) which rely on completely different physical principles. The development of PET/MR is quite challenging. The two main obstacles in combining the PET/MR is that the PET detectors need to be able to operate in the presence of a magnetic field and the limited space within the narrow MR tunnel which impose constrains on the PET detectors size [15].

1.2.2. Types of Coincidence events

A true coincidence occurs when the two annihilation photons originating from the same positron decay have not changed in direction or lost energy, and are detected at within a very short allowable known time known as the coincidence window. However, other types of events also occur, namely scatter and random coincidences, as shown in Figure 1.5, which contribute to the total coincidence rate. Some of these are detected and contribute to the total count rate, with a degrading effect on the image. Methods for correcting these are applied.

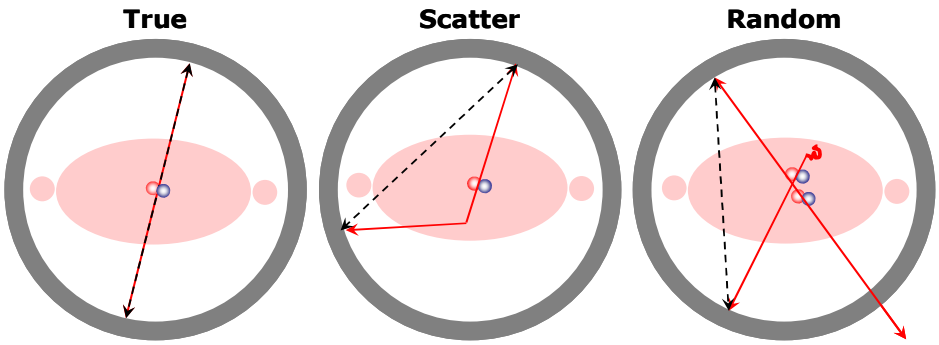

Figure 1.5: Illustration of the main types of coincidence events. The patient cross-section (light-pink) is shown inside the detector ring of a PET scanner (grey). The red line represents the direction of the annihilation photon and the black dotted line represents the LOR.

A scatter coincidence event occurs when one or both annihilated photons are scattered inside the patient and are detected within the time and energy limits of the coincidence window. The scatter fraction (SF) represents the ratio between the scattered and total coincidence rates. The SF is not dependent on the amount of activity within the FoV, but is dependent on the type of material responsible for the scattering process and increases with the size of the object (or patient). There are different approaches for estimating and correcting scattered coincidences. These approaches can be broadly divided into four main methods: empirical approaches [16], methods based on two or more energy windows [17, 18], convolution methods [19, 20] and methods which model the scatter distribution during forward projection based on knowledge of tissue densities (or attenuation coefficients) in the body and an initial estimate of the scatter-free image [21, 22].

A random coincidence event occurs when two annihilated photons from two different annihilation processes are detected within the coincidence window, and therefore appear as simultaneous to the PET scanner. The probability of the random coincidence increases with the size of the patient, because this increases the probability of one annihilation photon being attenuated completely. In the absence of detector dead time, the rate of random coincidence increases as the square of radioactivity within the field of view. Random coincidence increases with increasing the width of the energy window as well as the coincidence timing window and increasing the activity. Efforts have been made to minimize the random events by suing faster electronics and shorter time window; however, still further corrections are needed to improve the image contrast. A common correction technique is to employ two coincidence circuits, one with the standard time window (e.g. 6ns) and another with a delayed time window using the same energy window. The counts in the standard time window include both the random and true events, whereas the delayed time window contains only the random events. Thus, correction for random events is made by subtracting the delayed window counts from the standard window counts.

1.2.3. PET Image Reconstruction

PET reconstruction algorithms can be divided into two main types: analytical and iterative.

The most common analytical reconstruction algorithm is filtered-backprojection (FBP). The backprojection reconstruction techniques start by defining an image matrix (e.g. 128×128 pixels). For a detected LOR, a line is drawn between the two detectors and through the predefined image matrix.

The number of detected counts is added by a weighting factor proportional to each pixel that is intersected by the line path-length. The weighting factor is larger if the line passes across the centre of the pixel and smaller if the line passes through the corner of the pixel. This process is repeated for each detected LOR with adding counts to counts that have been backprojected from preceding detected LOR. A simple backprojection like this, results in a blurred image and places counts outside the object boundaries. To overcome these limitations, the Fourier theorem is used to relate the measured projection data from the sinogram with the activity distribution (i.e. the true image) using the Fourier transformation. A better approach is to modify the original sinogram by applying a ramp filter before backprojection, hence it is called filtered backprojection – FBP, and this is now the standard method. The ramp filter can be modified to improve the signal to noise ratio (SNR). Statistical noise, arising in the reconstructed image due to the Poisson statistical nature of the radioactive decay process, has a uniform contribution across the image. Reduction of the statistical noise and improvement in SNR can be achieved by rolling off the ramp filter at frequency smaller than the maximum frequency.

Iterative reconstruction techniques model the data collection process and attempt, in a series of iterations, to find the image that is most consistent with the measured data. Iterative reconstruction techniques were originally found to have less clinical use compared with FBP mainly due to the intensive computation required. However, as computer speeds continued to improve, these techniques now have more widespread clinical use. The basic idea behind iterative reconstruction techniques is to start with an initial guess of the image such as a uniform image. The next step is to calculate what projection data would be measured from the initial guess, a process called forward-projection which is typically the inverse of backprojection. Then this

projection data is compared with that corresponding to the true image using a function called a cost function. Obviously, there will be poor agreement between the initial guess and the true image. Based on the difference between the true and guessed projection data, the initial image is adjusted. Then the whole process is repeated while the estimated image starts to converge toward the true image until the estimated image closely matches the true image.

1.3. Potential Advantages of Using PET in Radiotherapy Treatment Planning

FDG is the most commonly used tracer in PET for radiotherapy treatment planning (RTP) [23]. FDG-PET has been used to assist with target volume delineation in RTP in patients, most commonly for non-small cell lung cancer (NSCLC) [24-30] and head and neck cancer [31-35], but also in cervix [36-38], oesophagus [39], lymphoma [40], rectum [41] and glioma [42].

PET has several advantages over other imaging modalities for cancer patients. Many forms of cancer become systematic, and the whole body PET scan provides a way to monitor the extent of the disease in a single setting. Moreover, because biochemical changes in the tumour occur before morphological changes, PET has the potential to detect disease earlier than morphological imaging modalities such as computed tomography and magnetic resonance imaging [43]. The use of FDG-PET images in radiotherapy treatment planning has been shown to decrease the intra- and inter-observer variation in delineating target volume [44, 45]. PET also offers two important features that could be used to improve the quality of radiotherapy treatment planning: (i) the effect of movement of the tumour, and (ii) the regional

variation of specific uptake within the tumour using positron-emitter labelled biomarkers to undertake molecular imaging of biological parameters such as hypoxia, angiogenesis, proliferation and apoptosis.

Many authors [45-47] have considered the effect of movement in the PET images to be a disadvantage. It could be considered as a drawback regarding the image quality due to the blurring effect at the target boundaries. However, it can be advantageous to predict tumour volume movements during normal respiration which occurs during a PET study. Therefore, using PET images to generate target volume is not a process of generating the gross target volume (GTV); rather it generates the internal target volume (ITV) as it considers the internal movement of the target [48, 49].

Ling et al [3] proposed the new concept of biological target volume (BTV) and multi-dimensional conformal radiotherapy (MD-CRT) which integrate the physical and biological conformity. The ability of intensity modulated radiotherapy (IMRT) to deliver a non-uniform dose pattern offers the ability of "dose painting" or "dose sculpting" which improves the physical conformity. On the other hand, the improvements of the functional images lead to the identification within a tumour of different biological areas representing hypoxia, tumour burden, and tumour growth, which can be individually targeted by radiotherapy. Some of these areas were considered a reason for radiotherapy failure such as the hypoxic region because it is radioinsensitive and needs higher radiation dose in order to be treated. By combining those two concepts, improvement in physical and biological conformity could be achieved.

1.4. Technical Issues Concerning The Use of FDG-PET Images in RT Target Volume Delineation

1.4.1. Lack of Specificity of FDG Uptake

Malignant tumours have a high metabolic rate and therefore take-up a higher amount of the FDG, which is a trapped tracer of glucose metabolism, than surrounding normal tissues.

However, not only tumour cells exhibit an increase of FDG uptake but also some inflammatory tissues such as occur in post-operative healing, and post radiotherapy [50, 51]. Many papers have shown that lesions with a high concentration of inflammatory cells show an increase in FDG uptake, which appears to increase the total tumour burden compared to that obtained from CT [52]. Using a tumour mouse model, Kubota et al. reported that 29% of FDG uptake was related to non-tumoural tissues [53]. In addition, FDG can accumulate in infected cells, whether acute or chronic such as tuberculosis [54], granulomatous diseases such as sarcoidosis [55], and autoimmune diseases such as Grave's disease [56].

Also, not all malignant tissues are avid to FDG. Tumours such as carcinoid, broncho-alveolar cancer, and mucinous adenocarcinoma have normal levels of glycolosis and are therefore not distinguishable by FDG-PET from normal surrounding tissues [52].

1.4.2. Image Artefacts

The main sources of these artefacts in PET images are due to scatter correction limitations, patient movement and emission-transmission scan

misalignments. However, the main reason for the image artefacts in PET/CT arises from the use of CT for attenuation correction of the PET images. These image artefacts are most commonly due to metallic implants, contrast medium, truncation and respiratory motion [57].

Metallic implants such as dental fillings, hip prosthetics or chemotherapy ports and contrast media such as iodine or barium sulphate result in high CT number (Hounsfield number). This increase in CT numbers results in correspondingly high PET attenuation coefficients, which lead to an overestimation of PET activity in that region and thereby to a false-positive finding [58]. Truncation artefacts in PET/CT are due to the difference in the size of the field of view (FoV) between the CT (Smaller) and the PET (larger) systems. These artefacts are frequently seen in large patients or patients scanned with arms by their side [59, 60]. Furthermore, respiratory motion produces artefacts due to the discrepancy in the chest position between the CT and PET images: because PET images are acquired during a long period while the patient is freely breathing, the final image is an average of many breathing cycles, whereas CT images are acquired during a very short time, usually while the patient's thorax is not moving during a breath hold.

Although the above image artefacts are potentially resolvable, the methods used can be time consuming and require more complex data processing. For example, many methods have been suggested to reduce or correct metallic and contrast artefacts [61-63]. These methods include generating a virtual sinogram from the affected CT images by forward back projection, segmenting the metallic or contract region from the CT images and then forward back projecting the metal only image to generate the metal only sinogram. The last is subtracted from the first and the missing projections are

replaced by interpolation from neighbouring data. Also, many authors have developed methods for correction of truncation artefacts [64-66]. A successful approach to removing truncation effects is to extrapolate the CT images outside the original FoV and hence produce a truncation free CT image. The respiratory motion artefacts can be overcome by using gated PET [67, 68] or 4D PET/CT [69].

1.4.3. Partial Volume Effect

The accuracy of PET for measuring regional activity is limited by the partial volume effect (PVE) [70]. The PVE for any PET system originates from the limited spatial resolution of an imaging system and is primarily due to two main phenomena: the point spread effect and the tissue fraction effect [71]. The point spread effect occurs because an imaging system has a limited spatial resolution so that a point in the object is spread out and appears larger in the image. Spatial resolution is usually expressed as the full width at half maximum (FWHM) of a Gaussian profile obtained when an object much smaller (less than half) than the system's resolution is imaged.

The direct consequence of the point spread effect is the loss of signal for structures with diameter smaller than about 2 to 3 times the system's spatial resolution [70]. This point spread effect can be characterised by measuring the point spread function (PSF) of the scanner [71, 72]. A correction factor, called the recovery coefficient (RC), then needs to be applied to recover the signal loss. The RC is defined as the ratio between the observed and true radioactivity concentration of the object and is influenced by the positron energy, detector spacing, object size and the mode of image reconstruction. The RC is 1 for large objects greater than several FWHM,

which for a modern PET scanner corresponds to > 4cm in diameter, and for a 1cm diameter object is approximately 0.2, see Figure 1.6.

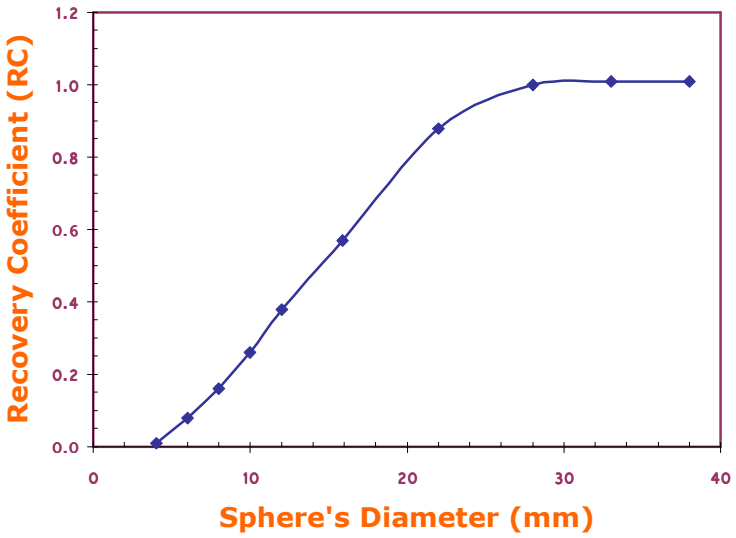

Figure 1.6: Schematic plot shows the maximum pixel recovery coefficient for different spheres diameters.

The tissue fraction effect causes one region's activity (the background) to spillover into the neighbouring regions. This effect refers to the underlying sub-resolution heterogeneity within the region of interest (ROI) which is un-resolvable by the scanner. In general, correction for this effect requires additional prior knowledge, for example from an adjunct MRI scan with intrinsically higher resolution enabling determination of the appropriate tissue fractions [70]. Most commercial PET systems now are offered with the option of resolution modelling sometimes also referred to as point spread function (PSF) reconstruction. This reduces the partial volume effect.

1.5. Overview of The Thesis

1.5.1. Project Aims

The main aim of this PhD thesis was to develop the use of PET/CT images for the use in radiotherapy treatment planning which have the potential to improve the accuracy of target volume delineation in radiotherapy. This included developing new thresholding techniques to accurately delineate the PET tumour volume. The primary objective was not only to develop and implement the new methods, but also to investigate their accuracies in more irregular shaped phantoms and then applying them to head and neck as well as lung patients.

This work forms the first step towards biologically adapted radiotherapy and may serve as a platform for developing these methods in different centres and also for further studies. Specific contributions can be summarized as follows:

- Study of the variations and correlations between the optimum threshold, true volume and observed contrast.
- Develop a semi-automated PET thresholding technique with two variants that accurately segments the true PET volume and compare the results with an established fixed thresholding technique.
- Develop phantoms to simulate irregular tumour volumes and investigate the use of the new segmentation technique in delineating their boundaries and volumes.
- Establish a concept of acceptable error of any segmentation technique tolerable for the purpose of radiotherapy treatment planning.

- Assess not only the accuracy of volume determination by the segmentation techniques, but also the similarity of lesion boundary outline and its location.
- Study the impact on the new technique of defining the maximum lesion uptake.
- Carry out preliminary patient evaluations using the newly developed techniques in comparison with the current best practice, which is manual delineation by an experienced radiologist as well as with manual delineation by the clinical oncologist.

1.5.2. Structure of The Thesis

Following this introductory chapter, chapter 2 contains a review of different segmentation techniques concentrating on techniques applicable to PET. Chapter 3 describes original work to develop and validate new PET thresholding segmentation technique. The results of investigating the accuracy of the new techniques in both spheres and irregular volumes are presented in chapter 4. Chapter 5 deals with the impact of determining lesion uptake in different ways on the new technique. The application of the techniques in head and neck and lung patients is presented in chapter 6. Chapter 7 gives summary, conclusions and suggestions for future work.

2

Chapter 2:

SEGMENTATION OF RADIOLOGICAL MEDICAL IMAGES

2.1. Introduction

The medical imaging modalities of computed tomography (CT), magnetic resonance imaging (MRI), ultrasound (US), single photon emission computed tomography (SPECT) and positron emission tomography (PET) are frequently used nowadays to provide key information to assist with the diagnoses, treatment planning and follow-up of individual patients in a wide range of diseases. Sometimes these imaging modalities are complementary rather than independent. For example, MRI, which is dependant on tissue water content, does not produce a good quality image for assessing bony structure, whereas CT, which is dependent on tissue attenuation of X-rays, is often

unsuitable for differentiating soft tissues which have similar levels of attenuation.

Segmentation is the process of dividing an image into regions, also called clusters, subsets, or classes, that share one or more particular characteristics or features. Soft segmentation allows these regions to overlap and hard segmentation produces nonoverlapping regions. An experienced radiologist can gain much information by visualizing each individual image, but segmentation may be able to additionally extract information of a quantitative nature. Because segmentation techniques depend on some characteristic of the image, there is no single segmentation technique that can be usable across all imaging modalities since for each the image formation process relies on different bio-physical mechanisms.

In the course of this project segmentation techniques on PET/CT have been developed to guide target volume delineation for the purpose of radiotherapy treatment planning (RTP). The quality of RTP depends on the accuracy of segmenting the organs at risk (OAR) and the gross tumour volume (GTV). The standard imaging modality for RTP is CT where the image is a map of tissue X-ray attenuation in Hounsfield units, and this allows accurate dose distribution calculations. However, the CT data relates to the anatomical distribution of tissues rather than information on the functional status. As a result, when undertaking post-therapy monitoring CT, it is not always possible for CT to differentiate between the different tissue types of residual tumour, fibrosis or a recurrence. A functional imaging modality such as PET is able to offer new information to help establish a more definitive differential tumour diagnoses.

2.2. Methods of Segmenting Radiological Medical Images

Segmentation of radiological medical images is typically achieved by either identifying all pixels or voxels that belong to an object or determining those that form its boundary. Therefore most segmentation techniques are based on one of two fundamental properties of digital images: (i) the discontinuity between regions in an image to detect isolated points, edges and contours, or (ii) similarities within regions to separate the image into distinct regions of coherence [73].

There are many segmentation techniques that have been proposed and used in different modalities. Most of these techniques can be summarized into six main approaches:

- Subjective visualization segmentation
- Thresholding segmentation
  - Adaptive thresholding
  - Fixed (simple) thresholding
  - Source/background thresholding
- Edge-based segmentation
  - Edge detection operators
  - Gradient-based approaches
- Region-based segmentation
  - Region growing
  - Watershed algorithms
- Deformable models
  - Active contour
- Fully-automated segmentation

- Adaptive fuzzy c-means (AFCM)
- Fuzzy locally adaptive Bayesian (FLAB)

These segmentation techniques will be discussed in detail in the following sections.

2.2.1. Subjective Visualization Segmentation

The subjective visualization technique is the first and simplest approach that allows manual drawing or delineation onto the radiological medical images using the computer pointer, usually a mouse. This technique is carried out on each 2D slice through the object of interest, and records the vertices at each mouse click and a straight or spline-fit line is drawn between each consecutive vertex to form a boundary. Alternatively, continuous sampling can be made of the mouse position to track a free-hand boundary. Voxels at this boundary and inside it are considered the segmented object. A surface triangulation algorithm is then applied to generate a surface mesh that represents the segmented volume in 3D.

The PET image has been used to aid in target volume delineation in CT images using the subjective visualization approach by comparing it with the corresponding co-registered CT image. Ciernik et al [74] have compared the variation in GTV size between using CT alone and co-registered PET/CT images. This study included 39 patients with various solid tumour diseases including head and neck, lung and pelvic cancer. The results showed that the GTV is significantly changed when incorporating the PET information, with a decrease in inter-observer variability. The study concluded that volume delineation is more consistent between observers when using PET/CT combined than CT alone.

Nishioka et al [75] studied the use of image fusion between PET and MRI/CT for better target delineation in radiotherapy planning of head and neck cancers. They reported that normal tissue sparing was more easily achieved due to clearer GTV and CTV determination on the fusion images. Moreover, after 18 months follow-up, no recurrence occurred in the CTV defined with PET assistance except for 1 patient (out of 12 patients) who experienced nodal recurrence in the CTV and simultaneous primary site recurrence. This preliminary study showed that image fusion between PET and MRI/CT was useful in GTV and CTV determination in conformal RT, and could improve sparing of normal tissues.

The subjective visualization segmentation approach has the limitations that it is time-consuming and depends critically on the user's skills. Caution must also be taken when segmenting irregular and complex volumes, where there are gaps and holes within the contours.

2.2.2. Thresholding Segmentation

Thresholding is the most widely used segmentation method [76], whereby regions are generated by binary partitioning of the image voxel intensities. The segmentation is achieved by identifying all pixels or voxels with intensities greater than the threshold value, and the rest of the image is marked as background [77]. The result of the thresholding segmentation is usually a binary image with all target segmented voxels given a value of 1 and all background voxels given a value of 0.

Different strategies have been used to determine the optimum threshold value, including use of a fixed (simple) threshold value, an adaptive threshold value or source/background thresholding algorithms. Such threshold

values could be based on the image histogram or other local properties, such as the maximum activity concentration in the tumour, or, for PET, the standardized uptake value (SUV).

2.2.2.1. Adaptive thresholding

Studies have demonstrated that the selection of the threshold value depends on the size, shape, and contrast of the organ of interest [76, 78]. It has been shown that when a-priori knowledge of the size, shape, and contrast of the lesion is available, threshold levels can be more precisely determined for improved accuracy.

Erdi et al [76] developed an automatic image segmentation schema to determine the volume of interest (VoI) of metastases to the lung from PET images, under conditions of variable background activity. By estimating the lesion size from CT and determining the signal to background ratio (S/B) from PET, the appropriate optimum threshold could be calculated. The adaptive thresholding method was successfully applied to a small group of patients using a priori information about the tumour size from the CT. In the authors' opinion, this establishes PET with CT-guided adaptive thresholding method as a potentially accurate method for estimating lesion volume in macroscopic disease.

2.2.2.2. Fixed (simple) thresholding

It has been found that if CT data is not available to initially estimate a priori lesion volumes, a fixed threshold of 36 to 44% (commonly 40%) of the maximum uptake results in a VoI that accurately predicts the true lesion volume for lesions larger than 4 ml [76]. This technique requires measurement of only the S/B value from the PET image, and a prior

calibration of threshold versus S/B for the PET scanner, over the range of imaging conditions encountered clinically. However, for smaller volumes (< 4 ml), fixed threshold levels may overestimate the volume by an amount that depends on the S/B ratio.

Biehl et al [79] have used different fixed SUV thresholds to determine which SUV value produced the most accurate tumour volume. The authors investigated different thresholds from 15 to 50% of the maximum SUV (SUV_{max}) and applied this in a series of patients with peripheral non-small cell lung cancer (NSCLC). They found that the optimal threshold was inversely correlated with the CT-determined GTV (R^2 = 0.79, P < 0.0001), and that there was no single threshold value that could accurately measure the PET volume. It concluded that the good correlation of the optimal threshold with the CT-determined GTV warrants further investigation.

2.2.2.3. Source/background Thresholding Algorithms

Source/background (S/B) algorithms are considered as a semi-automated approach that involve scanner calibration with a phantom, and are implemented without a priori information of the size of the volume of interest. As developed by Erdi et al. [80], this approach starts by deriving the relationship between the true volumes of uniform spheres and the optimum threshold for various S/B ratios. Daisne et al. [81], however, derived the relation between optimum threshold and S/B.

Jentzen et al [82] described an iterative thresholding method (ITM) where an iterative algorithm searches for the optimum threshold value based on the S/B of the VOI drawn around the lesion. This method employed phantom calibrations for two different tracers (^{18}F and ^{124}I), and was applied

to phantoms and patients with different disease sites, including lung, head and neck, and gastrointestinal carcinoma. Significant limitations were found with inaccuracies of predicting smaller, larger, and inhomogeneous volumes. Also, errors associated with lesion masses moving during data acquisition were not taken into account.

2.2.3. Edge-Based Segmentation

Edge-based segmentation techniques rely on the gradient in image data at the borders of the image structures as the pixel values change rapidly at the boundary between two different regions.

2.2.3.1. Edge detection operators

There are many ways to perform edge detection which usually require calculation of convolutions. The two most widely used techniques for edge detection are the Sobel gradient method [83] and the Laplacian second derivative approach [84]. The Sobel method detects the edge by searching for the minimum and maximum in the first derivative of the image, while the Laplacian method detects the edge by searching for the zero crossing in the second derivative of the image.

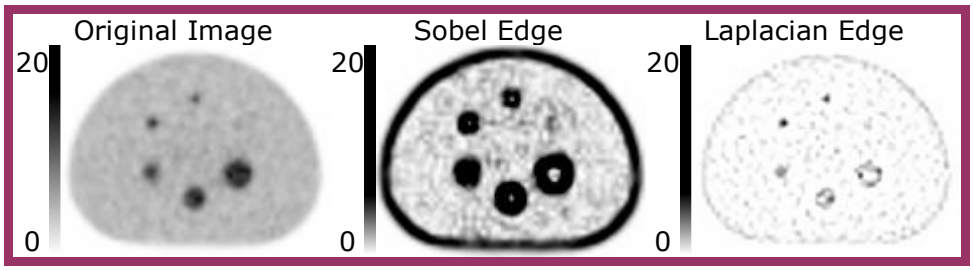

Figure 2.1: Edge detection using Sobel and Laplacian operators. The original image represents the IEC image quality phantom for contrast equal to 3. The colour scale bars are in kBq/ml.

Figure 2.1 shows the results of applying a pair of 3×3 Sobel masks to estimate the gradient in x and y direction respectively:

$$\boldsymbol{S}_x = \begin{bmatrix} -1 & 0 & +1 \\ -2 & 0 & +2 \\ -1 & 0 & +1 \end{bmatrix} \qquad \boldsymbol{S}_y = \begin{bmatrix} -1 & -2 & -1 \\ 0 & 0 & 0 \\ +1 & +2 & +1 \end{bmatrix}$$

The Laplacian edge detection technique uses a single 3×3 mask in both x and y direction, as shown below:

$$\begin{bmatrix} 0 & -1 & 0 \\ -1 & +4 & -1 \\ 0 & -1 & 0 \end{bmatrix}$$

This technique is very sensitive to noise as is evident in Figure 2.1.

2.2.3.2. Gradient-based Approaches

For the gradient-based approach, the boundaries of a region are given by peaks in the gradient intensity. The method works well for MRI and CT where the images have relatively low statistical noise, but it has been also explored for PET by Geets et al. [85] after the images have undergone processing to reduce the noise. In this study, a better estimation of the gradient intensity was achieved by denoising and deblurring the iteratively reconstructed PET images with an edge-preserving filter and a constrained iterative deconvolution algorithm. This gradient method was validated first on a computer-generated 3D phantom with spherical lesions, and then on a cylindrical Lucite phantom containing spheres ranging in size from 2.1 to 92.9 ml.

Geets found that the gradient-based approach underestimated volumes in simulated data by 1.3 – 10% for large and small volumes respectively; the corresponding results on real phantom lesions was found to be 10 – 20%. Geets applied his method to laryngeal tumours from seven patients and compared his results with those obtained following surgical resection, and the S/B algorithm employed by Daisne et al [81]. This comparison reveals that neither the threshold-based nor the gradient-based method could measure the volume of the laryngeal specimens with sufficient accuracy. However, the gradient-based method proved to be more accurate than the threshold-based method.

2.2.4. Region-Based Segmentation

An alternative to defining the lesion by delineating its edges is to use a region-based segmentation approach whereby the whole continuous lesion is identified. The first region-based segmentation technique to be developed was the split and merge algorithm [86] which starts by assuming that the entire image is a single region and then deciding whether the homogeneity criteria is achieved within this region or not. If not, the image is divided into four smaller squares and the process is repeated on each square until no further subdivision is necessary. The resulting regions are then merged to form the segmented object. Two other region-based segmentation techniques, region growing and watershed are presented in this section.

2.2.4.1. Region growing

Region growing is a segmentation technique for extracting an image region based on some predefined criteria based on parameters such as pixel intensity or the edge information in the image. Region growing, also called region

merging, starts by defining a pixel or group of pixels called seeds that belong to the region of interest. The seeds can be chosen manually or automatically by a seed finding programme. Neighbouring pixels are examined one by one and grouped to the growing region if they are sufficiently similar to the seed based on a uniformity test. This process continues until no more neighbouring pixels can be added according to the predefined criteria.

Confidence connected region growing (CCRG) is a region growing technique that was presented by Day [87] to segment PET positive regions. This method initiates by measuring the mean and the standard deviation of a sub-region surrounding the maximum intensity pixel. The decision of connecting the neighbouring pixels or not is based on a criterion that they have to be greater than a value derived from the mean and standard deviation of the region. The process is then repeated after measuring the mean and the standard deviation of the new region. The CCRG method was evaluated in a series of 18 patients who received radiotherapy. The segmented volumes derived using CCRG were compared with volumes determined by fixed thresholds of 2.5 SUV and 43% of SUV_{max}, and also with manually segmented volumes. CCRG provided the best results with a mean difference of 9% (range from 1% - 27%).

2.2.4.2. Watershed algorithms

Watershed is also a region-based segmentation technique which was first introduced by Digabel and Lantuejoul for image segmentation in 1977 [88]. The main idea of this segmentation technique came from geography where any grayscale image can be considered as a topographic surface with the altitude of each point represented by the pixel intensity. Let us imagine a

stream of water is running into this landscape topology under gravity causing pools to collect in the low basins. The water will fill up these small basins and start to spillover into neighbouring larger basins. This process will continue until the waters reach the highest peak in the landscape. This will end by dividing the landscape (or image) into large basins (or regions) separated by hills and ridges (or watersheds).

Watershed algorithms have been used to segment the noisy transmission PET scan to reduce the scanning time [89] as well as segmenting PET positive volumes for the purpose of RT target volume delineation [90]. In the latter study, a watershed algorithm using PET image characteristics was developed and implemented in both homogeneous and heterogeneous phantoms. This method starts by the user placing markers on the regions of interest and the background. The method is then considered as a topographic surface and simulates a flooding from each marker and preventing the merging the water coming from different sources. The percentage error in determining the PET volumes, which were greater than 4ml, using this watershed technique reached 52%.

2.2.5. Deformable Models

The pioneering work of Terzopoulos et al. [91] in 1988 introduced the concept of deformable models which draw on geometry, physics and approximation theory. The name "deformable models" is derived from the physics of elasticity theory, within a Lagrangian dynamics setting. The physical interpretation of the deformable models is an elastic body that respond naturally to applied forces and constraints.

2.2.5.1. Active contour

The active contour model, commonly known as snake , was first introduced in 1987 by Kass et al. [92]. The snake is a parametric curve defined within the image domain where its behaviour and properties are specified by an energy function. This parametric curve is allowed to deform under the influence of external force or energy. The snake attempts to minimize that energy associated with the parametric curve as a sum of internal and external energy. The snake evolves in a way that is determined by the sum of different types of velocities that act perpendicularly to each point of the snake curve. Some of these velocities are image-dependent while others depend on the shape of the snake. The movement of a point on the snake curve is determined by the sum of the velocities at that point. The process iterates until the energy minimization criterion is achieved. The internal energy is minimum when the snake shape is similar to the object, and the external energy is minimum when the snake is at the object boundary.

For 3D segmentation, snake models are applied slice by slice where the fitted contour in one slice has been taken as the initial contour in the neighbouring slice [93]. The snake method has also been extended to 3D by deforming surfaces instead of curves in a technique known as balloon segmentation [94]. Active contour models have the potential to be used in real-time analysis of shapes in motion.

El Naqa et al [95] attempted to segment a biophysical structure volume using the active contour model in multimodality images including PET, CT and MRI. They investigated a method to take advantage of all imaging modalities for radiotherapy treatment planning by segmenting the target volume using an active contour on each modality and combining the results.

The resulting volume error in phantoms was 1.28 ± 1.23%. This method was demonstrated in two patients with PET modality and showed the accuracy and the potential of using concurrent multimodality segmentation.

2.2.6. Fully-Automated Segmentation

All the previously mentioned techniques involve interaction from the user to some degree. A number of approaches have been described which are entirely automated, of which, the adaptive fuzzy c-means and fuzzy locally adaptive Bayesian will be presented here.

2.2.6.1. Adaptive fuzzy c-means (AFCM)

Clustering is a segmentation technique that relates to the similarity property of digital images. Clustering is the process of partitioning the image into subsets called clusters so that the data in each cluster share some common characteristic. Fuzzy c-mean clustering (FCM) developed by Dunn in 1973 [96] and improved by Bezdek in 1981 [97] is the most widely used clustering technique. The FCM clustering attempts to partition the image into a collection of c clusters in which each point within these clusters belongs to two or more clusters with varying degrees of membership instead of belonging to just one cluster. Thus, points at the edge of a cluster belong to lesser degree to that cluster than points in the cluster centre. However, the hard c-means (HCM) algorithm, also known as K-means, attempts to partition the image in which each point belongs to a single cluster. The FCM algorithm suffers from long computational time and sensitivity to the noise level and the initial guess, however there have been several attempts to improve its accuracy[98].

A new fuzzy c-means algorithm called adaptive fuzzy c-means algorithm (AFCM) has been developed [99] to reduce the errors associated with inhomogeneity within the image by simultaneously compensating for these inhomogeneities. The AFCM is an unsupervised clustering technique that iteratively clusters the image by minimizing the objective function and produces a fuzzy membership function that ranges between zero and one which reflects the degree of similarity.

2.2.6.2. Fuzzy Locally adaptive Bayesian (FLAB)

The fuzzy algorithms have been developed and implemented specifically for PET, as the Fuzzy Locally Adaptive Bayesian (FLAB) technique [100, 101]. FLAB is a segmentation model that takes place in the Bayesian framework of statistics to estimate the probability a voxel to be classified as part of the tumour or part of the background. Bayesian based image segmentations were shown to be less sensitive to noise rather than other segmentation techniques due to statistical modelling. This technique offers an unsupervised estimation of the parameters needed for the segmentation and limit the user's input.

The performance of the FLAB model was compared with other segmenting methods such as thresholding (fixed 42% and adaptive thresholding) and FCM [100]. The results showed that FLAB is better than these other methods especially for small volumes (down to 13mm, ~9.2 ml) where the error was 5-15%. In non-spherical and non-uniform volumes simulated from three different patient lung lesions with diameters 41, 29 and 15mm, and contrast ratios of 6:1, 5:1 and 2:1 respectively, the FLAB method produced errors less than 10%.

2.3. Evaluation of Volumetric Measurements

Among all the previously presented segmentation techniques, the percentage error in volume was the only measure employed to assess accuracy, without any indication of what magnitude of error would be acceptable for clinical use. Also, the intention in the previously cited publications was merely to obtain the absolute volume size without investigating other details such as the shape and location of the segmented volume. In this thesis, methods for defining the acceptable error, correctness of shape and location are introduced in the following sections.

2.3.1. Acceptable Error

The main focus of this thesis is the delineation of PET tumour for the RTP. It is therefore rational for the accuracy of this delineation to correspond with the accuracy that is acceptable for RTP. In treatment planning and according to ICRU reports 50 and 62 [1, 2], a ±2mm error in distance measurement is the acceptable limit for defining the tumour boundary. This ±2mm distance can be translated to an error in volume which will be dependent on the original volume size, as shown in Figure 2.2. Therefore the concept of an acceptable error, E_A, for the purpose of tumour segmentation intended for RTP can be defined using this criterion.

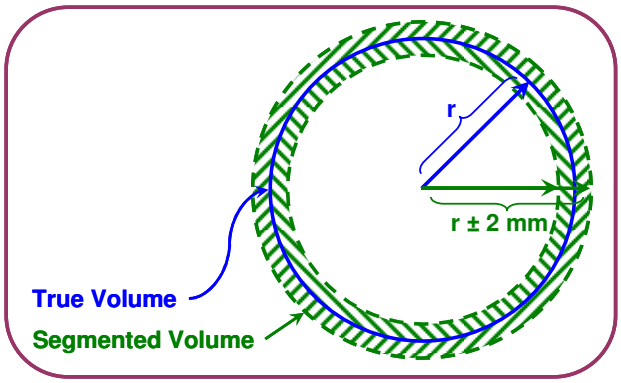

Figure 2.2: The basis of an acceptable error for the purpose of treatment planning.

Thus, in measuring the volume V_r of a sphere with radius r, compared with another sphere with radius r±2 mm, the acceptable error, E_A, can be given by equation (2.1).

$$E_A(\%) = \left(\frac{V_{r\pm2} \times 100}{V_r} \right) - 100 = \left(\frac{(r \pm 2)^3}{r^3} - 1 \right) \times 100 \quad \textbf{..... (2.1)}$$

The sphere has the lowest surface-to-volume ratio of all objects. Therefore, this equation describes a best case scenario. It is apparent that E_A will vary according to the volume of the lesion, as the modulus E_A presented in Figure 2.3. It can be seen that relatively large errors are tolerable for the purpose of RTP, with approximately 20% being acceptable at large volumes, and increasing to high values in excess of 50% at smaller volumes.

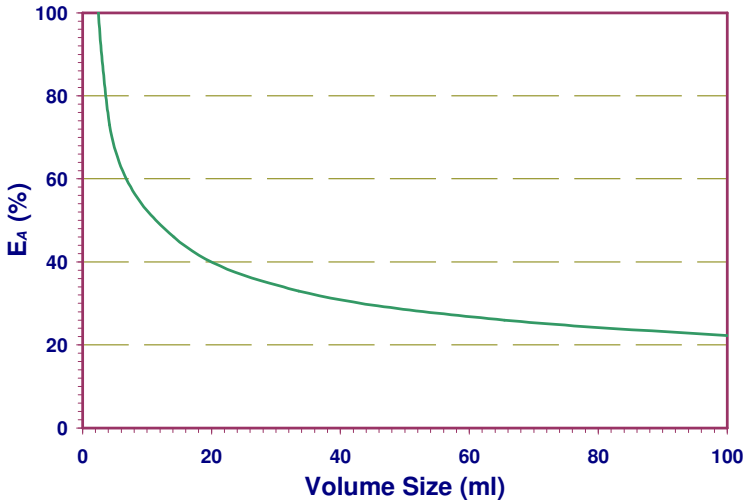

Figure 2.3: Curve representing the modulus acceptable error, E_A, as defined by equation (2.1).

2.3.2. Concordance Measurement

The aim of the concordance measurement is to measure the similarity of the boundaries between two 3D surfaces, which for the purpose of this work are the true volume and the volume determined by the segmented technique. Two statistical approaches are suitable for these measurements

- Jaccard Similarity Coefficient (*JSC*)
- Dice Similarity Coefficient (*DSC*).

2.3.2.1. Jaccard Similarity Coefficient (*JSC*)

The Jaccard similarity coefficient (*JSC*), also known as Jaccard coefficient index was originally proposed by Jaccard [102] as a statistical measure of similarity between sample sets. For two sample sets A and B, Figure 2.4, it is defined as the cardinality of their intersection divided by the cardinality of their union, as given by equation (2.2). The *JSC* index has a maximum value of 1 when both sample sets are identical.

$$JSC = \frac{|A \cap B|}{|A \cup B|} = \frac{c}{a + c + b} \qquad \text{..... (2.2)}$$

where c, is the number of voxels that are common to A and B, a, is the number of voxels unique to A, and b is the number of voxels unique to B.

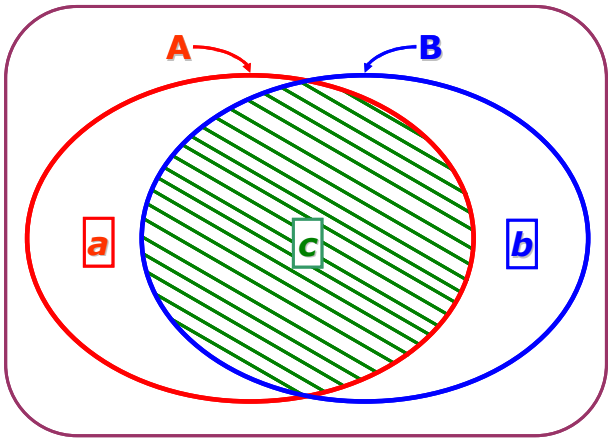

Figure 2.4: Two sample sets A and B where c, is the number of voxels common to A and B; a and b are the numbers of voxels unique to A and B respectively.

2.3.2.2. Dice Similarity Coefficient (*DSC*)

The Dice similarity coefficient (*DSC*) was originally proposed by Dice in 1945 [103] and it has been widely used [95, 104, 105] to evaluate the similarity between true and segmented volumes. *DSC* is defined as:

$$DSC = \frac{2|A \cap B|}{A + B} = \frac{2c}{a + 2c + b} \qquad \text{..... (2.3)}$$

Using the same nomenclature as for the *JSC*. The *DSC* index has a maximum value of 1 when both volumes are identical.

2.3.3. Distance Transformation Maps

In order to measure the distance between the boundary locations of the true and segmented volumes, a distance map needs to be computed. The distance map [106] is an image in which each voxel's value is the distance from this voxel to a reference object. The Euclidean distance transformation (EDT) is an algorithm that calculates the distance map for a binary image that represents the segmented volume [107] as below. Zhang et al. [105] have used this algorithm to measure the distance between the boundaries of reference and true volumes.

$$d(a,b) = \sqrt{\sum_{i=1}^{n} (a_i - b_i)^2} \qquad \textbf{..... (2.4)}$$

where *d(a,b)* is the distance between the voxel a of the true volume boundary to the voxel b of the segmented volume boundary and n is the number of voxels in the segmented boundary. The nearest distance between the two boundaries is obtained by comparing the boundary location of the segmented volume with the corresponding value on the distance map of the true volume.

2.4. Limitations of The Available PET/CT Segmentation Techniques

The PET/CT segmentation techniques that were presented in chapter 2 are variable in terms of computational complexity, the degree of user interaction required, and degree of accuracy. Although subjective visualization by experts is still the most widely used technique [108], it suffers from intra-observer variability which is due to its subjectivity and sensitivity to the display window

level settings. Thresholding techniques, however, are simple and efficient to put into practice although scanner specific parameters need to be accurately calibrated in order to gain accurate results [109].

Edge-based and region-based segmentation techniques for PET/CT are affected by the limitations of the system response of a PET scanner arising from the inherent characteristics of relatively low spatial resolution and high noise. It has been shown that the direct application of the Sobel edge detection and watershed techniques to PET images fails to accurately measure the volume size compared to thresholding techniques [110].

The fully-automated techniques have the disadvantage for routine clinical use of having a high computational burden. Therefore, the balance between the algorithm complexity and obtaining the right results is very important in selecting the optimum segmentation technique.

For all the techniques outlined in Chapter 2, the only evaluation criterion considered has been the percentage error in the volume measurement. However, it is possible that a small percentage error in volume can occur while the lesion boundary exhibits a very different shape from the true surface, and additionally the position may not be correctly located due to the motion of the patient physically or physiologically, such as in respiration. Therefore, in addition to the error in volume determination a more comprehensive evaluation of the techniques is warranted, such as determination of the shape and location of the segmented PET volume. In addition, most of these techniques have not been evaluated for accuracy in patient studies, but only in phantoms.

Furthermore, the phantoms used usually represent lesions of simple shapes such as spheres and cylinders, whereas not all tumours are spherical or cylindrical, and many are not homogeneous. For a realistic evaluation of a new method it is important that irregular and inhomogeneous volumes should be considered. These factors are taken in account for this project, as described below.

2.5. Justification for A New PET/CT Segmentation Technique

The aim of this research was to develop an accurate, practical and reliable PET segmentation technique that is easily implementable in a routine clinical setting. As described above, the most widely used PET segmentation techniques are thresholding and subjective visualization. However, the subjective visualization technique requires a consensus reading by nuclear medicine and radiation oncology physicians which is difficult to achieve in busy departments and is time consuming.

Previous studies [76, 78] have shown that the value of the optimum threshold depends on the size and shape of the lesion and the contrast. The aim for implementation was to be able to automatically compute a lesion boundary and lesion volume on any patient image using the optimum threshold for that particular patient lesion, using only a simple measurement the lesion contrast.

3

Chapter 3:

DEVELOPMENT OF NEW PET/CT VOLUME SEGMENTATION TECHNIQUES

3.1. Introduction

The main aim of this PhD study was to develop the use of PET/CT images for use in radiotherapy treatment planning (RTP). Among all the previously described methods for delineation of PET lesions, a standard method suitable for routine clinical use has not yet been demonstrated. Therefore, this study aims to develop a reliable and robust method which is suitable for application on a day to day basis in the clinic, and which does not require any a priori information about the size or shape of the lesion. So the aim was to develop a method for lesion delineation that is independent of the lesion's contrast, volume size or shape, and noise level in the image. In this chapter, the

development of two new semi-automated techniques based on thresholding that meet the above aims is presented.

3.2. Materials and Instruments

3.2.1. Scanner

Images were acquired using a GE Discovery STE 8 PET/CT scanner (GE Healthcare), which combines the two modalities, PET and CT, to create fused PET/CT images.

The PET component in the PET/CT scanner consists of a multi-ring bismuth germanate (BGO) block detector system arranged in 24 rings to acquire 47 slices over an axial length of 15.4 cm, with a 70 cm patient bore. The crystal dimensions are 6.3mm (axial), 4.7mm (transaxial), and 30mm (radial) with a total of 13,440 crystals (6×8 crystals in a block, 2×4 blocks in a module and 35 module in a ring). The PET scanner has a 3D spatial resolution FWHM of 5.05 mm transaxially, 5.39 mm axially, and a 3D sensitivity of 7.53 counts/sec/kBq and 8.33 counts/sec/kBq at the centre and 10 cm radially off the centre respectively [111].

The CT component in the PET/CT scanner consists of a single x-ray tube with an eight slice detector and can be operate in axial or helical mode, with a full rotation time of 0.5 second. Two types of image are produced: one for attenuation correction of the PET images where the Hounsfield values are scaled to attenuation factors at 511keV; and another have a diagnostic quality image for the purpose of fusion with the PET images.

The scan protocol usually starts by performing a low-dose scout image, a planar X-ray, also known as a topogram, which is used to identify the bed

positions needed for the PET and CT scans. Then the bed moves to the start of these defined bed positions to acquire the CT scan. Next, the whole bed assembly moves from the CT scanner location to the first bed position for the PET acquisitions.

3.2.2. Phantoms

3.2.2.1. Spherical phantom

An image quality phantom made of Perspex, IEC Body Phantom Set™, as specified by National Electrical Manufacturers Association (NEMA) [112, 113], was used for a number of data acquisitions in this project. This phantom and its components are fillable with liquid, as shown in Figure 3.1, and it consists of a body phantom (torso cavity), a lung insert (removable), and a set of six removable spheres of volumes 26.6, 11.5, 5.55, 2.57, 1.15 and 0.53 ml.

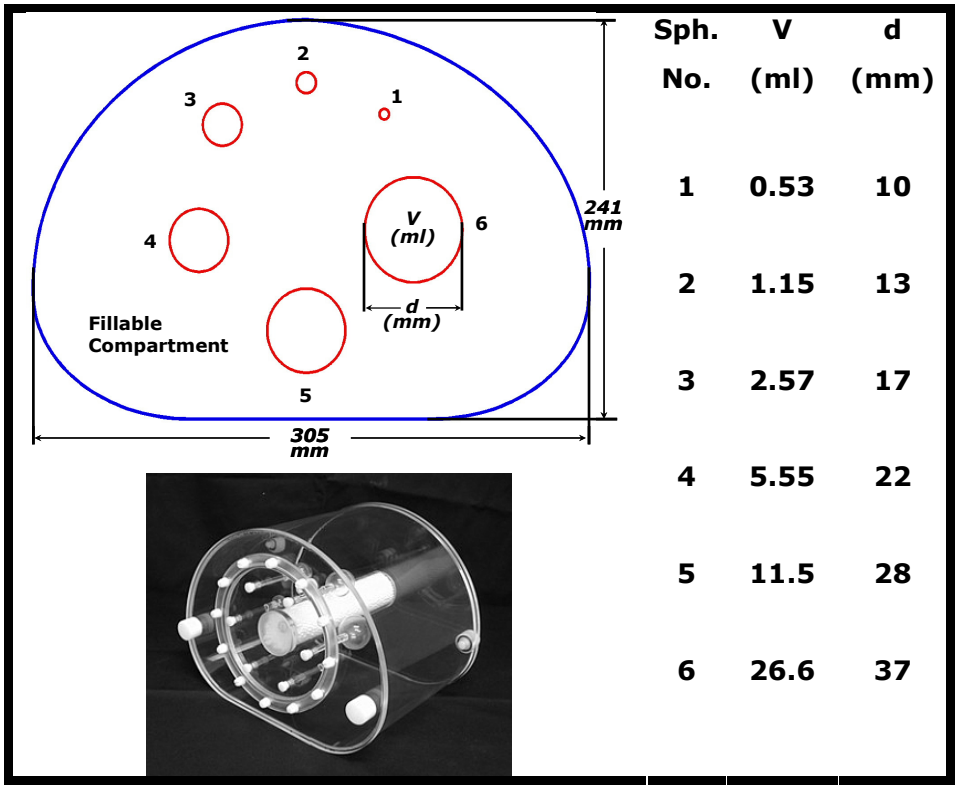

Sph. No.	V (ml)	d (mm)
1	0.53	10
2	1.15	13
3	2.57	17
4	5.55	22
5	11.5	28
6	26.6	37

Figure 3.1: IEC body phantom with fillable spheres of different volume and diameter

3.2.2.2. Irregular phantom

Two families of irregularly shaped phantoms, named "top-hat" and "crescent" as shown in Figure 3.2 (a) and (b) respectively, were constructed. Each family consisted of two fillable thin wall thickness, 0.1 mm, Perspex cylinders of different radii. In the first case, one smaller cylinder was joined concentrically to a larger second cylinder to create a fillable region in a top-hat shape, and in the second case, the smaller cylinder was fixed off-centre inside the larger to create a fillable region, which, in axial cross section, forms a crescent shape. There were four top-hat volumes of 101.8, 71.4, 30.0 and 8.69 ml, and four crescent volumes of 96.1, 66.8, 29.1 and 4.89 ml (appendix I presents the detailed dimensions). These were each inserted into the torso cavity of the IEC Body Phantom Set™ (after removing the spherical inserts), and fastened to the lung insert. The lung insert was filled with a mix of water and expanded polystyrene beads to simulate a region of inhomogeneity in the background. For the crescent family, the inside cylinder (smaller volume) was filled with a different activity concentration from the outer volume.

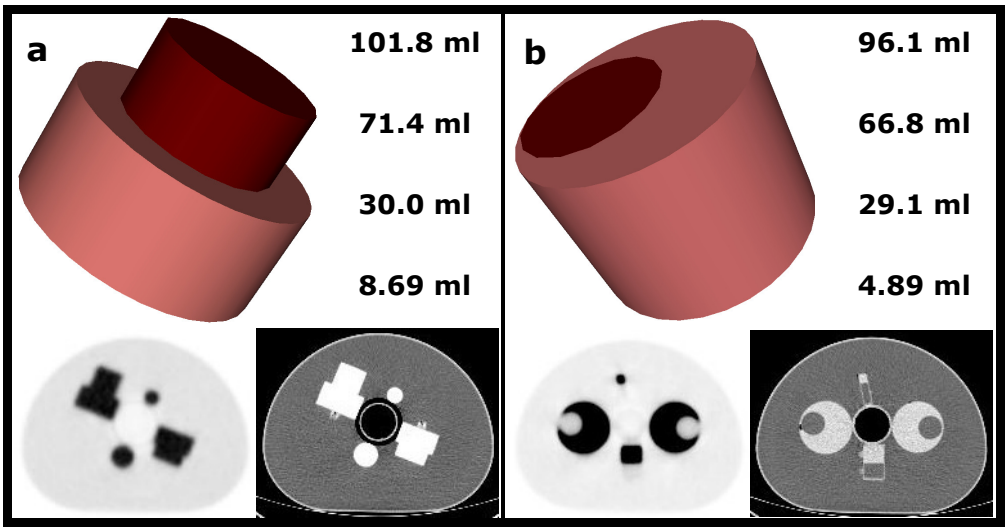

Figure 3.2: Validation irregular phantoms represent 3D, PET and CT images of the Top-hat (a) and Crescent (b), with different volume sizes.

3.2.3. Data Analysis

Image analysis and implementation of both VCAT and CAT methods were carried out using in-house software developed in IDL (Interactive Data Language, ITT Visual Information Solutions). The full IDL code is presented in appendix II.

3.3. Phantom Image Acquisition and Reconstruction

In all phantom acquisitions, the phantom was placed centrally and a single bed position was acquired in 3D mode. A dynamic protocol was set to acquire a series of eight different acquisitions of: 1, 2.5, 5, 10, 15, 20, 30 and 60 minute acquisition times (t_{AC}) to produce different image noise levels. CT-based attenuation correction and randoms correction from singles were applied.

Two different reconstruction techniques were investigated during this study: fully 3D filtered back projection (FBP) [114] and iterative (IT) [115] reconstruction. The reconstruction parameters used were the same as for routine patient studies in the department. In case of FBP, transaxial Hanning filter (cutoff of 0.12 mm^{-1}) was used, and in case of IT, 28 subsets and two iterations with a Gaussian post-filter of 6 mm were used. The PET matrix size in both IT and FBP was 128×128×47 for a field of view (FoV) of 70 cm, with voxel size 5.47×5.47×3.27 mm. For the purpose of evaluating the concordance of the PET segmentation with object boundaries seen on CT, the PET images were reconstructed to match the CT matrix size, using the same parameters but using a FoV of 50 cm and voxel size of 3.91×3.91×3.27 mm.

The CT acquisition parameters were 120kVp, automatic current ranging from 30 – 44 mA with noise index of 40, and a pitch of 1.675. The CT images were reconstructed with 3.27mm slice separation (to match that of the PET images), and a matrix size of 512×512×47 (voxel size, 0.98×0.98×3.27 mm) for a FoV of 50 cm. These are the same as for routine patient studies in the department.

3.4. Volume and Contrast Adjusted Thresholding (VCAT) Method

The new method developed in this project requires calibrations to be carried out to determine the relationship between the optimum threshold and the true volume. This relationship is contrast dependant. The threshold value is effectively adjusted automatically allowing for both the contrast and volume of the lesion, to be the optimum value to obtain the correct volume measurement, hence the terminology: Volume and Contrast Adjusted Thresholding, VCAT. A set of calibration curves are required to represent the relationship between the optimal threshold, T_{opt}, and lesion volume, V, for fixed contrast, C. The VCAT method does not depend on a priori information from the PET or CT images, and the only parameter that needs to be measured is C, which references a previously determined calibration curve, as described below.

A key factor in measuring small volumes on PET images is the partial volume effect, which causes the observed contrast (C_o) to be different from the true contrast (C_t), as previously described in chapter 1. In patients, it is easy to measure C_o but it is difficult to accurately determine C_t. Therefore, in this study, C_o has been used in all measurements. C_o is defined as the ratio

between the maximum voxel count within a volume of interest (VoI) drawn around the lesion, and the mean counts within a background VoI, manually delineated in all planes that contain the lesion. Alternative definitions will be investigated in chapter 5.

To develop the VCAT calibration curves the relationship between the true volume (V) and the optimum threshold (T_{opt}) needs to be calculated for a fixed observed contract (C_o). First, the relationship between T_{opt} and C_o needs to be determined to correct the T_{opt} value to a corresponding fixed C_o, then the corresponding T_{opt} was used when determining the relationship between T_{opt} and V. Therefore, the process of developing the VCAT calibration curves is in two stages as set out in sections 3.4.1 and 3.4.2 below.

3.4.1. Variation of Threshold with Lesion Contrast

The process of generating the VCAT calibration curves starts by determining the relationship between T_{opt} and C_o. Acquisitions of the IEC Body phantom with spheres containing ^{18}F were carried out to simulate true lesion contrasts, C_t, of 2, 3, 5, 9 and ∞ (i.e. no background). To emulate tissue background, the body of the phantom was filled with a solution of ^{18}F at a concentration of 5 kBq/ml for all values of C_t, except for $C_t = \infty$ where the background was plain water. These acquisitions were performed three times, the results averaged, and the standard deviation and error were calculated to incorporate the effects of repeatability and to minimise errors.

For each sphere, 3D volumes were derived for incremental percent threshold values, where 100% represents the maximum voxel value within a VoI manually drawn around the sphere. By plotting these volume values against threshold and by knowing the true volume of each sphere, the T_{opt} for

each sphere at each C_o was measured, as shown in Figure 3.3. For each experiment, this generated a series of values for T_{opt} that measures the true volume V at a particular observed contrast C_o.

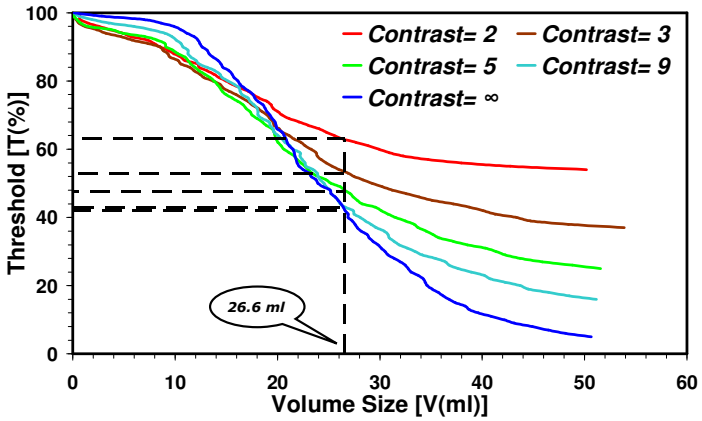

Figure 3.3: Threshold volume curves for 26.6 ml spherical volumes at different contrast values to obtain the contrast-dependent optimal threshold, T_{opt}.

Figure 3.4 shows the relation between T_{opt} and C_o for two spherical volumes.

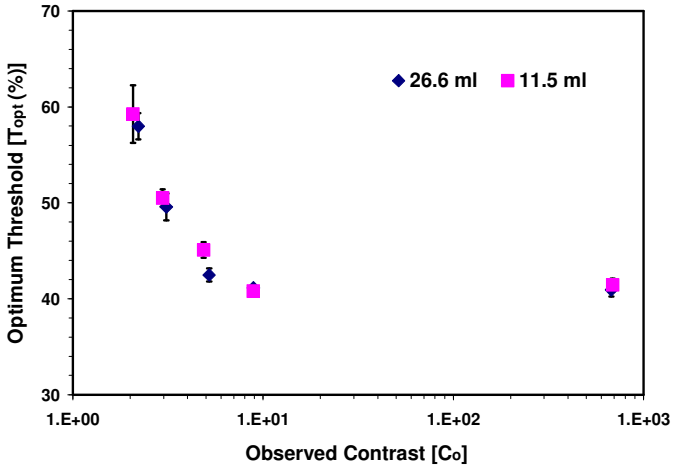

Figure 3.4: The relation between T_{opt} and C_o for 26.6 and 11.5 ml volumes. A logarithmic scale used in C_o direction to show the ∞ values. The error bars represent the standard error from three different experiments.

The behaviour of this relationship is of the form $y = f(x^{-1})$, equation 3.1, or $y = f(x^{-2})$, equation 3.2.

$$y = f\left(x^{-1}\right) = \left(\frac{a}{x}\right) + b \qquad \textbf{..... (3.1)}$$

$$y = f\left(x^{-2}\right) = \left(\frac{a}{x^2}\right) + \left(\frac{b}{x}\right) + c \qquad \textbf{..... (3.2)}$$

Therefore, with $y = T_{opt}$ and $x = C_o$, a weighted least squares fit of the data to these two equations was carried out and the Chi-square (χ^2) test was applied to determine the goodness of the fit.

In determining the relationship between optimum threshold (T_{opt}) and observed contrast (C_o), a weighted least square fitting technique was used to fit T_{opt} with C_o to two possible equations (3.1) and (3.2). Figure 3.5 shows the fitting of T_{opt} and C_o to equation (3.2) for different spherical volumes, 26.6, 11.5, 5.55, 2.57, 1.15 and 0.53 ml, at 1, 2.5, 5, 10 and 60 minute acquisition times (t_{AC}) for both iterative (IT) and FBP reconstruction techniques. The error bars represent the standard error of three experiments undertaken with the same C_t value. A χ^2 test demonstrated that the second order equation (3.2) provided the overall best fit across all volumes, acquisition times and reconstruction techniques.

Close observation of the data in Figure 3.5 indicated that a single equation could represent the relation between T_{opt} and C_o for volumes > 1.15ml, and if this were to be the case it would be possible to determine the value of T_{opt} for different volumes by measuring only the value of C_o. The results of this method are going to be presented in the next section (section 3.5).

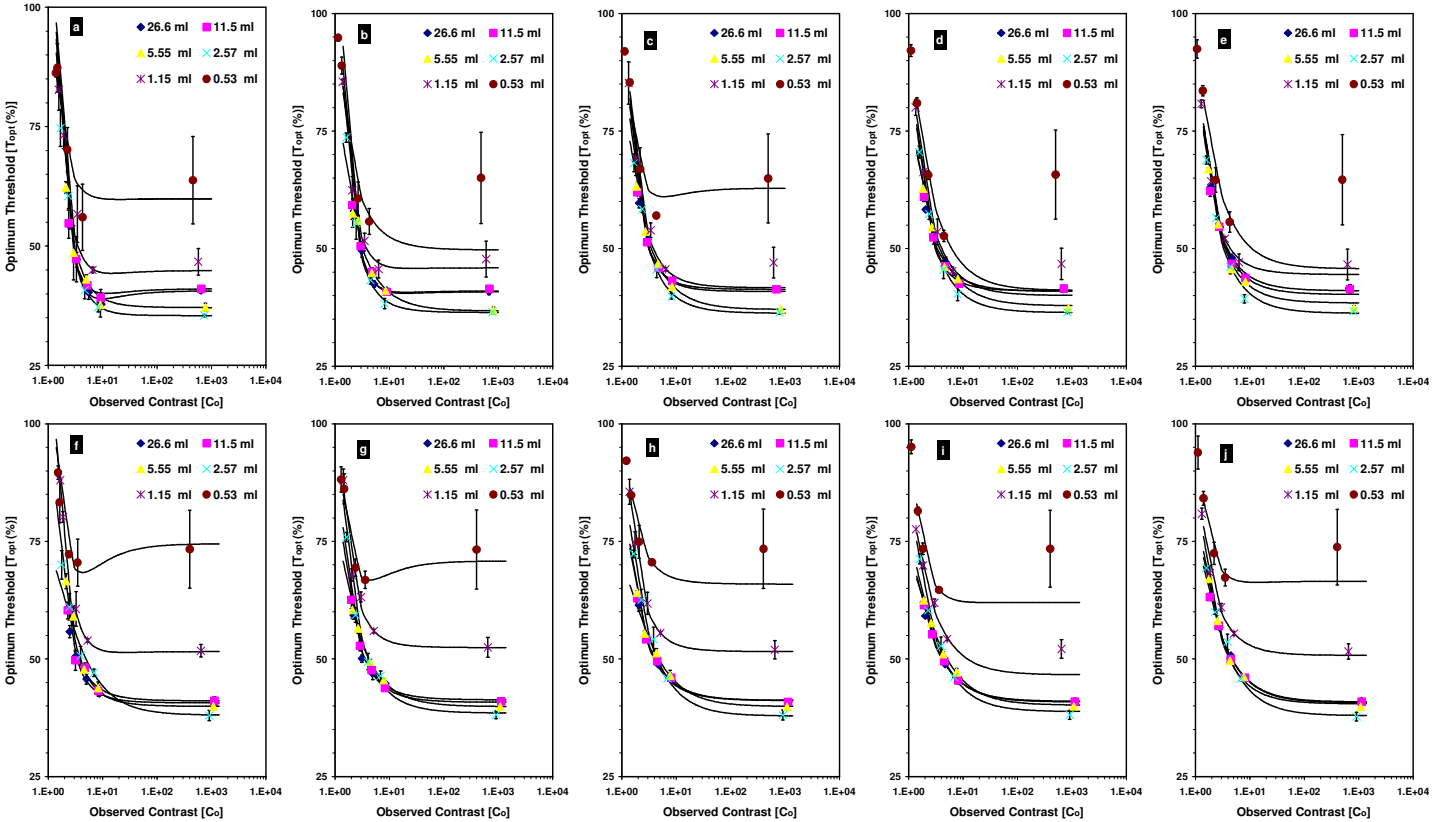

Figure 3.5: Variation of T_{opt} with C_o for all sphere volumes at 1, 2.5, 5, 10 and 60 minute acquisition times for IT (a, b, c, d, e) and FBP (f, g, h, i, j) reconstruction techniques respectively. The points represent the data points and the error bars in T_{opt} direction represents the standard error of three experiments. The solid black lines represent the fitting for each volume size to equation (3.2). A logarithmic scale has been used in C_o axis.

3.4.2. VCAT Calibration Curves

The VCAT calibration curves are given by the variation of T_{opt} with V at different values of C_o. Because the value of C_o for all volumes with the same C_t varies due to the PVE, the values of T_{opt} were adjusted to a corresponding fixed C_o using the previously determined relationship between C_o and T_{opt}.

Un-weighted least squares fits to equations (3.1) and (3.2) were carried out with $y = T_{opt}$ and $x = V$ at fixed values of C_o = 2, 3, 5, 9, ∞. Again, the Chi-square (χ^2) test was used to determine the goodness of the fit. The resulting χ^2 values demonstrated that the best fit was obtained with equation (3.2). Figure 3.6 demonstrates the variation of optimal threshold, T_{opt}, with lesion volume, V at different C_o.

Each of the three parameters a, b and c from equation (3.2) of fitting T_{opt} and V was found to show a good correlation with C_o for all volumes. Therefore, a correlation between the value of each parameter and C_o was performed using a least square fitting to equations (3.1) and (3.2). The calculated χ^2 of this correlation showed that the best correlation function to correlate each parameter with C_o is equation (3.2). So, each fit parameter, a, b and c, from equation (3.2) is replaced by the same full equation as a function on C_o. Therefore, the value of T_{opt} can be represented by a function on C_o and V, as follows:

$$T_{opt}(C_o,V)=\left(a+\frac{b}{C_o}+\frac{c}{C_o^{\,2}}\right)+\frac{\left(d+\frac{e}{C_o}+\frac{f}{C_o^{\,2}}\right)}{V}+\frac{\left(g+\frac{h}{C_o}+\frac{i}{C_o^{\,2}}\right)}{V^2} \quad \textbf{..... (3.3)}$$

This equation, with the nine parameters a-i, was used to implement the VCAT method in spheres and irregular volumes. Table 3.1 shows the values of the nine fitting parameters, a-i, for all acquisition times (t_{AC}: 1, 2.5, 5, 10, 15, 20, 30 and 60 min) and for IT and FBP reconstruction images.

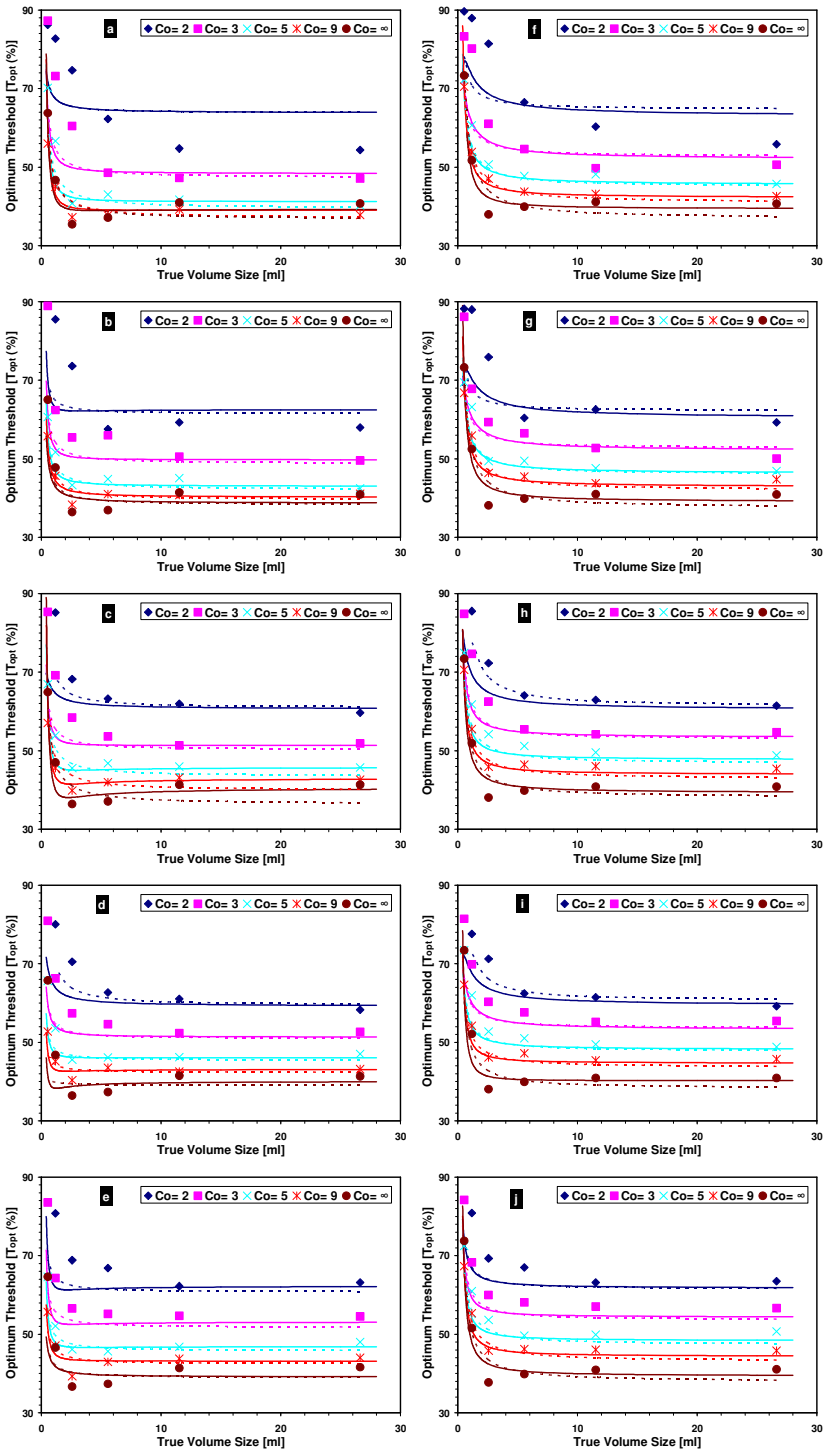

Figure 3.6: The VCAT calibration curves generated from spheres phantom by correlation T_{opt} and V at different C_o. a, b, c, d and e are the calibration curves for IT and f, g, h, i and j are for FBP reconstruction techniques at 1, 2.5, 5, 10 and 60 minute acquisition times respectively. The points represent the data and the dotted and solid lines represent the fitted equation (3.1) and (3.2) respectively.

t_{AC}	***IT reconstruction***								
min	***a***	***b***	***c***	***d***	***e***	***f***	***g***	***h***	***i***
1	39.3	- 16.9	131.8	- 3.39	24.6	- 18.8	7.69	- 9.98	- 10.8
2.5	38.7	4.07	87.3	3.85	- 3.03	- 17.6	1.20	7.03	- 6.07
5	40.5	17.1	46.2	- 11.0	32.3	0.12	12.2	- 27.9	4.49
10	40.1	24.4	27.7	- 4.42	20.4	- 0.26	2.72	- 2.50	- 7.04
15	40.8	17.8	43.5	- 11.2	65.4	- 67.8	8.85	- 33.2	30.9
20	39.6	25.9	31.7	- 2.59	6.81	3.25	3.55	- 0.83	- 6.19
30	39.2	27.0	34.0	- 0.46	- 7.17	16.4	3.40	3.00	- 11.4
60	39.1	33.9	24.9	2.63	- 26.3	25.6	0.58	17.3	- 19.1

t_{AC}	***FBP reconstruction***								
min	***a***	***b***	***c***	***d***	***e***	***f***	***g***	***h***	***i***
1	39.3	19.6	55.5	4.41	23.7	- 0.04	7.66	- 33.5	17.3
2.5	39.0	32.3	20.9	8.02	- 2.74	36.8	4.82	- 17.6	- 4.07
5	39.2	42.1	0.90	7.42	- 19.1	55.7	3.69	0.56	- 22.0
10	40.2	40.6	- 4.23	0.49	27.5	- 8.65	5.95	- 26.5	17.7
15	38.8	51.4	- 17.4	10.3	- 33.6	63.7	1.61	3.68	- 18.6
20	38.3	52.7	- 13.1	12.6	- 39.4	56.6	- 1.04	12.5	- 20.9
30	38.6	45.1	0.37	11.3	- 16.3	17.3	1.23	- 5.57	2.55
60	39.3	45.7	- 1.56	6.23	- 16.3	28.1	4.48	- 5.93	- 3.02

Table 3.1: The values of the nine fitting parameters in equation (3.3) for correlating T_{opt} and V to generate the VCAT calibration curves for IT and FBP reconstructions.

When applying the VCAT method the operator begins by drawing a loose region around the lesion on the PET image to constrain the auto-delineation. Next, in all slices that contain lesion the operator defines a region of background in a suitable area close to the lesion. A flowchart of this algorithm is presented in Figure 3.7. The ratio of lesion maximum to background mean is obtained to determine C_o. Within the loose region VCAT then estimates an initial threshold value, T_1 that corresponds to the largest volume on the calibration curve corresponding to the measured C_o. T_1 is applied to obtain a first estimate of the volume, V_1. V_1 is applied to the calibration curve to obtain the corresponding T_{opt} (%) which becomes the second estimate of threshold, T_2. If the difference between T_1 and T_2 is greater than 10^{-3}, T_2 is applied to the image to obtain a second volume estimate, V_2. This process continues until $T_{i+1} - T_i < 10^{-3}$. The full IDL program written to implement this method is presented in appendix II.

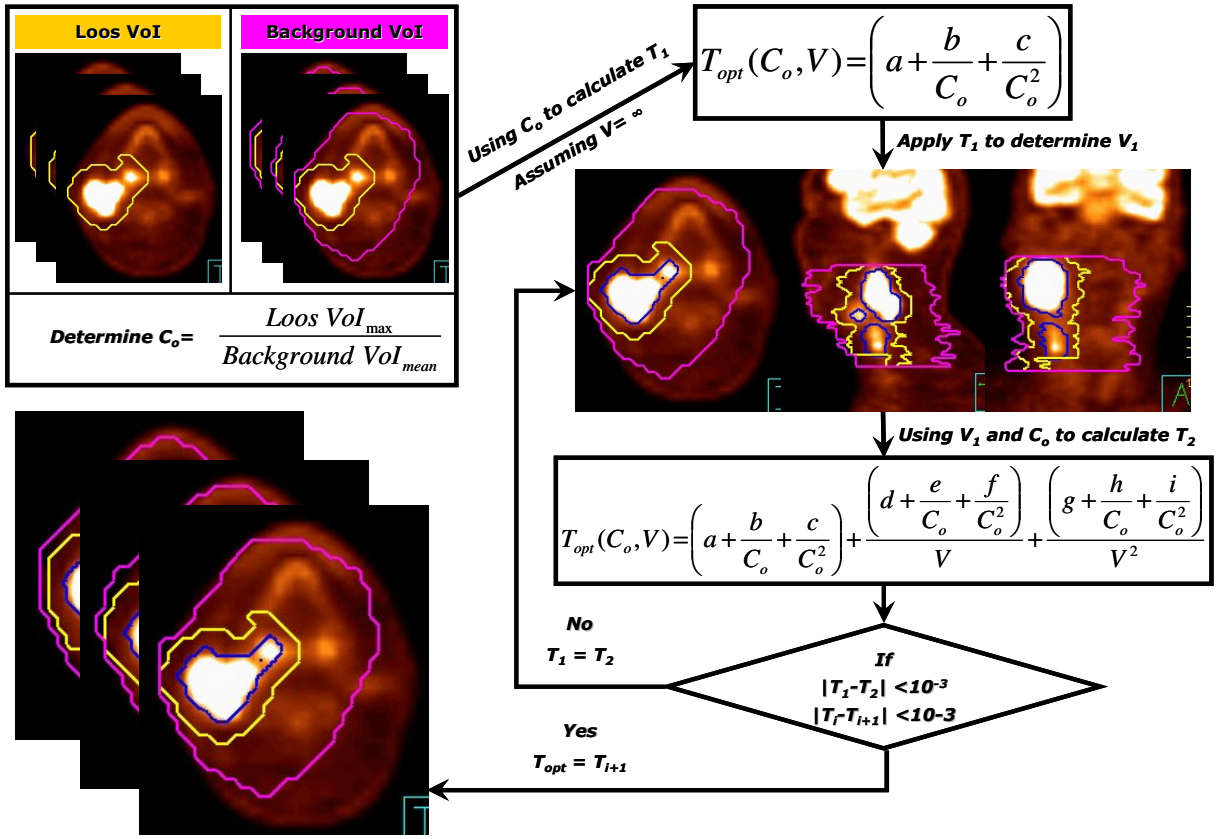

Figure 3.7: A flowchart of the VCAT method. The process is explained in the text (Section 3.4.2).

3.5. Contrast Adjusted Thresholding (CAT) Method

The experimental findings for the variation of threshold with lesion contrast (presented in section 3.4.1) revealed the possibility that for all volumes greater than those affected by PVE (> 1.15 ml), the variation with V could be considered constant. Therefore, a simplification of the VCAT method was considered whereby it was only necessary to obtain the relation between T_{opt} and C_o. This simplified method is referred to as CAT – Contrast Adjusted threshold.

3.5.1. CAT Calibration Curves

The values of T_{opt} and C_o for all volumes greater than 1.15 ml from the spherical phantom at each reconstruction technique and acquisition time were used to generate the CAT calibration curves. A weighted least squares fit was carried out and the χ^2 test employed to determine whether equation (3.1) or (3.2) provided the best fit to the data.

Table 3.2 represents the resulting Chi-square values (χ^2) of correlating T_{opt} with C_o for all spherical volumes > 1.15ml. These χ^2 values demonstrated that there is a good correlation between T_{opt} and C_o and that the fitting to the second order equation (3.2) is better than the first order equation (3.1).

Figure 3.8 shows the results of this fitting T_{opt} and C_o at 1, 2.5, 5, 10 and 60 minute acquisition times for both IT and FBP reconstruction images. This figure represents the calibration curves for the CAT PET segmentation technique, which can be represented by equation (3.4). It is clear that the second order equation represents the data points more closely than the first

order equation. The second order term enable the curve to pined harder at the small volumes and maintain the constant term better.

$$T_{opt}(C_o) = a + \frac{b}{C_o} + \frac{c}{C_o^2} \qquad \textbf{…… (3.4)}$$

Table 3.3 shows the values of the CAT calibration equation, i.e. equation (3.4), for all acquisition times (t_{AC}: 1, 2.5, 5, 10, 15, 20, 30 and 60 min) for IT and FBP reconstruction images. The constant term of equation (3.4) seems to coincide for the different acquisition times with the values of (38.3 ± 0.55) and (40.4 ± 0.50) for iterative and FBP reconstruction images; (average ± SD).

t_{AC}	***Iterative reconstruction***	
min	x^{-1}	x^{-2}
1	8.86	1.23
2.5	3.26	1.26
5	1.68	0.95
10	1.45	1.42
60	1.68	1.24

t_{AC}	***FBP reconstruction***	
min	x^{-1}	x^{-2}
1	5.54	2.23
2.5	2.16	0.92
5	1.14	0.88
10	0.72	0.71
60	0.43	0.54

Table 3.2: The Chi-square (χ^2) values of correlating T_{opt} with C_o for all spherical volumes > 1.15ml.

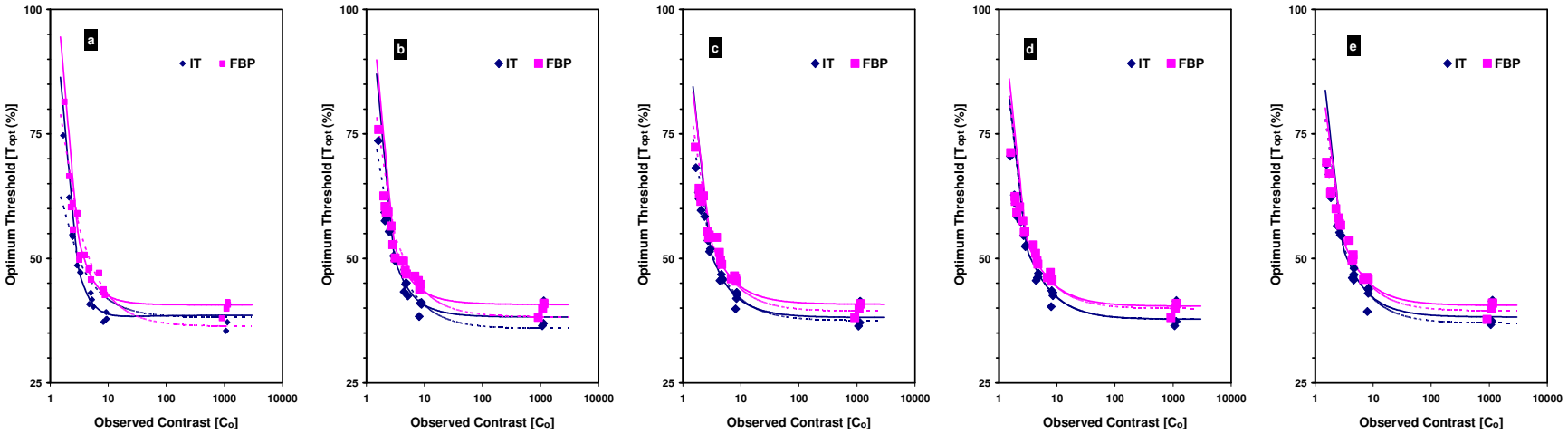

Figure 3.8: The CAT calibration curves generated from spherical phantom by correlation T_{opt} with C_o. a, b, c, d and e are the calibration curves for IT and FBP reconstruction techniques at 1, 2.5, 5, 10 and 60 minute acquisition times. The points represent the data points, the doted lines represent the fitting to equation (3.1) and the solid lines represent the fitting to equation (3.2). A logarithmic scale has been used C_o direction.

t_{AC}	***IT reconstruction***		
min	***a***	***b***	***c***
1	38.6	-9.76	122.3
2.5	38.2	18.4	58.5
5	38.1	31.7	28.7
10	37.8	43.7	1.08
15	37.8	39.0	14.8
20	39.5	28.5	23.4
30	38.0	37.2	18.7
60	38.2	36.6	21.8

t_{AC}	***FBP reconstruction***		
min	***a***	***b***	***c***
1	40.7	7.32	110.2
2.5	40.7	19.2	58.1
5	40.8	33.1	21.7
10	40.4	38.3	7.43
15	40.3	44.5	-3.73
20	39.2	49.4	-5.48
30	40.2	43.1	3.05
60	40.6	37.2	12.5

Table 3.3: The values of the fitting parameters for correlating T_{opt} and C_o to generate the CAT calibration curves for IT and FBP reconstructions.

3.6. Discussion

Two new PET lesion delineation techniques have been described investigated: volume and contrast adjusted thresholding (VCAT), and contrast adjusted thresholding (CAT). These techniques do not depend on a priori information about the volume size or shape of a lesion. A one-off calibration of the PET scanner system using a standard NEMA image quality phantom can be carried out to generate a set of calibration curves specific to the scanner. From a measurement of only the lesion's observed contrast on the PET image, the 3D boundary and volume is then computed by automatically adjusting the threshold value to the optimum for the actual contrast and volume.

The VCAT calibration curves, Figure 3.6, for FBP and IT reconstruction techniques were in good agreement. Additionally they were in close agreement for different acquisition times, indicating that the technique should be applicable to images with differing statistical quality, as typically encountered with different size patients. However the user must be aware of the potential for observed biases between FBP and IT reconstruction techniques [116], and that it is therefore useful to match the conditions for the calibration acquisition and reconstruction with those used for patient studies.

The CAT calibration curves, Figure 3.8, for FBP and IT reconstruction were in good agreement. However, as the observed contrast increases above 5 the calibration curves for the IT and FBP begin to separate then level off at different optimum threshold values with a 2% higher value for FBP. It is apparent also from the figure that above an observed contrast of approximately 20 the optimum threshold remains constant, the value being

that of the fit parameter "a" in the CAT calibration formula, equation (3.4). It would be possible to use this value for a fixed thresholding technique, but only for high values of observed contrast in excess of 20.

4

Chapter 4:

EVALUATING THE ACCURACY OF THE CAT AND VCAT METHODS

This chapter represents the results of evaluating the CAT and VCAT accuracies in a range of different conditions simulating those encountered in clinical patient studies.

The accuracies of CAT and VCAT methods were evaluated in the spherical and irregular lesions phantoms described in sections (4.1 and 2.4), for different image noise levels, and for both iterative (IT) and filtered back projection (FBP) reconstruction techniques. The different noise levels were obtained by using five different acquisition times (t_{AC} = 1, 2.5, 5, 10 and 60 minute), with a high noise image at 1 min and a very low noise level at 60 min.

4.1. Investigating the Accuracy of CAT and VCAT Methods in Spheres

4.1.1. CAT Accuracy in Spheres

Figure 4.1 represents the modulus of percentage error in spherical volumes measurements using the CAT method in iterative and FBP reconstruction images at 1, 2.5, 5, 10 and 60 min t_{AC}. The dotted line represents the acceptable error, E_A, for the radiotherapy treatment planning.

These results demonstrate that the error in spherical volume measurements using the CAT method were well within the acceptable error for radiotherapy treatment planning even for small volumes, i.e. < 1.15ml, with for C_o > 3 or V > 1.15ml. These results were unforeseen because the CAT calibration curves do not take into consideration volumes < 1.15ml. Also, the CAT method proves to have low sensitivity to the noise because it accurately segmented the spherical volumes for the highest noise level, t_{AC} = 1 at C_o~ 2, where the images were visually very noisy.

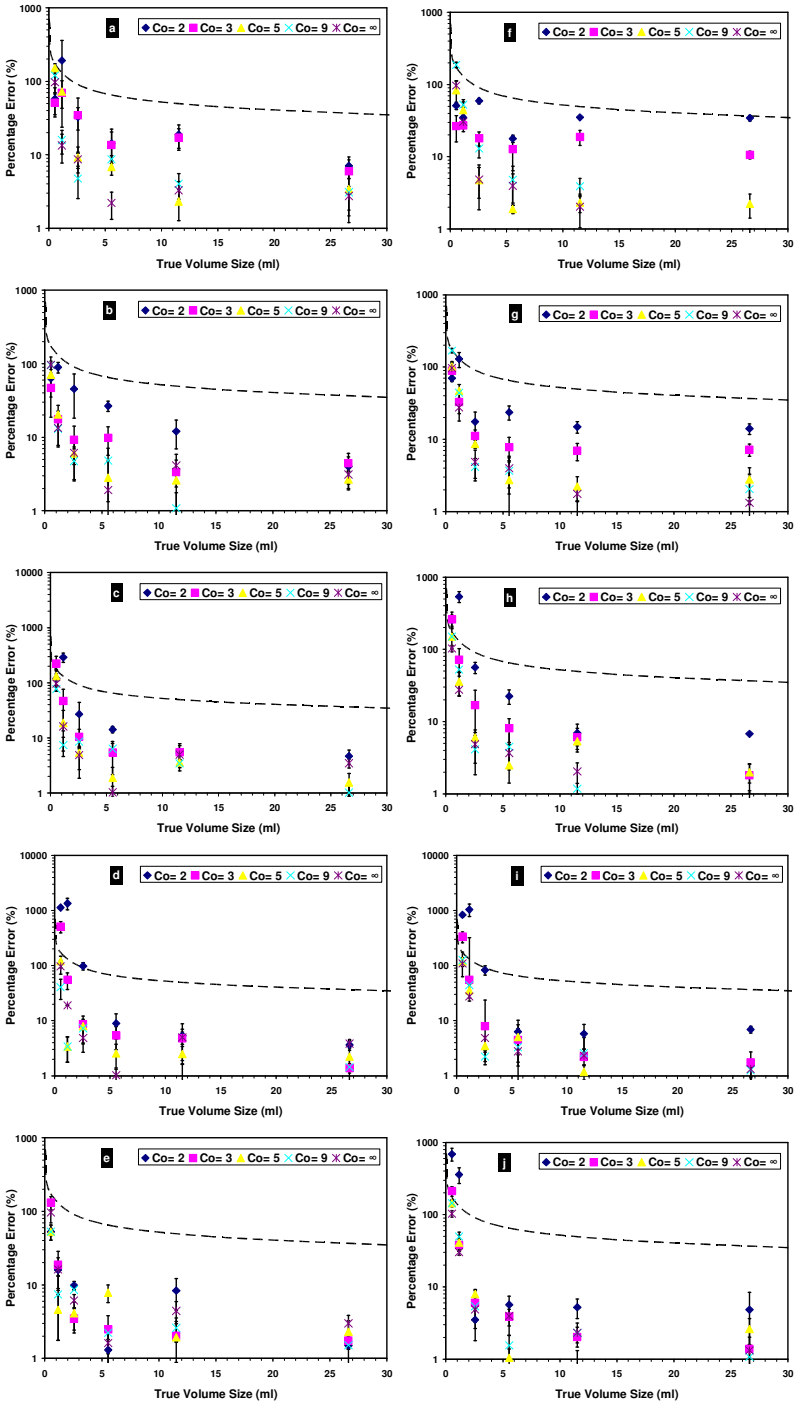

Figure 4.1: The modulus of percentage error in measuring spherical volumes using the CAT method for IT (left side) with different t_{AC} = 1(a), 2.5(b), 5(c), 10(d), 60(e) minute and FBP (right side) with the same t_{AC} values (f, g, h, i, j). The error bars represent the standard error from three experiments. The black dotted line represents the acceptable error. A logarithmic scale in the percentage error direction has been used.

4.1.1.1. CAT using 60 minute single calibration curve

Investigations were carried out for using a single calibration curve obtained at one value of t_{AC}. This simplified approach could significantly reduce the data needed to generate the CAT calibration curves and also simplify the method by just using a single equation (for a specific reconstruction technique) with three parameters and one variable, i.e. C_o. These resulting calibration equations were:

$$T_{opt}(IT) = 38.2 + \frac{36.6}{C_o} + \frac{21.8}{C_o^2} \qquad \textbf{..... (4.1)}$$

$$T_{opt}(FBP) = 40.6 + \frac{37.2}{C_o} + \frac{12.5}{C_o^2} \qquad \textbf{..... (4.2)}$$

Figure 4.2 shows the modulus percentage error in the use of 60min CAT single calibration curve for IT and FBP at 1, 2.5, 5 and 10 min t_{AC}. Firstly, these results showed that the use of single CAT calibration curve produced better results for IT compared with FBP. For IT, this method worked well determining lesion volumes within the acceptable error except for small volumes at low contrast, namely V < 1.15ml for $C_o \leq 3$,. In the case of FBP, the similar results were found, however for $C_o \sim 2$ the method failed to segment V = 2.57ml at t_{AC} = 1 and 2.5 min.

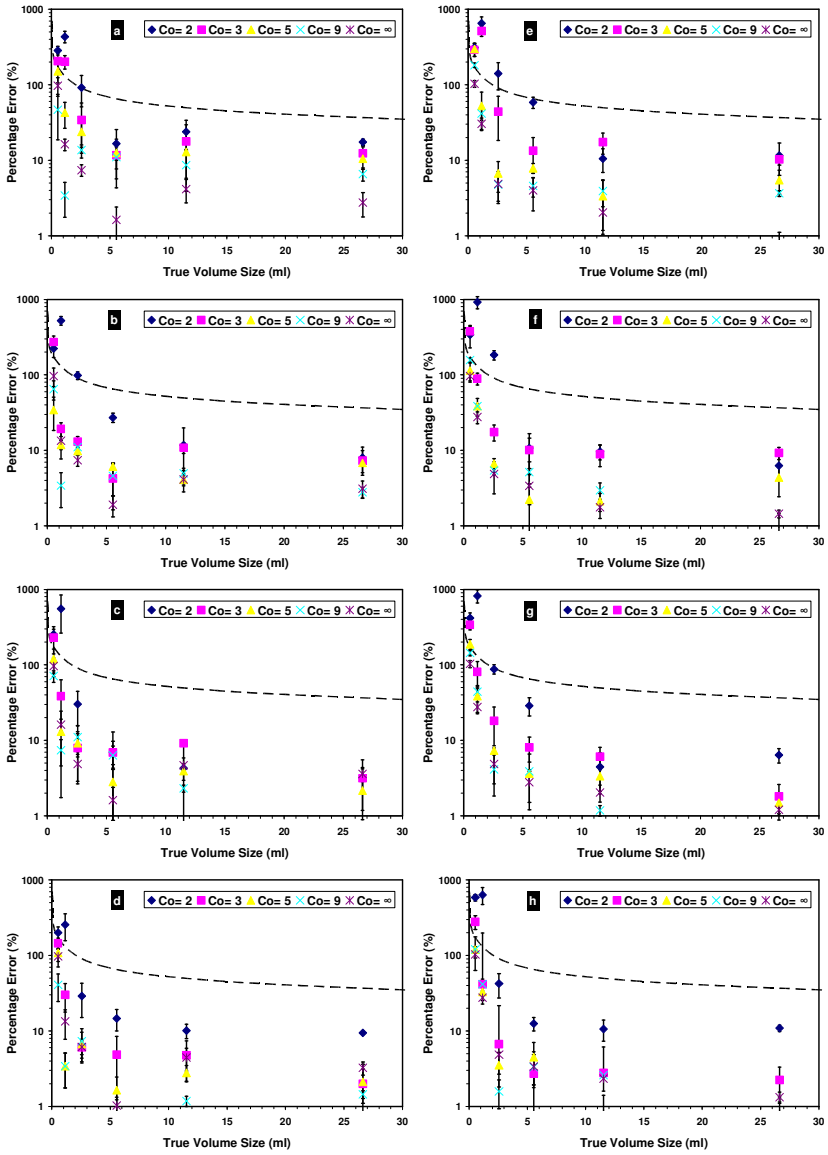

Figure 4.2: The modulus of percentage error in measuring spherical volumes using 60 minute CAT calibration curve method for IT (left side) with different t_{AC} = 1(a), 2.5(b), 5(c), 10(d) minute and FBP (right side) with the same t_{AC} values (e, f, g, h). The error bars represent the standard error from three experiments. The black dotted line represents the acceptable error. A logarithmic scale in the percentage error direction has been used.

4.1.1.2. Comparison with fixed thresholding method

The results of applying a 40% fixed threshold for both IT and FBP images are presented in Figure 4.3. The use of 40% fixed threshold failed to segment the correct spheres volumes with C_o = 2 and 3, and also for C_o ~ 5 it failed in volumes < 1.15ml.

These results demonstrate the limitations of using a fixed threshold approach. It is interesting to note that in equation 3.4 for the CAT calibration curves the fit parameter, a, is approximately 40%, and the other two terms represent modification to this depending on the value of C_o.

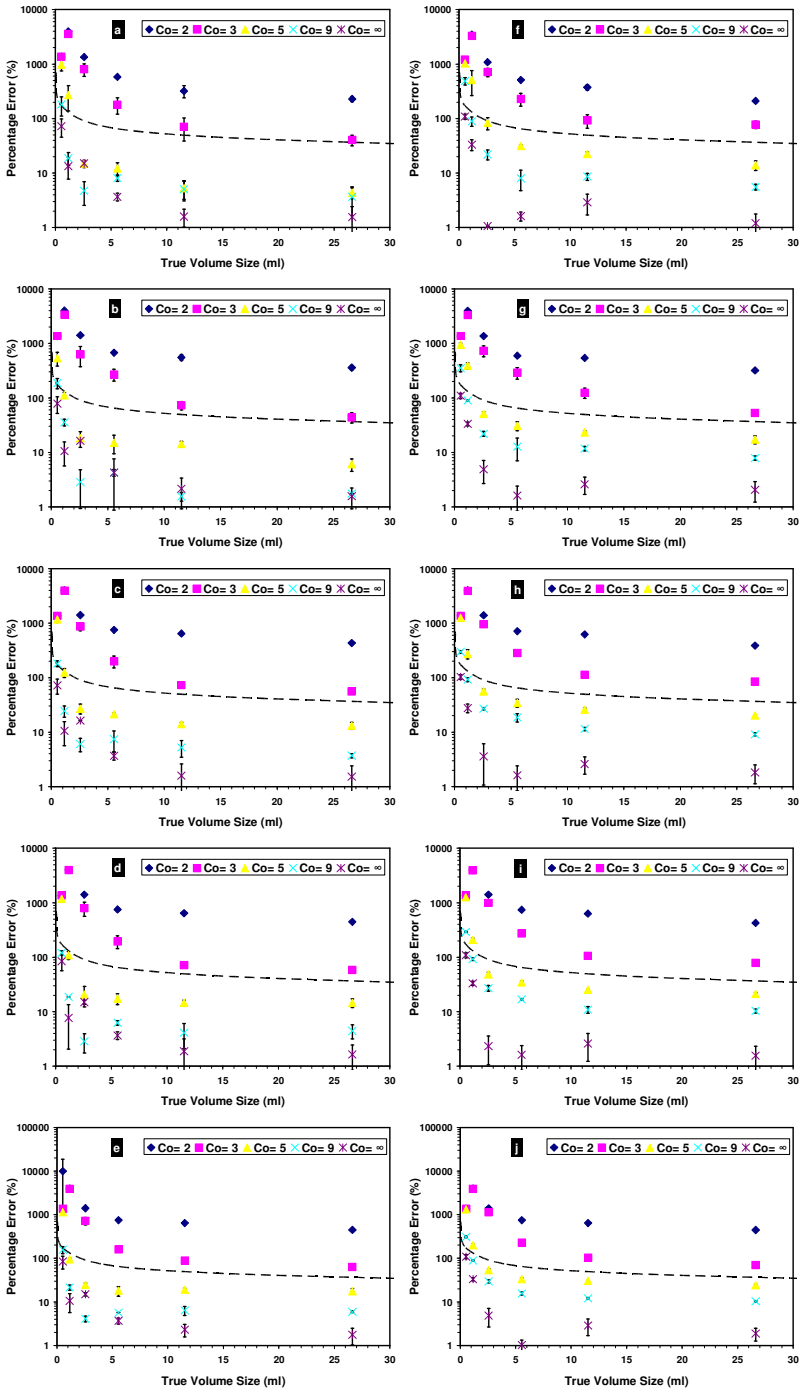

Figure 4.3: The modulus of percentage error in measuring spherical volumes using 40% fixed thresholding method for IT (left side) with different t_{AC} = 1(a), 2.5(b), 5(c), 10(d), 60(e) minute and FBP (right side) with the same t_{AC} values (f, g, h, i, j). The error bars represent the standard error from three experiments. The black dotted line represents the acceptable error. A logarithmic scale in the percentage error direction has been used

4.1.2. VCAT Accuracy in Spheres

Figure 4.4 shows the error in volume determination by VCAT in spheres. The dotted line represents the E_A for RTP and the error bars indicate the standard error of three sets of measurements. A logarithmic scale has been used in the C_o direction in order to show the values of high percentage error seen with the smaller volumes (0.53, 1.15 and 2.57 ml).

These data demonstrate that the error in measuring the volume of spherical lesions using the VCAT method is in general smaller for iterative reconstruction than for FBP reconstruction. The results of both reconstruction techniques are well within the acceptable error for RTP purposes, but for $V \leq 1.15$ ml at low contrast the errors increase to a borderline acceptability. Even for the highest noise level investigated, with t_{AC} = 1 min, the accuracy of the VCAT method is acceptable, indicating that a satisfactory performance is probable in large patients. For volumes > 2.57ml the errors were higher in low contrast than high contrast, but still within the acceptable level for RTP.

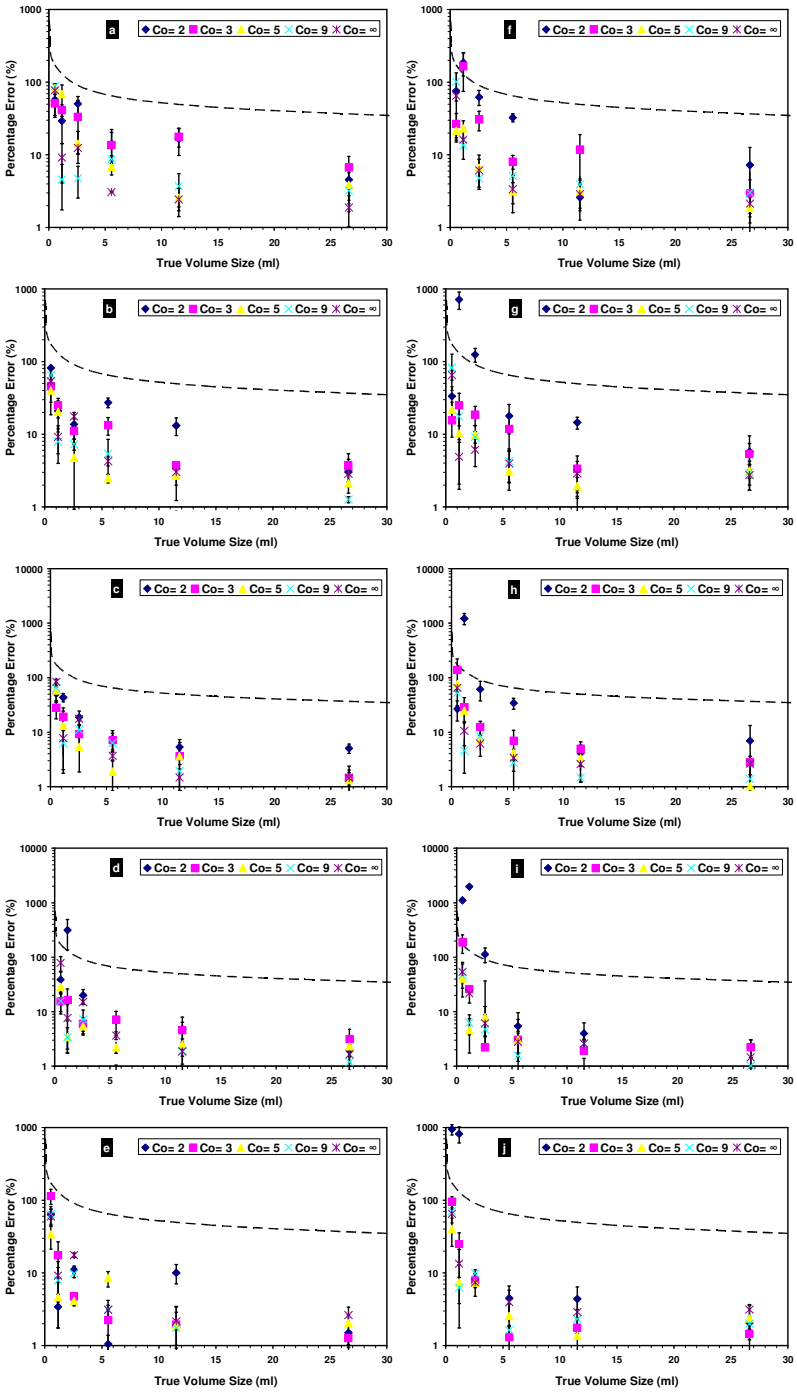

Figure 4.4: The modulus of percentage error in measuring spherical volumes using the VCAT method for IT (left side) with different t_{AC} = 1(a), 2.5(b), 5(c), 10(d), 60(e) minute and FBP (right side) with the same t_{AC} values (f, g, h, i, j). The error bars represent the standard error from three experiments. The black dotted line represents the acceptable error. A logarithmic scale in the percentage error direction has been used.

4.1.2.1. VCAT using 60 minute single calibration curve

The possibility was explored of using a single calibration curve obtained with the lowest noise calibration data, i.e. obtained using 60 min acquisition times. This would simplify the calibration process, if it produced acceptably low errors. These results shown in Figure 4.5 demonstrate sufficient accuracy for $C_o \geq 3$ with volumes ≤ 1.15ml and ≤ 2.57ml for IT and FBP respectively.

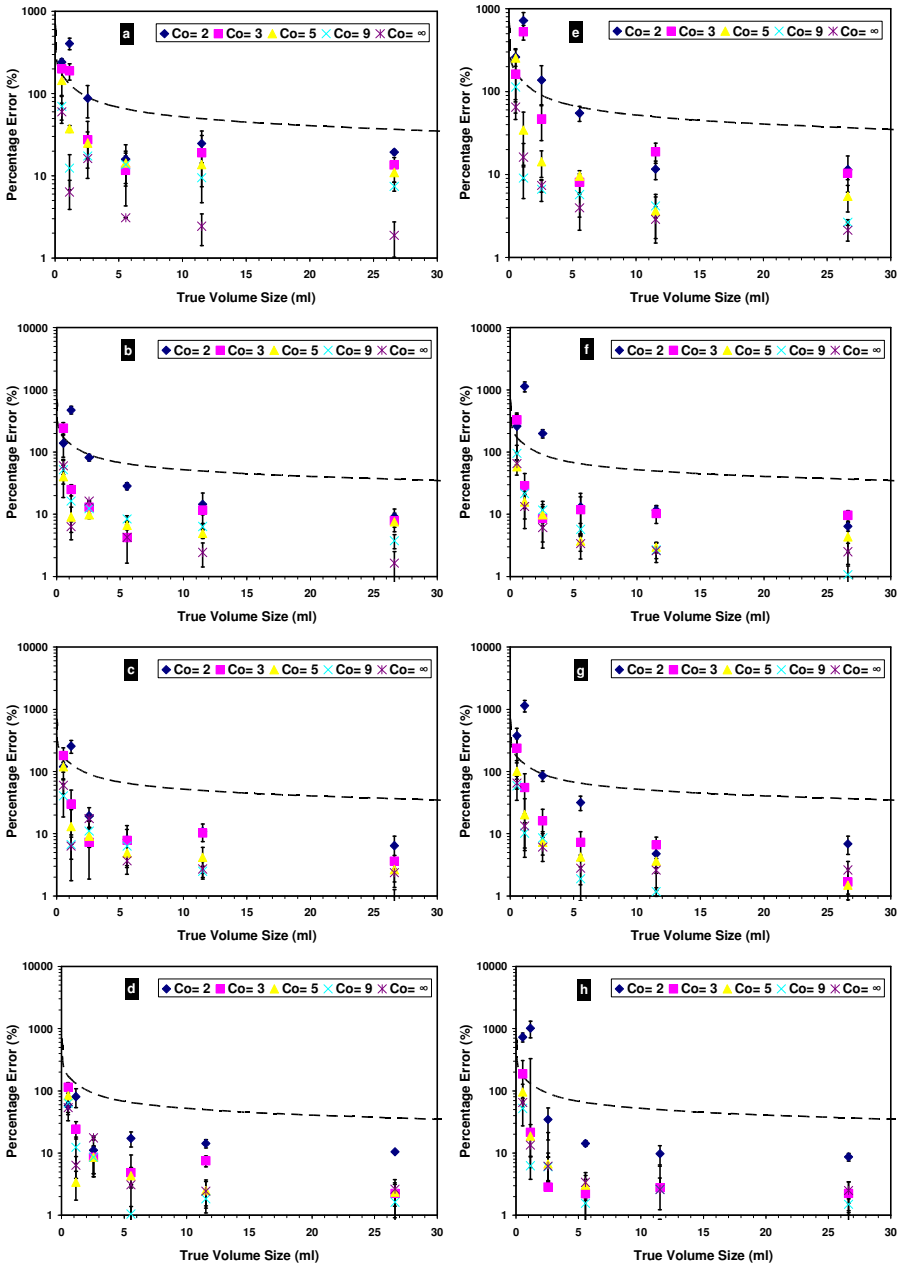

Figure 4.5: The modulus of percentage error in measuring spherical volumes using 60 minute VCAT calibration curve method for IT (left side) with different t_{AC} = 1(a), 2.5(b), 5(c), 10(d) minute and FBP (right side) with the same t_{AC} values (e, f, g, h). The error bars represent the standard error from three experiments. The black dotted line represents the acceptable error. A logarithmic scale in the percentage error direction has been used

4.1.2.2. Comparison with fixed thresholding method

Figure 4.3 demonstrates the results of applying a fixed threshold of 40% of the maximum uptake on spherical lesions. It is clear that this fixed thresholding method produces results which are considerably worse than using the VCAT method. The results were outside the acceptable error for all volumes at contrasts, $C_o < 5$ the errors were acceptable only for $C_o \geq 5$ and V > 1.15ml, regardless of image noise level given by the various t_{AC}

4.2. Investigating the CAT and VCAT Accuracy in Irregular Volumes

4.2.1. CAT Accuracy in Irregular Volumes

To test the CAT method in different geometries than those used to generate the calibration curves, the CAT method was applied to the two families of irregular volumes; top-hat and crescent shapes. Figure 4.6 shows the modulus percentage error in segmenting these irregular shapes using the CAT method for both IT and FBP images at 1, 2.5, 5, 10 and 60 min t_{AC}.

The resulting percentage errors of using the CAT method in the irregular shapes were well below the acceptable error for both reconstruction techniques and all acquisition times. The results for IT were better than those for FBP in the crescent shape at small volume (4.89ml). Otherwise, the resulting percentage errors were under 10% for all volumes.

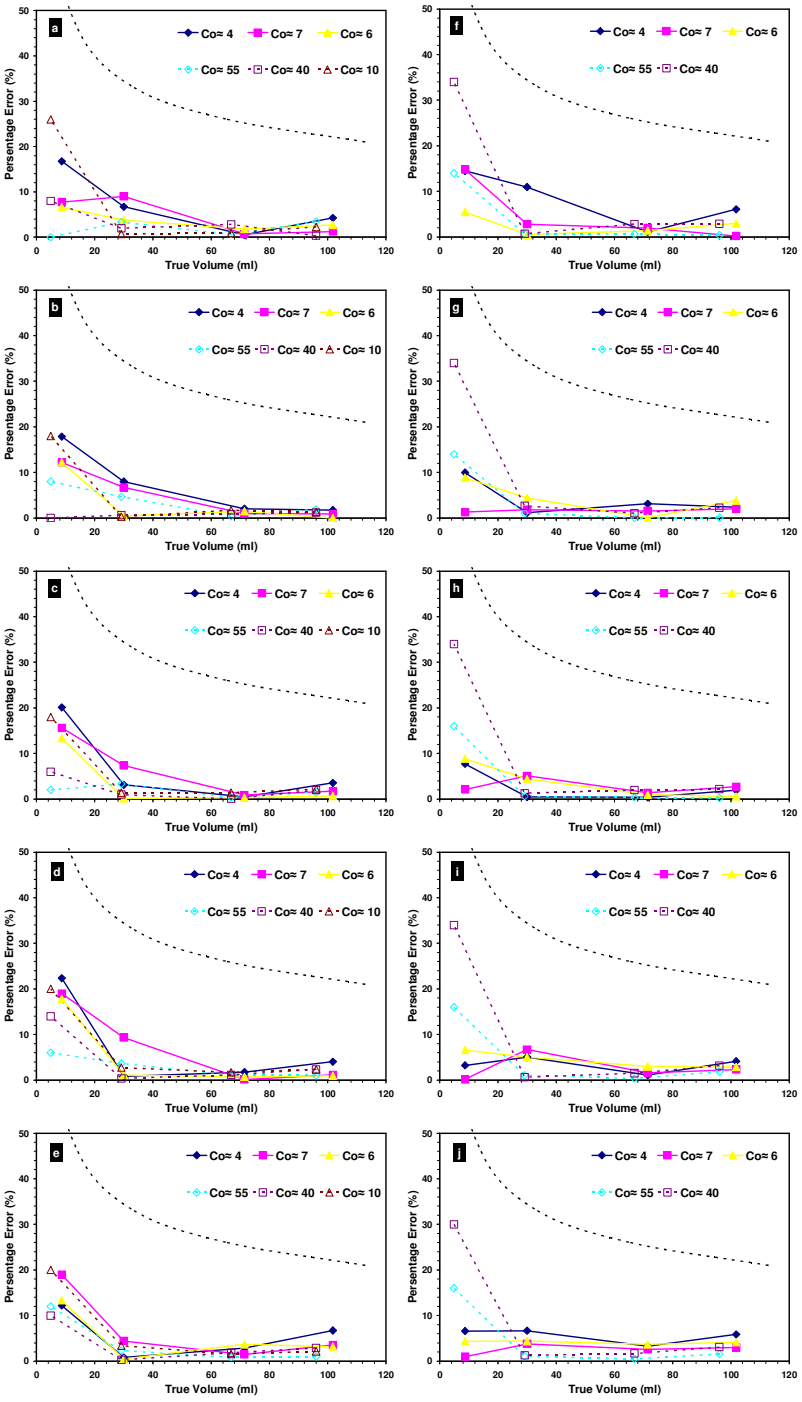

Figure 4.6: The modulus of percentage error in measuring irregular volumes using the CAT method for IT (left side) with different t_{AC} = 1(a), 2.5(b), 5(c), 10(d), 60(e) minute and FBP (right side) with the same t_{AC} values (f, g, h, i, j). The black dotted line represents the acceptable error. A logarithmic scale in the percentage error direction has been used

4.2.1.1. CAT using 60 minute single calibration curve

The idea of using a CAT single calibration curve to segment the PET true volumes needed also to be tested in the irregular shapes. Therefore, the 60 min CAT single calibration curve was used to segment the PET irregular volumes at different acquisition times.

Figure 4.7 presents the results of applying the 60 min CAT single calibration curve to segment the irregular shapes for IT and FBP at 1, 2.5, 5 and 10 min t_{AC}. Similar results to that obtained with the CAT method using individual calibration curves were obtained using the 60 min single calibration curve except in case of 1 min t_{AC}. Also, the results of applying the 60 min CAT single calibration curve in the case of 1 min t_{AC} were well within the acceptable error. These results strongly support the idea of using a single calibration curve that is obtained in long acquisition time which reduces the amount of data collected to establish the CAT method to be applied to different acquisition times.

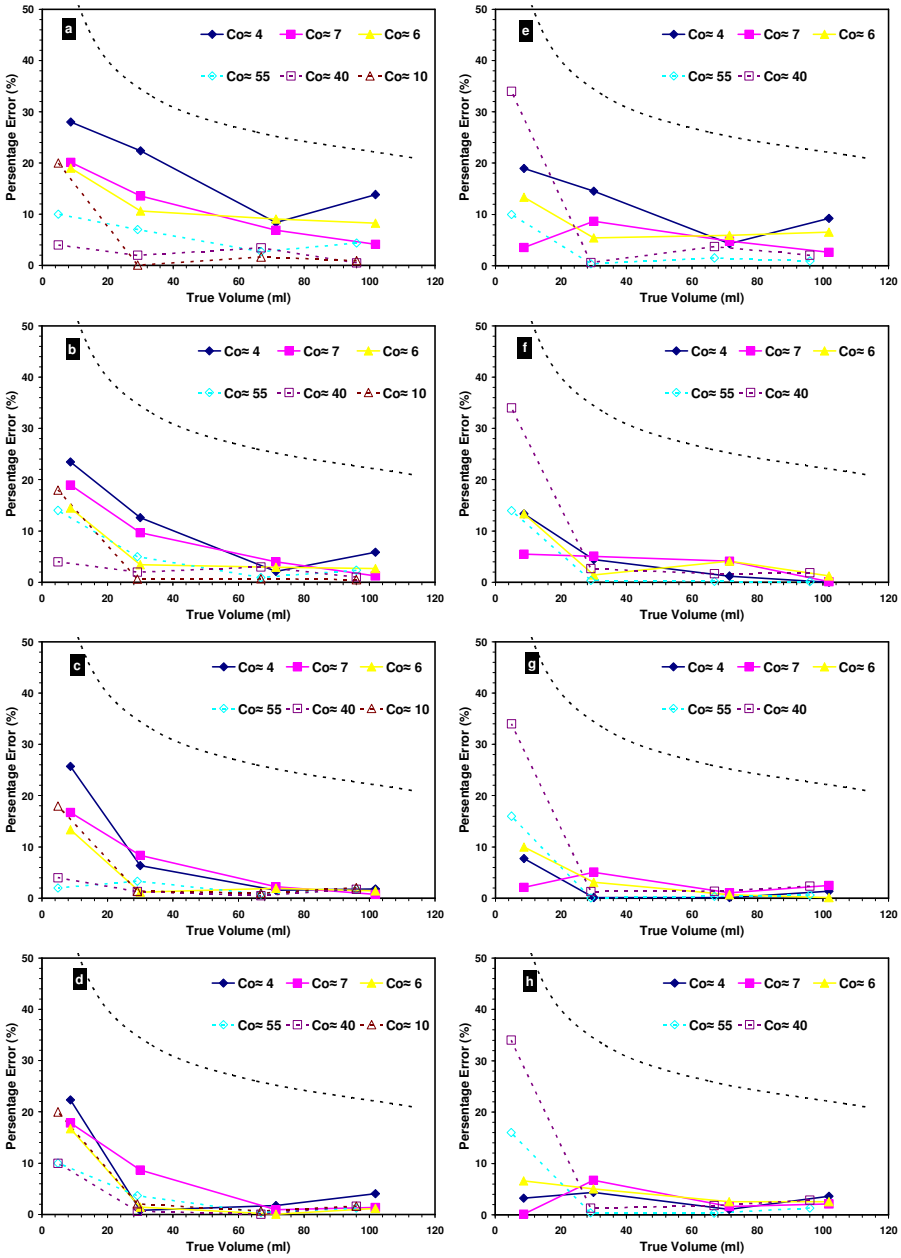

Figure 4.7: The modulus of percentage error in measuring irregular volumes using the 60 minute CAT calibration curve method for IT (left side) with different t_{AC} = 1(a), 2.5(b), 5(c), 10(d) minute and FBP (right side) with the same t_{AC} values (e, f, g, h). The black dotted line represents the acceptable error. A logarithmic scale in the percentage error direction has been used.

4.2.1.2. Comparison with fixed thresholding method

The results of applying a 40% fixed threshold to measure the PET irregular volumes for both IT and FBP images at 1, 2.5, 5, 10 and 60 min t_{AC} are presented in Figure 4.8. The use of 40% fixed threshold failed to accurately segment the top-hat irregular volumes for FBP with C_o~ 4. Also in the case of IT, fixed threshold failed to segment the small volume (V = 4.89ml) across all studied t_{AC} as well as for top-hat volumes 71.4 and 101.8ml at 60 min t_{AC}. All these errors lead to uncertainty in applying the 40% fixed threshold which can be solved by using one of the adjusting thresholding techniques described here.

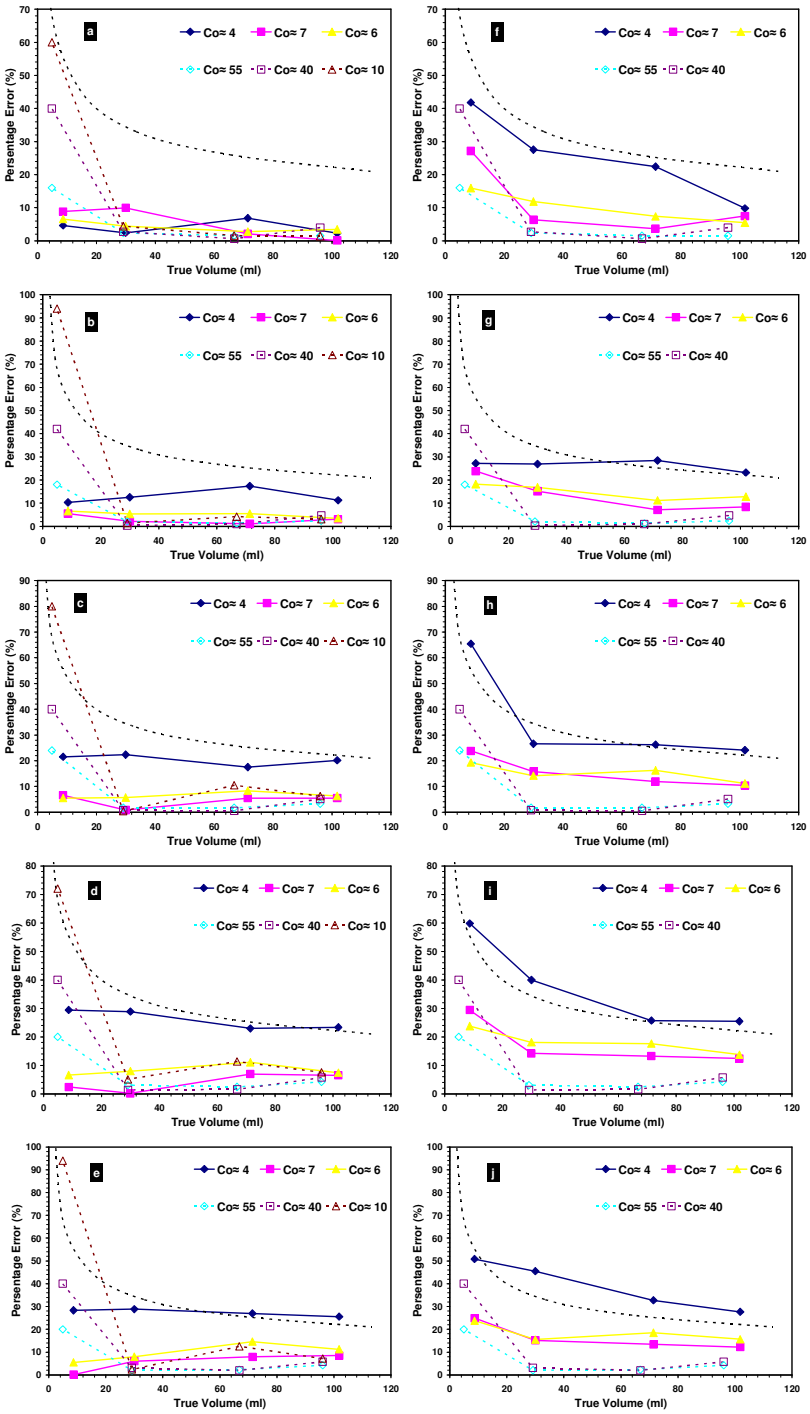

Figure 4.8: The modulus of percentage error in measuring irregular volumes using 40% fixed thresholding method for IT (left side) with different t_{AC} = 1(a), 2.5(b), 5(c), 10(d), 60(e) minute and FBP (right side) with the same t_{AC} values (f, g, h, i, j). The black dotted line represents the acceptable error. A logarithmic scale in the percentage error direction has been used.

4.2.2. VCAT Accuracy in Irregular Volumes

The VCAT calibration curves were generated using the phantom with spherical lesions. However tumours in patients studies are often not of spherical but irregular shapes. Therefore the accuracy of VCAT method was investigated in two families of irregular volumes termed top-hat and crescent, as described in section 3.4.2.2). These results are shown in Figure 4.9, where it can be seen that all results were well below the acceptable error for RTP, even at the smallest volumes and lowest contrast. For volumes $\geq$ 30.0 ml, the errors were less than 10% for all values of C_o , t_{AC} , and reconstruction technique, decreasing to approximately 5% at large volume and high contrast. For the smaller volumes (top-hat = 8.69 ml, crescent = 4.89 ml) the errors across all acquisition times were less than 20% and 40% respectively. For top-hat volumes iterative reconstruction gave slightly higher errors than FBP especially for small volumes.

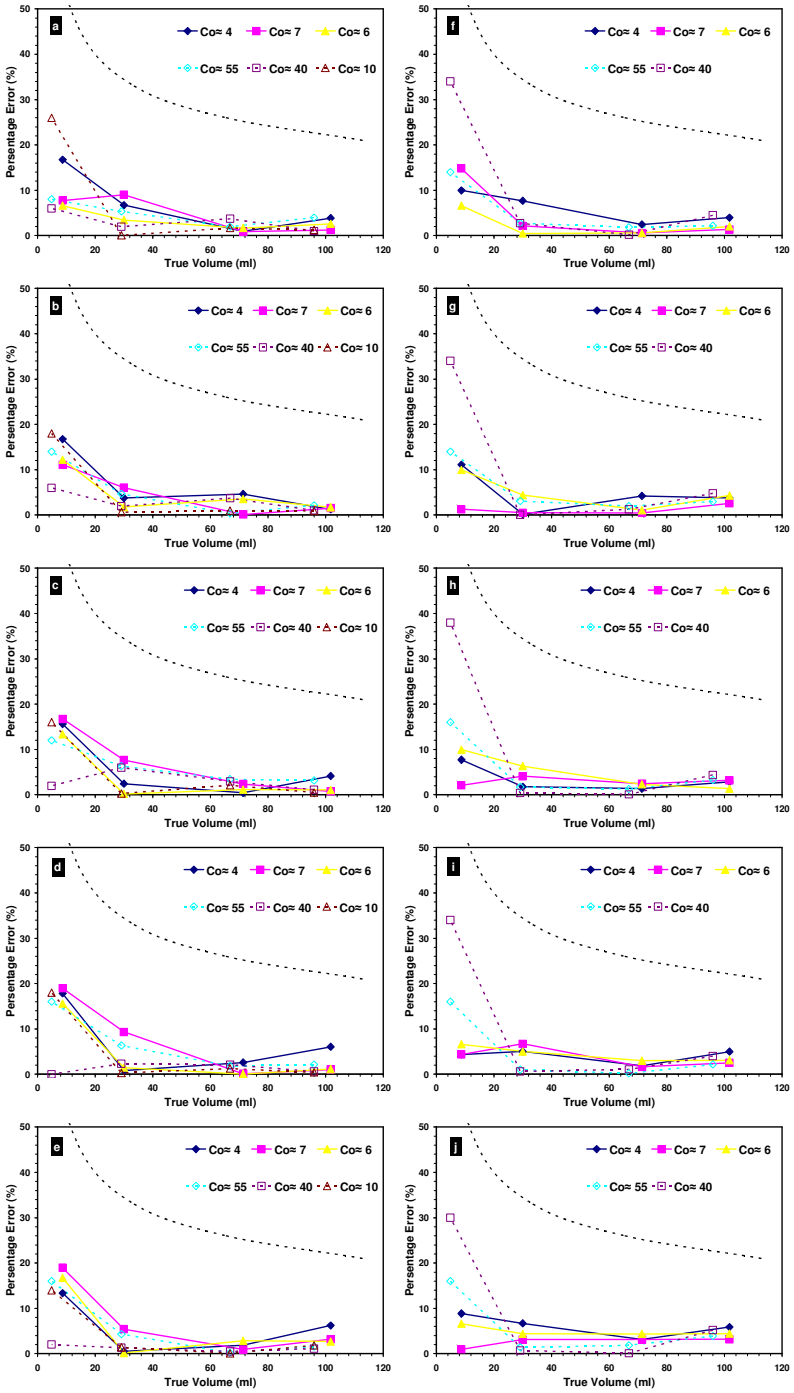

Figure 4.9: The modulus of percentage error in measuring irregular volumes using the VCAT method for IT (left side) with different t_{AC} = 1(a), 2.5(b), 5(c), 10(d), 60(e) minute and FBP (right side) with the same t_{AC} values (f, g, h, i, j). The black dotted line represents the acceptable error. A logarithmic scale in the percentage error direction has been used.

4.2.2.1. VCAT using 60 minute single calibration curve

As for spherical lesions, the possibility was explored of using a single calibration curve obtained with the lowest noise calibration data obtained with 60 min acquisition times. The results shown in Figure 4.10 demonstrate sufficient accuracy across all variables investigated. Further, these results show a decrease in percentage error for the smaller crescent volumes than using the full set of calibration curves.

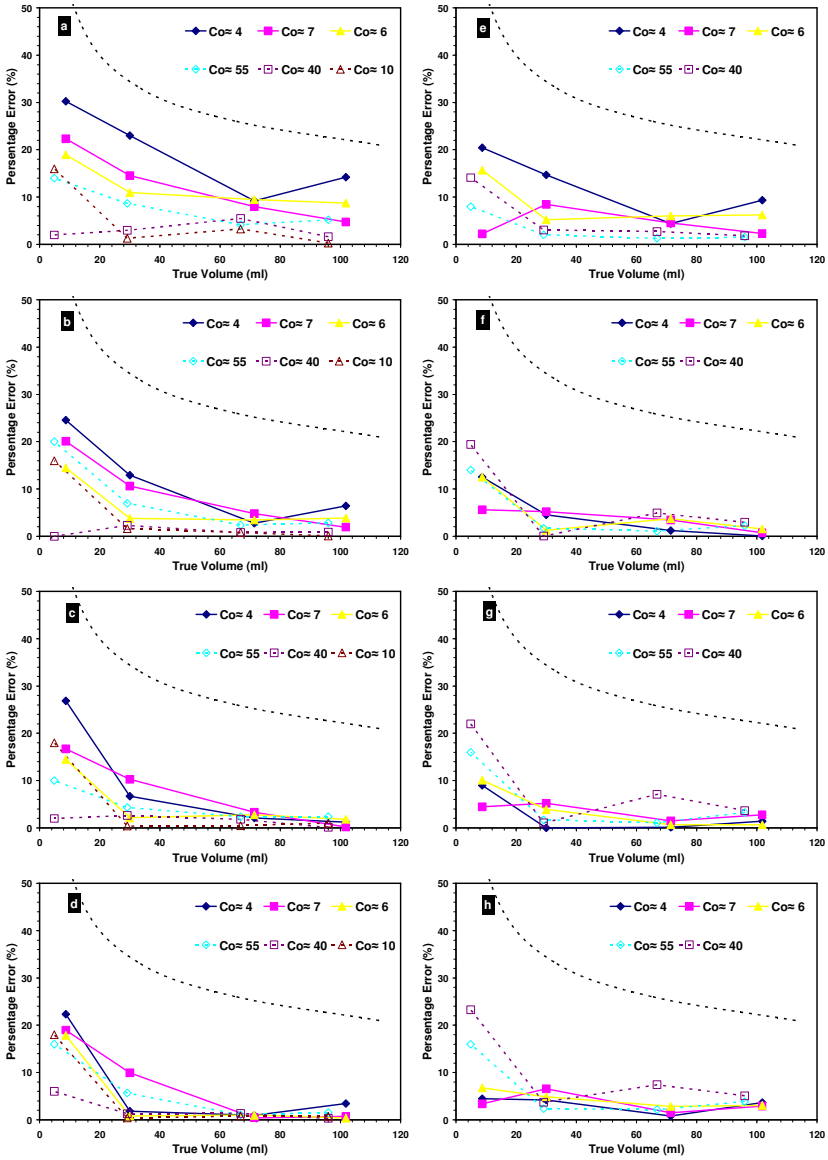

Figure 4.10: The modulus of percentage error in measuring irregular volumes using VCAT 60 minute single calibration curve method for IT (left side) with different t_{AC} = 1(a), 2.5(b), 5(c), 10(d) minute and FBP (right side) with the same t_{AC} values (e, f, g, h). The black dotted line represents the acceptable error. A logarithmic scale in the percentage error direction has been used.

4.2.2.2. Comparison with fixed thresholding method

Figure 4.8, presented in section 4.2.1.2, demonstrates the results of applying a fixed threshold of 40% of the maximum uptake on irregular lesions. It is clear that this fixed thresholding method produces results which are considerably worse than using the VCAT method. However, for contrast values greater than 4, and all irregular volumes except the smallest, the results were generally within the acceptable value for RTP.

4.3. Concordance Measurements Results

The volumes derived by the CAT and VCAT methods from the PET image of the irregular phantoms were tested for concordance against the volume measured on a CT image of the phantom obtained by filling it with Iodine contrast (concentration ranging from 4.5 – 3.5 mg/ml). This CT data was considered to represent the true shape of the volume. These concordance measurements were carried out on the two families of irregular lesion volumes, top-hat and crescent.

The segmented VCAT volume on PET was written into a binary image with the same matrix size, 128 × 128 × 47, as the PET images, re-scaled from the PET FoV of 70cm to the CT FoV of 50 cm using linear interpolation, and then up-sampled using bilinear interpolation to match the CT matrix size of 512 × 512 × 47.

Figure 4.11 shows the results of Dice and Jaccard similarity coefficients measurements in top-hat and crescent irregular volumes segmented using the CAT method at 1, 2.5, 5, 10 and 60 min acquisition times for both IT and FBP images. These results represent a very good similarity between the CAT

segmented volume and the CT for volumes > 30ml, while the goodness of this similarity decreases with volume decreases (< 30ml). A very similar result was obtained using the VCAT method, Figure 4.12, which may suggest that this error associated with CAT and VCAT methods was mainly due to the image sampling and matrix dimensions. The results of the DSC and JSC using both the CAT and VCAT showed no large difference between IT and FBP reconstruction techniques for top-hat and crescent especially for larger volumes. These results demonstrate a very good similarity between the CAT and VCAT segmented PET and the CT volumes.

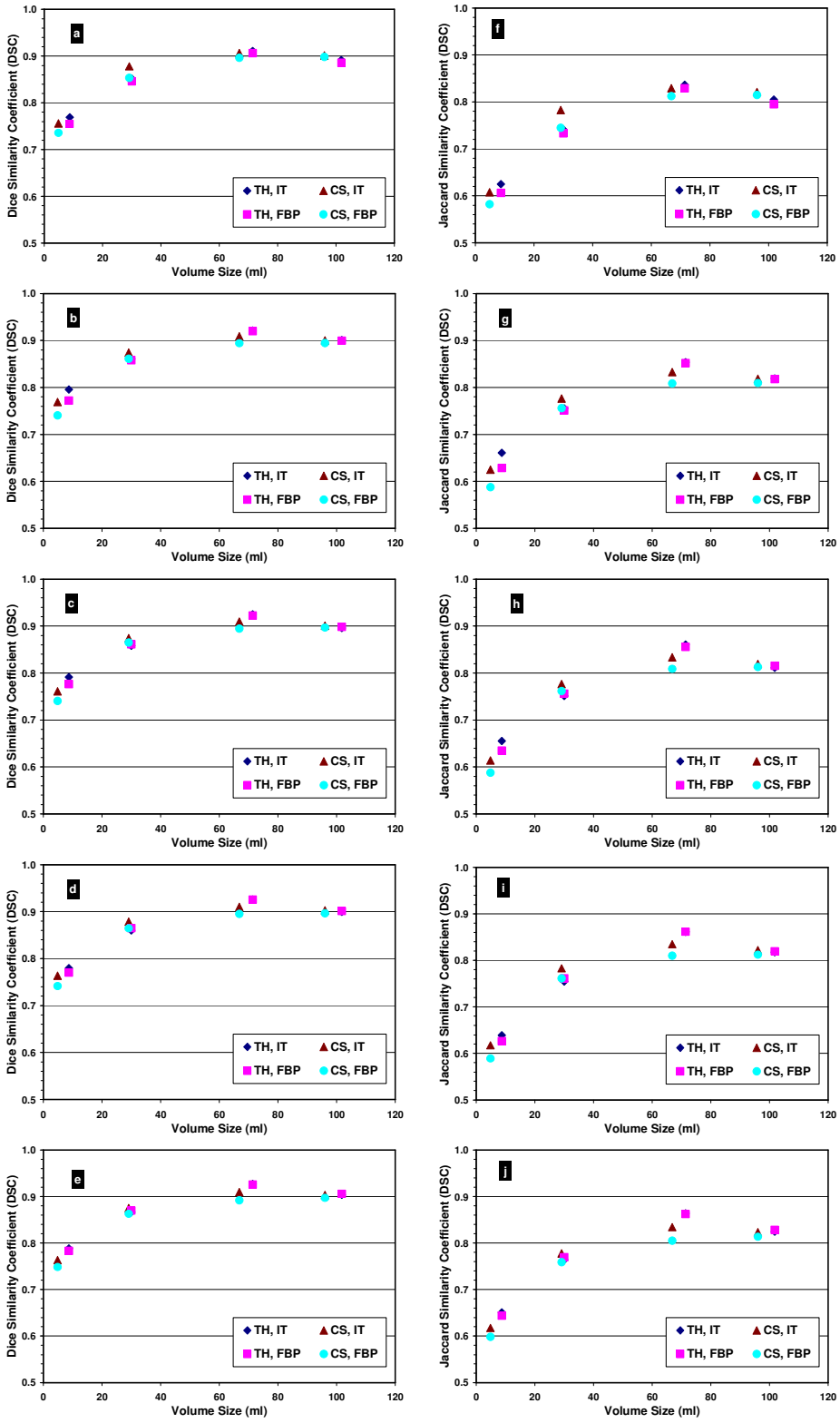

Figure 4.11: Dice similarity coefficient at 1, 2.5, 5, 10 and 60 min acquisition times (a, b, c, d and e) and Jaccard similarity coefficient (f, g, h, i and j) for segmented top-hat (TH) and crescent (CS) volumes using the CAT method for IT and FBP reconstruction techniques.

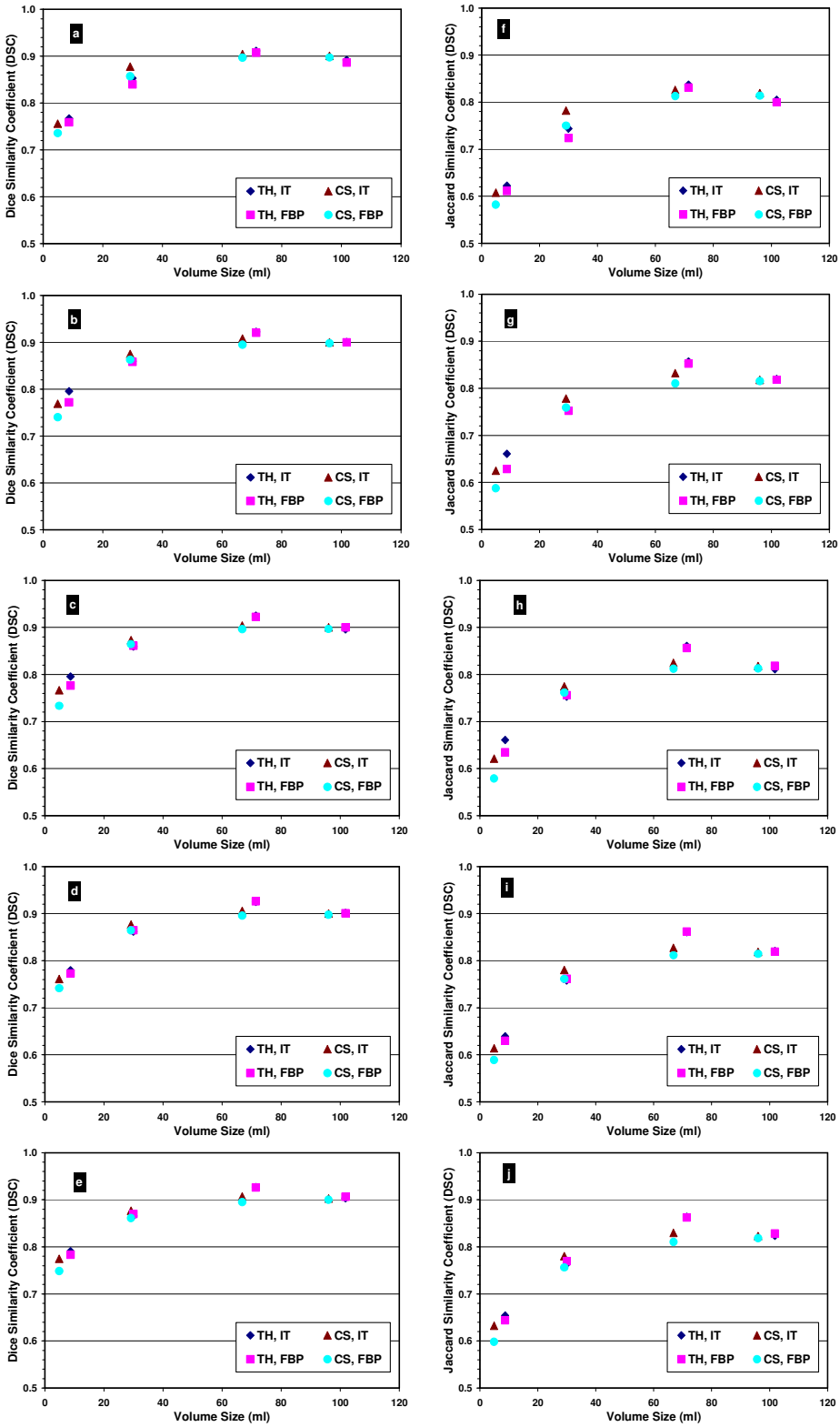

Figure 4.12: Dice similarity coefficient at 1, 2.5, 5, 10 and 60 min acquisition times (a, b, c, d and e) and Jaccard similarity coefficient (f, g, h, i and j) for segmented top-hat (TH) and crescent (CS) volumes using the VCAT method for IT and FBP reconstruction techniques.

4.4. Euclidean Distance Transformation

The Euclidean distance transformation was used to compare the spatial location between the true volume (obtained from the CT) and the CAT segmented PET volume. Two distance maps were generated from the true binary image. One distance map represents the distances in mm inside (VoI) the true volume and the other represents the distance in mm outside (background) the true volume. These two distance maps were combined with positive distance to be outside the true volume and negative distance inside it. The surface of the CAT segmented volume was then calculated and compared its location with the new combined distance map. So, the resulting distance value will be negative if the surface of the CAT segmented volume was inside the true volume and will be positive if it was outside the true volume.

Figure 4.13 shows the histograms of the distances between the surface of true volumes (CT) and the surface of CAT segmented volumes at 1, 2.5, 5, 10 and 60 min t_{AC} for IT and FBP images. These results were similar to that obtained with the VCAT method where it showed that more than 60% of the distances were centred on the zero distance, and more than 95% of these distances were within ±2 mm.

Figure 4.14 shows the results of the Euclidean distance transformation tests, carried out on the families of top-hat and crescent lesions. Histograms are shown of the distances between the true volume (CT) surface and the VCAT volume surface at 1, 2.5, 5, 10 and 60 min acquisition time and for IT and FBP. These histograms demonstrate that the distances between the two surfaces were centred on zero distance, and that more than 60% of the surfaces overlapped. The histograms show also that the distance variations

using the VCAT method were mostly (95%) within ±2 mm which is in agreement with the RTP acceptable error.

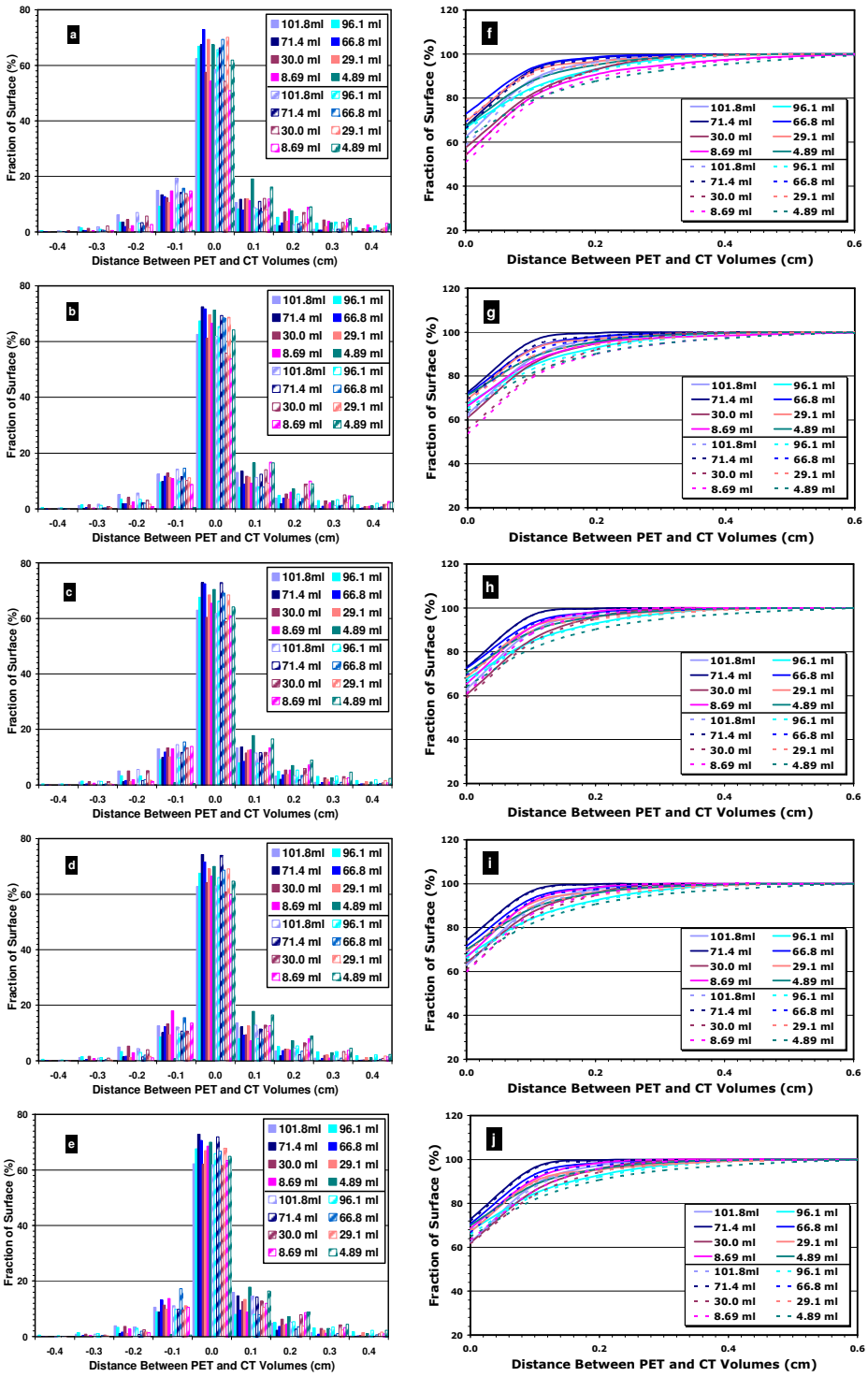

Figure 4.13: Deferential (a, b, c, d, e) and cumulative (f, g, h, i, j) histograms of the nearest distance between the surface of reference CT images and segmented PET volumes at 1, 2.5, 5, 10 and 60 minute acquisition times using CAT method for top-hat and crescent volumes for IT (solid) and FBP (dashed) respectively developed by using the Euclidean distance transformation.

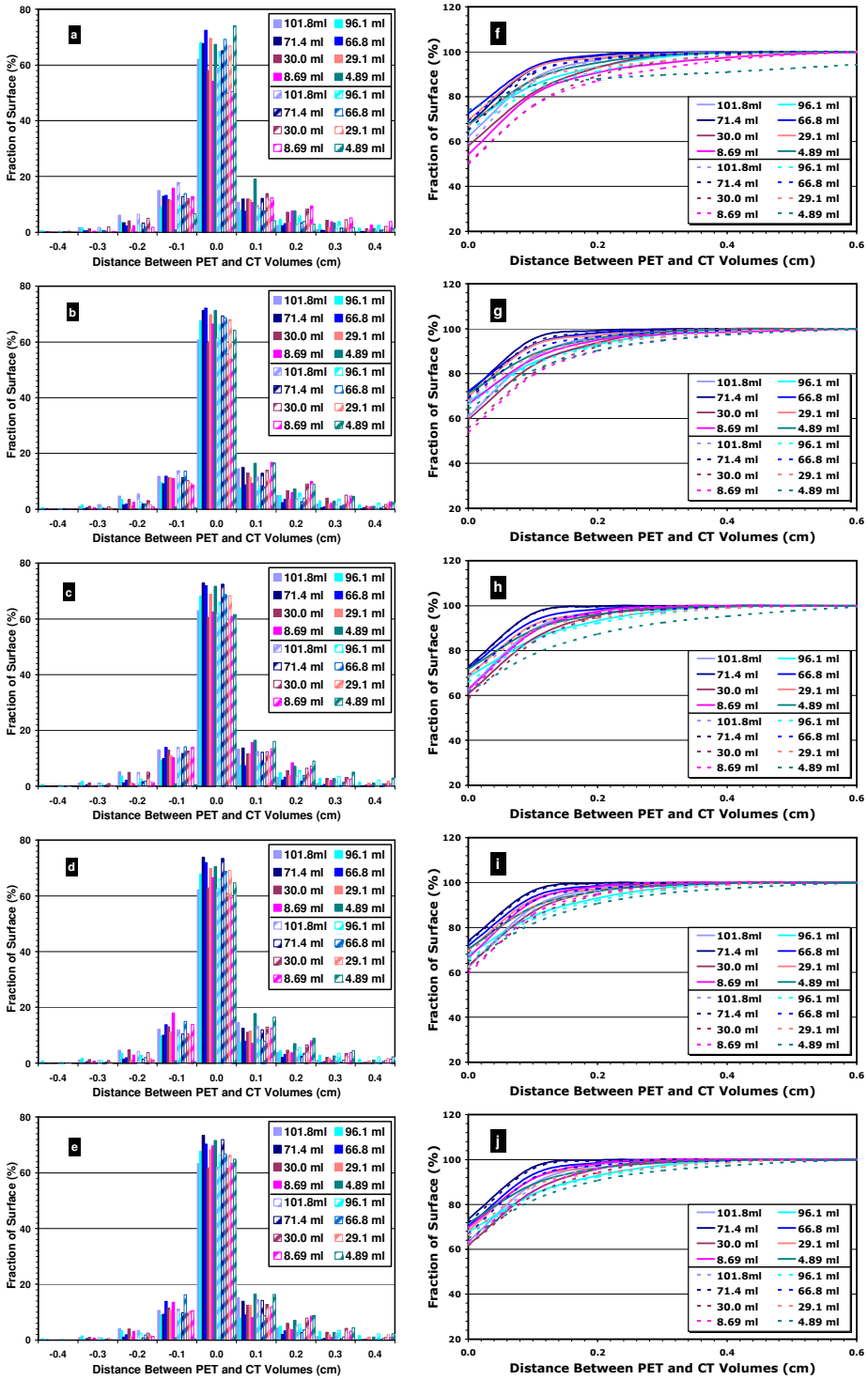

Figure 4.14: Deferential (a, b, c, d, e) and cumulative (f, g, h, i, j) histograms of the nearest distance between the surface of reference CT images and segmented PET volumes at 1, 2.5, 5, 10 and 60 minute acquisition times using VCAT method for top-hat and crescent volumes for IT (solid) and FBP (dashed) respectively developed by using the Euclidean distance transformation.

4.5. Comparison of VCAT and CAT Variant

4.5.1. Spherical Lesions

In the previous sections, four versions of implementing VCAT/CAT have been described: VCAT, VCAT using 60 min calibration curve (VCAT-60), CAT, and CAT using 60 min calibration curve (CAT-60). In this section, the results of these four variants are compared with each other and with the results of using a simple 40% fixed thresholding technique. In spherical volumes, the performance of these five different techniques were analysed with statistical methods for a total of 300 different conditions (6 volume sizes $\times$ 5 contrasts $\times$ 5 acquisition times $\times$ 2 reconstruction techniques). The analysis was undertaken using the conformity index (CI) as defined by the following equation:

$$CI = \left| \log\left(\frac{Segmented\_Volume}{True\_Volume} \right) \right| \qquad \textbf{..... (4.3)}$$

This conformity index will equal zero if the segmented volume equals the true volume, and increases as the difference between these two volumes increases. This CI has the advantage of treating the difference in larger and smaller volumes in a symmetrical fashion.

The calculated CI values for using the five techniques on spherical lesions are shown in Figure 4.15, Figure 4.16 and Figure 4.17 for observed contrasts of 2, 5, and ∞ respectively. It is clear from these figures that the VCAT technique performed best, with the lowest CI values across nearly all studied conditions. The 40% fixed thresholding technique produced the worst results, with the highest CI values, especially at low contrast levels. The CI

values using 40% fixed thresholding decrease with increasing the volume size at the same contrast level and with increasing the contrast level at the same volume size to record a closer value to the other four techniques at V = 26.6 ml and $C_o = \infty$.

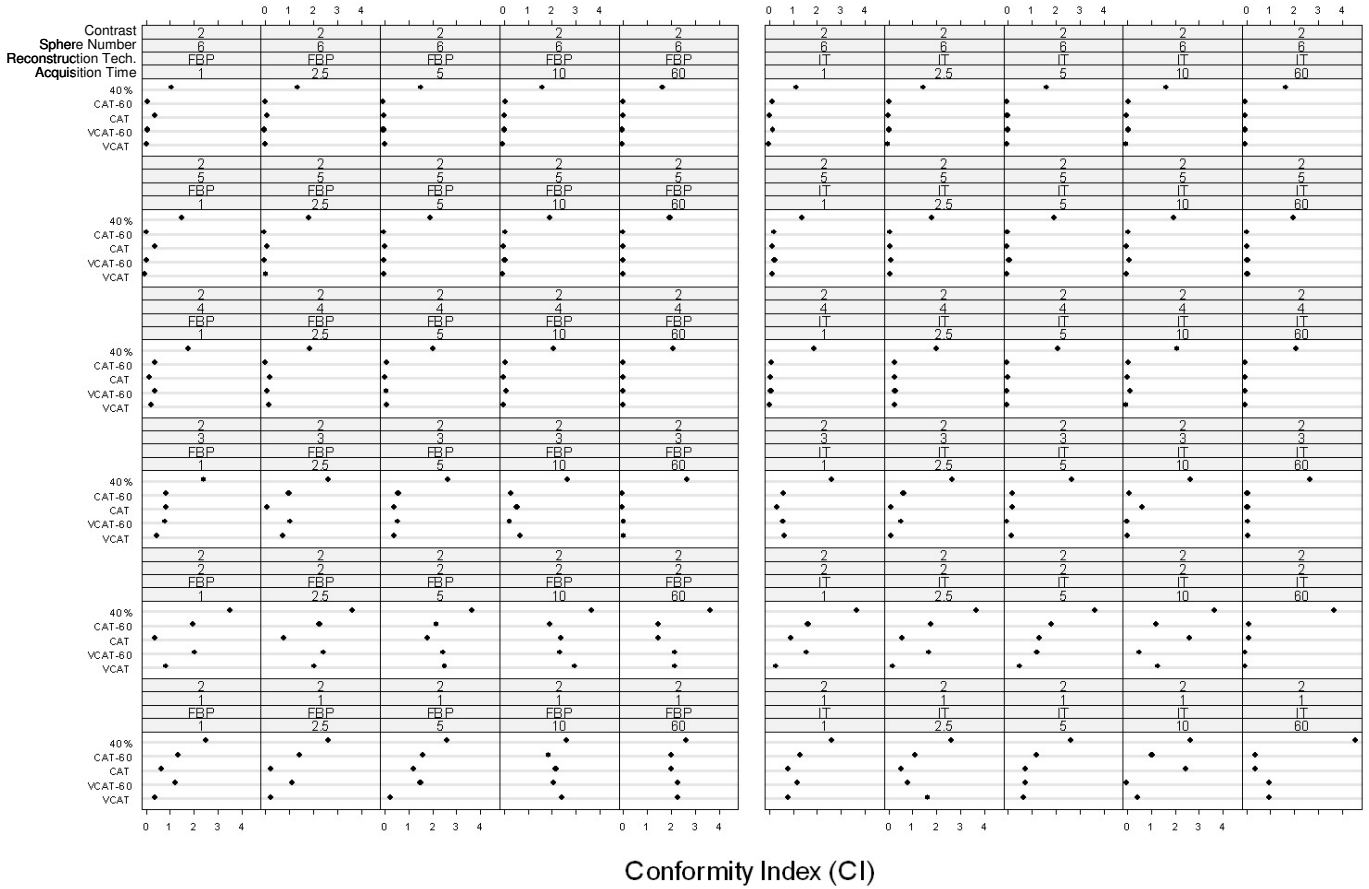

Figure 4.15: Conformity index in measuring PET spherical lesions using the VCAT, VCAT-60, CAT, CAT-60, and 40% fixed threshold for contrast = 2 for spherical volumes number 1 (0.53 ml), 2 (1.15 ml), 3 (2.57 ml), 4 (5.55 ml), 5 (11.5 ml), and 6 (26.6 ml) at 1, 2.5, 5, 10, and 60 min t_{AC}. Left panel FBP and right panel IT.

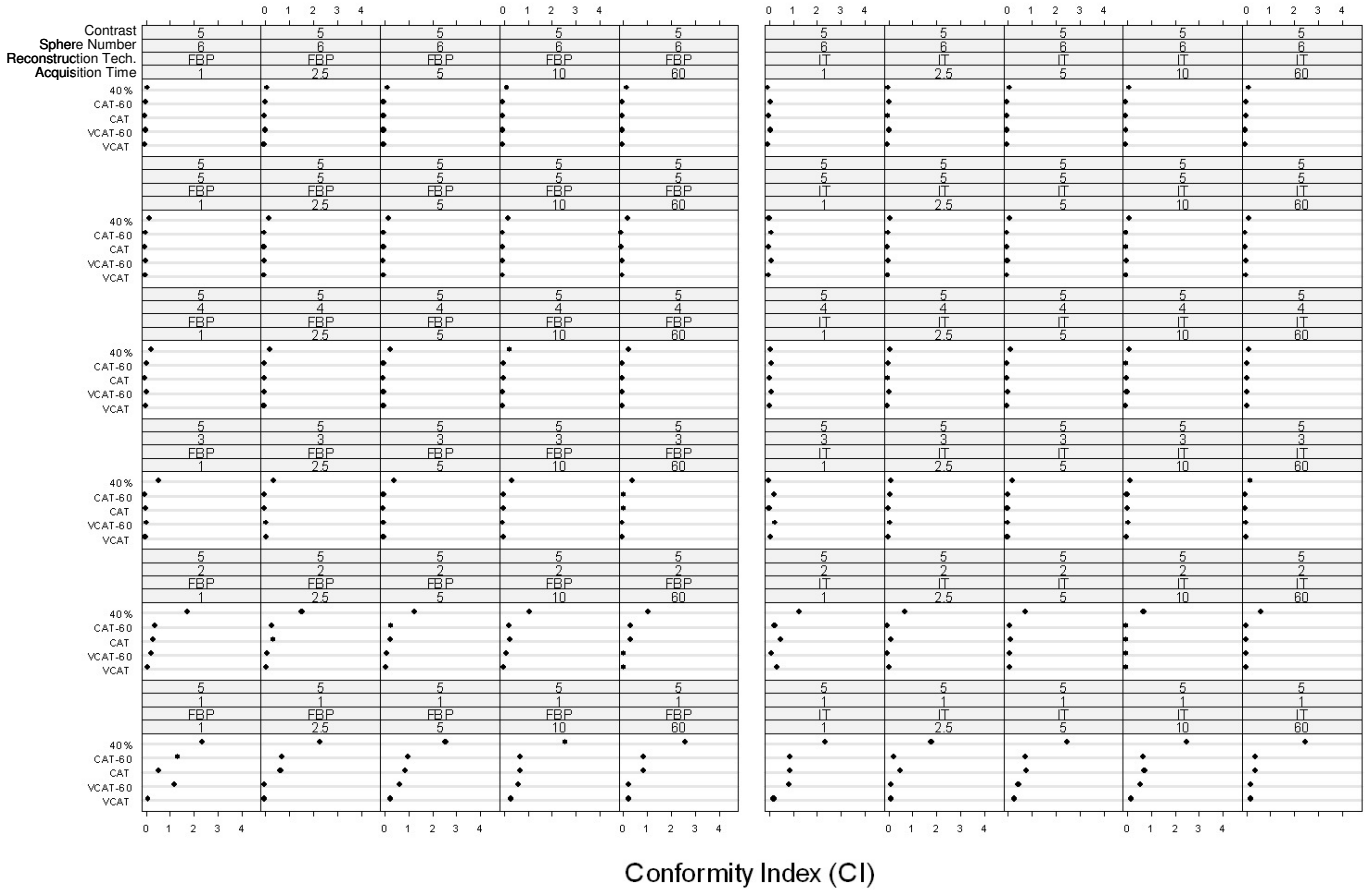

Figure 4.16: Conformity index in measuring PET spherical lesions using the VCAT, VCAT-60, CAT, CAT-60, and 40% fixed threshold for contrast = 5 for spherical volumes number 1 (0.53 ml), 2 (1.15 ml), 3 (2.57 ml), 4 (5.55 ml), 5 (11.5 ml), and 6 (26.6 ml) at 1, 2.5, 5, 10, and 60 min t_{AC}. Left panel FBP and right panel IT.

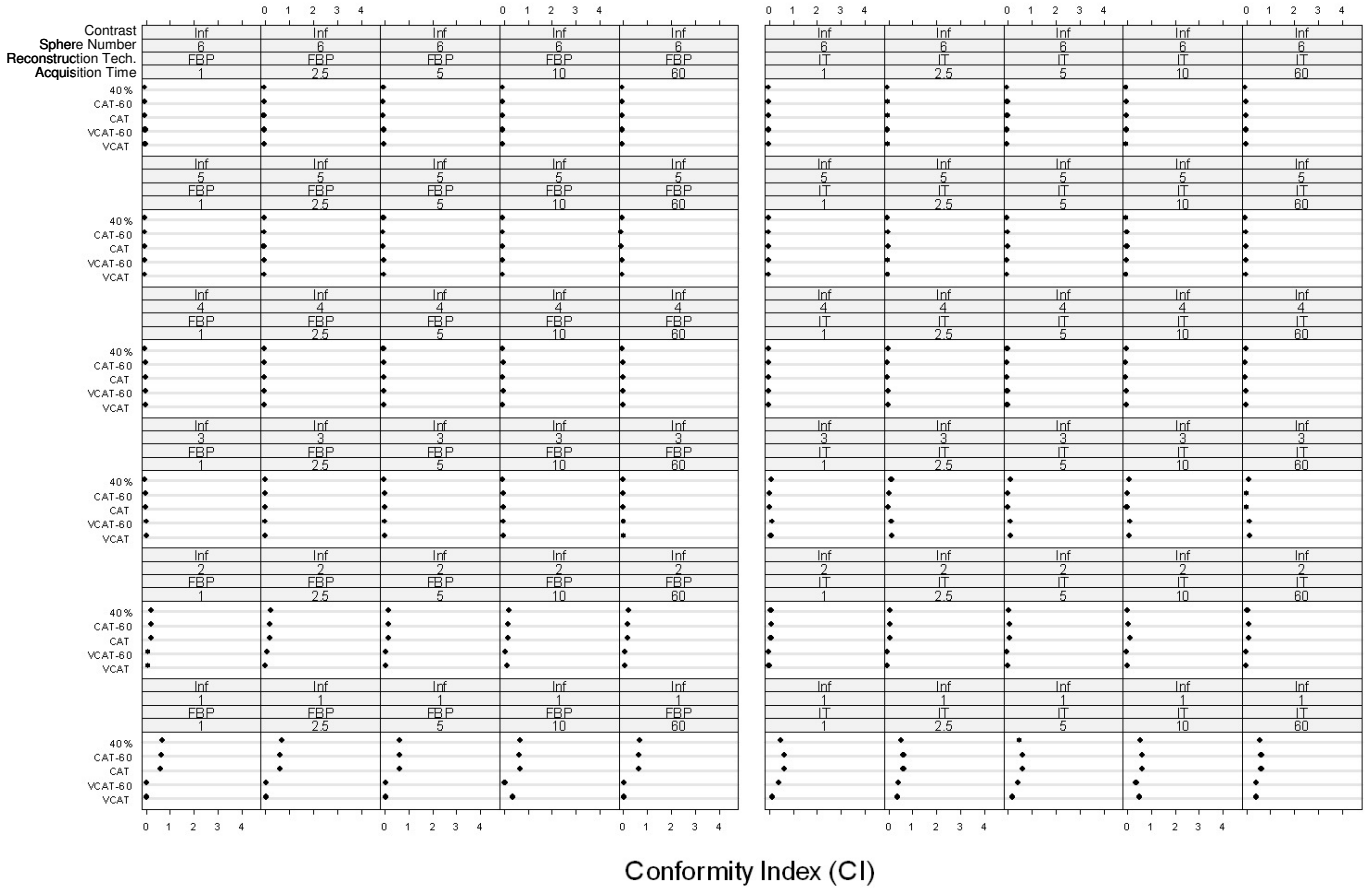

Figure 4.17: Conformity index in measuring PET spherical lesions using the VCAT, VCAT-60, CAT, CAT-60, and 40% fixed threshold for contrast = ∞ for spherical volumes number 1 (0.53 ml), 2 (1.15 ml), 3 (2.57 ml), 4 (5.55 ml), 5 (11.5 ml), and 6 (26.6 ml) at 1, 2.5, 5, 10, and 60 min t_{AC}. Left panel FBP and right panel IT.

A ranking approach was then employed placing the techniques in a ranking order where the best technique, with lowest CI, was ranked lowest. Figure 4.18, Figure 4.19, and Figure 4.20 show the rank results graphically for C_o values of 2, 5, and ∞ respectively. These results show that VCAT technique was the best in many groups. However, the use of 40% fixed threshold was almost the highest rank, which means less preferable, across all studied conditions, except in few groups in larger volumes and contrast = ∞.

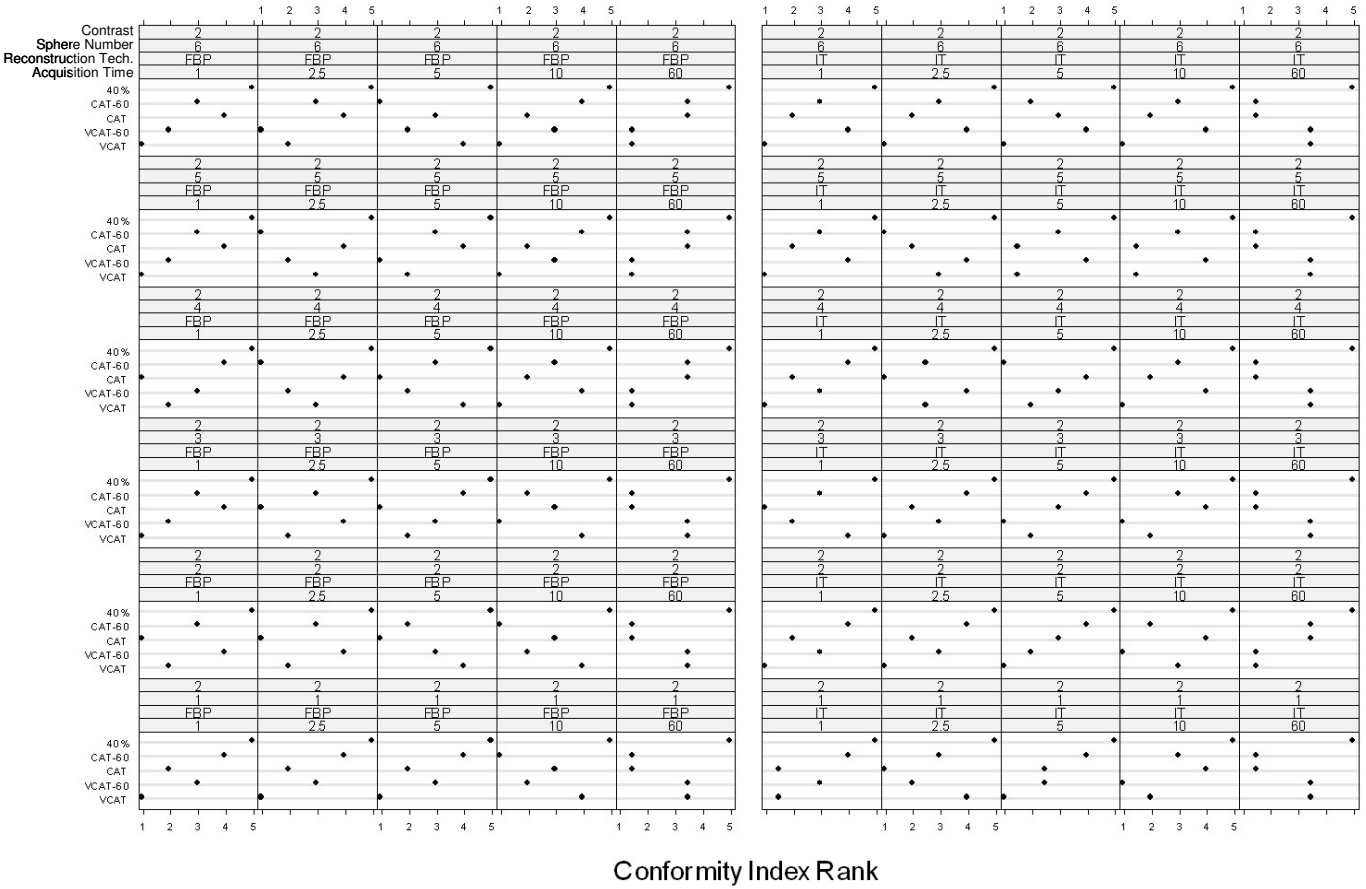

Figure 4.18: Conformity index rank in measuring PET spherical lesions using the VCAT, VCAT-60, CAT, CAT-60, and 40% fixed threshold for contrast = 2 for spherical volumes number 1 (0.53 ml), 2 (1.15 ml), 3 (2.57 ml), 4 (5.55 ml), 5 (11.5 ml), and 6 (26.6 ml) at 1, 2.5, 5, 10, and 60 min t_{AC}. Left panel FBP and right panel IT.

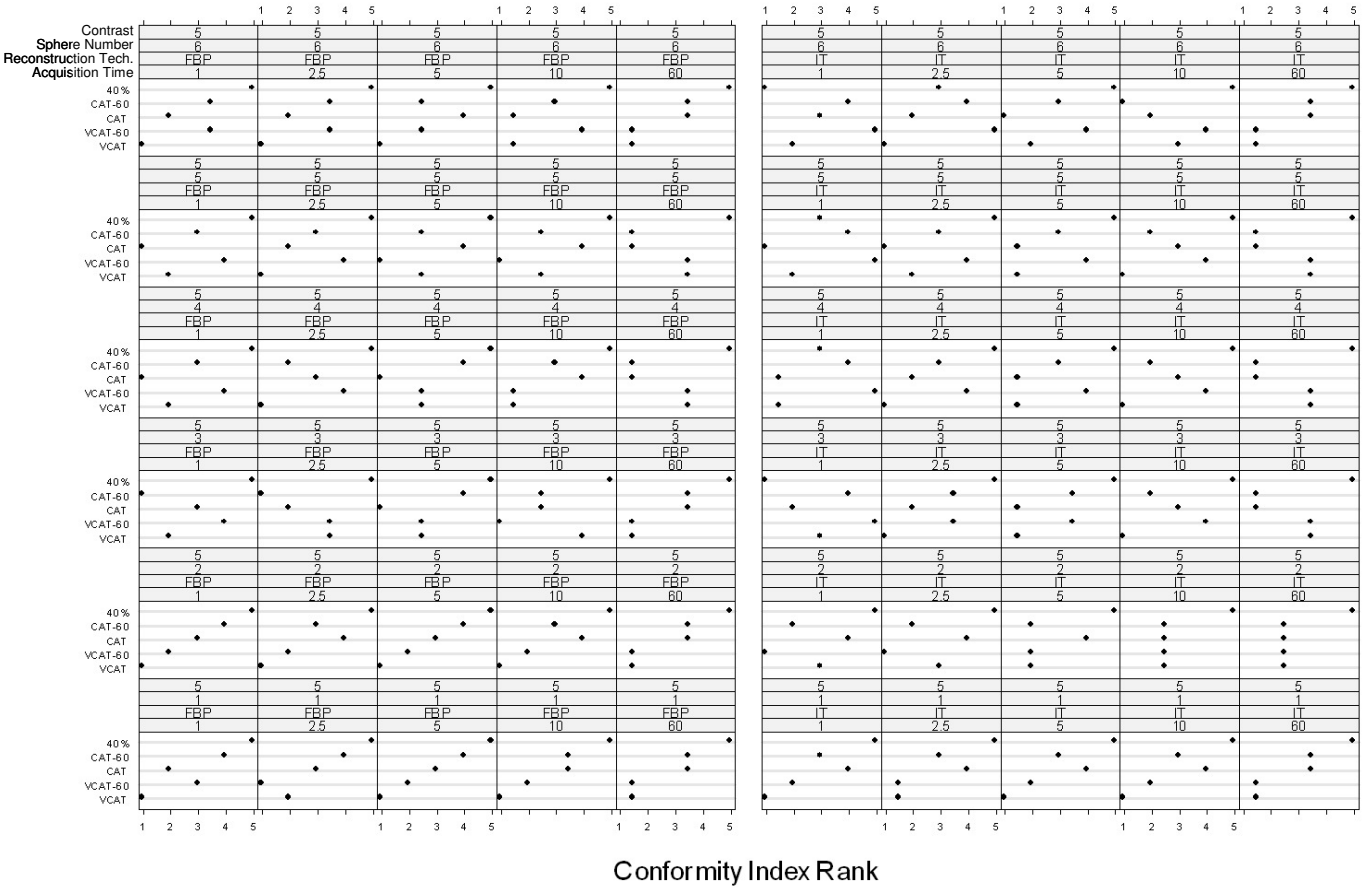

Figure 4.19: Conformity index rank in measuring PET spherical lesions using the VCAT, VCAT-60, CAT, CAT-60, and 40% fixed threshold for contrast = 5 for spherical volumes number 1 (0.53 ml), 2 (1.15 ml), 3 (2.57 ml), 4 (5.55 ml), 5 (11.5 ml), and 6 (26.6 ml) at 1, 2.5, 5, 10, and 60 min t_{AC}. Left panel FBP and right panel IT.

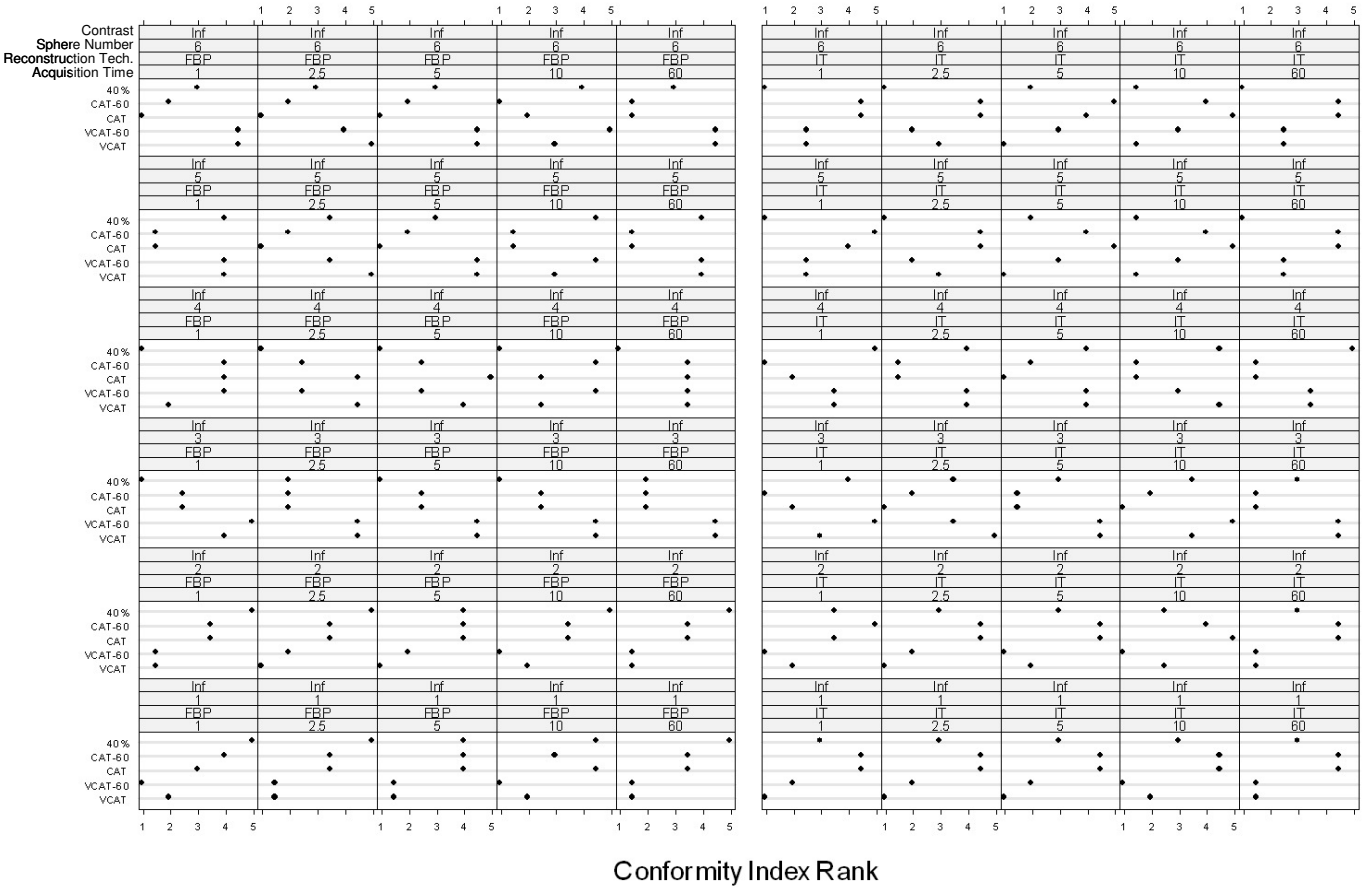

Figure 4.20: Conformity index rank in measuring PET spherical lesions using the VCAT, VCAT-60, CAT, CAT-60, and 40% fixed threshold for contrast = ∞ for spherical volumes number 1 (0.53 ml), 2 (1.15 ml), 3 (2.57 ml), 4 (5.55 ml), 5 (11.5 ml), and 6 (26.6 ml) at 1, 2.5, 5, 10, and 60 min t_{AC}. Left panel FBP and right panel IT.

The Friedman ranking test [117] was used to test the statistical significance in the mean rank across all studied conditions. The Friedman test statistic for all techniques was 368.98 ($p << 0.0001$), which means that the difference between one technique (or more) and the other techniques was highly significant, but not indicating precisely which technique. Therefore, a least significant difference procedure following the Friedman test was carried out to test the pairwise significance between the five techniques (10 pairs) using a calculated critical difference maintaining an overall error rate of 5% for all paired comparisons. The mean ranks for the five techniques across all studied conditions and the critical difference are presented in Table 4.1.

VCAT	**CAT**	**VCAT-60**	**CAT-60**	**40%**	**Critical Difference**
2.15	2.68	2.85	2.89	4.43	**0.362**

Table 4.1: The mean rank order with the calculated critical difference for the pairwise comparisons between the use of CAT, CAT-60, VCAT, VCAT-60, and 40% techniques in all spherical lesions. The techniques sharing the same green bar are not statistically significantly different.

These mean ranks show the ranking order of these five techniques from lowest to highest rank. The VCAT technique, having a critical difference greater than 0.362 from the second technique in order, CAT, was significantly better than all the other four techniques. There was no significant difference between CAT, VCAT-60, and CAT-60. It is clear that the 40% fixed threshold technique was the worst, by a very large factor, than the other four.

4.5.2. Irregular Lesions

The same five techniques, CAT, CAT-60, VCAT, VCAT-60, and 40%, were tested in four different volume sizes of the two types of irregular lesions, top-

hat and crescent. The same strategy as for spherical lesions was employed in comparing the difference between the five segmentation techniques, which was to calculate the CI for each irregular volume under all studied conditions, rank these five techniques based on the calculated CI, take the mean rank for the five techniques across all conditions, and, finally, test the significance of the differences using the Friedman ranking test.

Three experiments using top-hat and crescent volumes (3 experiments $\times$ 2 shapes $\times$ 4 volumes $\times$ 5 t_{AC} $\times$ 2 reconstruction techniques) were evaluated in this statistical analysis. Figure 4.21 and Figure 4.22 show the calculated CI in two experiments of top-hat and crescent volumes measurements using the VCAT, VCAT-60, CAT, CAT-60, and 40% fixed thresholding techniques. The figures show that similar CI values were calculated using the five techniques in case of crescent volumes rather than top-hat volumes especially in larger volumes. This could be due to the larger contrasts (40 and 55) in crescent experiments than the contrasts in top-hat experiments (4 and 7). The figures show also similar results between IT and FBP for each irregular shape.

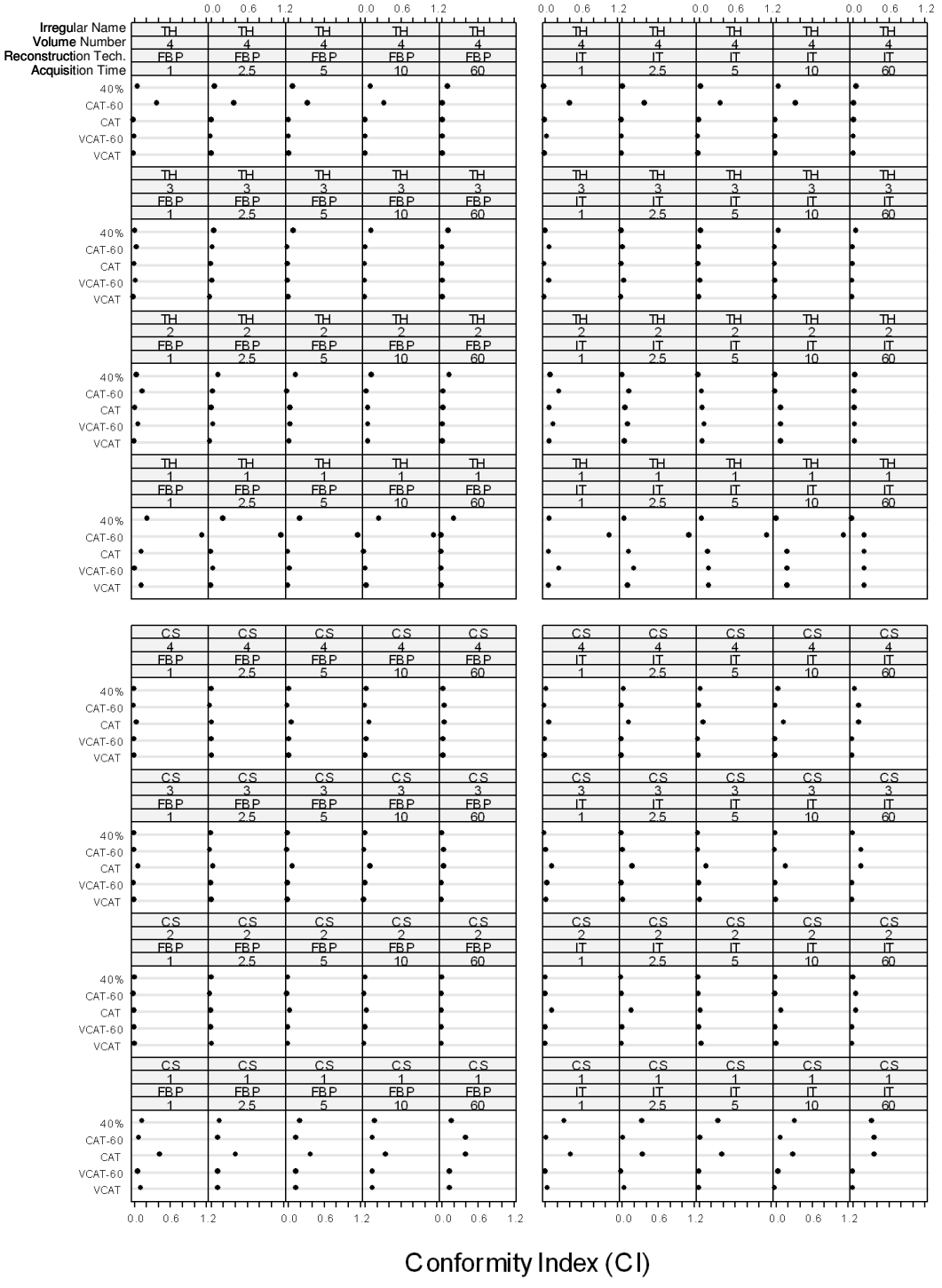

Figure 4.21: Conformity index in measuring PET irregular lesions using the VCAT, VCAT-60, CAT, CAT-60, and 40% fixed threshold for experiment one (top-hat, TH, C_o = 4 and crescent, CS, C_o = 40) for irregular volumes number (TH, CS): 1 (8.69, 4.89 ml), 2 (30.0, 29.1 ml), 3 (71.4, 66.8 ml), and 4 (101.8, 96.1 ml) at 1, 2.5, 5, 10, and 60 min t_{AC}. Left panels FBP and right panels IT.

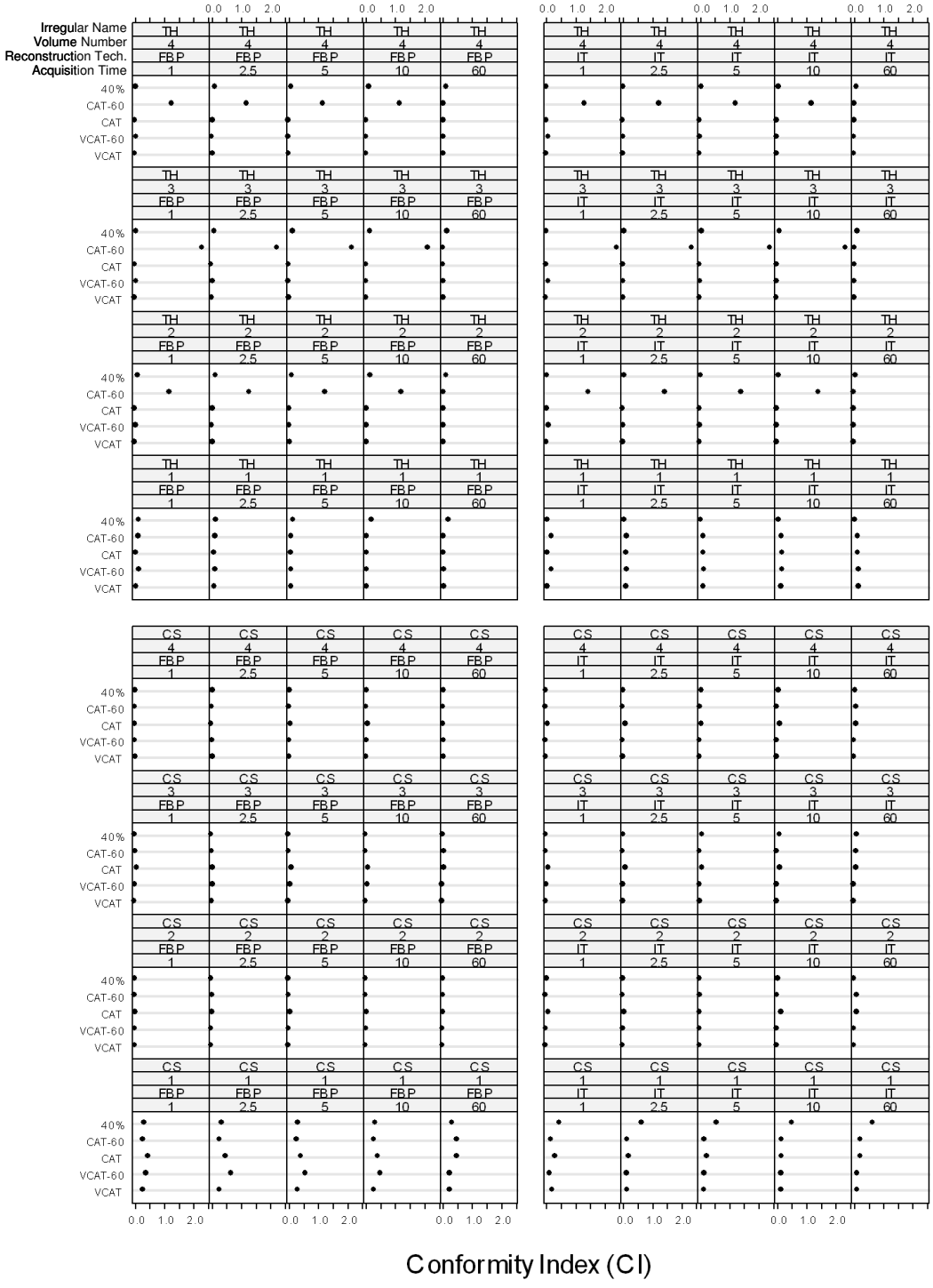

Figure 4.22: Conformity index in measuring PET irregular lesions using the VCAT, VCAT-60, CAT, CAT-60, and 40% fixed threshold for experiment two (top-hat, TH, C_o = 7 and crescent, CS, C_o = 55) for irregular volumes number (TH, CS): 1 (8.69, 4.89 ml), 2 (30.0, 29.1 ml), 3 (71.4, 66.8 ml), and 4 (101.8, 96.1 ml) at 1, 2.5, 5, 10, and 60 min t_{AC}. Left panels FBP and right panels IT.

Although the five techniques produced most similar CI values, Figure 4.23 and Figure 4.24 show the ranking order for these five techniques across each group of studied conditions. It is clear from the figures that the 40% fixed threshold produced the highest rank in many groups, and therefore performed worst of all. However, the other four techniques performed in varying inconsistent ways across the groups, with no particular technique having the advantage.

The Friedman test statistic for all techniques was 95.49 ($p << 0.0001$), which means that the difference between one technique (or more) and the other techniques was highly significant. A least significant difference procedure following the Friedman test was carried out to test the pairwise significance between the five techniques (10 pairs) using a calculated critical difference maintaining an overall error rate of 5% for all paired comparisons. The mean ranks for the five techniques across all studied conditions and the critical difference are presented in Table 4.2.

VCAT	VCAT-60	CAT	CAT-60	40%	Critical Difference
2.28	2.68	3.21	3.29	3.54	**0.424**

Table 4.2: The mean rank order with the calculated critical difference for the pairwise comparisons between the use of CAT, CAT-60, VCAT, VCAT-60, and 40% techniques in all irregular lesions. The techniques sharing the same green bar are not statistically significantly different.

These mean ranks show the ranking order of these five techniques from lowest to highest rank, showing that VCAT had the lowest rank, being significantly better than all techniques except VCAT-60 for which the rank difference, 0.4, was of borderline significance (close to the critical difference of 0.424). The two CAT techniques were significantly worse than the two

VCAT techniques. Although the worst technique proved to be 40% fixed threshold, the difference in mean rank value from CAT (or CAT-60) was not statistically significant.

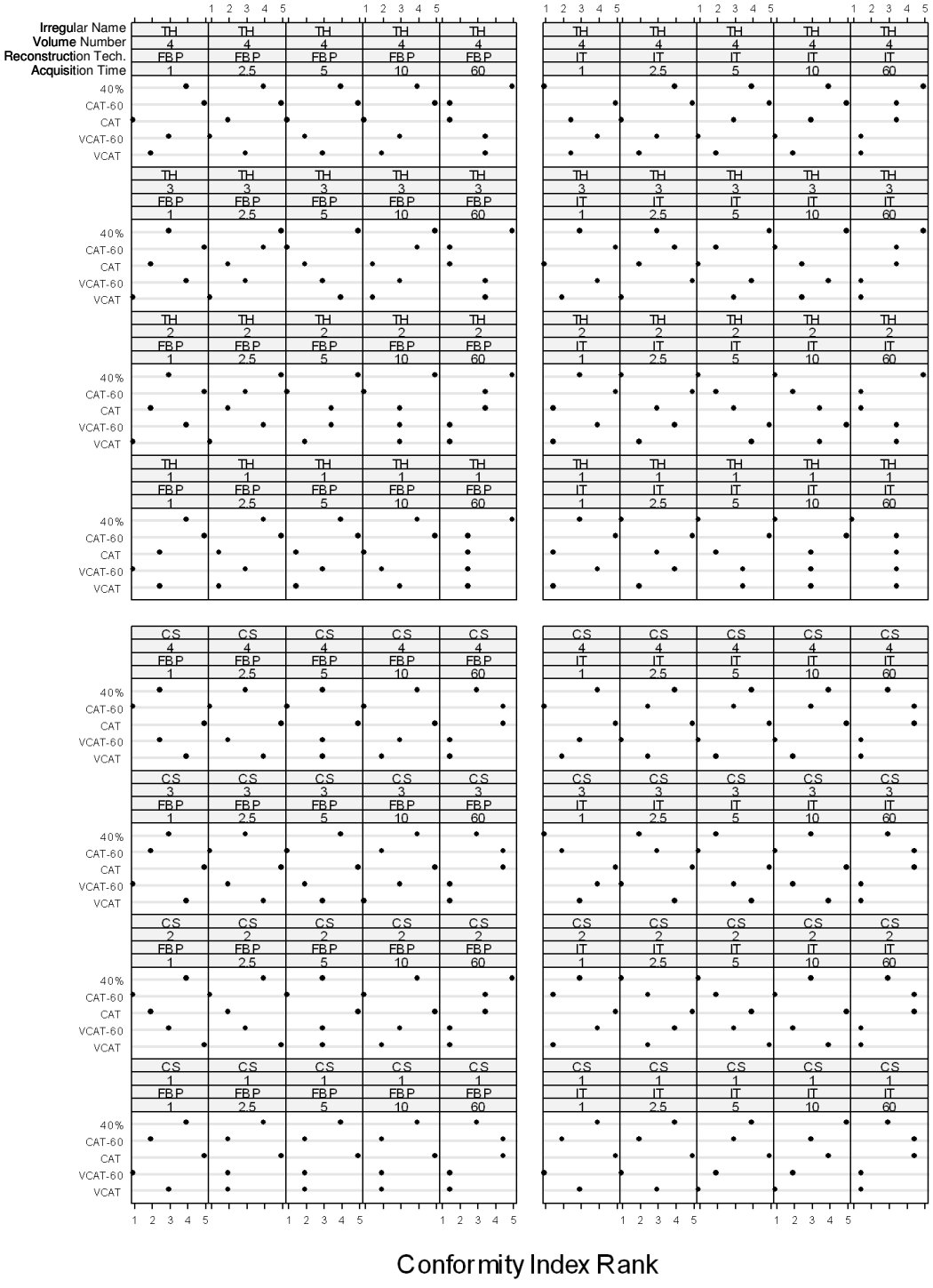

Figure 4.23: Conformity index rank in measuring PET irregular lesions using the VCAT, VCAT-60, CAT, CAT-60, and 40% fixed threshold for experiment one (top-hat, TH, C_o = 4 and crescent, CS, C_o = 40) for irregular volumes number (TH, CS): 1 (8.69, 4.89 ml), 2 (30.0, 29.1 ml), 3 (71.4, 66.8 ml), and 4 (101.8, 96.1 ml) at 1, 2.5, 5, 10, and 60 min t_{AC}. Left panels FBP and right panels IT.

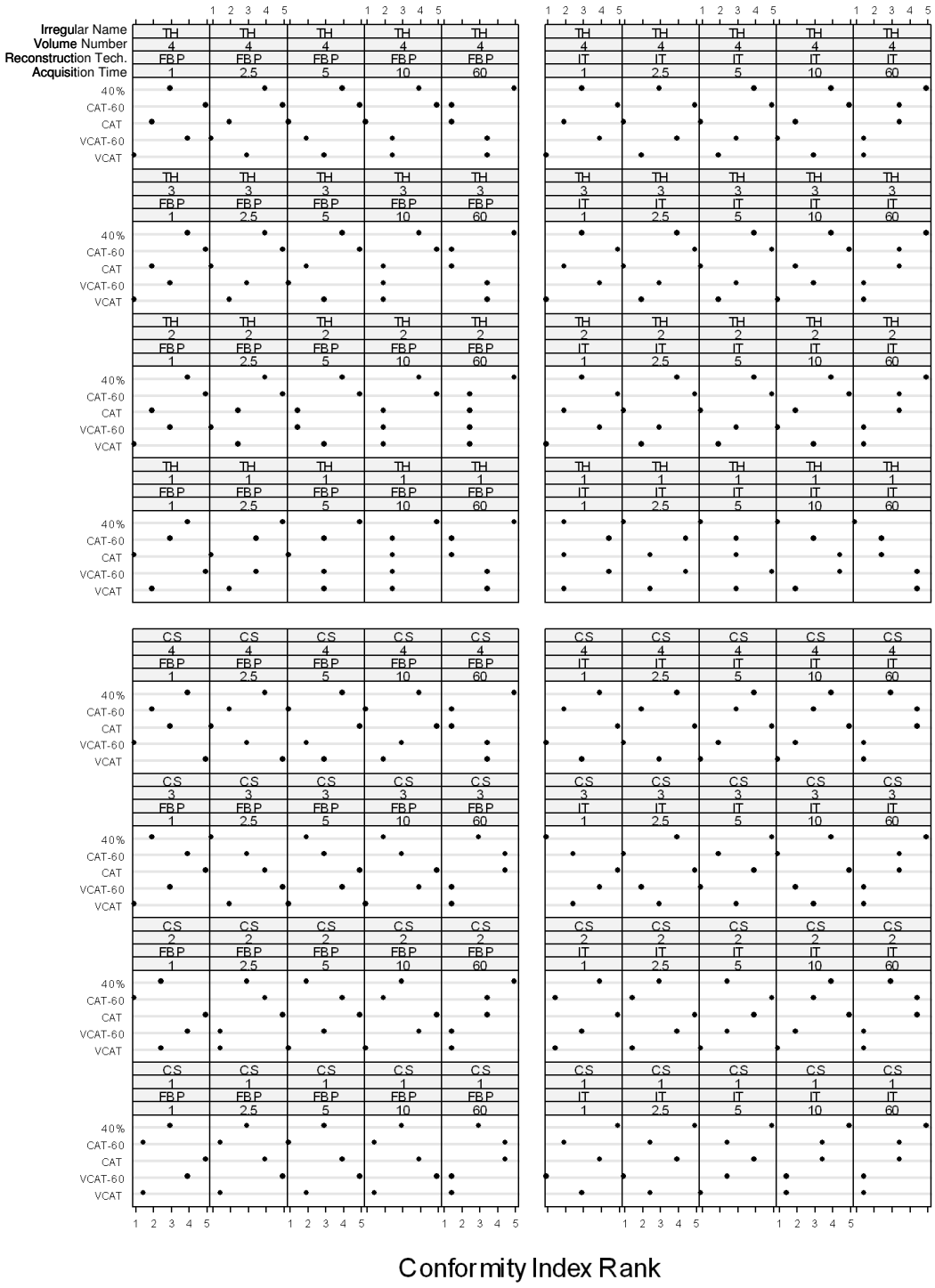

Figure 4.24: Conformity index rank in measuring PET irregular lesions using the VCAT, VCAT-60, CAT, CAT-60, and 40% fixed threshold for experiment two (top-hat C_o = 7 and crescent C_o = 55) for irregular volumes number (top-hat, crescent): 1 (8.69, 4.89 ml), 2 (30.0, 29.1 ml), 3 (71.4, 66.8 ml), and 4 (101.8, 96.1 ml) at 1, 2.5, 5, 10, and 60 min t_{AC}. Left panels FBP and right panels IT.

4.6. Discussion

It is important that the errors in any new technique should be related to the errors that are acceptable in a radiotherapy treatment planning context. This has been evaluated here by defining the magnitude of the errors acceptable in the treatment planning context. The VCAT method does indeed produce results that are sufficiently accurate to be usable for planning purposes. The VCAT method could determine the volumes of spherical lesions down to 0.53 ml with IT reconstruction, and with FBP reconstructed images for volumes > 1.15ml with the $C_o \geq 3$. These findings held at all the image noise levels studied, i.e. for all acquisition times.

Surprisingly, the CAT method was able to determine volumes within acceptable errors for true volumes less than 1.15ml in both IT and FBP at low observed contrasts, except for a few acquisition times. These results were surprising because the calibration curves do not take in account the data for volumes < 1.15ml; however, it seems that the extrapolation of the data has worked satisfactorily in low observed contrasts.

Using the CAT single calibration curve at 60 min resulted in determination of spherical lesion volumes > 1.15ml within acceptable errors across all other acquisition times, reconstruction techniques and observed contrasts. It also produced results within acceptable error for sphere volumes < 1.15ml provided observed contrast was greater than 3. Those conditions where the use of CAT 60min single calibration curve failed may be considered rare in patients undergoing radiotherapy where lesion volumes are expected to be larger than 1ml and the observed contrast is expected to be > 3. Therefore, it is possible to use the CAT 60min single calibration curve bearing

in mind these limitations. Better results were found in using a single VCAT 60 min calibration curve across all other studied acquisition times especially for IT reconstruction images.

The constant, a, in the fitting equations 3.3 and 3.4, was very close to 40% for both reconstruction methods and all acquisition times. This percentage represents the value of threshold that could be employed in a fixed thresholding method, as has been used by others, e.g. [80]. Investigation using this fixed threshold of 40% failed to segment the spherical volumes accurately as demonstrated in sections 4.1.1.2 and 4.1.2.2, except for large volumes (≤ 1.15 ml) at high contrasts ($C_o \geq 3$). These results emphasise the importance of fully characterising the situation through equations 3.3 and 3.4 and not attempting to employ a simple fixed thresholding technique.

Both CAT and VCAT techniques have been applied to irregular volume shapes that more closely represent what may be seen in patients' tumours which are often irregular and contain inhomogeneities. The errors found with both VCAT and CAT proved to be very small compared with the acceptable error. Moreover, the use of a 60min single calibration curve was able to segment the irregular volumes with sufficient accuracy. Not surprisingly, using a 40% fixed threshold produced unacceptably high errors for the small crescent volume (4.89 ml) in IT and for $C_o \sim 4$ in FBP.

For the irregular lesions the use of the DSC to quantify the shape similarity and the EDT to quantify the distance between the boundaries is an important aspect of the investigation of the accuracy of the method. The results of DSC, JSC and the EDT proved that both CAT and VCAT techniques performed extremely well, showing a high degree of concordance for

delineation of irregularly shaped lesions, accurately segmenting not only the true volume size but also the true shape and location within acceptable error levels for treatment planning.

The statistical comparisons of the five techniques, VCAT, VCAT-60, CAT, CAT-60, and 40% fixed threshold, in both spherical and irregular lesions showed that VCAT was better than the other techniques, while the use of a 40% fixed threshold was the worst technique. However, there was no statistical significance between the use of VCAT-60, CAT, or CAT-60, which performed at intermediate rankings between VCAT and 40% fixed threshold. In the spherical volumes, the difference between CAT and CAT-60 and 40% fixed threshold was statistically significant, whereas this was not the case for the irregular volumes. This is probably due to the irregular lesion phantoms having larger volumes and a much higher contrast than the spheres, conditions where the fixed threshold method performs reasonably well.

The observed contrast (C_o) in all the above studies was defined as the ratio between the maximum voxel count within a VoI drawn loosely around the lesion, and the mean counts within VoI drawn in the background region. With this manner of defining the maximum there is potential for statistical noise since it relies on the value of a single voxel. An improvement could be to use the mean over a small number of voxels around the maximum, and this is investigated in the next chapter.

5

Chapter 5:

THE IMPACT OF DEFINING THE MAXIMUM LESION UPTAKE

5.1. Introduction

In the previous two chapters, two new semi-automated PET segmentation techniques, VCAT and CAT, were developed and evaluated in phantoms. These two techniques are dependent on the observed contrast of the lesion as has been demonstrated previously. The observed contrast, C_o, of the lesion was defined as the ratio between the maximum lesion uptake, defined as the maximum voxel value (Lmax), and the mean counts of the delineated background regions. Because of the probability the maximum value, a single voxel, being affected by statistics of the imaging and reconstruction process, as well as data corrections, it is important to evaluate the impact of defining the lesion maximum in a more robust way. Therefore, two alternative

definitions of maximum lesion uptake were investigated: (i) the mean of the maximum voxel and eight neighbouring corner voxels from the same maximum voxel slice, a in Figure 5.1(a), 9 voxels in total ($Lmax_9$); (ii) the mean of the maximum voxel and the twenty-six neighbouring voxels, b in Figure 5.1(b), 27 voxels in total ($Lmax_{27}$).

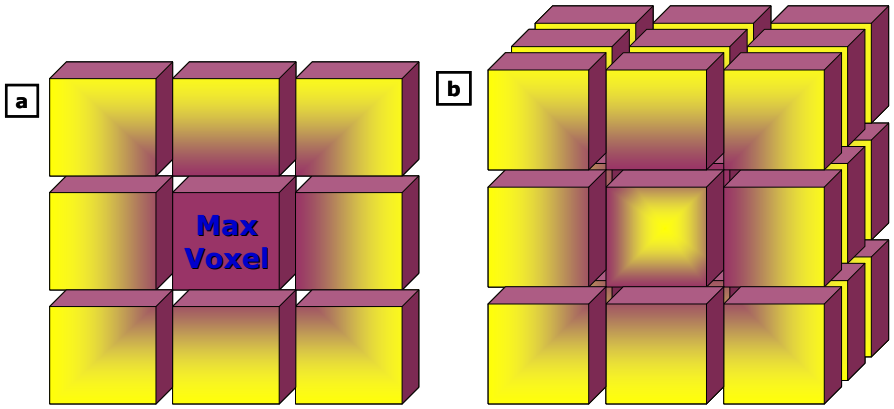

Figure 5.1: Schematic diagram shows the 9 (a) and 27 (b) voxels that used to calculate the C_o using $Lmax_9$ and $Lmax_{27}$ respectively.

Because the lesion uptake has a great impact not only in the implementation of the techniques but also on the calibration curves, new calibration curves have also been developed using $Lmax_9$ and $Lmax_{27}$ for both VCAT and CAT techniques. When applying $Lmax_9$ the segmentation techniques will be referred to as $VCAT_9$ and CAT_9 respectively, and similarly $VCAT_{27}$ and CAT_{27} when using $Lmax_{27}$. In order to ensure clarity of meaning within this chapter, when applying the initial definition of maximum lesion uptake to be the single highest voxel value, the segmentation techniques will be referred to as $VCAT_1$ and CAT_1.

5.2. Variation of Threshold with Lesion Contrast

The relationship between the optimum threshold (T_{opt}) and the observed contrast (C_o) using $Lmax_9$ and $Lmax_{27}$ was explored. A weighted least square

fitting approach was used to evaluate these relationships. As for Lmax, least square fits to equations (3.1) and (3.2) were investigated, and the Chi-square (χ^2) test was used to test for the best fit.

Figure 5.2 shows the result of fitting T_{opt} and C_o using $Lmax_9$ for both IT and FBP reconstruction techniques at 1, 2.5, 5, 10 and 60 min acquisition times. Because the volume size of the 9 voxels (9×voxel's volume: 9×~0.1 ml: ~ 1 ml) is large compared to the two small spherical volumes (0.53 and 1.15 ml), the two small spherical volumes were excluded from the fitting process. Figure 5.2 shows the results of both the first and second order fitting for T_{opt} versus C_o using $Lmax_9$, and the χ^2 test demonstrated that the second order equation is the best fit especially for iterative reconstruction images.

Figure 5.3 shows the results of fitting T_{opt} and C_o using $Lmax_{27}$ for both IT and FBP reconstruction techniques at 1, 2.5, 5, 10 and 60 min acquisition times. The volume size of the 27 voxels (2.7 ml) is large compared to the two small spherical volumes (0.53 and 1.15 ml), so these volumes were excluded from the fitting process. Figure 5.3 shows the results of both the first and second order fitting for T_{opt} versus C_o using $Lmax_{27}$, and the χ^2 test demonstrated that the second order equation is the best fit especially for iterative reconstruction images.

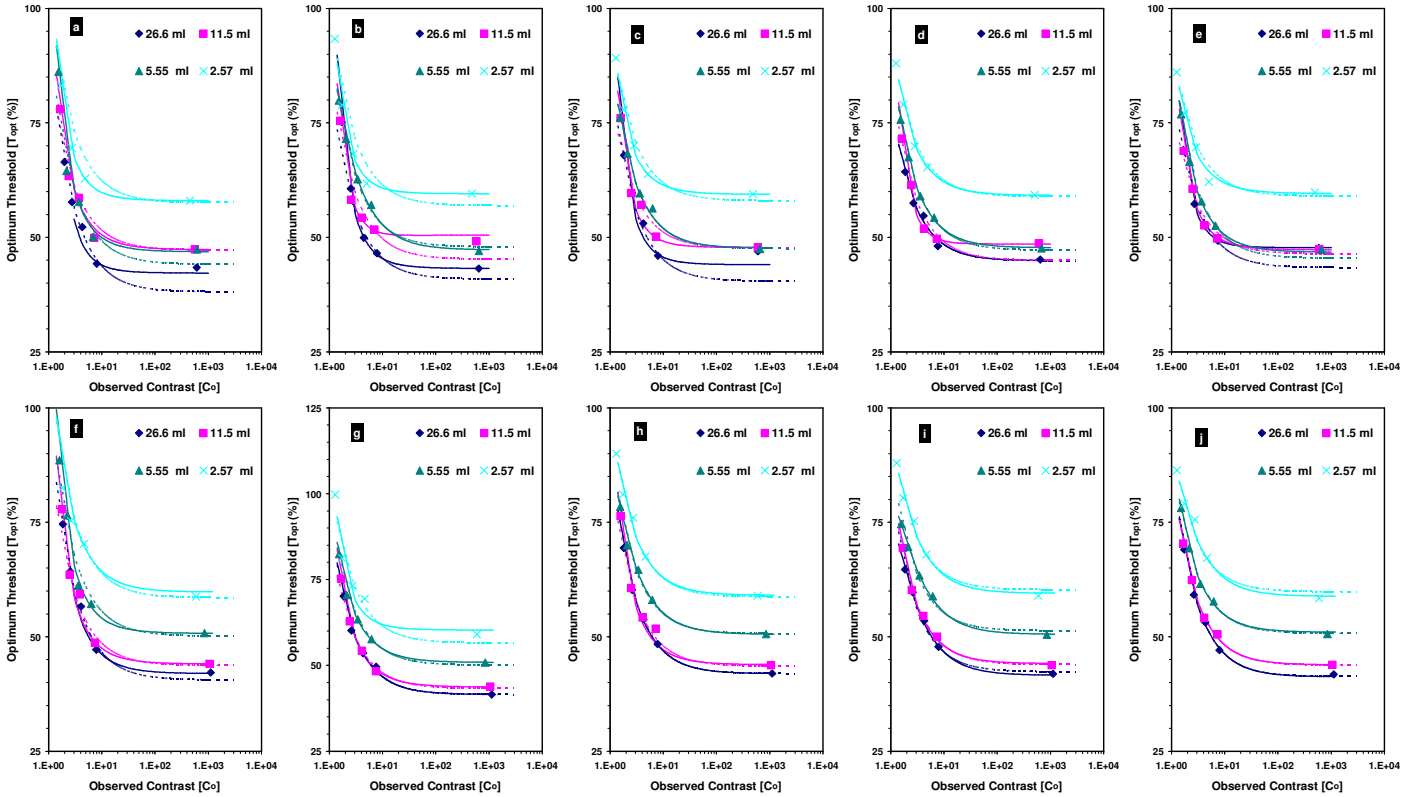

Figure 5.2: Variation of T_{opt} with C_o using the mean of 9 voxels to define the maximum lesion uptake, $Lmax_9$, for sphere volumes > 1.15ml; a, b, c, d and e are for iterative and f, g, h, i and j are for FBP reconstruction techniques at 1, 2.5, 5, 10 and 60 minute acquisition times respectively. The points represent the data points, the dotted lines represent the fitting of these data points to equation (3.1) and the solid lines represent the fitting of these data points to equation (3.2). A logarithmic scale has been used in C_o axis.

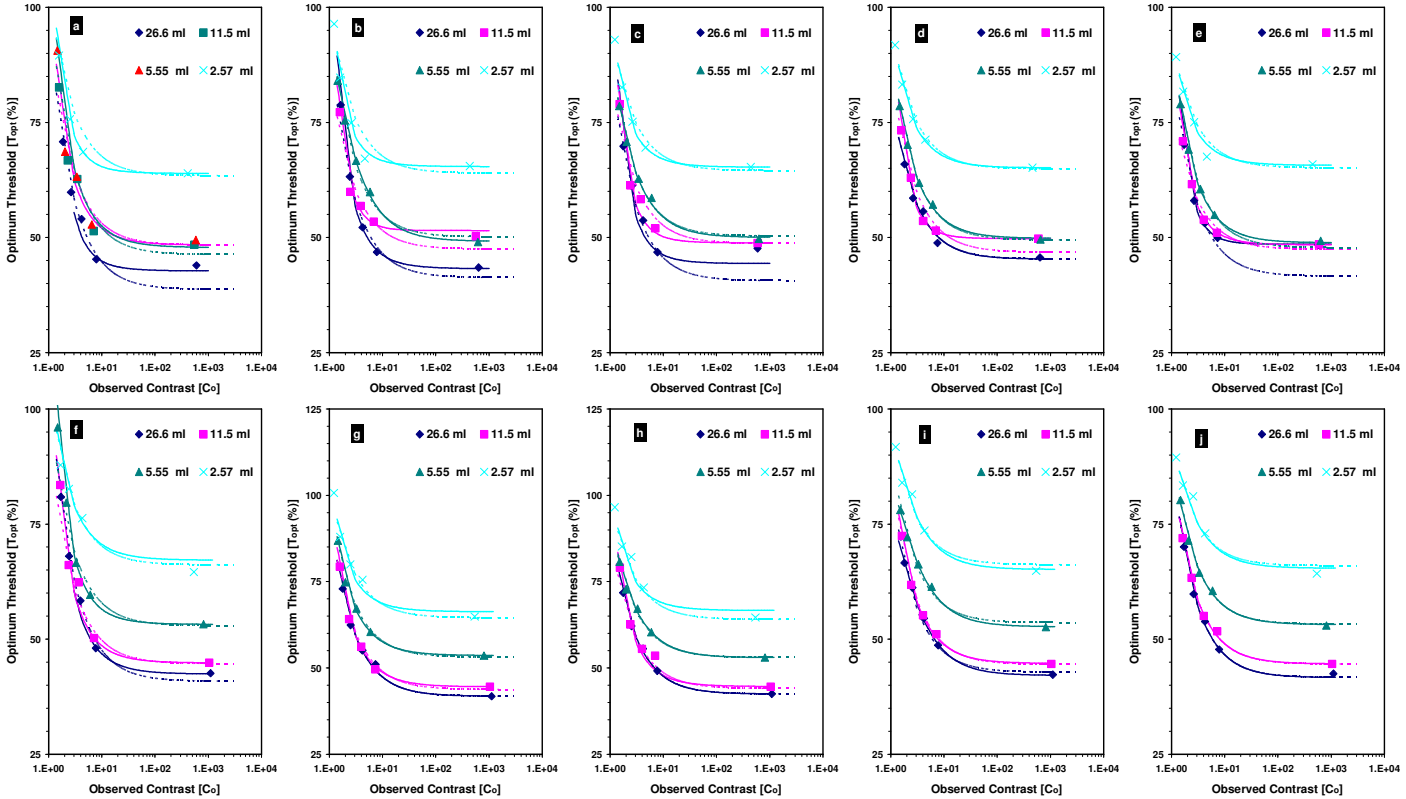

Figure 5.3: Variation of T_{opt} with C_o using the mean of 27 voxels to define the maximum lesion uptake, $Lmax_{27}$, for sphere volumes > 1.15ml; a, b, c, d and e are for iterative and f, g, h, i and j are for FBP reconstruction techniques at 1, 2.5, 5, 10 and 60 minute acquisition times respectively. The points represent the data points, the dotted lines represent the fitting of these data points to equation (3.1) and the solid lines represent the fitting of these data points to equation (3.2). A logarithmic scale has been used in C_o axis.

5.3. $CAT_{9/27}$ Calibration Curves

A weighted least square fitting approach was employed to test the correlation between T_{opt} and C_o using both $Lmax_9$ and $Lmax_{27}$ for all volumes > 1.15ml. This correlation was tested to fit these data points to the first and second order equations (3.1) and (3.2) respectively. The resulting χ^2 values demonstrated that there is a good correlation between T_{opt} and C_o and that the fitting to the second order equation (3.2) is better than the first order equation (3.1).

Figure 5.4 shows the results of the fitting of T_{opt} and C_o using $Lmax_9$ and $Lmax_{27}$ at 1, 2.5, 5, 10 and 60 minute acquisition times for both iterative and FBP reconstruction images. This figure represents the calibration curves for the CAT PET segmentation technique using $Lmax_9$ (CAT_9) and $Lmax_{27}$ (CAT_{27}), which can be represented by the general form in equation (5.1). It shows that the second order equation represents the data points more closely than the first order equation.

Table 5.1 shows the values of the CAT_9 and CAT_{27} calibration equation for all studied acquisition times (t_{AC}: 1, 2.5, 5, 10, 15, 20, 30 and 60 min) for iterative and FBP reconstruction images. It is clear that there is a slight difference in the constant, a, in the calibration equation between CAT_9 and CAT_{27}: for IT CAT_9 a = 53 ± 3.01 (average ± SD), whereas for CAT_{27} a = 56 ± 4.15 and for FBP CAT_9 a = 46 ± 1.07, whereas for CAT_{27} a = 48 ± 1.63. These small differences may reflect the reduction of the impact of the noise on these calibration equations.

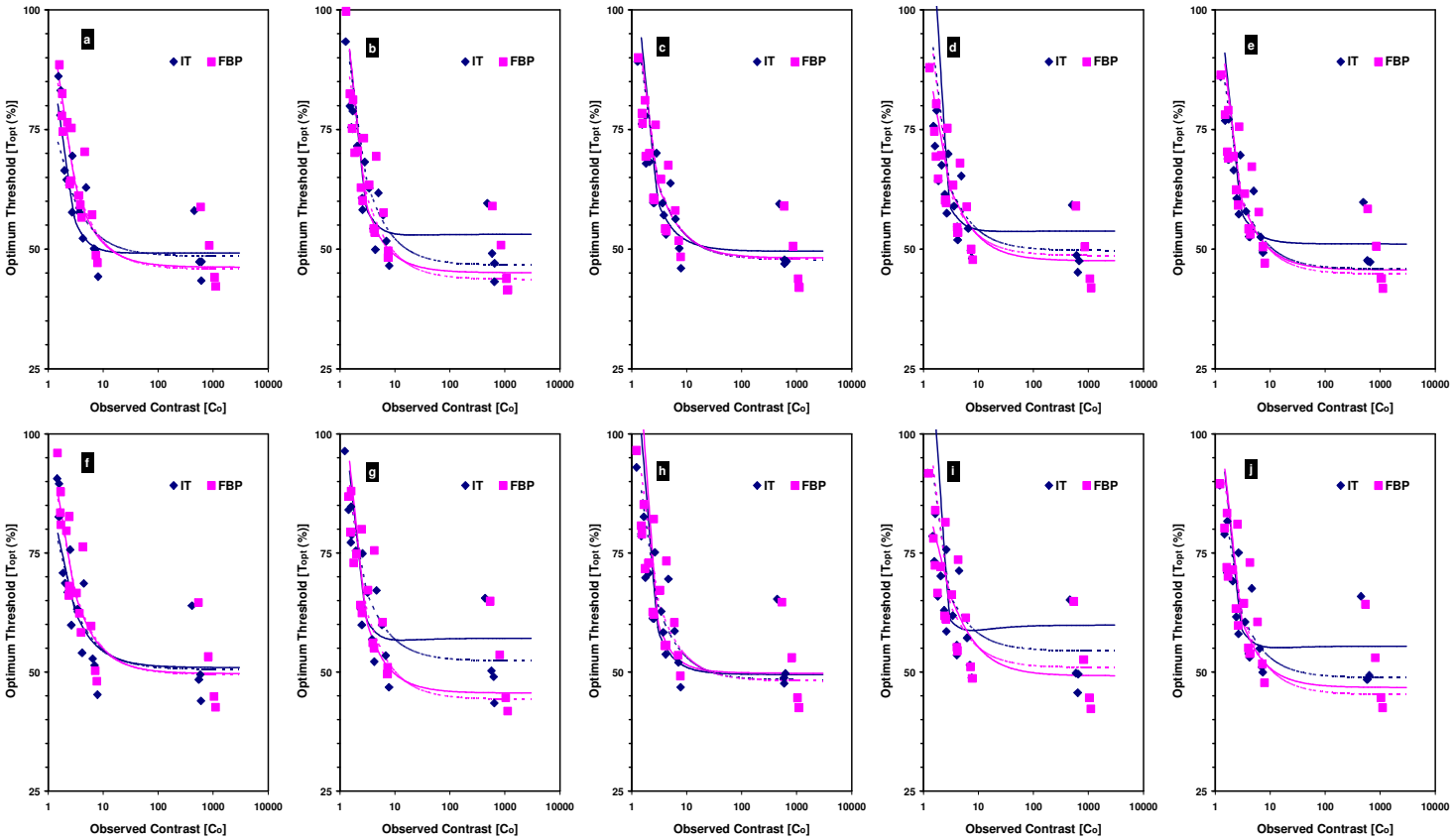

Figure 5.4: The CAT_9 (a, b, c, d, e) and CAT_{27} (f, g, h, i, j) calibration curves generated from spherical phantom > 1.15ml by correlation T_{opt} with C_o using $Lmax_9$ and $Lmax_{27}$ for iterative and FBP reconstruction techniques at 1, 2.5, 5, 10 and 60 min t_{AC} respectively. The points represent the data points, the doted lines represent the fitting to equation (3.1) and the solid lines represent the fitting to equation (3.2). A logarithmic scale has been used C_o direction.

t_{AC}	*Iterative reconstruction*					
	CAT_9			CAT_{27}		
min	*a*	*b*	*c*	*a*	*b*	*c*
1	49.17	-1.12	71.71	50.94	32.85	14.16
2.5	53.09	-6.25	73.00	57.09	-10.82	73.40
5	49.54	18.40	42.14	49.47	9.21	61.65
10	53.76	-3.53	62.62	59.85	-17.33	67.59
15	58.74	-43.80	108.1	61.66	-46.42	104.3
20	52.91	-2.16	57.27	53.66	-11.98	73.53
30	53.54	-0.04	58.63	56.12	-7.21	66.81
60	51.08	3.83	52.86	55.44	-8.92	63.31

t_{AC}	*FBP reconstruction*					
	CAT_9			CAT_{27}		
min	*a*	*b*	*c*	*a*	*b*	*c*
1	46.22	48.70	19.78	49.69	49.54	11.15
2.5	45.07	33.10	35.95	45.58	36.65	34.61
5	48.14	45.87	6.17	49.76	10.77	69.44
10	47.57	53.75	-18.41	49.22	63.22	-31.96
15	45.48	47.11	13.68	46.39	46.83	17.38
20	46.64	61.32	-27.42	48.71	65.26	-37.74
30	45.75	38.40	17.60	47.22	30.28	27.62
60	45.66	41.86	11.66	46.75	38.39	19.99

Table 5.1: The values of the fitting parameters for correlating T_{opt} and C_o using $Lmax_9$ and $Lmax_{27}$ to generate the CAT_9 and CAT_{27} calibration curves for iterative and FBP reconstructions respectively at all studied acquisition times.

5.4. $VCAT_{9/27}$ Calibration Curves

The fitting parameters of correlating T_{opt} with C_o using $Lmax_9$ and $Lmax_{27}$ were used to adjust the values of T_{opt} to a corresponding fixed C_o values equal to 2, 3, 5, 9 and ∞. The χ^2 test demonstrated that the best fit of equations (3.1) and (3.2) was obtained with equation (3.2). Figure 5.5 and Figure 5.6 demonstrate the variation of T_{opt} with V using $Lmax_9$ and $Lmax_{27}$ respectively. These two figures show the VCAT calibration curves using $Lmax_9$ ($VCAT_9$) and $Lmax_{27}$ ($VCAT_{27}$) respectively. Neither the first nor the second order equations were able to match the data points when using $Lmax_9$ or $Lmax_{27}$ for small volumes (< 11.5 ml) at low contrast, C_o, and high noise (low t_{AC}).

The three parameters – a, b and c – from equation (3.2) of fitting T_{opt} and V when using $Lmax_9$ and $Lmax_{27}$ were found to show a good correlation with C_o for all volumes. Once again using the χ^2 test best fit was with equation (3.2). So, each fit parameter, a, b and c, from equation (3.2) was used to form a similar equation to (3.3) as previously presented for the $VCAT_1$ method

Table 5.2 and Table 5.3 show the values of the nine fitting parameters for IT and FBP reconstruction images at all studied acquisition times (t_{AC}: 1, 2.5, 5, 10, 15, 20, 30 and 60 min).

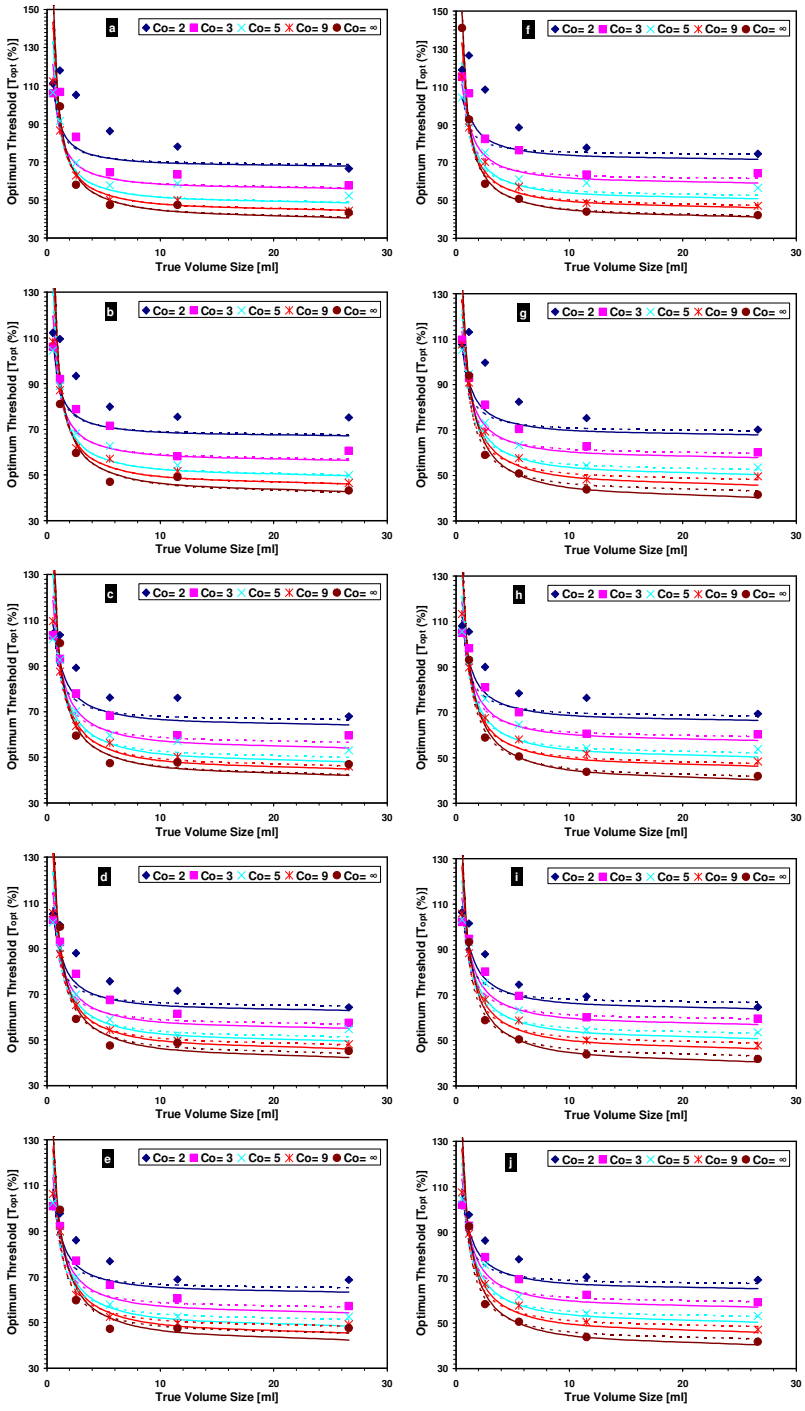

Figure 5.5: The $VCAT_9$ calibration curves generated by correlating T_{opt} with V at different C_o using $Lmax_9$. a, b, c, d and e are the calibration curves for iterative and f, g, h, i and j are for FBP reconstruction techniques at 1, 2.5, 5, 10 and 60 minute acquisition times respectively. The points represent the data points, the dotted lines represent the fitting of the data points to equation (3.1) and the solid lines represent the fitting of the data points to equation (3.2).

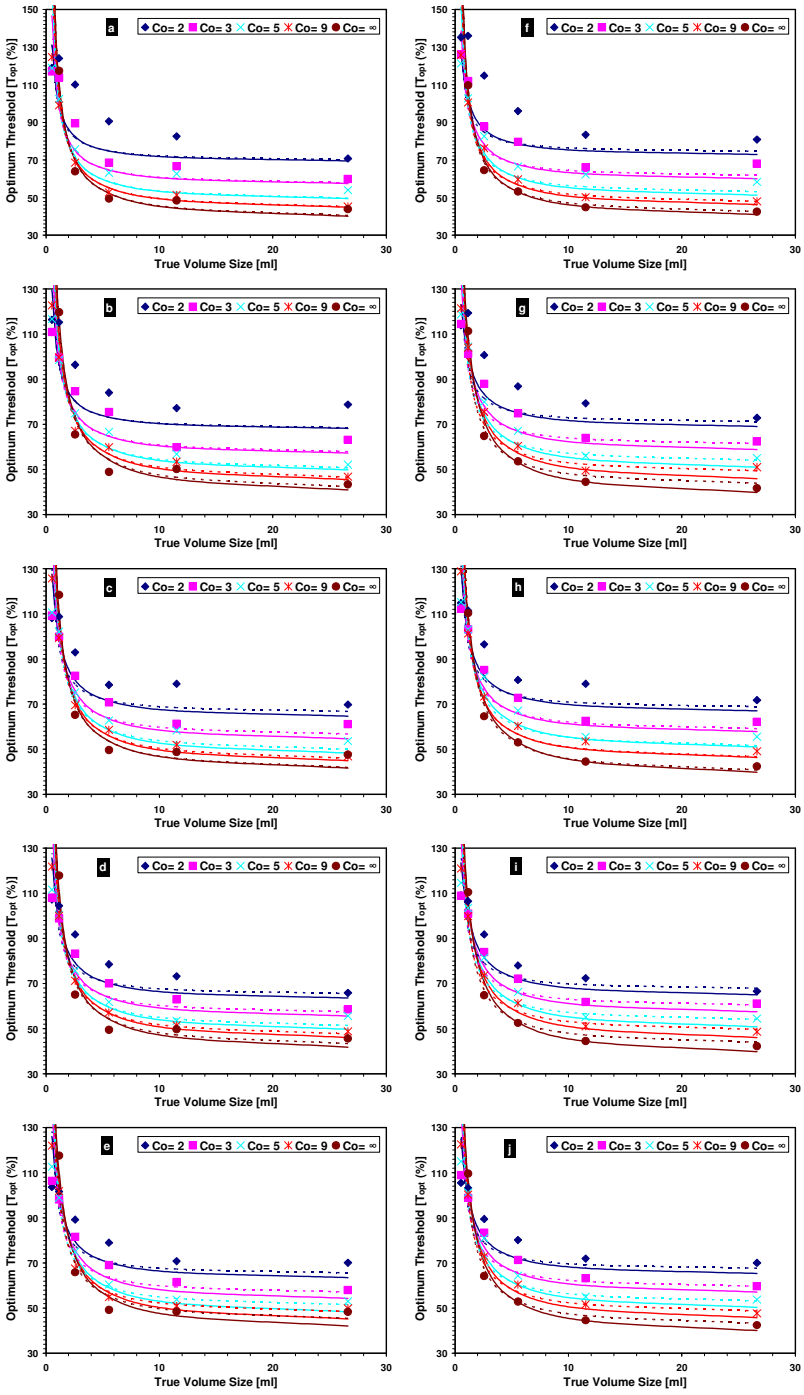

Figure 5.6: The $VCAT_{27}$ calibration curves generated by correlating T_{opt} with V at different C_o using $Lmax_{27}$. a, b, c, d and e are the calibration curves for iterative and f, g, h, i and j are for FBP reconstruction techniques at 1, 2.5, 5, 10 and 60 minute acquisition times respectively. The points represent the data points, the dotted lines represent the fitting of the data points to equation (3.1) and the solid lines represent the fitting of the data points to equation (3.2).

t_{AC}	***Iterative reconstruction***								
min	***a***	***b***	***c***	***d***	***e***	***f***	***g***	***h***	***i***
1	38.06	33.98	46.72	65.79	-102.8	58.47	-1.15	5.81	-18.30
2.5	40.45	27.70	47.41	59.30	-60.51	-11.67	1.46	-16.33	19.61
5	39.65	20.38	51.45	62.44	-2.60	-85.48	-1.27	-40.08	52.33
10	39.75	35.68	15.81	66.49	-73.98	29.57	-6.44	0.05	-2.35
15	42.90	14.24	47.17	51.75	7.39	-70.51	4.93	-48.93	49.25
20	39.75	32.09	22.80	62.92	-54.34	0.74	-3.03	-13.37	13.00
30	36.15	45.23	14.72	76.55	-87.84	15.95	-11.40	7.78	2.39
60	39.74	25.01	38.75	70.16	-48.36	-35.90	-10.75	-2.27	19.66

t_{AC}	***FBP reconstruction***								
min	***a***	***b***	***c***	***d***	***e***	***f***	***g***	***h***	***i***
1	38.81	42.32	41.40	62.02	-55.34	9.69	-1.77	-26.96	20.92
2.5	37.54	51.29	13.86	72.25	-103.8	51.97	-10.33	15.14	-14.21
5	38.48	50.55	5.10	63.32	-62.27	21.63	-3.13	-10.64	5.20
10	37.86	57.88	-17.64	69.38	-85.72	61.85	-9.47	5.57	-12.83
15	38.13	52.78	-4.34	67.35	-65.30	22.05	-6.81	-9.32	8.53
20	37.41	57.63	-13.01	71.31	-80.13	38.72	-11.63	6.46	-5.23
30	37.32	51.15	1.79	72.08	-54.01	-9.41	-12.79	-6.74	18.47
60	37.78	53.27	-2.72	68.63	-70.61	18.54	-9.18	0.66	3.22

Table 5.2: The values of the nine fitting parameters for correlating T_{opt} and V to generate the $VCAT_9$ calibration curves for iterative and FBP reconstructions.

t_{AC}	***Iterative reconstruction***								
min	***a***	***b***	***c***	***d***	***e***	***f***	***g***	***h***	***i***
1	36.82	43.82	37.58	86.42	-126.1	56.69	-1.47	5.78	-14.25
2.5	37.30	43.57	31.22	95.41	-141.7	42.13	-5.14	9.89	-3.01
5	38.48	26.76	44.00	84.16	-44.16	-53.02	-0.98	-33.26	39.95
10	38.51	40.94	11.38	88.55	-101.1	38.09	-5.50	-2.48	-1.97
15	42.34	16.41	45.00	69.60	-9.48	-66.07	8.88	-56.12	49.78
20	39.25	32.39	22.25	80.45	-63.59	-2.13	1.63	-27.13	19.50
30	35.58	43.32	20.52	94.17	-87.49	-8.82	-7.95	-7.08	17.26
60	38.62	27.04	38.42	92.86	-71.76	-34.14	-11.97	-0.92	19.53

t_{AC}	***FBP reconstruction***								
min	***a***	***b***	***c***	***d***	***e***	***f***	***g***	***h***	***i***
1	37.69	47.80	39.28	85.97	-100.2	19.09	-5.79	-5.03	8.95
2.5	36.18	59.32	6.38	96.60	-130.7	50.97	-14.54	18.88	-10.23
5	37.98	50.37	8.42	80.92	-79.57	22.16	0.93	-20.43	10.45
10	36.27	62.99	-18.69	94.34	-120.7	71.55	-14.69	18.08	-19.43
15	37.42	51.97	0.87	86.66	-77.08	10.10	-6.03	-14.20	14.36
20	34.67	70.21	-25.58	100.4	-145.9	89.59	-19.22	37.06	-34.56
30	36.11	52.57	4.45	92.70	-62.49	-22.64	-13.31	-13.11	25.91
60	36.60	56.63	-5.38	91.09	-102.7	34.57	-11.61	8.97	-4.99

Table 5.3: The values of the nine fitting parameters for correlating T_{opt} and V to generate the $VCAT_{27}$ calibration curves for iterative and FBP reconstructions.

5.5. Investigating the Accuracy of $CAT_{9/27}$ and $VCAT_{9/27}$ in Spheres

5.5.1. $CAT_{9/27}$ Accuracy in Spheres

The CAT_9 and CAT_{27} calibration equations with the three parameters presented in Table 5.1 were used to segment the PET spherical volumes in order to evaluate accuracy. Figure 5.7 and Figure 5.8 represent the modulus of percentage error in spherical volumes measurements using the CAT_9 and CAT_{27} techniques respectively in IT and FBP reconstruction images at 1, 2.5, 5, 10 and 60 min t_{AC}. The data points represent the average of three measurements and the error bars in the percentage error direction represent the standard error between these three measurements.

These results demonstrated that the percentage error in spherical volume measurements using the CAT_9 and CAT_{27} were well within the acceptable error for radiotherapy treatment planning for volumes > 1.15 ml in case of using the $Lmax_9$ and volumes > 2.57 ml in case of using the $Lmax_{27}$. Moreover, the $CAT_{9/27}$ method proved to have low sensitivity to the noise because it accurately segmented the spheres volumes (except for the previously mentioned small volumes compared to the 9 and 27 voxels volumes for low contrast and high noise with $C_o \sim 2$ and $t_{AC} = 1$ min).

The CAT method failed to segment the smallest spherical volume (0.53 ml) at $C_o \sim 2$ and $t_{AC} = 2.5$ min in case of using $Lmax_9$, and $t_{AC} = 2.5$ and 5 min in case of using $Lmax_{27}$. This failure was due to calculating an optimum threshold which was higher than the maximum uptake within this sphere volume. This may be due to the difference between the 9 and 27 voxels volumes compared with the sphere volume (0.53 ml).

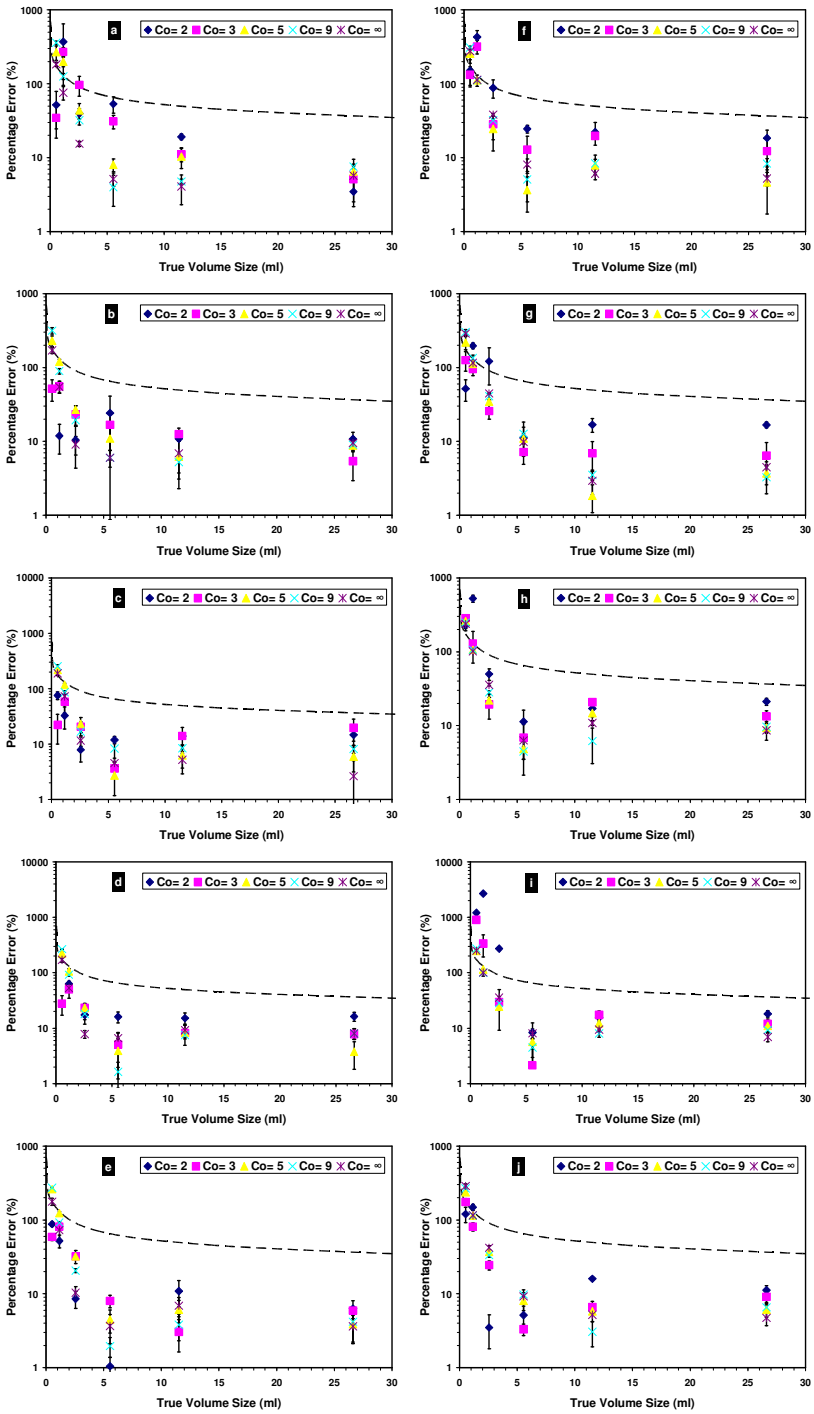

Figure 5.7: The modulus of percentage error in measuring spherical volumes using the CAT_9 for IT (left side) with different t_{AC} = 1(a), 2.5(b), 5(c), 10(d), 60(e) minute and FBP (right side) with the same t_{AC} values (f, g, h, i, j). The error bars represent the standard error from three experiments. The black dotted line represents the acceptable error. A logarithmic scale in the percentage error direction has been used.

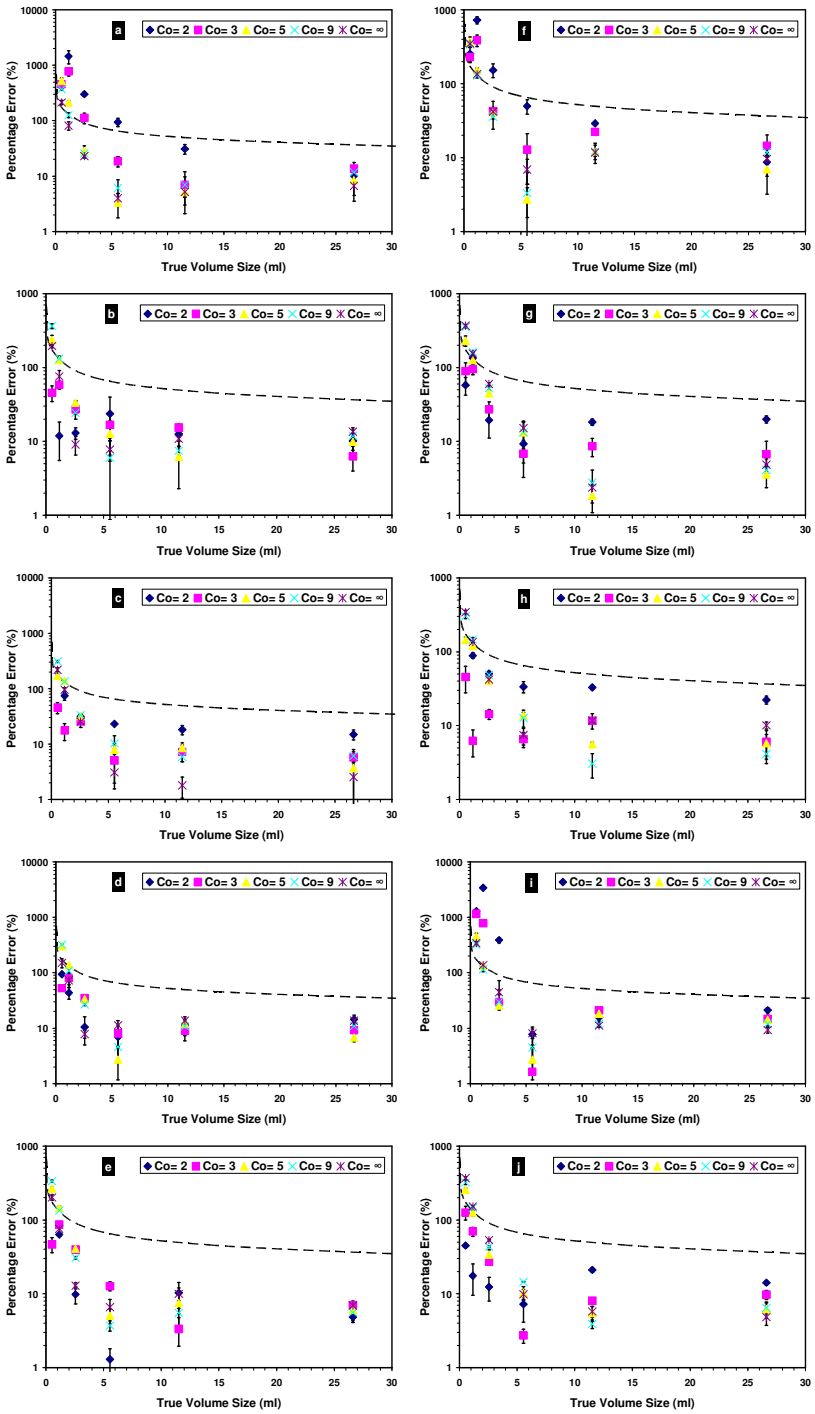

Figure 5.8: The modulus of percentage error in measuring spherical volumes using the CAT_{27} for IT (left side) with different t_{AC} = 1(a), 2.5(b), 5(c), 10(d), 60(e) minute and FBP (right side) with the same t_{AC} values (f, g, h, i, j). The error bars represent the standard error from three experiments. The black dotted line represents the acceptable error. A logarithmic scale in the percentage error direction has been used.

5.5.2. $VCAT_{9/27}$ Accuracy in Spheres

The $VCAT_9$ and $VCAT_{27}$ calibration equations with the nine parameters presented in Table 5.2 and Table 5.3 respectively were used to segment the PET spherical volumes in order to evaluate accuracy. Figure 5.9 and Figure 5.10 show the percentage errors in spherical volume measurements using the $VCAT_9$ and $VCAT_{27}$ techniques in IT and FBP reconstructed images at t_{AC} = 1, 2.5, 5, 10 and 60 min.

These data demonstrate that the percentage error in measuring the spherical lesions using the $VCAT_9$ and $VCAT_{27}$ was better in general for IT than FBP reconstruction technique; however the results of both reconstruction techniques were well within the acceptable error. Regarding the IT data, surprisingly, the $VCAT_9$ and $VCAT_{27}$ was adequate enough to segment the whole spheres volumes in all acquisition times; except for V = 1.15ml at t_{AC} = 10 min. In the FBP data, the $VCAT_9$ and $VCAT_{27}$ proved also to be able to determine the PET spherical volumes in case of $C_o > 3$ where $V \leq 1.15$ ml. Also, the methods proved to work acceptably at the highest noise level with t_{AC} = 1 min. These results indicate that $VCAT_9$ and $VCAT_{27}$ could be used with confidence on the large patients. Generally, the percentage errors continue to decline with the large volumes and C_o values.

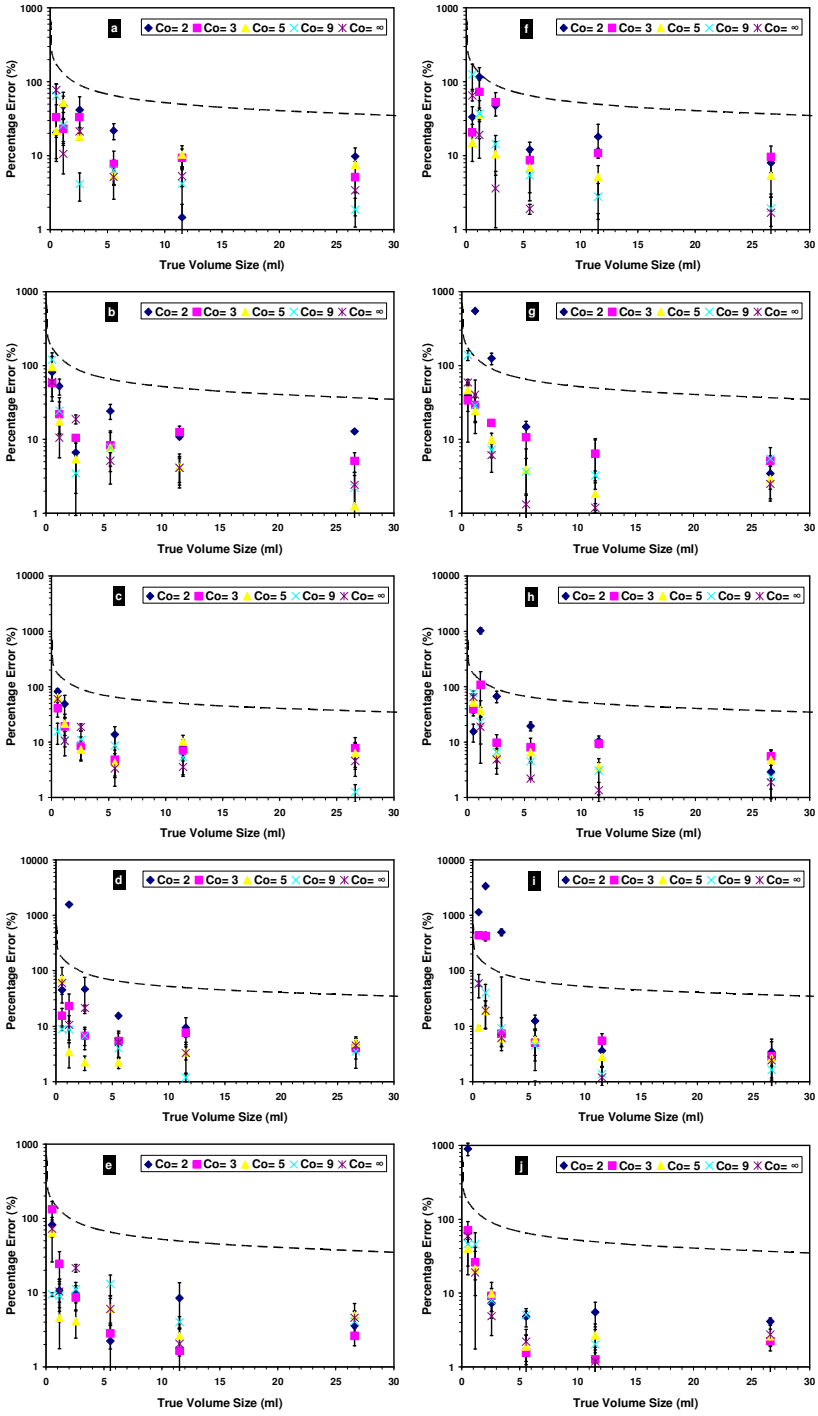

Figure 5.9: The modulus of percentage error in measuring spherical volumes using the $VCAT_9$ for IT (left side) with different t_{AC} = 1(a), 2.5(b), 5(c), 10(d), 60(e) minute and FBP (right side) with the same t_{AC} values (f, g, h, i, j). The error bars represent the standard error from three experiments. The black dotted line represents the acceptable error. A logarithmic scale in the percentage error direction has been used.

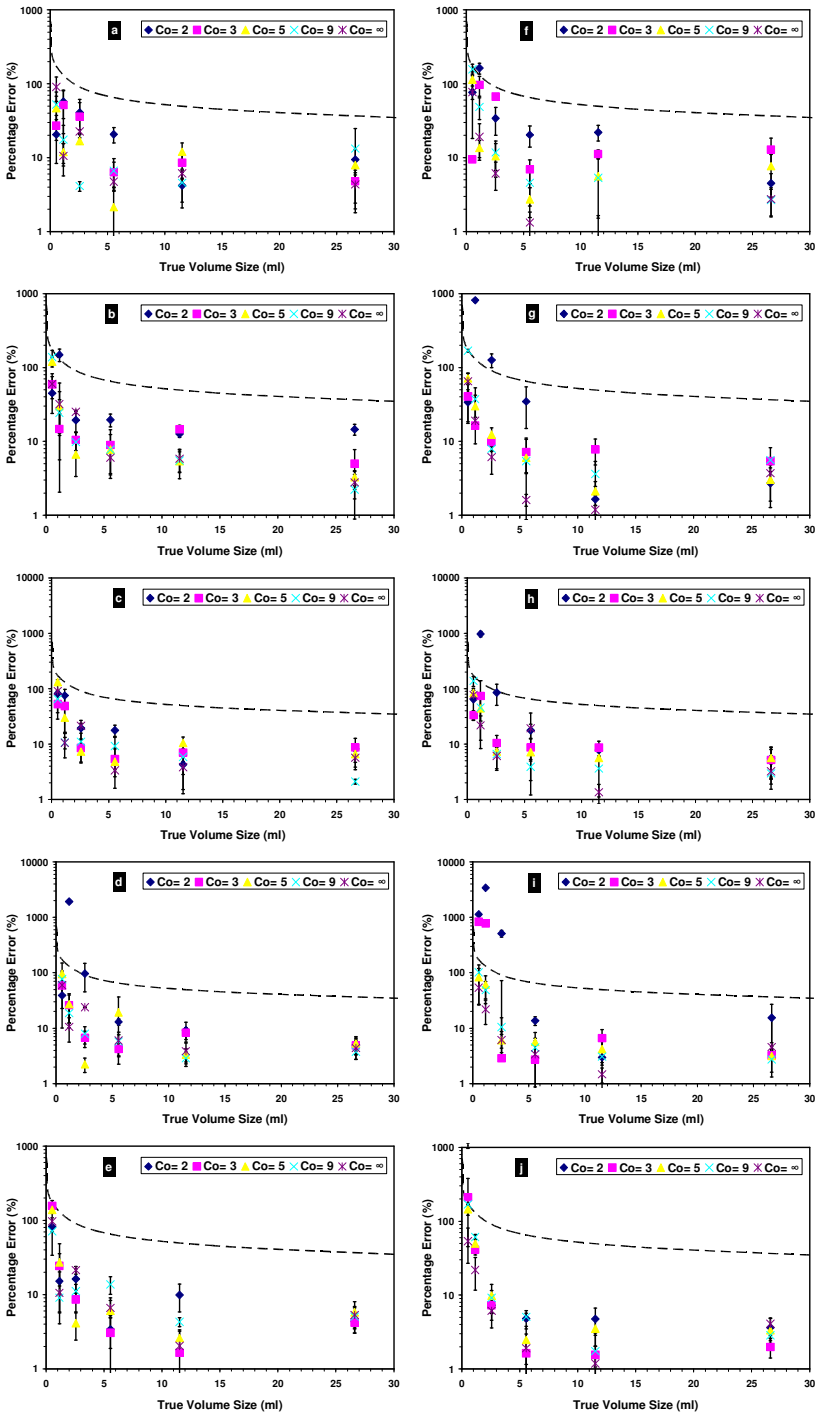

Figure 5.10: The modulus of percentage error in measuring spherical volumes using the $VCAT_{27}$ for IT (left side) with different t_{AC} = 1(a), 2.5(b), 5(c), 10(d), 60(e) minute and FBP (right side) with the same t_{AC} values (f, g, h, i, j). The error bars represent the standard error from three experiments. The black dotted line represents the acceptable error. A logarithmic scale in the percentage error direction has been used.

5.5.3. $CAT_{9/27}$ and $VCAT_{9/27}$ Accuracy Using 60 Minute Single Calibration Curve

Investigations were carried out to evaluate the accuracy of using a single calibration curve obtained at one value of t_{AC}, namely 60 min. The 60 minute calibration curves for CAT_9 (CAT_9-60), CAT_{27} (CAT_{27}-60), $VCAT_9$ ($VCAT_9$-60), and $VCAT_{27}$ ($VCAT_{27}$-60) were used to segment the spherical lesions across all values of t_{AC} (1, 2.5, 5, and 10 min).

Figure 5.11 and Figure 5.12 show the modulus error in segmenting spherical lesions using CAT_9-60 and CAT_{27}-60 respectively for IT and FBP at 1, 2.5, 5, and 10 min t_{AC}. Generally, the use of CAT_9-60 and CAT_{27}-60 produced similar errors for both IT and FBP across all t_{AC}. The resulting percentage error continued to decrease with increasing t_{AC} for the two techniques. Both techniques failed to segment for $V \leq 5.55$ ml at $t_{AC} = 1$ min in the two reconstruction techniques. However, in for $t_{AC} > 1$ min, the two techniques were able to segment for $V > 1.15$ ml and $C_o > 3$.

Figure 5.13 and Figure 5.14 show the modulus error in segmenting spherical lesions using $VCAT_9$-60 and $VCAT_{27}$-60 respectively for IT and FBP at 1, 2.5, 5, and 10 min t_{AC}. As seen in CAT_9-60 and CAT_{27}-60, both $VCAT_9$-60 and $VCAT_{27}$-60 produced similar errors for both IT and FBP reconstructions, with the IT results were better than FBP across all t_{AC}. The figures show that in case of IT reconstruction the use of $VCAT_9$-60 and $VCAT_{27}$-60 were able to segment all volumes across all studied t_{AC} within the acceptable error, except for $V = 1.15$ ml and $C_o = 2$ at $t_{AC} = 60$ min. Similar results were found in using $VCAT_{27}$-60. The two techniques were also able to segment all volumes

at all studied C_o in case of FBP at t_{AC} = 1min. With increasing the t_{AC}, the resulting percentage error for small volumes at low C_o using the two techniques increased where the two techniques failed to segment for V ≤ 2.57 ml and C_o < 3 at t_{AC} = 60 min.

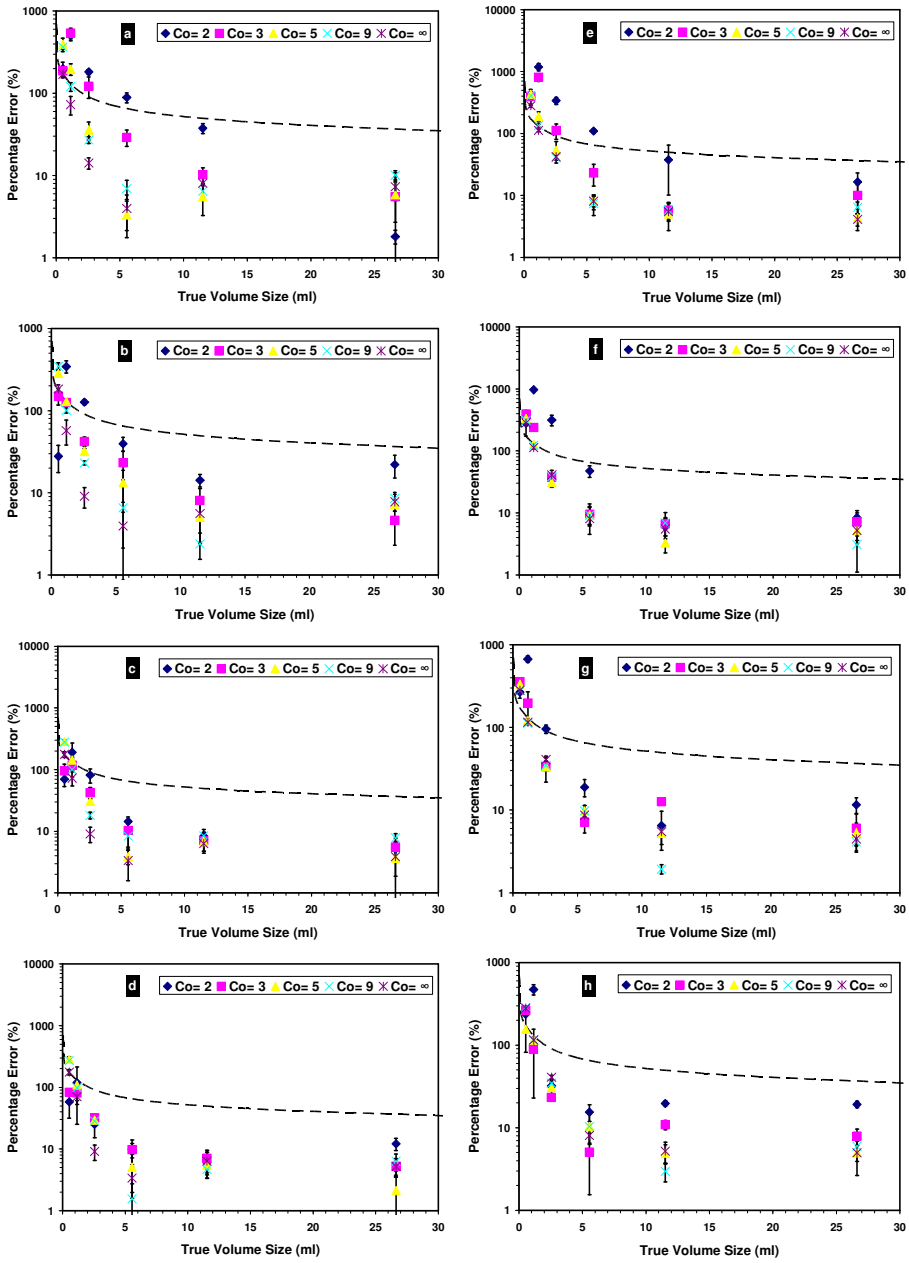

Figure 5.11: The modulus of percentage error in measuring spherical volumes using 60 minute CAT_9 calibration curve method for IT (left side) with different t_{AC} = 1(a), 2.5(b), 5(c), 10(d) minute and FBP (right side) with the same t_{AC} values (e, f, g, h). The error bars represent the standard error from three experiments. The black dotted line represents the acceptable error. A logarithmic scale in the percentage error direction has been used.

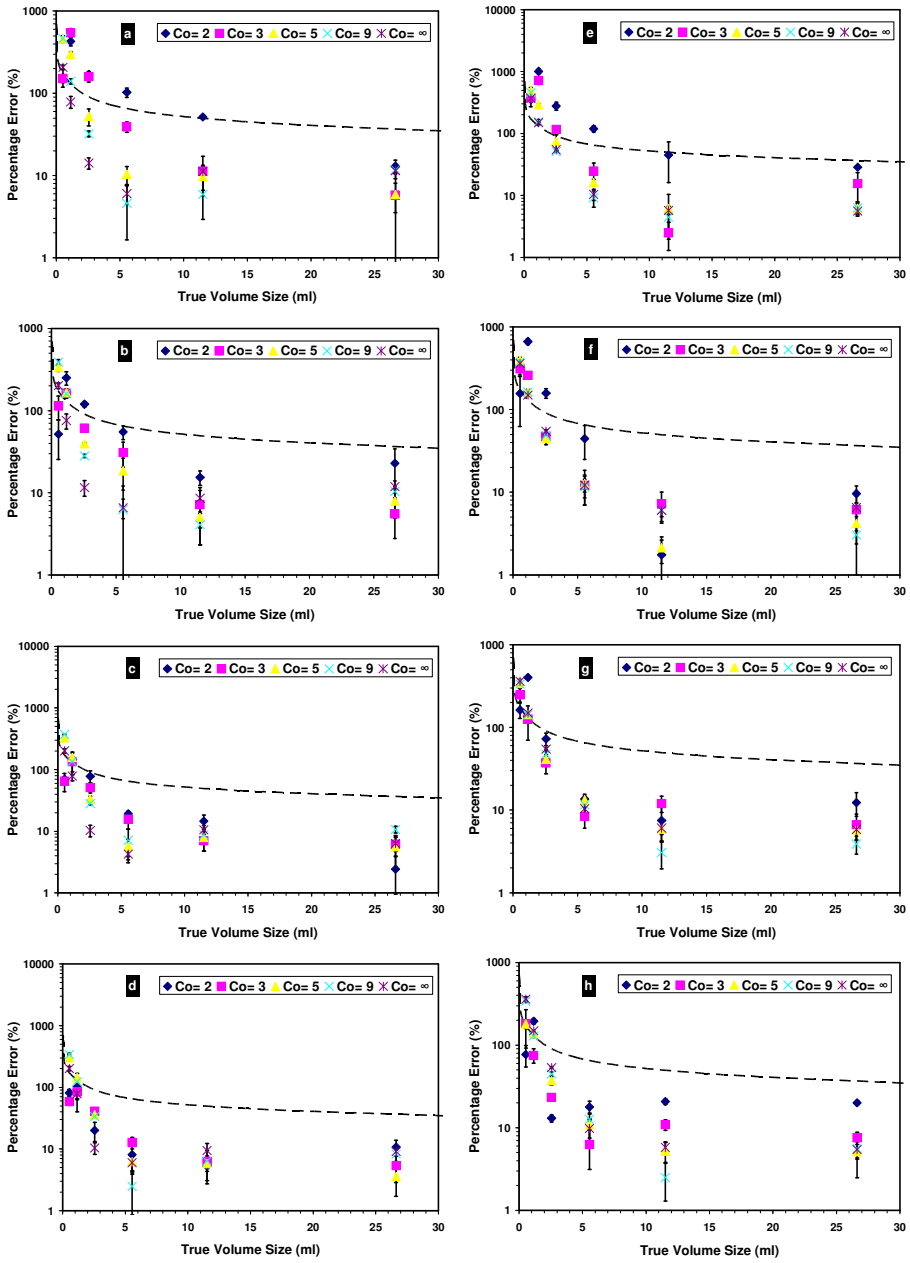

Figure 5.12: The modulus of percentage error in measuring spherical volumes using 60 minute CAT_{27} calibration curve method for IT (left side) with different t_{AC} = 1(a), 2.5(b), 5(c), 10(d) minute and FBP (right side) with the same t_{AC} values (e, f, g, h). The error bars represent the standard error from three experiments. The black dotted line represents the acceptable error. A logarithmic scale in the percentage error direction has been used.

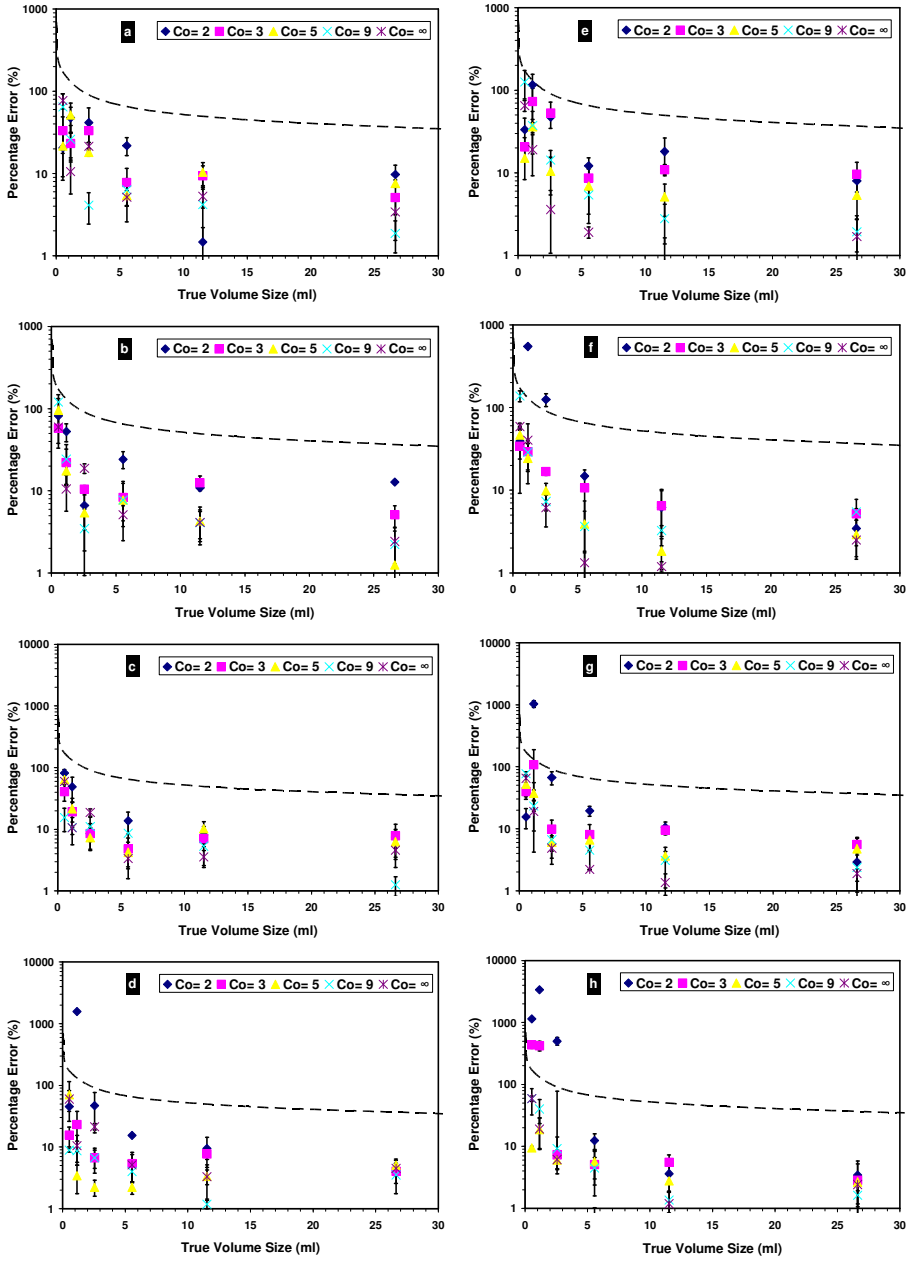

Figure 5.13: The modulus of percentage error in measuring spherical volumes using 60 minute $VCAT_9$ calibration curve method for IT (left side) with different t_{AC} = 1(a), 2.5(b), 5(c), 10(d) minute and FBP (right side) with the same t_{AC} values (e, f, g, h). The error bars represent the standard error from three experiments. The black dotted line represents the acceptable error. A logarithmic scale in the percentage error direction has been used.

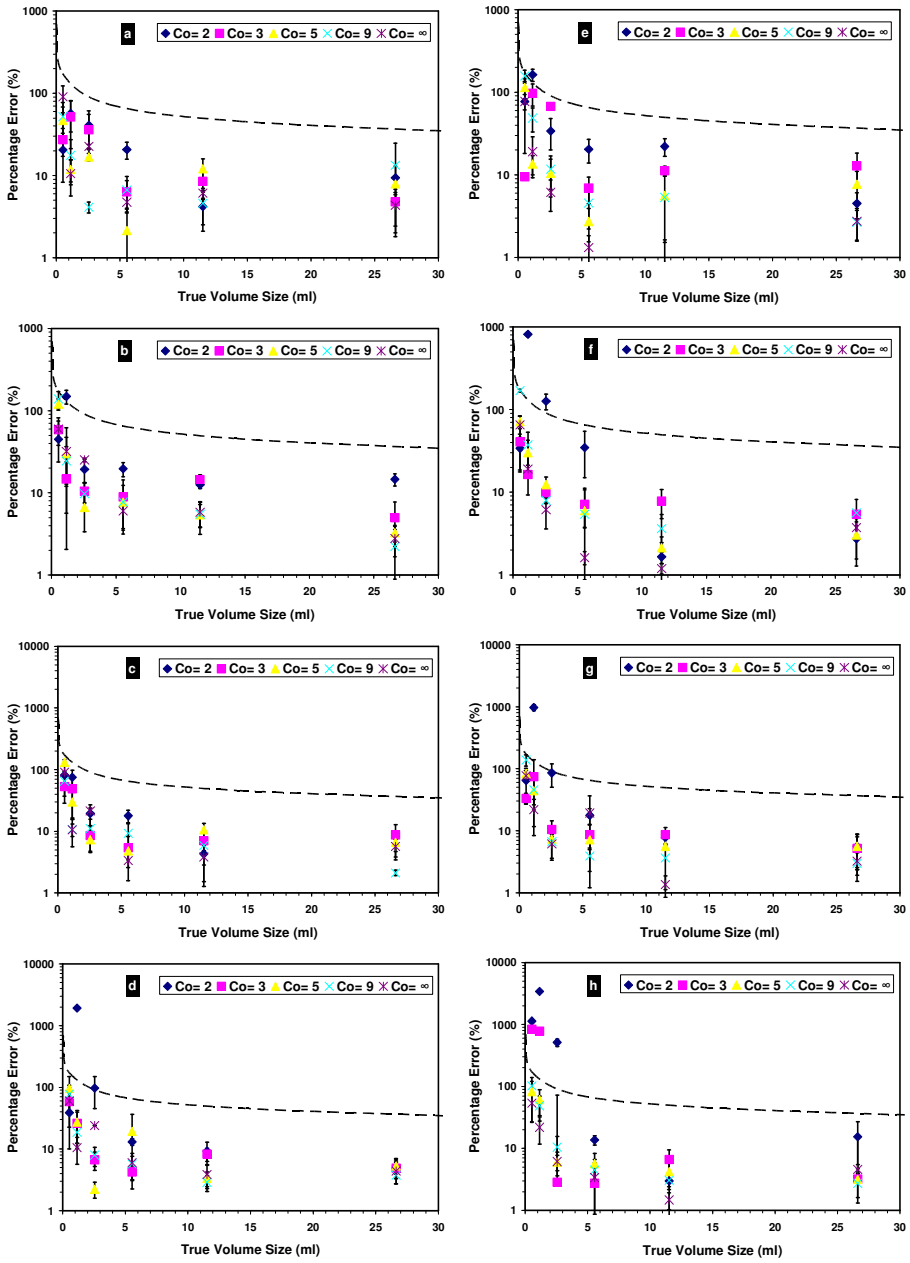

Figure 5.14: The modulus of percentage error in measuring spherical volumes using 60 minute $VCAT_{27}$ calibration curve method for IT (left side) with different t_{AC} = 1(a), 2.5(b), 5(c), 10(d) minute and FBP (right side) with the same t_{AC} values (e, f, g, h). The error bars represent the standard error from three experiments. The black dotted line represents the acceptable error. A logarithmic scale in the percentage error direction has been used.

5.5.4. Comparison with fixed thresholding method

Figure 5.15 and Figure 5.16 show the modulus percentage error in spherical lesions measurements using the 40% fixed threshold method applied using the 9 ($40\%_9$) and 27 ($40\%_{27}$) voxel lesion maxima for IT and FBP at t_{AC} = 1, 2.5, 5, 10, and 60 min. It is clear form the figures that the use of $40\%_9$ and $40\%_{27}$ failed to accurately segment for V < 1.15 ml what ever the contrast even if $C_o = \infty$, as well as for $C_o < 5$ in all spherical lesion sizes.

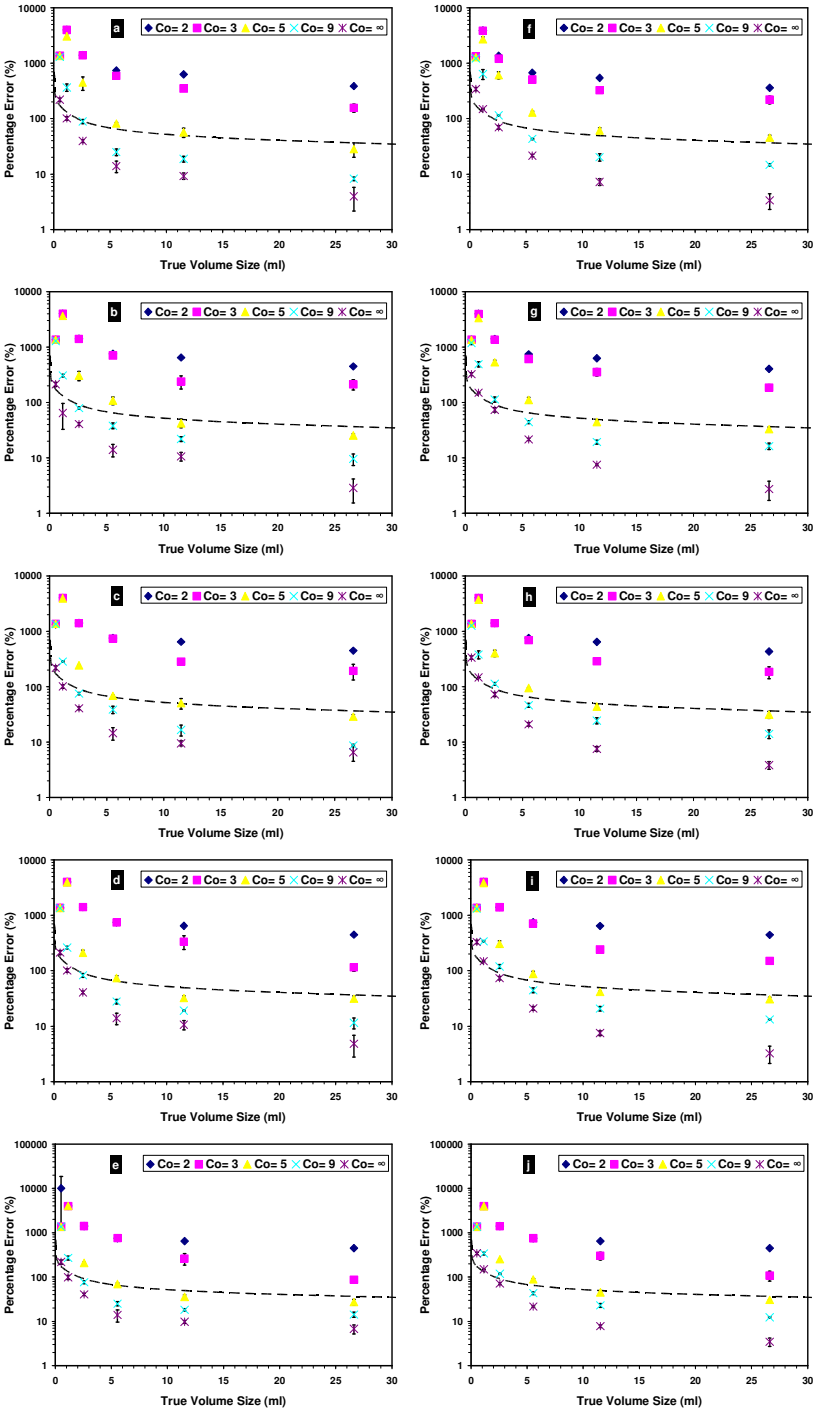

Figure 5.15: The modulus of percentage error in measuring spherical volumes using 40% of $Lmax_9$ fixed thresholding method for IT (left side) with different t_{AC} = 1(a), 2.5(b), 5(c), 10(d), 60(e) minute and FBP (right side) with the same t_{AC} values (f, g, h, i, j). The error bars represent the standard error from three experiments. The black dotted line represents the acceptable error. A logarithmic scale in the percentage error direction has been used.

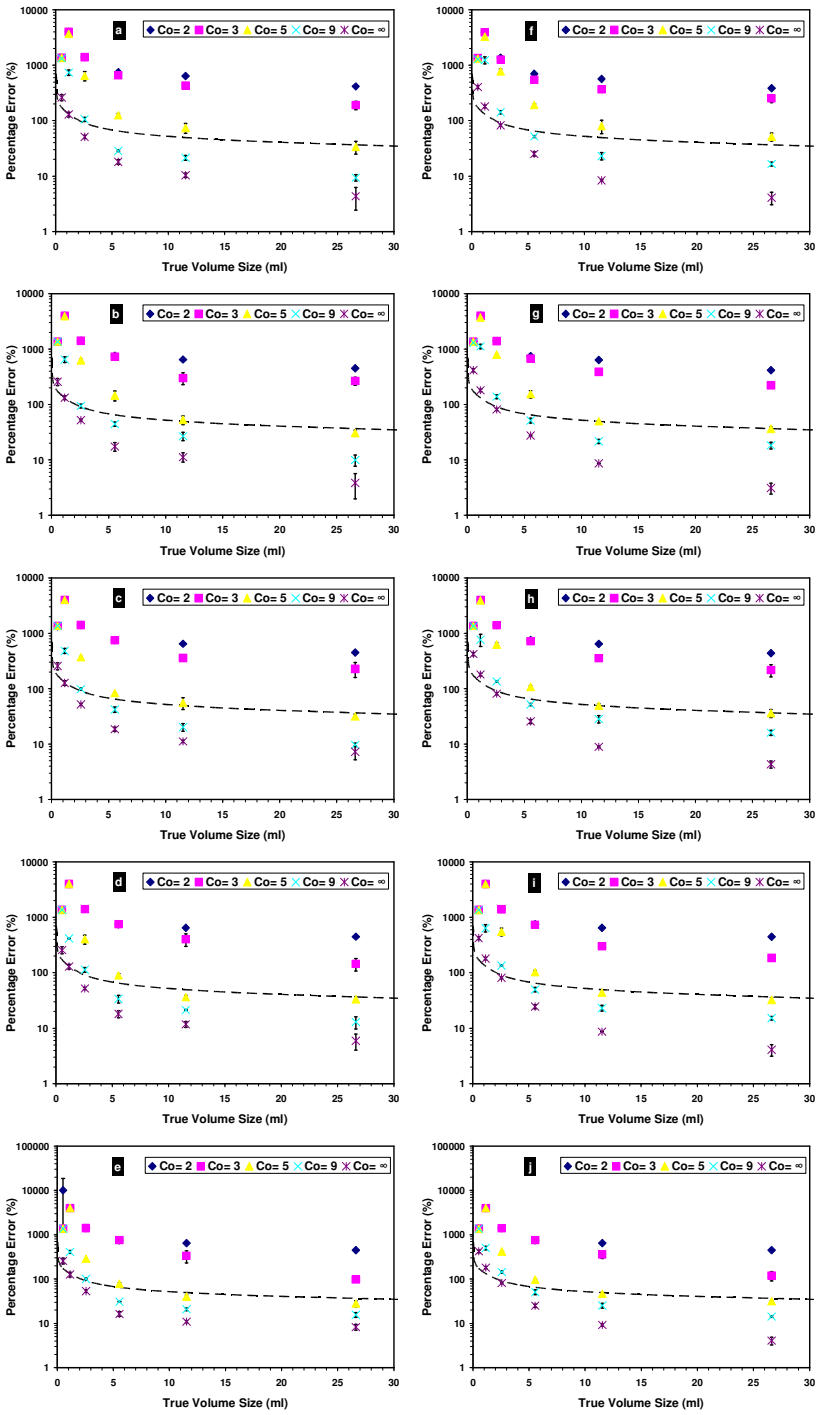

Figure 5.16: The modulus of percentage error in measuring spherical volumes using 40% of $Lmax_{27}$ fixed thresholding method for IT (left side) with different t_{AC} = 1(a), 2.5(b), 5(c), 10(d), 60(e) minute and FBP (right side) with the same t_{AC} values (f, g, h, i, j). The error bars represent the standard error from three experiments. The black dotted line represents the acceptable error. A logarithmic scale in the percentage error direction has been used.

5.6. Investigating the Accuracy of $CAT_{9/27}$ and $VCAT_{9/27}$ in Irregular Volumes

5.6.1. $CAT_{9/27}$ Accuracy in Irregular Volumes

The CAT_9 and CAT_{27} were investigated in different geometries than those used to generate the calibration curves. Therefore, the CAT_9 and CAT_{27} were applied to the two families of irregular volumes, top-hat and crescent shapes, and the results are shown in. Figure 5.17 and Figure 5.18.

The resulting percentage errors of using the CAT_9 and CAT_{27} in the irregular shapes showed similar results in case of IT reconstruction techniques. Similar results were found for FBP reconstruction, although for CAT_{27}, the method was unable to segment the crescent smallest volume (4.89 ml). Generally, the resulting percentage errors of IT were better than those of FBP. For IT, the resulting percentage errors for the crescent volume 4.89ml were higher than the acceptable error in all acquisition times when $C_o \sim 50$; similar results were obtained for top-hat volume 30.0 ml at t_{AC} = 1 min for both CAT_9 and CAT_{27}. For FBP, the use of the CAT_9 and CAT_{27} was unable to segment the top-hat volume 8.69 ml for all t_{AC}, and the crescent volume 4.89 ml in the case of CAT_{27}.

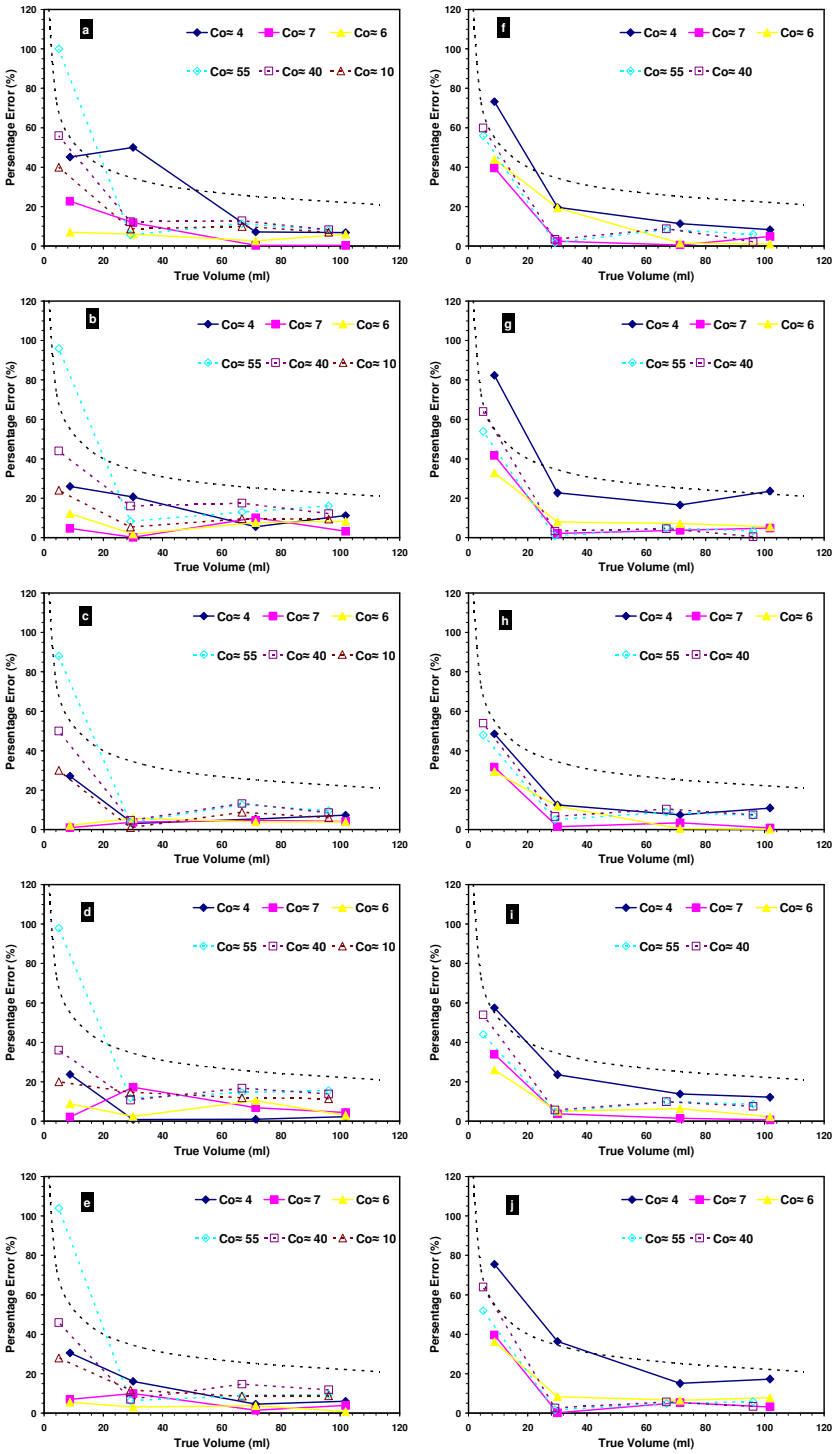

Figure 5.17: The modulus of percentage error in measuring irregular volumes using the CAT_9 for IT (left side) with different t_{AC} = 1(a), 2.5(b), 5(c), 10(d), 60(e) minute and FBP (right side) with the same t_{AC} values (f, g, h, i, j). The solid points and lines represent the top-hat while the hollow points and dotted lines represent the crescent irregular volumes. The black dotted line represents the acceptable error.

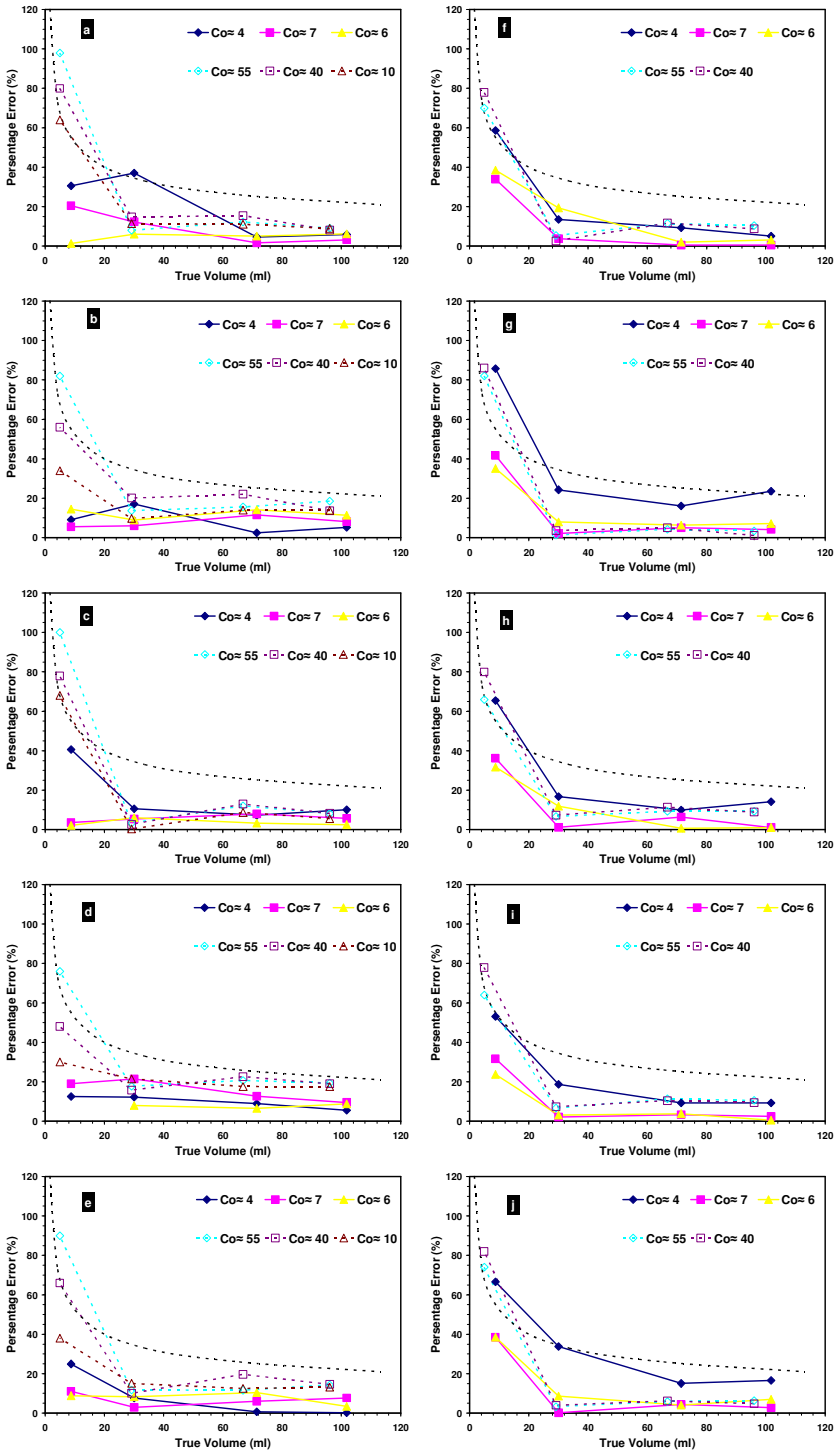

Figure 5.18: The modulus of percentage error in measuring irregular volumes using the CAT_{27} for IT (left side) with different t_{AC} = 1(a), 2.5(b), 5(c), 10(d), 60(e) minute and FBP (right side) with the same t_{AC} values (f, g, h, i, j). The solid points and lines represent the top-hat while the hollow points and dotted lines represent the crescent irregular volumes. The black dotted line represents the acceptable error.

5.6.2. $VCAT_{9/27}$ Accuracy in Irregular Volumes

The accuracy of the $VCAT_9$ and $VCAT_{27}$ techniques were investigated for the irregular top-hat and crescent volumes. Figure 5.19 and Figure 5.20 show the resulting percentage errors.

The percentage errors of applying the $VCAT_9$ and $VCAT_{27}$ were within the acceptable error for all acquisition times for both IT and FBP except for crescent volume 4.89 ml with IT reconstruction. The error decreases to a minimum of approximately 10% at large volume and high contrast. The errors across all acquisition times for the smallest top-hat (8.69 ml) and crescent (4.89 ml) were less than 20% and 60% respectively.

The percentage errors of applying the $VCAT_{27}$ were within the acceptable error for all acquisition times for both IT and FBP except for crescent volume 4.89 ml. Otherwise, the resulting percentage errors were well within the acceptable error across all shapes, sizes, and reconstruction techniques. The percentage errors remain under 20% for all volumes and observed contrasts.

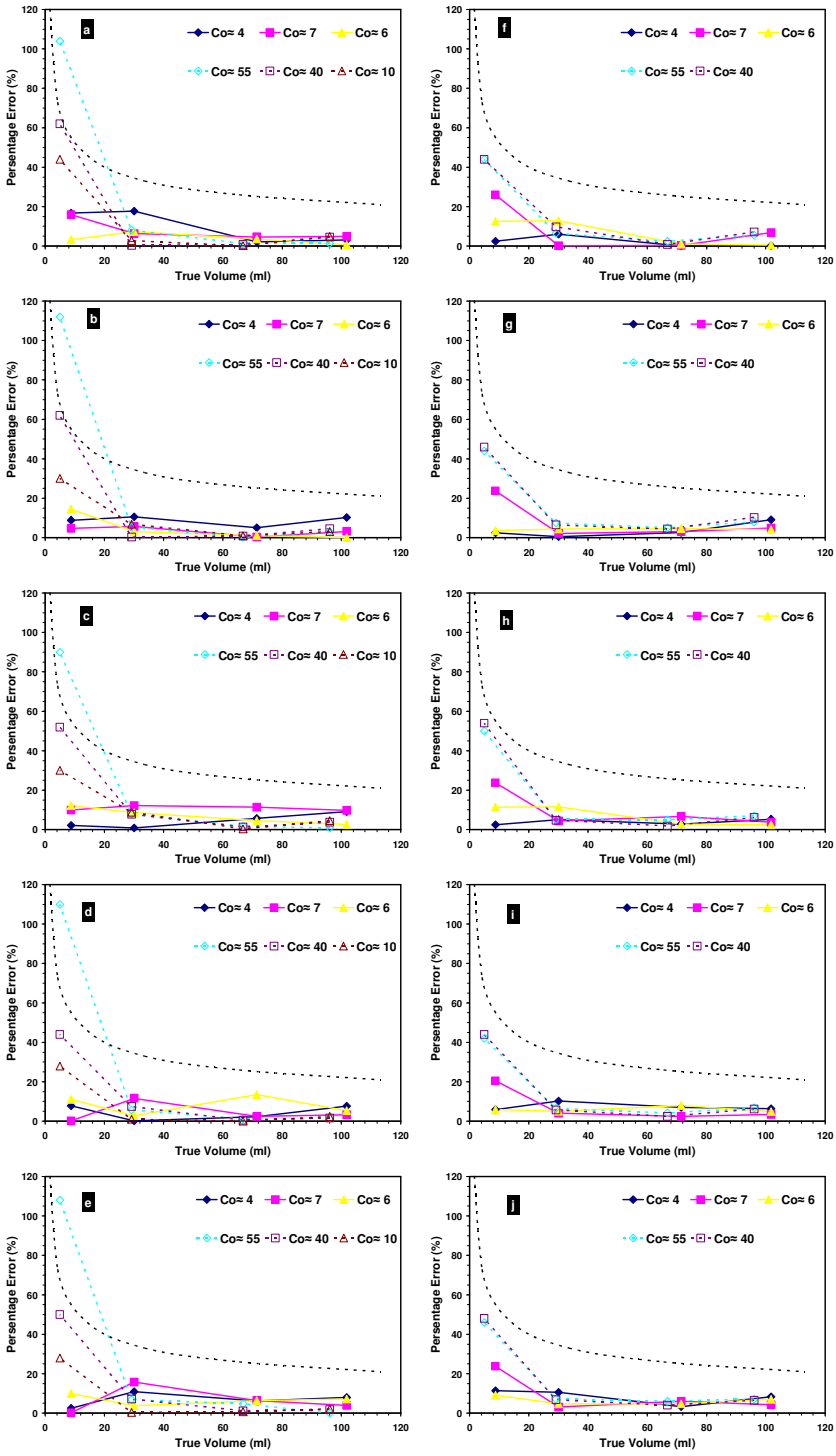

Figure 5.19: The modulus of percentage error in measuring irregular volumes using the $VCAT_9$ for IT (left side) with different t_{AC} = 1(a), 2.5(b), 5(c), 10(d), 60(e) minute and FBP (right side) with the same t_{AC} values (f, g, h, i, j). The solid points and lines represent the top-hat while the hollow points and dotted lines represent the crescent irregular volumes. The black dotted line represents the acceptable error.

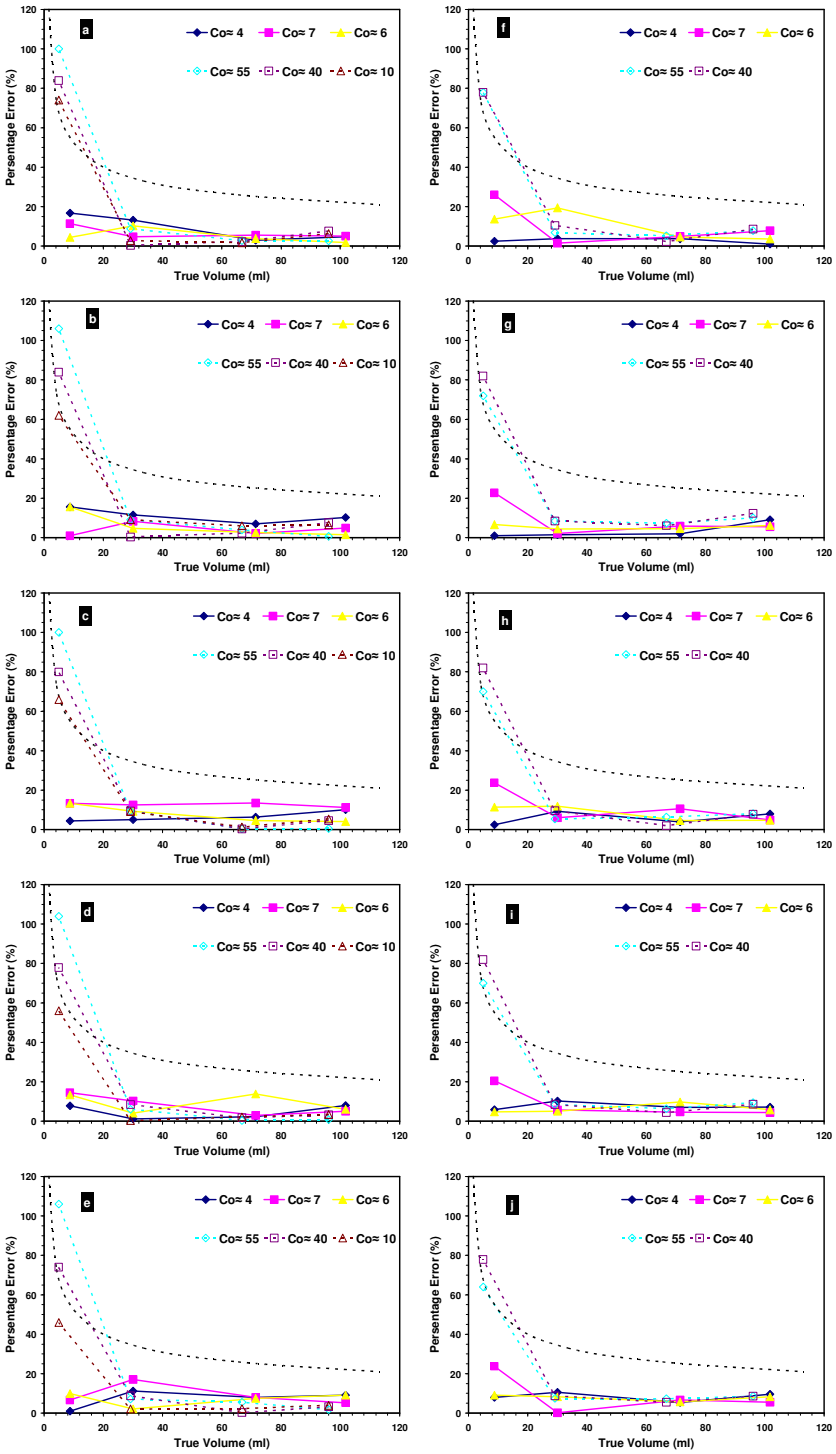

Figure 5.20: The modulus of percentage error in measuring irregular volumes using the $VCAT_{27}$ for IT (left side) with different t_{AC} = 1(a), 2.5(b), 5(c), 10(d), 60(e) minute and FBP (right side) with the same t_{AC} values (f, g, h, i, j). The solid points and lines represent the top-hat while the hollow points and dotted lines represent the crescent irregular volumes. The black dotted line represents the acceptable error.

5.6.3. $CAT_{9/27}$ and $VCAT_{9/27}$ Accuracy Using 60 Minute Single Calibration Curve

Investigations were carried out to evaluate the accuracy of using a single calibration curve obtained at one value of t_{AC}. The 60 minute calibration cures for CAT_9 (CAT_9-60), CAT_{27} (CAT_{27}-60), $VCAT_9$ ($VCAT_9$-60), and $VCAT_{27}$ ($VCAT_{27}$-60) were used to segment the irregular lesions across other different t_{AC} (1, 2.5, 5, and 10 min).

Figure 5.21 and Figure 5.22 show the modulus error in segmenting irregular lesions using CAT_9-60 and CAT_{27}-60 for IT and FBP respectively. Generally, the use of CAT_9-60 and CAT_{27}-60 produced similar errors for both IT and FBP across all t_{AC} where IT was better than FBP reconstructions, except for a small difference in the smallest crescent volume = 4.89 ml. CAT_{27}-60 succeeded in segmenting the top-hat volume 30.0 ml within the acceptable error, whereas CAT_9-60 did not. This suggests that image noise reduction in defining Lmax is achieved with the 27 voxel zone but not with the 9 voxel zone.

Figure 5.23 and Figure 5.24 show the modulus error in segmenting irregular lesions using $VCAT_9$-60 and $VCAT_{27}$-60 respectively for IT and FBP. As with CAT_9-60 and CAT_{27}-60, both $VCAT_9$-60 and $VCAT_{27}$-60 produced similar errors for both IT and FBP reconstructions, except for a small difference in the smallest crescent volume = 4.89 ml. The figures show that the two techniques, $VCAT_9$-60 and $VCAT_{27}$-60, accurately segmented all irregular lesions within the acceptable error except for the smallest crescent volume (4.89 ml).

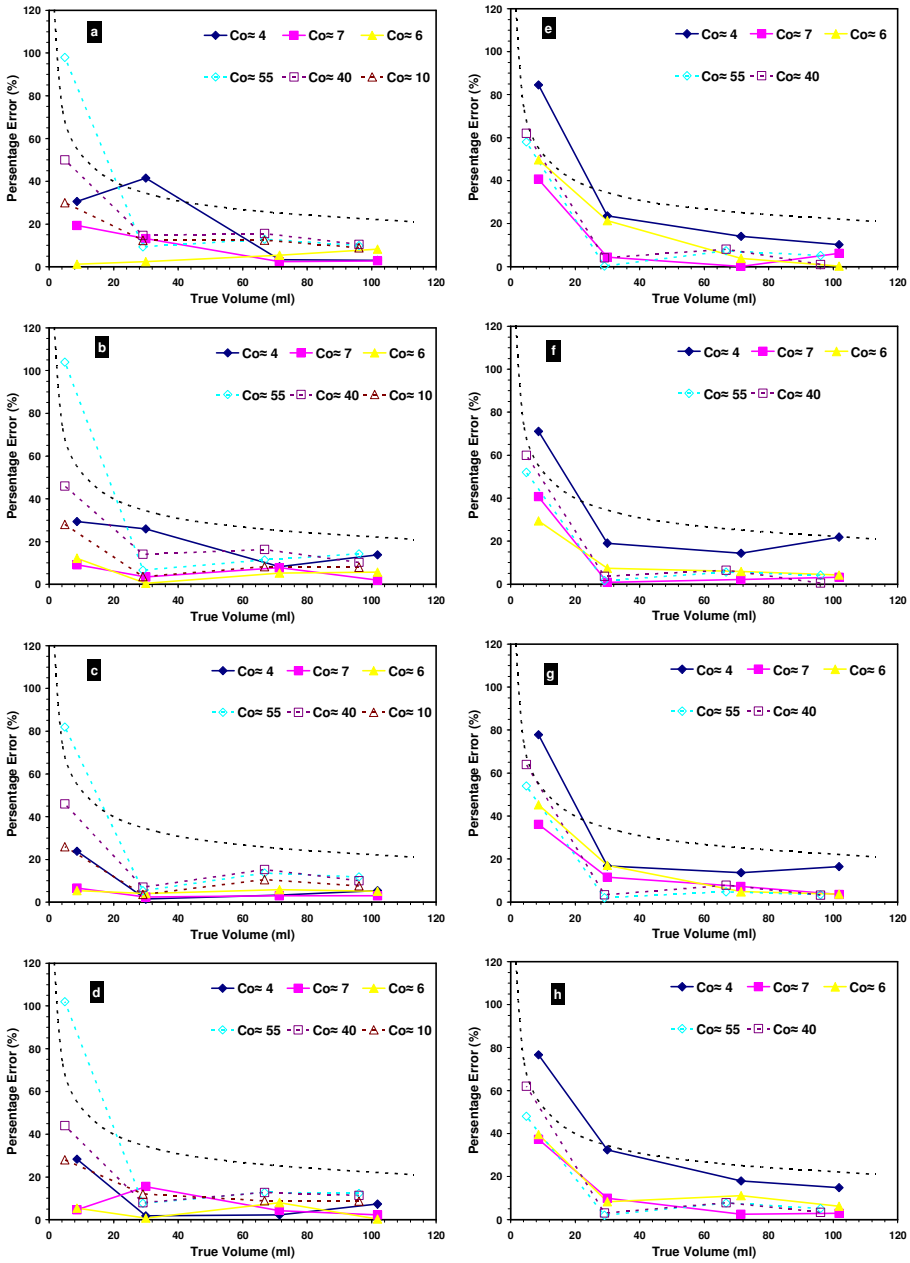

Figure 5.21: The modulus of percentage error in measuring irregular volumes using 60 minute CAT_9 calibration curve method for IT (left side) with different t_{AC} = 1(a), 2.5(b), 5(c), 10(d) minute and FBP (right side) with the same t_{AC} values (e, f, g, h). The solid points and lines represent the top-hat while the hollow points and dotted lines represent the crescent irregular volumes. The black dotted line represents the acceptable error.

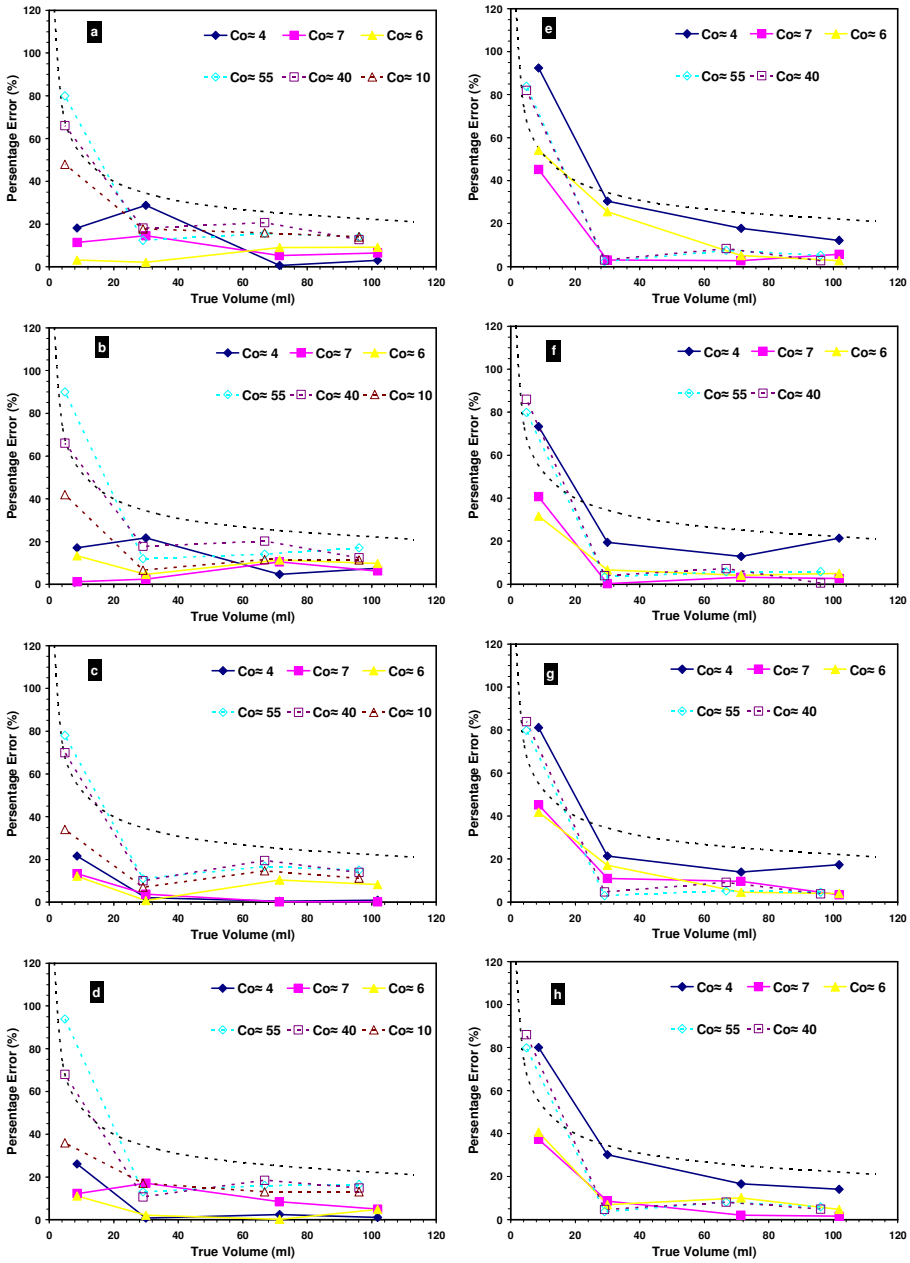

Figure 5.22: The modulus of percentage error in measuring irregular volumes using 60 minute CAT_{27} calibration curve method for IT (left side) with different t_{AC} = 1(a), 2.5(b), 5(c), 10(d) minute and FBP (right side) with the same t_{AC} values (e, f, g, h). The solid points and lines represent the top-hat while the hollow points and dotted lines represent the crescent irregular volumes. The black dotted line represents the acceptable error.

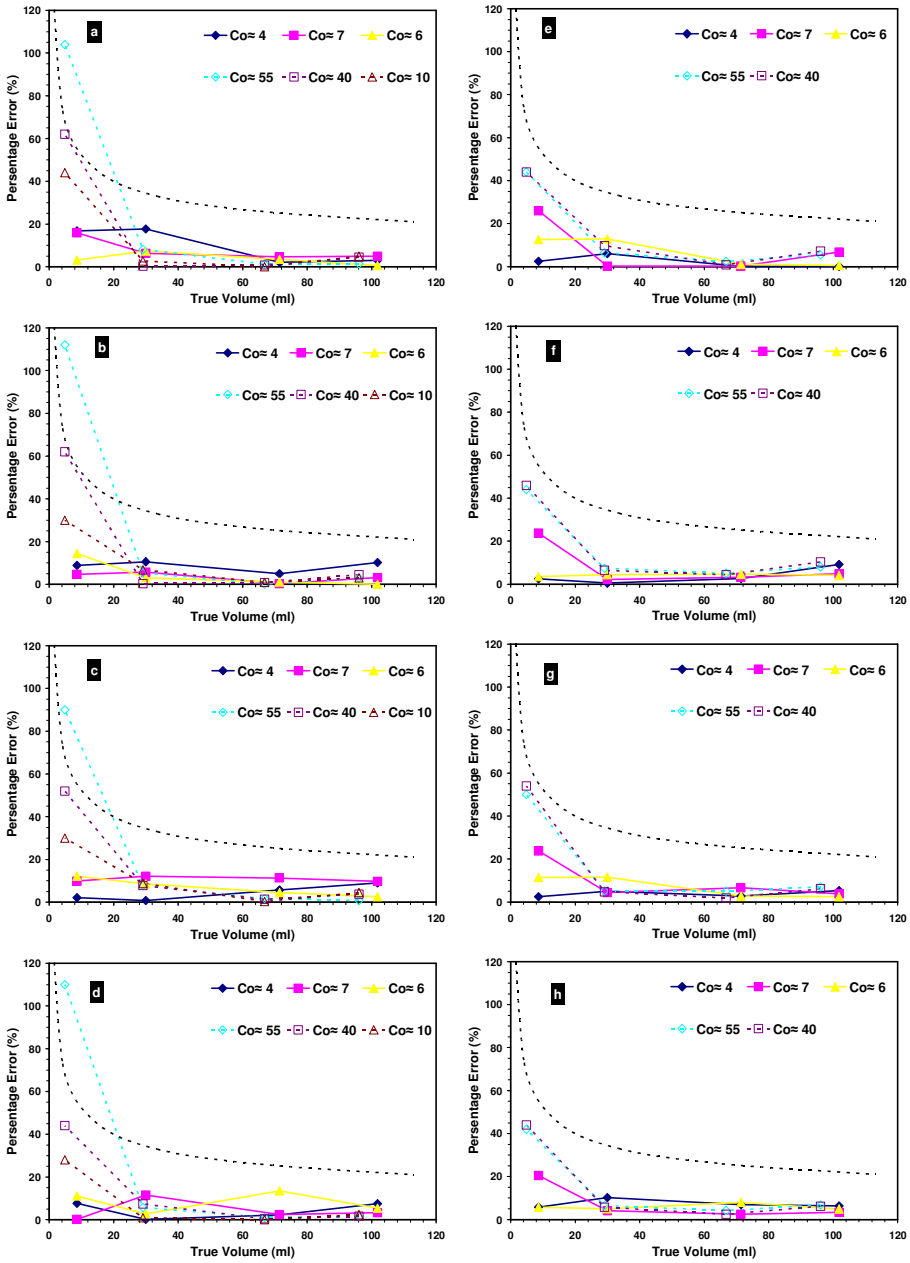

Figure 5.23: The modulus of percentage error in measuring irregular volumes using 60 minute $VCAT_9$ calibration curve method for IT (left side) with different t_{AC} = 1(a), 2.5(b), 5(c), 10(d) minute and FBP (right side) with the same t_{AC} values (e, f, g, h). The solid points and lines represent the top-hat while the hollow points and dotted lines represent the crescent irregular volumes. The black dotted line represents the acceptable error.

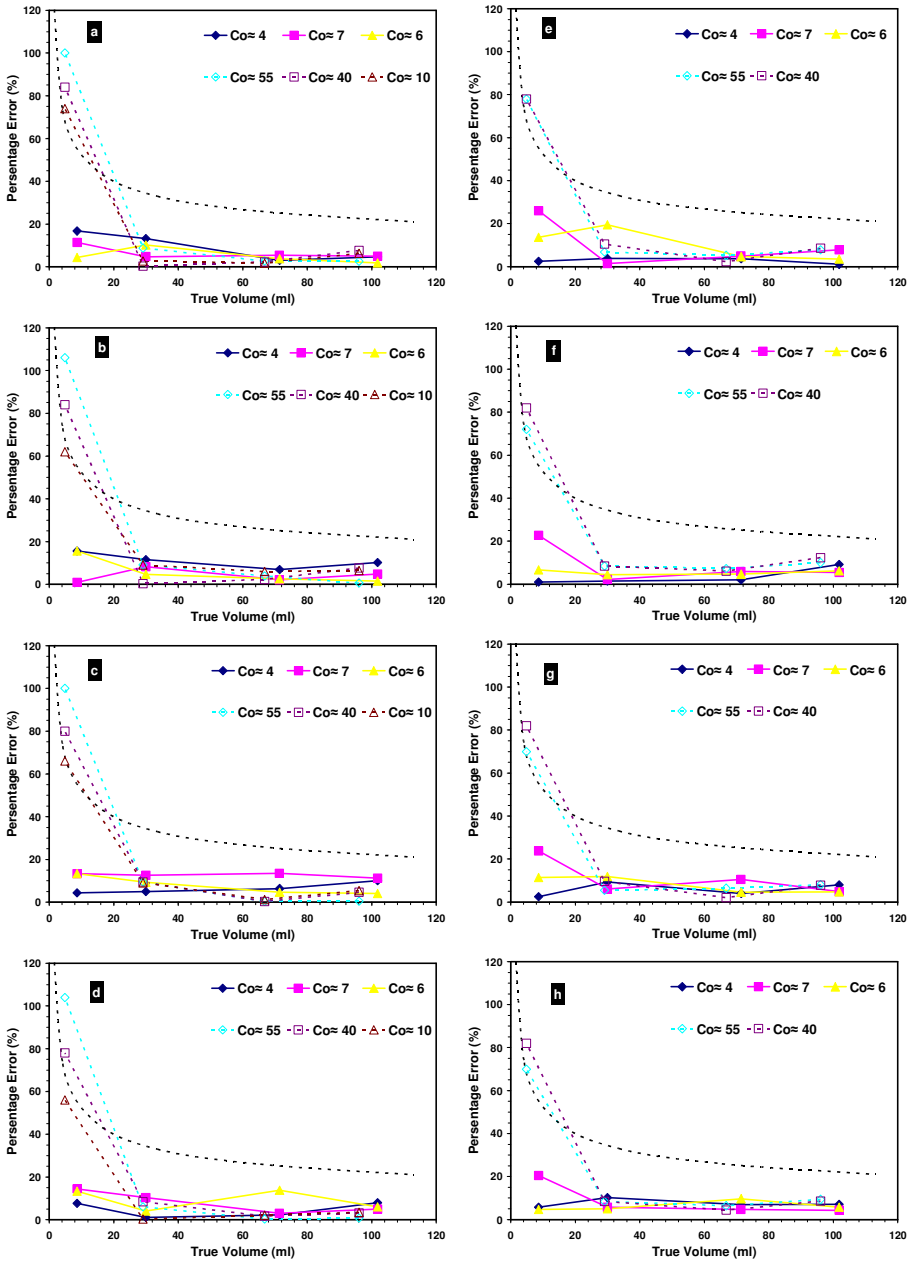

Figure 5.24: The modulus of percentage error in measuring irregular volumes using 60 minute $VCAT_9$ calibration curve method for IT (left side) with different t_{AC} = 1(a), 2.5(b), 5(c), 10(d) minute and FBP (right side) with the same t_{AC} values (e, f, g, h). The solid points and lines represent the top-hat while the hollow points and dotted lines represent the crescent irregular volumes. The black dotted line represents the acceptable error.

5.6.4. Comparison With Fixed Thresholding Method

The use of 40% fixed thresholding technique with $Lmax_9$ ($40\%_9$) and $Lmax_{27}$ ($40\%_{27}$) were investigated in irregular lesions.

Figure 5.25 and Figure 5.26 present the modulus percentage error in measuring irregular lesions using $40\%_9$ and $40\%_{27}$ respectively. It showed similar percentage errors in using the two techniques. It also showed that neither $40\%_9$ nor $40\%_{27}$ segmented the smallest crescent volume (4.89 ml) across all studied conditions within the acceptable error; also, for all top-hat volumes having $C_o \sim 4$.

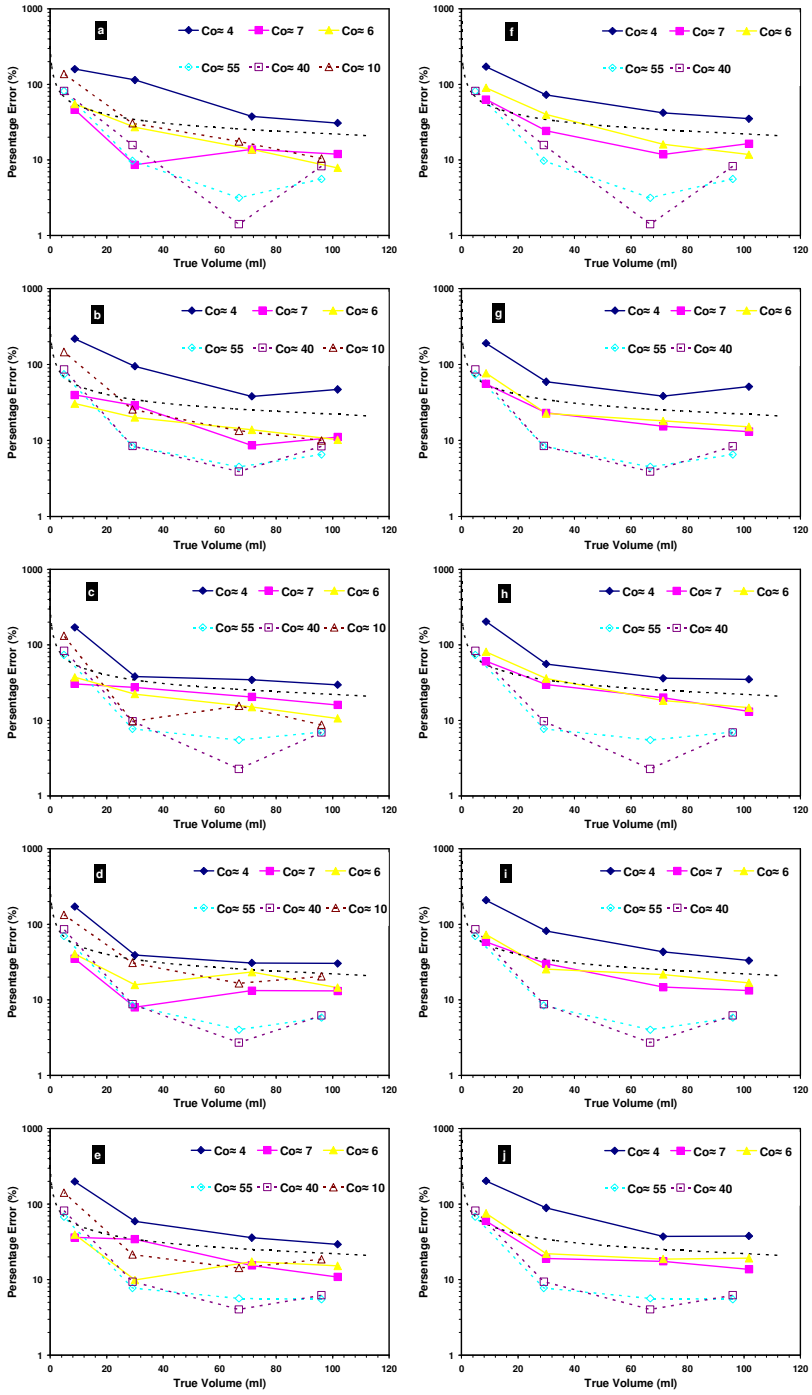

Figure 5.25: The modulus of percentage error in measuring irregular volumes using 40% of $Lmax_9$ fixed thresholding method for IT (left side) with different t_{AC} = 1(a), 2.5(b), 5(c), 10(d), 60(e) minute and FBP (right side) with the same t_{AC} values (f, g, h, i, j). The solid points and lines represent the top-hat while the hollow points and dotted lines represent the crescent irregular volumes. The black dotted line represents the acceptable error.

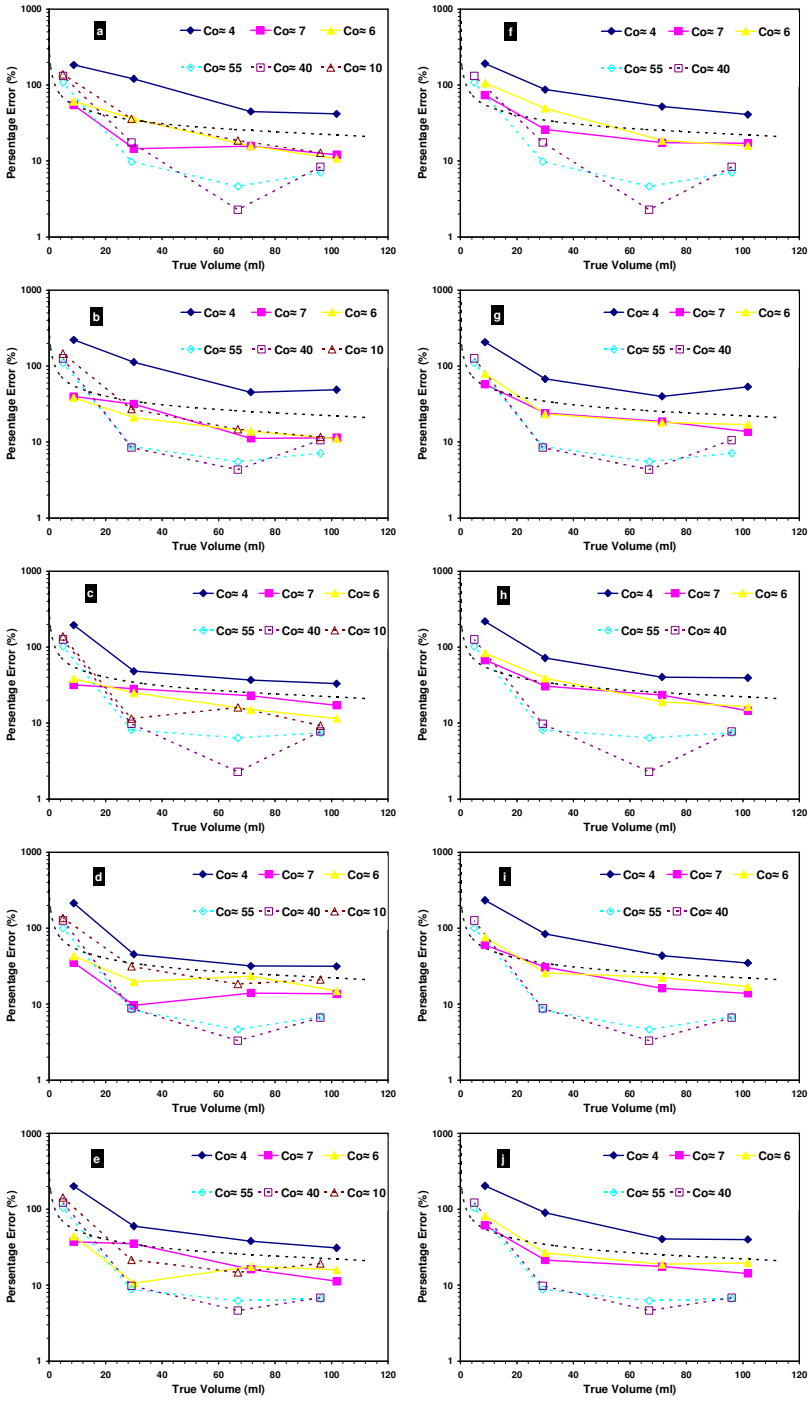

Figure 5.26: The modulus of percentage error in measuring irregular volumes using 40% of $Lmax_{27}$ fixed thresholding method for IT (left side) with different t_{AC} = 1(a), 2.5(b), 5(c), 10(d), 60(e) minute and FBP (right side) with the same t_{AC} values (f, g, h, i, j). The solid points and lines represent the top-hat while the hollow points and dotted lines represent the crescent irregular volumes. The black dotted line represents the acceptable error.

5.7. Concordance Measurement Results

Concordance measurements were carried out to investigate the similarity between the true irregular volumes, from the CT, and the $CAT_{9/27}$ and $VCAT_{9/27}$ segmented PET volumes. Jaccard and Dice similarities measurements were employed for these comparisons.

The PET segmented volumes were written into a binary image with the same matrix size of the PET images (128 × 128 × 47). The true volumes were determined from the CT images using Iodine contrast (concentration ranging from 4.5 – 3.5 mg/ml). A threshold value was determined for each individual phantom volume that produced a CT volume equal to the true volume and then written into a binary image with the same matrix size of 512 × 512 × 47. A bilinear interpolation was used to up-sampled the PET segmented volumes to match the CT matrix size. Also, the PET segmented volumes were re-scaled to 50 cm FoV using a linear interpolation.

Figure 5.27 and Figure 5.28 show the results of Dice and Jaccard similarity coefficients measurements in segmenting top-hat and crescent irregular volumes using the CAT_9 and CAT_{27} respectively at 1, 2.5, 5, 10 and 60 min acquisition times for both IT and FBP images. These results demonstrate that the top-hat volumes were closer in similarity with the true volume than the crescent volumes. There was no difference in the resulting similarity coefficient between using CAT_9 and CAT_{27}.

Figure 5.29 and Figure 5.30 show the results of Dice and Jaccard similarity coefficients measurements in segmenting top-hat and crescent irregular volumes using the $VCAT_9$ and $VCAT_{27}$ respectively at 1, 2.5, 5, 10 and 60 min acquisition times for both IT and FBP images. Generally, these

results were better than those obtained using the CAT_9 and CAT_{27}. There was agreement in the results of the top-hat and crescent volumes. These results demonstrate good agreement between the $VCAT_9$ and $VCAT_{27}$ in both the top-hat and crescent volumes > 1.15ml in case of IT and volumes > 2.57ml in case of FBP. Also, there was found to be no difference in the resulting similarities coefficient between using $Lmax_9$ and $Lmax_{27}$.

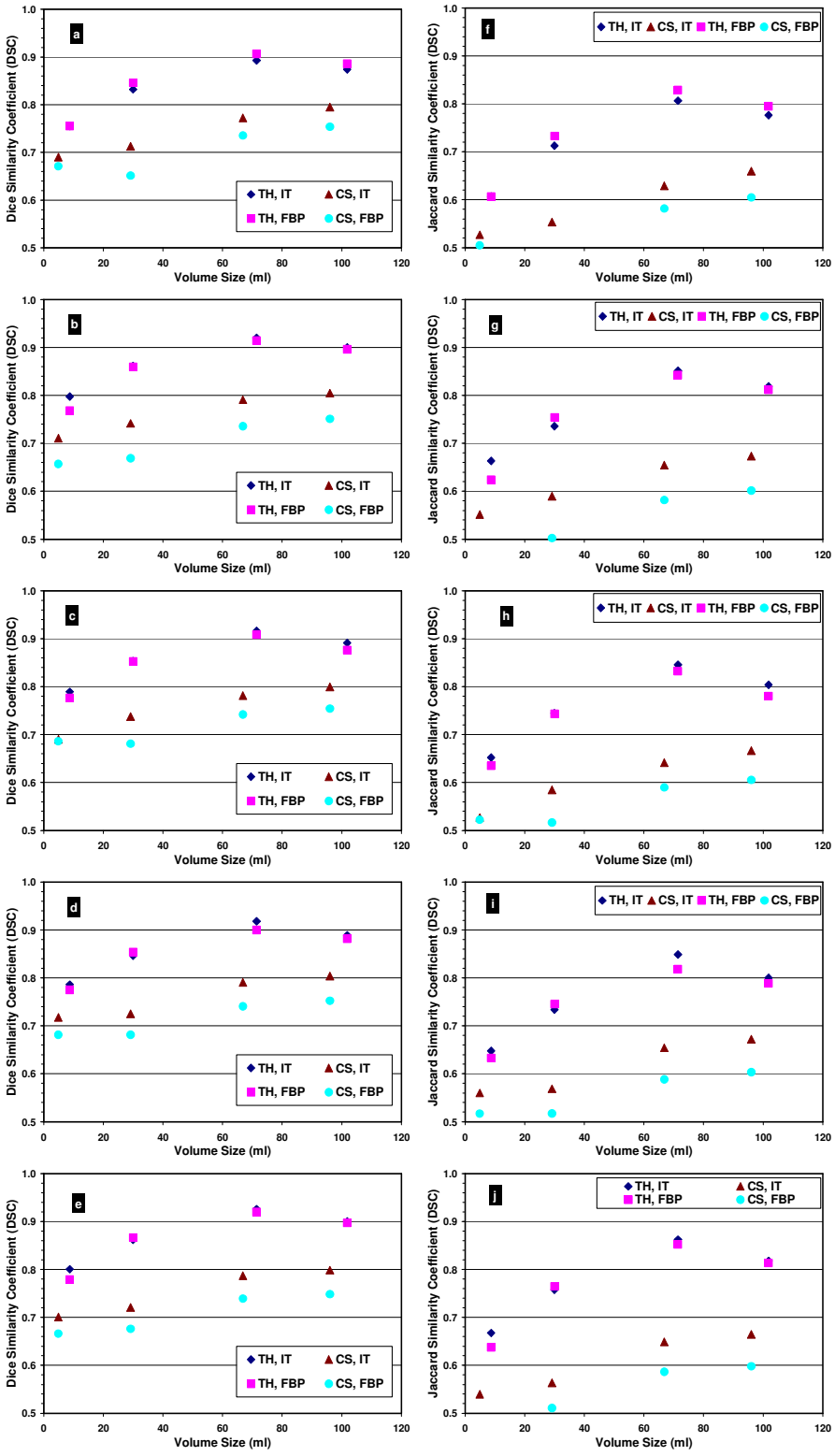

Figure 5.27: Dice similarity coefficient at 1, 2.5, 5, 10 and 60 min acquisition times (a, b, c, d and e) and Jaccard similarity coefficient (f, g, h, i and j) for the top hat (TH) and crescent (CS) phantoms with IT and FBP reconstruction techniques using CAT_9.

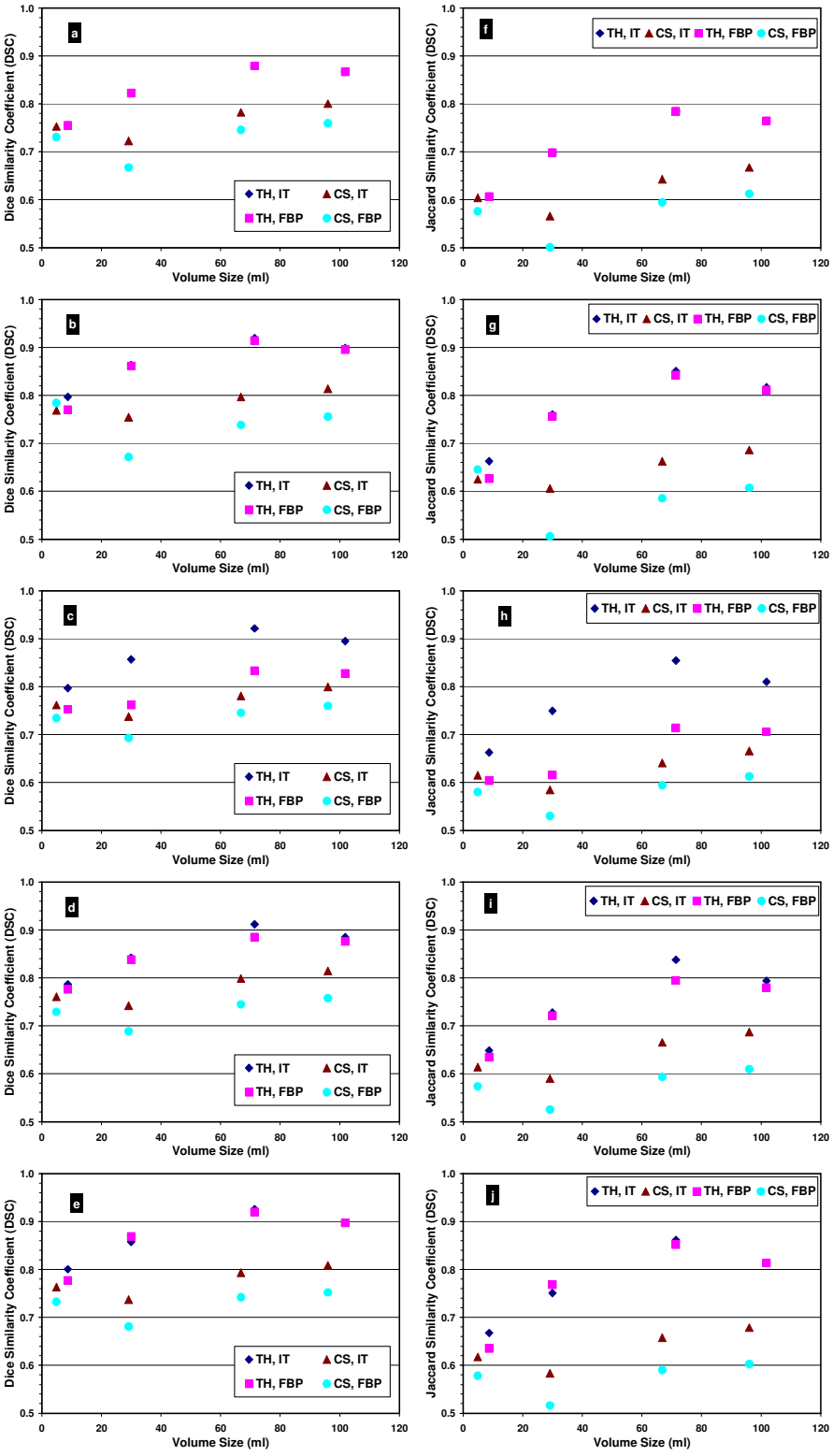

Figure 5.28: Dice similarity coefficient at 1, 2.5, 5, 10 and 60 min acquisition times (a, b, c, d and e) and Jaccard similarity coefficient (f, g, h, i and j) for the top hat (TH) and crescent (CS) phantoms with IT and FBP reconstruction techniques using CAT_{27}.

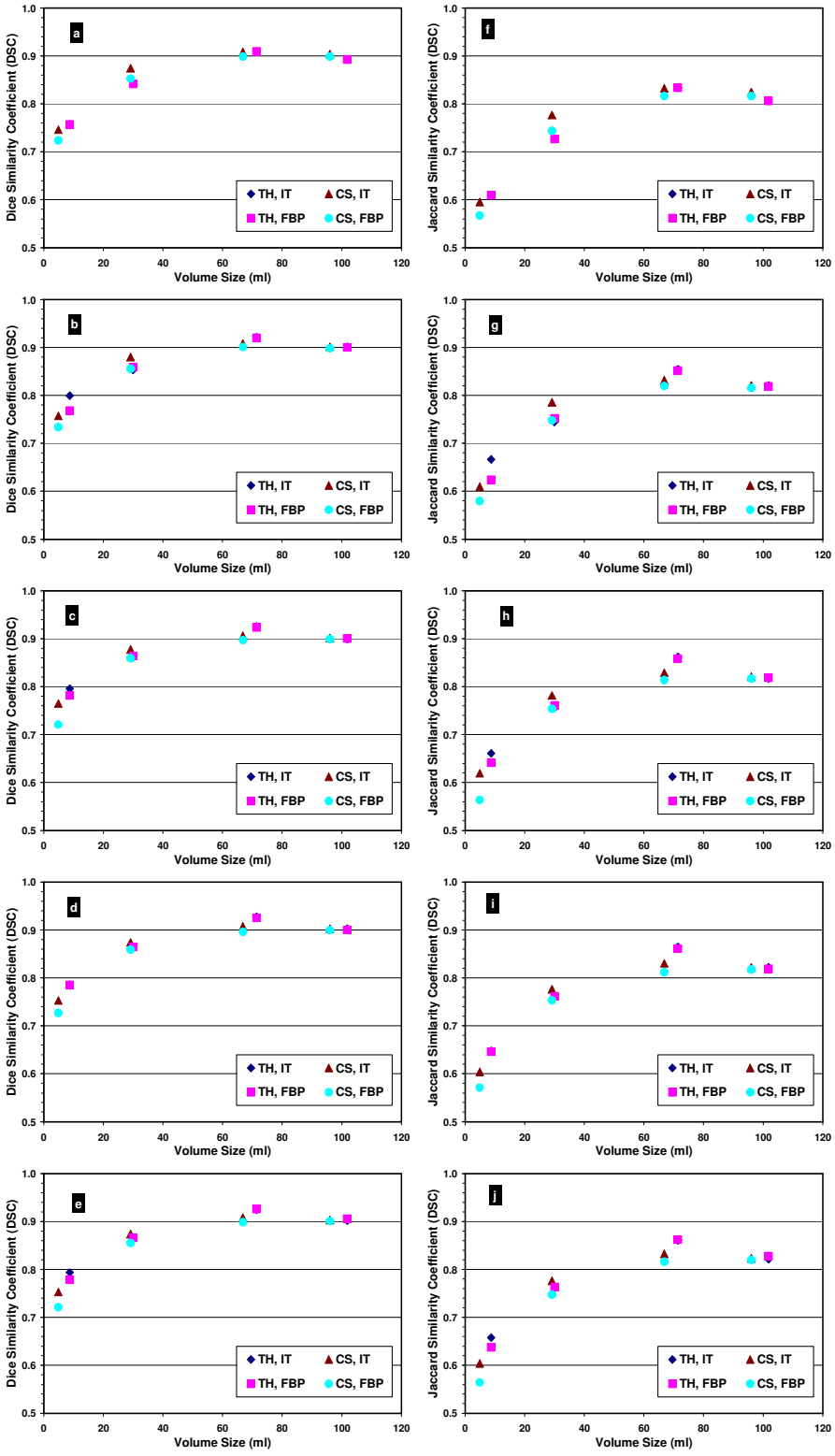

Figure 5.29: Dice similarity coefficient at 1, 2.5, 5, 10 and 60 min acquisition times (a, b, c, d and e) and Jaccard similarity coefficient (f, g, h, i and j) for the top hat (TH) and crescent (CS) phantoms with IT and FBP reconstruction techniques using $VCAT_9$.

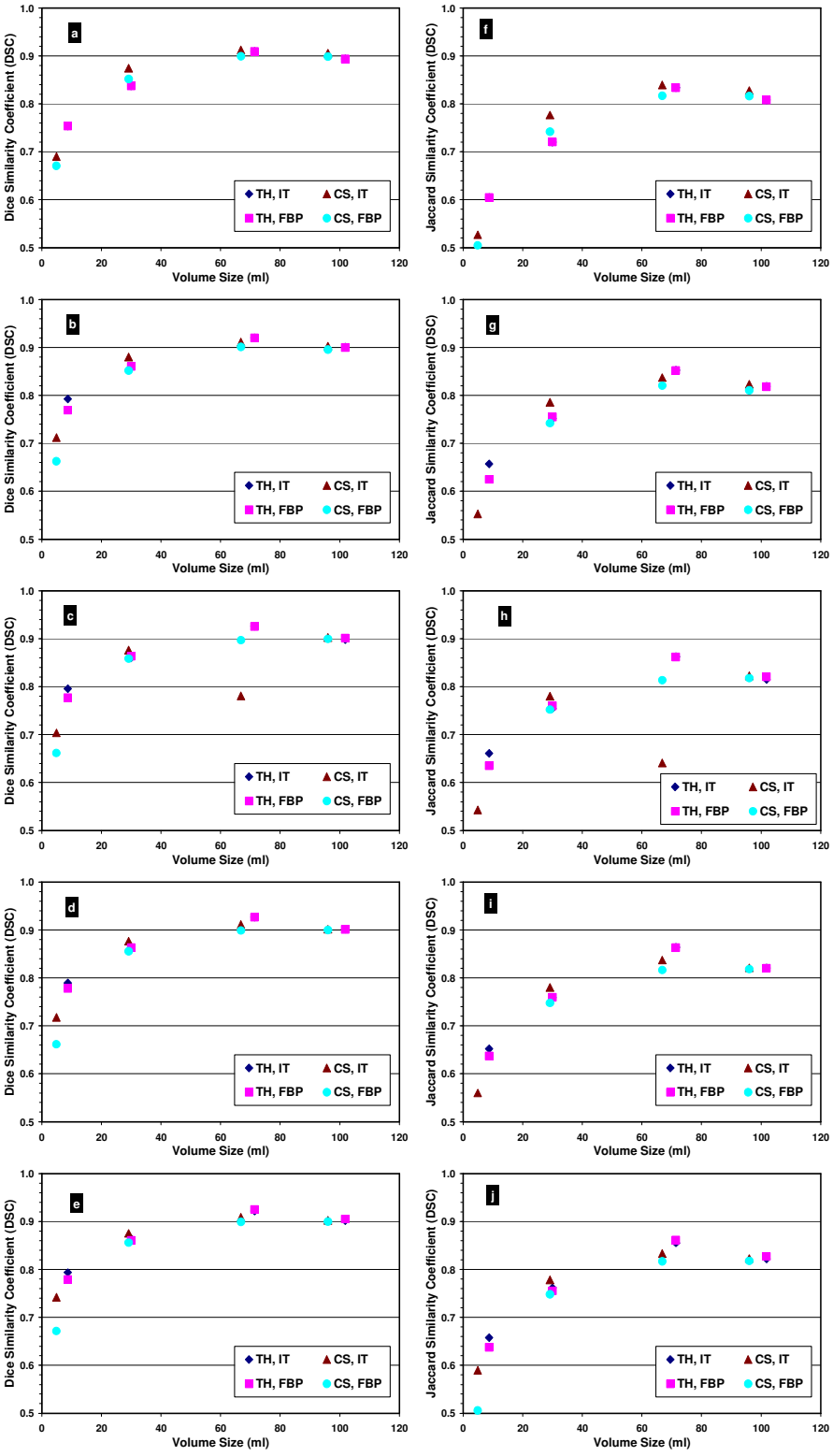

Figure 5.30: Dice similarity coefficient at 1, 2.5, 5, 10 and 60 min acquisition times (a, b, c, d and e) and Jaccard similarity coefficient (f, g, h, i and j) for the top hat (TH) and crescent (CS) phantoms with IT and FBP reconstruction techniques using $VCAT_{27}$.

5.8. Euclidean Distance Transformation

The Euclidean distance transformation was used to compare the spatial location between the true volume (obtained from the CT) and the segmented PET volumes. Two distance maps were generated from the true binary image. One distance map represents the distances in mm inside the true volume (negative) and the other represents the distance in mm outside the true volume (positive). The surface of the PET segmented volume was then calculated and its location compared with the new combined distance map. So, the resulting distance value will be negative if the surface of the PET segmented volume was inside the true volume and will be positive if it was outside the true volume.

Figure 5.31 and Figure 5.32 show the histograms of the distances between the surface of true volumes (CT) and the surface of the segmented volumes using the CAT_9 and CAT_{27} at 1, 2.5, 5, 10 and 60 min t_{AC} for IT and FBP images. These histograms demonstrate that the distances between the two surfaces were centred on zero distance; however a small percentage of the surfaces were overlapped. The percentages of the overlap between the two surfaces vary among the volume sizes, shapes and reconstruction techniques.

Figure 5.33 and Figure 5.34 show the histograms of the distances between the surface of true volumes and the surface of the segmented volumes using the $VCAT_9$ and $VCAT_{27}$ at t_{AC} = 1, 2.5, 5, 10 and 60 min for IT and FBP images. These results were better than those obtained using the CAT method with the maximum lesion uptake defined by the mean of 9 and 27 voxels.

Generally, the results of using the $CAT_{9/27}$ and $VCAT_{9/27}$ techniques in top-hat volumes were better than in crescent volumes. The top-hat results were more centralized while the crescent results were more shifted towards the positive distance, indicating that the methods segmented larger volumes.

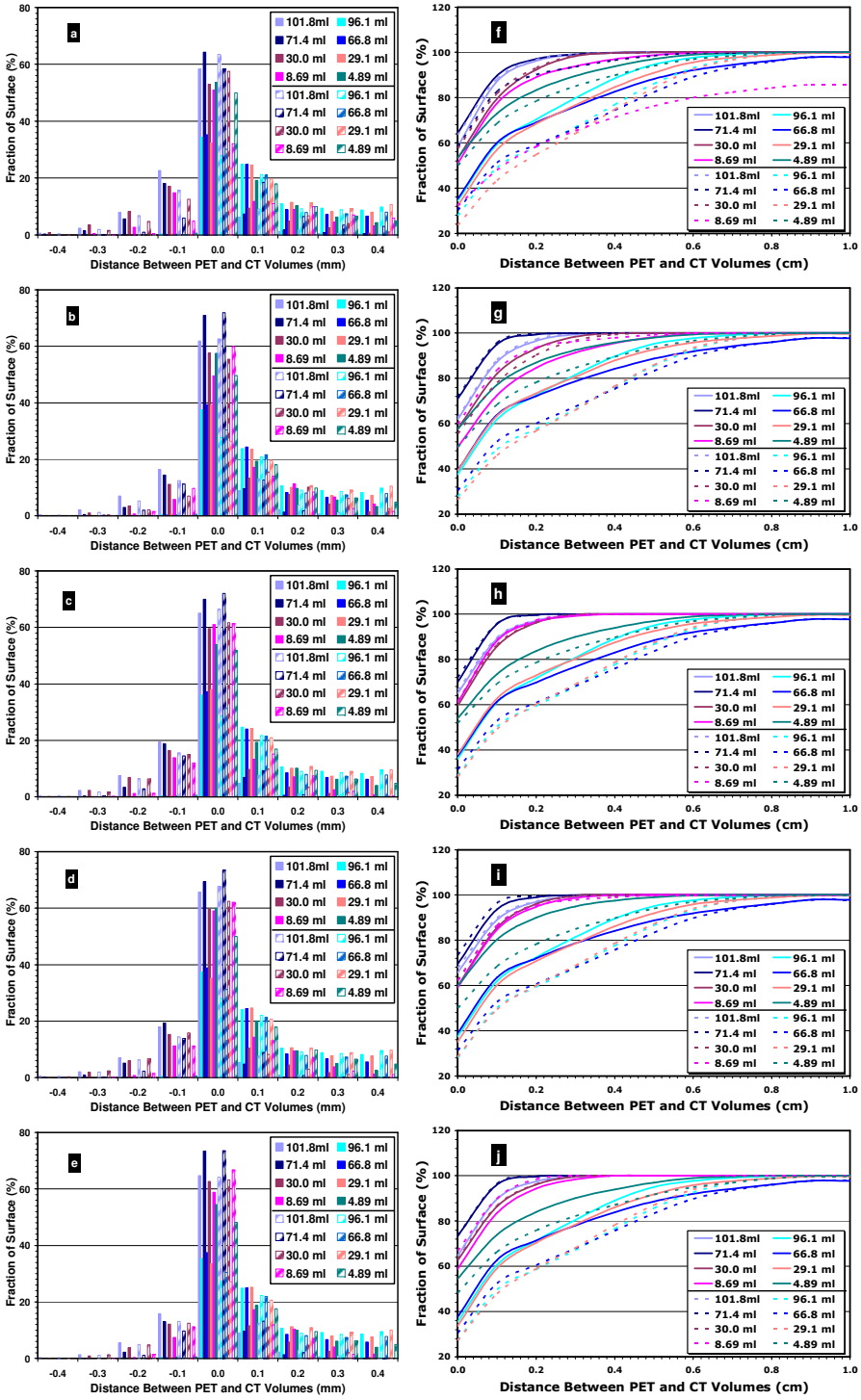

Figure 5.31: Differential (a, b, c, d, e) and cumulative (f, g, h, i, j) histograms of the nearest distance between the surface of reference CT images and segmented PET volumes using CAT_9 for top-hat and crescent irregular volumes at 1, 2.5, 5, 10 and 60 min t_{AC} for IT (solid) and FPB (dashed) respectively developed by using the Euclidean distance transformation.

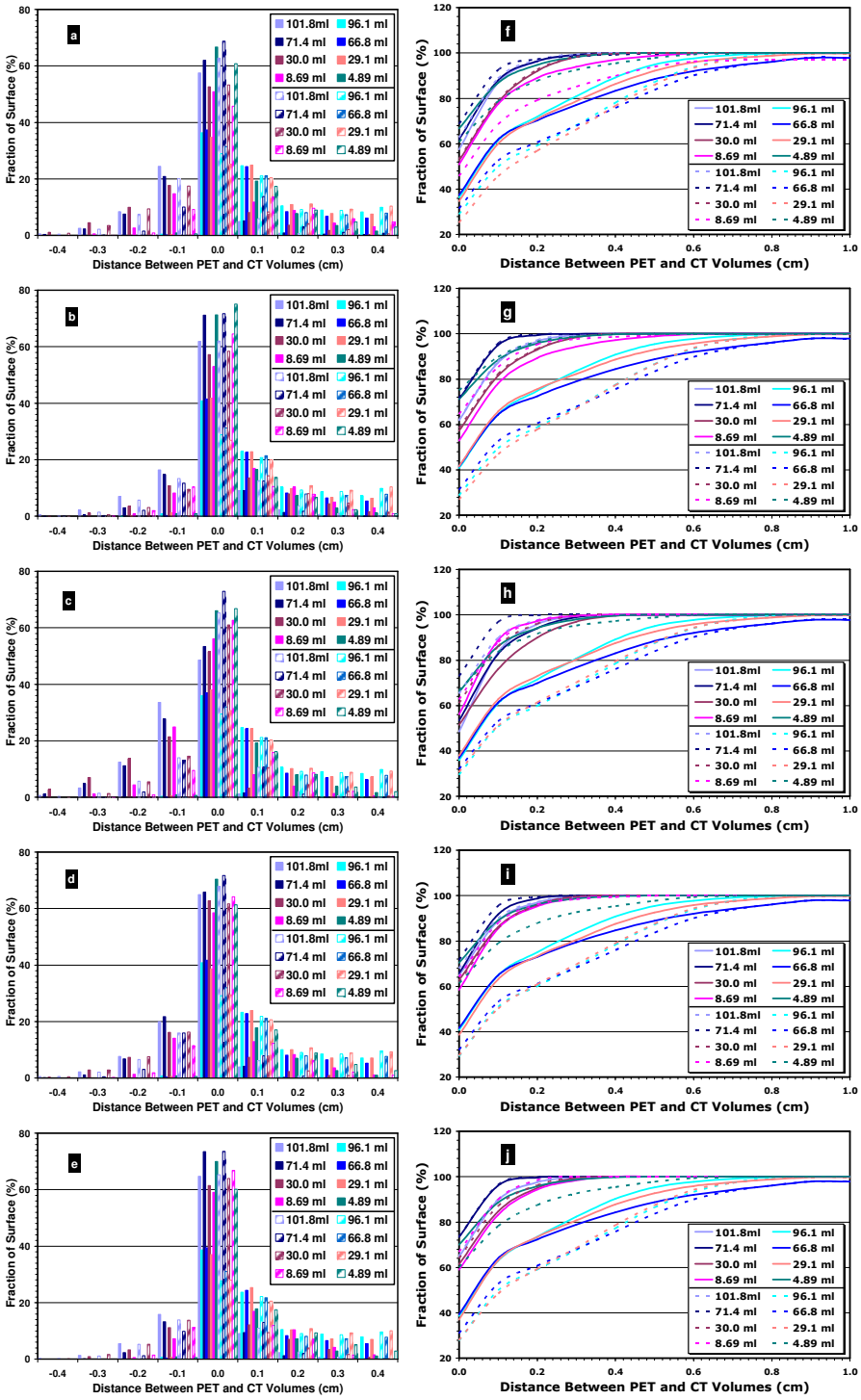

Figure 5.32: Differential (a, b, c, d, e) and cumulative (f, g, h, i, j) histograms of the nearest distance between the surface of reference CT images and segmented PET volumes using CAT_{27} for top-hat and crescent irregular volumes at 1, 2.5, 5, 10 and 60 min t_{AC} for IT (solid) and FPB (dashed) respectively developed by using the Euclidean distance transformation.

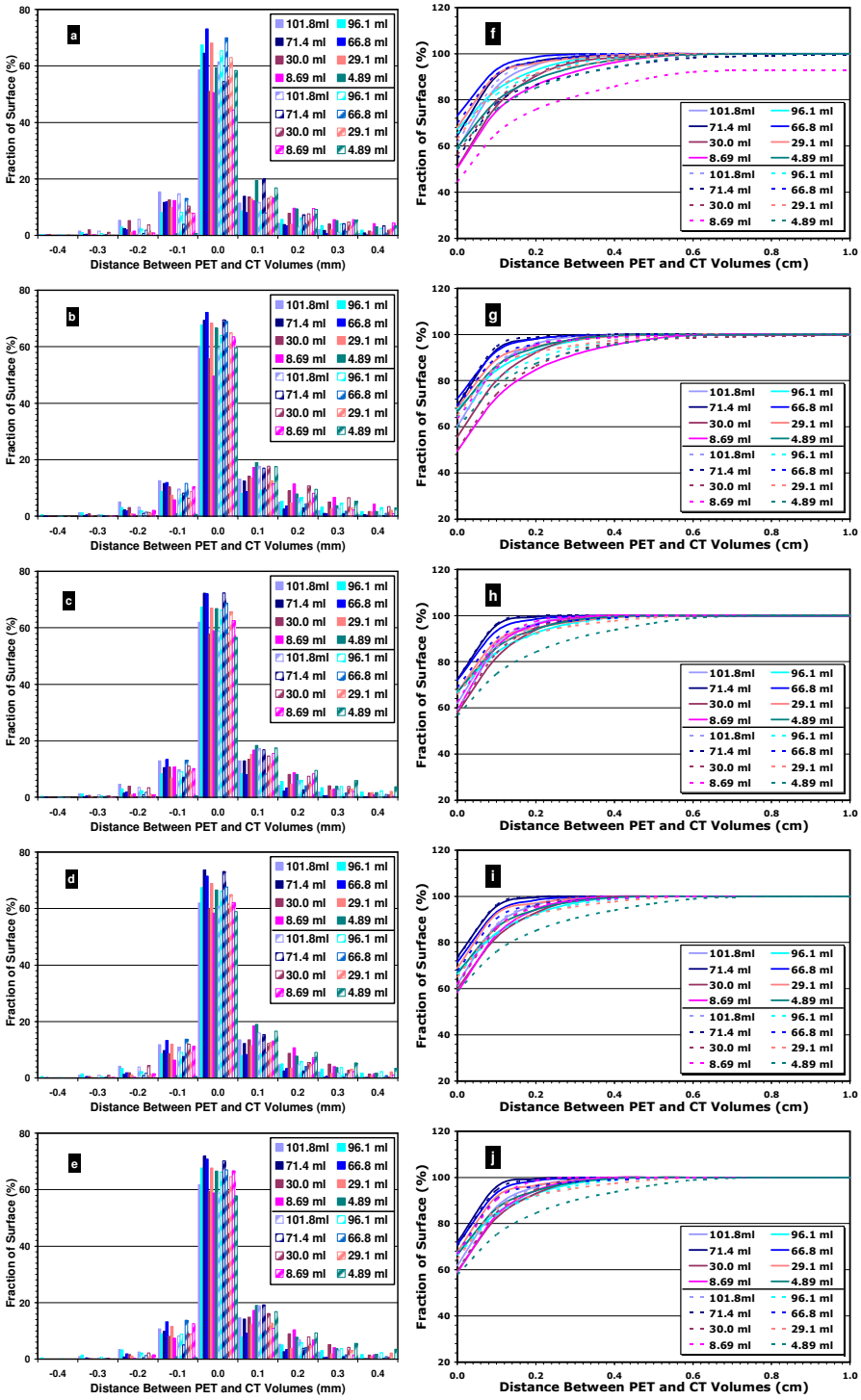

Figure 5.33: Differential (a, b, c, d, e) and cumulative (f, g, h, i, j) histograms of the nearest distance between the surface of reference CT images and segmented PET volumes using $VCAT_9$ for top-hat and crescent irregular volumes at 1, 2.5, 5, 10 and 60 min t_{AC} for IT (solid) and FPB (dashed) respectively developed by using the Euclidean distance transformation.

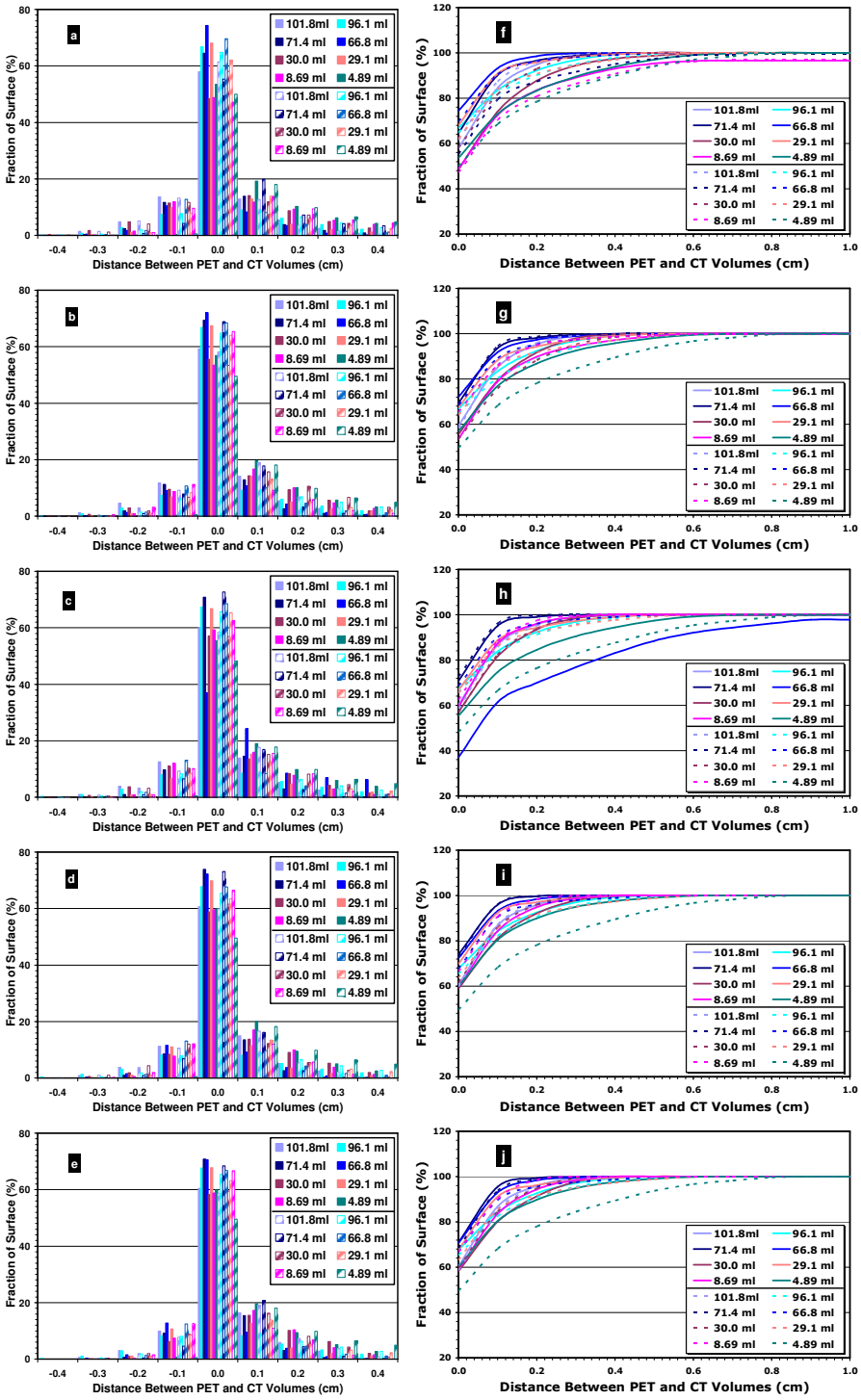

Figure 5.34: Differential (a, b, c, d, e) and cumulative (f, g, h, i, j) histograms of the nearest distance between the surface of reference CT images and segmented PET volumes using $VCAT_{27}$ for top-hat and crescent irregular volumes at 1, 2.5, 5, 10 and 60 min t_{AC} for IT (solid) and FPB (dashed) respectively developed by using the Euclidean distance transformation.

5.9. Statistical Comparison of $VCAT_{9/27}$ and $CAT_{9/27}$

5.9.1. Spherical Lesions

A further eight new PET segmentation techniques, in total, based on the definition of $Lmax_9$ (CAT_9, CAT_9-60, $VCAT_9$, $VCAT_9$-60) and $Lmax_{27}$ (CAT_{27}, CAT_{27}-60, $VCAT_{27}$, $VCAT_{27}$-60) were evaluated and were compared with the corresponding use of $40\%_9$ and $40\%_{27}$ fixed thresholding techniques. Statistical analyses were carried out to evaluate the performance of each corresponding five different techniques having the same Lmax definition. The same strategy employed for comparing the differences between the techniques presented in chapter 4 was also employed: the CI was calculated for each spherical volume under all studied conditions, then these five techniques were ranked based on the calculated CI, the mean rank across all the conditions was determined for each techniques, and, finally, a test of statistical significance, the Friedman ranking test, was carried out on the differences between these techniques.

The Friedman test statistic for CAT_9, CAT_9-60, $VCAT_9$, and $VCAT_9$-60 techniques was 746.44 ($p << 0.0001$), which means that the difference between one technique (or more) and the other techniques was highly significant. A least significant difference procedure following the Friedman test was carried out to test the pairwise significance between the five techniques (10 pairs) using a calculated critical difference, maintaining an overall error rate of 5% for all paired comparisons. The mean ranks for these five techniques across all studied conditions and the critical difference are presented in Table 5.4.

$VCAT_9$	$VCAT_9$-60	CAT_9	CAT_9-60	$40\%_9$	Critical Difference
1.71	2.20	3.04	3.12	4.94	**0.363**

Table 5.4: The mean rank order with the calculated critical difference for the pairwise comparisons between the use of CAT_9, CAT_9-60, $VCAT_9$, $VCAT_9$-60, and $40\%_9$ techniques in all spherical lesions. The techniques sharing the same green bar are not statistically significantly different.

These mean ranks show the ranking order of these five techniques from lowest to highest rank, and that there was a statistically significant difference between the use of $VCAT_9$ and the other four techniques, as well as a significant difference between $VCAT_9$-60 and the followed three techniques. There was no significant difference between CAT_9 and CAT_9-60, while there was a significant difference between these two techniques and the use of $40\%_9$.

The Friedman test statistic for CAT_{27}, CAT_{27}-60, $VCAT_{27}$, and $VCAT_{27}$-60 techniques was 746.44 ($p << 0.0001$), which means that the difference between one technique (or more) and the other techniques was highly significant. The mean ranks and the critical difference for these five techniques across all studied conditions are presented in Table 5.5.

$VCAT_{27}$	$VCAT_{27}$-60	CAT_{27}	CAT_{27}-60	$40\%_{27}$	Critical Difference
1.72	2.30	2.99	3.09	4.89	**0.363**

Table 5.5: The mean rank order with the calculated critical difference for the pairwise comparisons between the use of CAT_{27}, CAT_{27}-60, $VCAT_{27}$, $VCAT_{27}$-60, and $40\%_{27}$ techniques in all spherical lesions. The techniques sharing the same green bar are not statistically significantly different.

These mean ranks show the ranking order of these five techniques from lowest to highest rank. There was a statistically significant difference between the use of $VCAT_{27}$ and the other four techniques, as well as a significant

difference between the use of $VCAT_{27}$-60 and the remaining three techniques. There was no significant difference between the use of CAT_{27} and CAT_{27}-60 while there was a significant difference between these two techniques and the use of $40\%_{27}$. These results of for using $Lmax_{27}$ were identical to the use of $Lmax_9$.

5.9.2. Irregular lesions

The same strategy employed for comparing the differences between the ten techniques presented in spherical lesions was also employed in the irregular lesions comparisons.

The Friedman test statistic for CAT_9, CAT_9-60, $VCAT_9$, and $VCAT_9$-60 techniques was 244.23 ($p << 0.0001$), which means that the difference between one technique (or more) and the other techniques was highly significant. The mean ranks and the critical difference for these five techniques across all studied conditions are presented in Table 5.6.

$VCAT_9$	**$VCAT_9$-60**	**CAT_9**	**CAT_9-60**	**$40\%_9$**	**Critical Difference**
2.11	2.42	2.79	3.56	4.10	**0.424**

Table 5.6: The mean rank order with the calculated critical difference for the pairwise comparisons between the use of CAT_9, CAT_9-60, $VCAT_9$, $VCAT_9$-60, and $40\%_9$ techniques in all irregular lesions. The techniques sharing the same green bar are not statistically significantly different.

These mean ranks show the ranking order of these five techniques from lowest to highest rank and that there were no significant differences between using either $VCAT_9$ and $VCAT_9$-60 or $VCAT_9$-60 and CAT_9 techniques, however, there was a significant difference between these three techniques and the use of CAT_9-60 and $40\%_9$. It also show that there was a significant difference in

using $VCAT_9$ compared with CAT_9, CAT_9-60 and $40\%_9$, as well as between CAT_9 and CAT_9-60 and between these two techniques and $40\%_9$.

The Friedman test statistic for CAT_{27}, CAT_{27}-60, $VCAT_{27}$, and $VCAT_{27}$-60 techniques was 216.19 ($p << 0.0001$), which means that the difference between one technique (or more) and the other techniques was highly significant. The mean ranks and the critical difference for these five techniques across all studied conditions are presented in Table 5.7.

$VCAT_{27}$	**$VCAT_{27}$-60**	**CAT_{27}**	**CAT_{27}-60**	**$40\%_{27}$**	**Critical Difference**
2.21	2.46	2.75	3.51	4.07	**0.424**

Table 5.7: The mean rank order with the calculated critical difference for the pairwise comparisons between the use of CAT_{27}, CAT_{27}-60, $VCAT_{27}$, $VCAT_{27}$-60, and $40\%_{27}$ techniques in all irregular lesions. The techniques sharing the same green bar are not statistically significantly different.

These mean ranks show exactly the same statistical significances between these five techniques that were seen in using $Lmax_9$.

5.10. Statistical Comparison of techniques using Lmax, $Lmax_9$ or $Lmax_{27}$

All the comparisons done in the previous two sections or in the statistical analysis section in chapter 4 were done within the same definitions of the observed contrast; i.e. using Lmax, $Lmax_9$, or $Lmax_{27}$. Further analyses were carried out to compare the difference between all 15 techniques studied (CAT_1, $VCAT_1$, CAT_1-60, $VCAT_1$-60, CAT_9, $VCAT_9$, CAT_9-60, $VCAT_9$-60, CAT_{27}, $VCAT_{27}$, CAT_{27}-60, $VCAT_{27}$-60, $40\%_1$, $40\%_9$, $40\%_{27}$) across all the studied conditions using the same strategy as employed in the previous statistical analyses.

5.10.1. Comparisons of all techniques in spherical lesions

The Friedman test statistic for the fifteen techniques in spherical lesions was 2300.72 ($p << 0.0001$), which means that the difference between one technique (or more) and the other techniques was highly significant. The calculated critical difference for the pairwise significance to maintaining an overall error rate of 5% for all paired comparisons was 1.28. The mean rank, presented in Table 5.8, showed that the $VCAT_1$ technique performed best with the lowest rank, and was not significantly different from CAT_1 and $VCAT_9$. However, the fixed threshold method using of either $40\%_1$, $40\%_9$, or $40\%_{27}$ had the worst performance with the highest values of rank. There was no significant difference between the use of $40\%_9$ and $40\%_{27}$, or between $40\%_1$, CAT_{27}-60 and CAT_{27}.

It was observed that the smallest spherical lesion results were having a large impact on the above, probably due to this lesion being comparable in size to the volume of the 9 and 27 voxel zones being used to determine the maximum lesion uptake. Therefore, the analyses were repeated excluding the two smallest spherical lesions (0.53 and 1.15 ml). The Friedman test statistic for the fifteen techniques in spherical lesions > 1.15 ml was 1479.60 ($p << 0.0001$), which means that the difference between one technique (or more) and the other techniques was highly significant. The calculated critical difference for the pairwise significant to maintaining an overall error rate of 5% for all paired comparisons was 1.56. The mean ranks for these fifteen techniques across all studied conditions are presented in Table 5.9. It is clear that this analysis produced the same rank order as in using the whole range of spherical volumes for the fifteen techniques; however, differences were obtained in the significance grouping (represented by the green bars). The $VCAT_1$ technique produced the lowest rank order with no statistically

significant difference from CAT_1, $VCAT_9$, and CAT_1-60. The use of $40\%_1$, $40\%_9$, or $40\%_{27}$ produced the highest values of rank, with no significant difference between the use of $40\%_9$ and $40\%_{27}$, or between the use of $40\%_1$ and CAT_9-60, CAT_9, CAT_{27}-60 and CAT_{27}.

$VCAT_1$	CAT_1	$VCAT_9$	CAT_1-60	$VCAT_{27}$	$VCAT_9$-60	$VCAT_1$-60	$VCAT_{27}$-60	CAT_9-60	CAT_9	CAT_{27}-60	CAT_{27}	$40\%_1$	$40\%_9$	$40\%_{27}$
3.81	4.47	4.98	5.41	5.65	5.82	6.04	7.60	8.68	8.87	9.78	9.96	10.47	13.78	14.68

Table 5.8: The mean rank order for the pairwise comparisons between the use of the 15 techniques in all spherical lesions. The calculated critical difference for these pairwise comparisons was 1.28. The techniques sharing the same green bar are not statistically significantly different.

$VCAT_1$	CAT_1	$VCAT_9$	CAT_1-60	$VCAT_{27}$	$VCAT_9$-60	$VCAT_1$-60	$VCAT_{27}$-60	CAT_9-60	CAT_9	CAT_{27}-60	CAT_{27}	$40\%_1$	$40\%_9$	$40\%_{27}$
4.30	4.37	4.81	5.27	5.90	6.07	6.18	7.27	8.65	8.90	9.86	9.90	10.14	13.72	14.68

Table 5.9: The mean rank order for the pairwise comparisons between the use of the 15 techniques in spherical lesions > 1.15 ml. The calculated critical difference for these pairwise comparisons was 1.56. The techniques sharing the same green bar are not statistically significantly different.

5.10.2. Comparisons of all techniques in irregular lesions

The Friedman test statistic for the fifteen techniques in irregular lesions was 1039.18 ($p << 0.0001$), which means that the difference between one technique (or more) and the other techniques was highly significant. The calculated critical difference for the pairwise significant to maintaining an overall error rate of 5% for all paired comparisons was 1.49. The mean ranks for these fifteen techniques across all studied conditions are presented in Table 5.10. It is clear that $VCAT_1$ technique produced the lowest rank with no statistically significant difference from $VCAT_1$-60. However, the using either CAT_{27}-60, $40\%_9$, or $40\%_{27}$ produced the highest values of rank, with no statistically significant difference between these three techniques, or between the use of CAT_9-60, CAT_{27}-60 and $40\%_9$.

Another analysis was carried out for the difference in using the fifteen techniques in top-hat and crescent irregular lesions and separately. The Friedman test statistic for the fifteen techniques in top-hat lesions was 782.89 ($p << 0.0001$), which means that the difference between one technique (or more) and the other techniques was highly significant. The calculated critical difference for the pairwise significant to maintaining an overall error rate of 5% for all paired comparisons was 2.03. The mean ranks for these fifteen techniques across all studied conditions are presented in Table 5.11. It revealed a change in the ranking order of the fifteen techniques where, in this analysis, the use of CAT_1 technique was the least rank while there was no significant difference between this technique and the use of $VCAT_1$, $VCAT_9$, and $VCAT_1$-60. On the other hand, the use of $40\%_{27}$ maintained its position of being the highest rank order.

The Friedman test statistic for the fifteen techniques in crescent lesions was 618.86 ($p << 0.0001$), which means that the difference between one technique (or more) and the other techniques was highly significant. The calculated critical difference for the pairwise significant to maintaining an overall error rate of 5% for all paired comparisons was 2.21. The mean ranks for these fifteen techniques across all studied conditions are presented in Table 5.12. It revealed a slightly change in the ranking order compared with taking in consideration the whole types of irregular volumes in terms of lowest and highest rank ordered techniques, $VCAT_1$ and $40\%_{27}$ respectively.

$VCAT_1$	$VCAT_1$-60	$VCAT_9$	CAT_1	$VCAT_9$-60	$40\%_1$	CAT_1-60	CAT_9	$VCAT_{27}$	$VCAT_{27}$-60	CAT_{27}	CAT_9-60	CAT_{27}-60	$40\%_9$	$40\%_{27}$
3.64	4.68	5.78	6.15	6.53	6.92	7.26	7.78	7.92	8.47	9.22	10.16	11.28	11.43	12.77

Table 5.10: The mean rank order for the pairwise comparisons between the use of the 15 techniques in all irregular lesions. The calculated critical difference for these pairwise comparisons was 1.49. The techniques sharing the same green bar are not statistically significantly different.

CAT_1	$VCAT_1$	$VCAT_9$	$VCAT_1$-60	$VCAT_9$-60	CAT_9	$VCAT_{27}$	CAT_{27}	$VCAT_{27}$-60	$40\%_1$	CAT_1-60	CAT_{27}-60	CAT_9-60	$40\%_9$	$40\%_{27}$
3.74	3.93	5.24	5.45	6.02	6.74	6.76	7.32	7.76	8.58	10.14	11.25	11.58	12.24	13.25

Table 5.11: The mean rank order for the pairwise comparisons between the use of the 15 techniques in all top-hat lesions. The calculated critical difference for these pairwise comparisons was 2.03. The techniques sharing the same green bar are not statistically significantly different.

$VCAT_1$	$VCAT_1$-60	CAT_1-60	$40\%_1$	$VCAT_9$	$VCAT_9$-60	CAT_9-60	CAT_1	CAT_9	$VCAT_{27}$	$VCAT_{27}$-60	$40\%_9$	CAT_{27}-60	CAT_{27}	$40\%_{27}$
3.30	3.78	3.84	4.94	6.42	7.13	8.47	9.03	9.03	9.30	9.32	10.47	11.32	11.48	12.20

Table 5.12: The mean rank order for the pairwise comparisons between the use of the 15 techniques in all crescent lesions. The calculated critical difference for these pairwise comparisons was 2.21. The techniques sharing the same green bar are not statistically significantly different.

5.11. Discussion

The $VCAT_1$ and CAT_1 techniques require a measurement of the observed lesion contrast, which in turn requires a measurement of the maximum lesion uptake. In the initial implementation of the techniques, presented in chapter 3, this maximum lesion uptake was taken to be that of the highest voxel value, Lmax, in the lesion. Due to the possibility of this being influenced by image noise, the impact was investigated of defining the maximum lesion uptake $Lmax_9$ or $Lmax_{27}$ as the mean of the 9 or 27 neighbouring voxels respectively. Because this could impact not only on the application of the technique, but also on the system calibration, new calibration curves were generated for the $CAT_{9/27}$ and $VCAT_{9/27}$ techniques. These were evaluated on the spherical and irregular phantom volumes, for a range of parameters giving a total of 12 instances of VCAT/CAT, which were compared with a fixed 40% threshold method. This 40% threshold was applied using the different definitions of maximum lesion uptake, Lmax, $Lmax_9$ and $Lmax_{27}$, giving a total of 15 techniques; the performances of which were compared by statistical analyses.

The volumes of the 9 and 27 voxel regions (~1 ml and ~2.7 ml respectively) are not insignificant relative to the size of small tumours and the smaller lesions used in the phantom studies, and this appeared to be the main limitation of using $Lmax_9$ and $Lmax_{27}$ for maximum lesion uptake. For example, from Figure 5.2, Figure 5.3 and Figure 5.4 it can be seen that the values of the observed contrast using $Lmax_9$ and $Lmax_{27}$ are the same for all volumes greater than or equal to 11.5 ml for FBP (panel f – j).

The calibration curves for CAT_9 and CAT_{27}, Figure 5.4, were almost the same, with only a 2% difference in the constant, a, in the $CAT_{9/27}$ calibration

equations, as listed in Table 5.1. However, comparing IT and FBP there was a greater difference, 13%, between the values of the constant, a, 54 ± 4 and 47 ± 1.6. For the $VCAT_9$ and $VCAT_{27}$ calibrations the same small 2% difference was found , as listed in Table 5.2 and Table 5.3, and this case only 2% difference also between IT (a = 39 ± 2) and FBP (a = 37 ± 1).

For spherical volumes, both CAT_9 and CAT_{27} were able to segment spherical volumes greater than 1.15 ml, for observed contrasts in excess of 2. These methods were unable to segment volumes smaller than 1.15 ml even with high contrast, because the low background level has been included in the 9 and 27 voxel regions reducing the $Lmax_9$ and $Lmax_{27}$., thereby artificially reducing the value of C_o. Otherwise, the CAT_9 and CAT_{27} were sufficiently accurate for the purpose of radiotherapy treatment planning, as shown in Figure 5.7 and Figure 5.8. The results of the $VCAT_9$ and $VCAT_{27}$ for determining spherical lesion volumes were even better than for $CAT_{9/27}$, especially in the case of IT reconstruction. $VCAT_9$ and $VCAT_{27}$ were accurate over a wider range than CAT_9 and CAT_{27}, accurately segmenting all volumes down to the smallest sphere, 0.53 ml, at all acquisition times including t_{AC} = 1 min.

For the irregular volumes, the application of the CAT_9 and CAT_{27} were better in IT than in FBP. The method tended to segment the top-hat volumes more accurately than the crescent volumes, as shown in Figure 5.17 and Figure 5.18. This may be due to the more extreme complexity of the crescent volume than the top-hat. Which could results in locating the maximum, and hence the 9 and 27 voxels regions, near or next to the background or the inner cylinder which contains a different activity, thereby artificially affecting C_o. As with spherical lesions, for irregular volumes $VCAT_9$ and $VCAT_{27}$ were

better than the $CAT_{9/27}$ techniques. The $VCAT_{27}$ was able to segment the irregular volumes except the smallest crescent volume, for the same reasons given above for $CAT_{9/27}$. However, surprisingly $VCAT_9$ performed better on FBP images than IT, being able to segment all the irregular volumes, including the smallest.

Concordance measurements also revealed that $VCAT_9$ and $VCAT_{27}$ were better than CAT_9 and CAT_{27}. The Euclidean distance transformation revealed that the distances between the surfaces of the true and segmented volumes using both $VCAT_{9/27}$ and $CAT_{9/27}$ on FBP images tended to bias towards the positive distance, i.e. segment a larger volume, whereas on IT images there was no such bias and the distances were normally distributed.

The statistical analyses in the spherical and irregular lesions, comparing five techniques of using $Lmax_9$ ($VCAT_9$, CAT_9, $VCAT_9$-60, CAT_9-60, $40\%_9$) and $Lmax_{27}$ ($VCAT_{27}$, CAT_{27}, $VCAT_{27}$-60, CAT_{27}-60, $40\%_{27}$) revealed a different ranking orders, but the lowest and highest were the same for both spherical and irregular lesions: $VCAT_{9/27}$ had the lowest (best) rank and $40\%_{9/27}$, had the highest (worst) rank value.

The statistical analyses of all fifteen techniques in spherical lesions revealed that $VCAT_1$ was always ranked lowest, and is therefore the best technique. Similar findings were found for all irregular lesions combined, for crescent lesions alone, with $VCAT_1$ having the lowest rank, but for the top-hat lesions alone, CAT_1 had the lowest rank, but there was not a statistically significant difference between it and the next ranked technique, $VCAT_1$.

Therefore, $VCAT_1$ has proven to be the best overall technique.

6

Chapter 6:

PRELIMINARLY INVESTIGATION IN PATIENTS

6.1. Introduction

Having proven the accuracy of the newly developed PET/CT segmentation techniques, VCAT and CAT*, in spherical and irregular lesions phantoms, the next stage was to investigate their application to real patient situations. The main aim of was to carry out a preliminary evaluation in comparison to the current best practice, which is manual delineation on the PET/CT image set by an experienced radiologist. Comparison was also made with manual delineation by the clinical oncologist.

* Note that from this point onwards, VCAT and CAT refer to the instances defined in the previous chapter as $VCAT_1$ and CAT_1.

Among the published studies of delineating the GTV on PET, most interest has been regarding NSCLC where the use of FDG PET/CT has been shown to be relevant both in tumour staging and in target volume delineation [118-122]. Similar results have been found in head and neck cancers with FDG PET/CT demonstrating improved definition of primary disease and nodal areas [74, 123, 124]. Generally, it has been shown that the use of PET allows consideration of treatment areas beyond merely defining the target volume for the primary lesion.

Many processes and stages are required to establish the use of PET in RTP, including positioning the patient for imaging in the radiotherapy treatment position, defining lesion outlines in the treatment planning system, and applying radiation beams to the plan. Ideally, PET imaging requires the patient to lay down in the radiotherapy treatment position, which requires immobilization devices and an iso-centric external laser light with a motorized sagittal laser alignment. The time period taken to accomplish the whole scan is crucial because for the purpose of the RTP a whole-body image set is not required and the lesion area is the most important. Therefore, rather than carrying out a full whole body scan, only one to two bed positions may be enough to cover the whole lesion area, reducing the scanning time significantly, and thereby minimising the chance of patient movements between the CT and PET images [125]. After imaging, the reconstructed images are usually held on the PET scanner computer ready to be transferred to the treatment planning system or to any other computer to undergo any desired image processing. There are many different scenarios that could be employed in these stages in order to reproduce the lesion outline delineation from the PET scan on the treatment planning system.

Tumour delineation techniques in PET are associated with a number of limitations not due to the technique itself, such as the normal variance in FDG uptake, or lesion motion due either to respiratory movements or the absence of the immobilization devices. There are also some practical difficulties due to the use of either flat or curved couch tops, the possibility of movement between the CT and the PET scan, and the difference in speed of acquiring the CT and the PET scan with the potential to acquire the images in different respiratory phases.

In this chapter, head and neck (H&N) and non-small cell lung cancer (NSCLC) patients were investigated using the VCAT and CAT PET semi-automated segmentation techniques. Section 6.2 describes the methodology and the scenario used to investigate the accuracy of the VCAT and CAT method in these patients. Section 6.3 describes the results of these investigations, with discussion in section 6.4, and conclusions in section 6.5.

6.2. Methodology

The main difficulty in validating any PET segmentation technique in patient studies is the absence of gold standard which is the true lesion boundary and volume size. To overcome this obstacle, the VCAT and CAT segmented volumes in patients were compared with the tumour outlines drawn manually by both an experienced radiologist on the PET images (radiologist-delineation), and tumour outlines drawn manually by an experienced clinical oncologist on the CT images (oncologist-delineation).

As a preliminary study, the VCAT and CAT methods were evaluated in two head and neck (H&N) and two NSCLC patients. For the H&N patients, the

radiologist and oncologist delineated the GTV and any PET positive lymph nodes. For the NSCLC patients, however, the radiologist and oncologist delineated only the GTV, because in this case the lymph nodes are usually some distance from the GTV, which is not so in H&N patients. In The Christie PET/CT department, all patients are routinely scanned on a couch with a flat top identical to that used for radiotherapy.

In order to eliminate any errors associated with the image registration between PET/CT and the planning CT scan, the CT component of the PET/CT scan was used instead of the one used for radiotherapy treatment planning. Only those PET slices that covered the lesion area were selected, and these were transferred to a personal computer that has the IDL program for VCAT/CAT segmentation, where the VCAT and CAT delineations as well as the radiologist-delineation were carried out. The CT component of PET/CT was transferred to the Pinnacle treatment planning system where the oncologist-delineation was carried out.

6.2.1. VCAT and CAT

The tumour loose regions required to start the VCAT and CAT techniques were drawn by an experienced radiologist. The resulting segmented regions were then written to a binary interfile format readable by the Pinnacle treatment planning system. These binary files consist of a header file that contains the patient and image metadata and an image file that contains the images. These files were then transferred to the treatment planning system and the outlines of the lesions were reproduced in the Pinnacle treatment planning system.

6.2.2. Radiologist-Delineation

An experienced radiologist reviewed the PET images for each individual patient and manually delineated the outlines of each lesion by drawing a 2D outline slice by slice, and the stack of 2D outlines were used to form the 3D radiologist delineated volume.

6.2.3. Oncologist-Delineation

The CT image component of the PET/CT scan was transferred to the Pinnacle treatment planning system using the DICOM image import option. The oncologist delineated the GTV on these CT images taking into account all the available information whether from the PET/CT or any anatomical abnormality. In this way clinical oncologist delineated the GTV exactly as would happen in routine practice.

6.2.4. Impact of Loose Region Definition in Multiple Lesions

For the patients with more than one lesion (e.g. primary tumour and lymph nodes) two VCAT/CAT segmented volumes were produced: i) using a single loose region that encompassed all lesions, or ii) separate loose regions for each lesion and then combining the segmented volumes into a single binary image file.

6.3. Results

6.3.1. Head and Neck Patients

6.3.1.1. Comparison of VCAT/CAT with radiologist outlines

Figure 6.1 and Figure 6.2 show the lesion outlines delineated for the H&N cases by the radiologist-delineation (green) and by VCAT and CAT. The slices shown in these figures were a carefully selected subset of the full image set, chosen to show where the main differences occurred. Generally, the figure demonstrates that there was better agreement between the VCAT and CAT segmented volume in the first H&N case compared with the second case. Also, VCAT/CAT and the radiologist were in closer agreement in the central than in the peripheral slices.

In Figure 6.2 it can be seen that neither VCAT nor CAT segmented the two peripheral slices (slice 1 and 16) which were drawn by the radiologist. The figure shows also that the radiologist outline is generally larger than the VCAT/CAT outline in all slices.

The observed contrasts, C_o, for H&N case one and case two were 11 and 18 respectively. The resulting VCAT and CAT optimum thresholds in case one were 39.9% and 40.3% respectively, while in case two were 39.3% and 39.4% respectively.

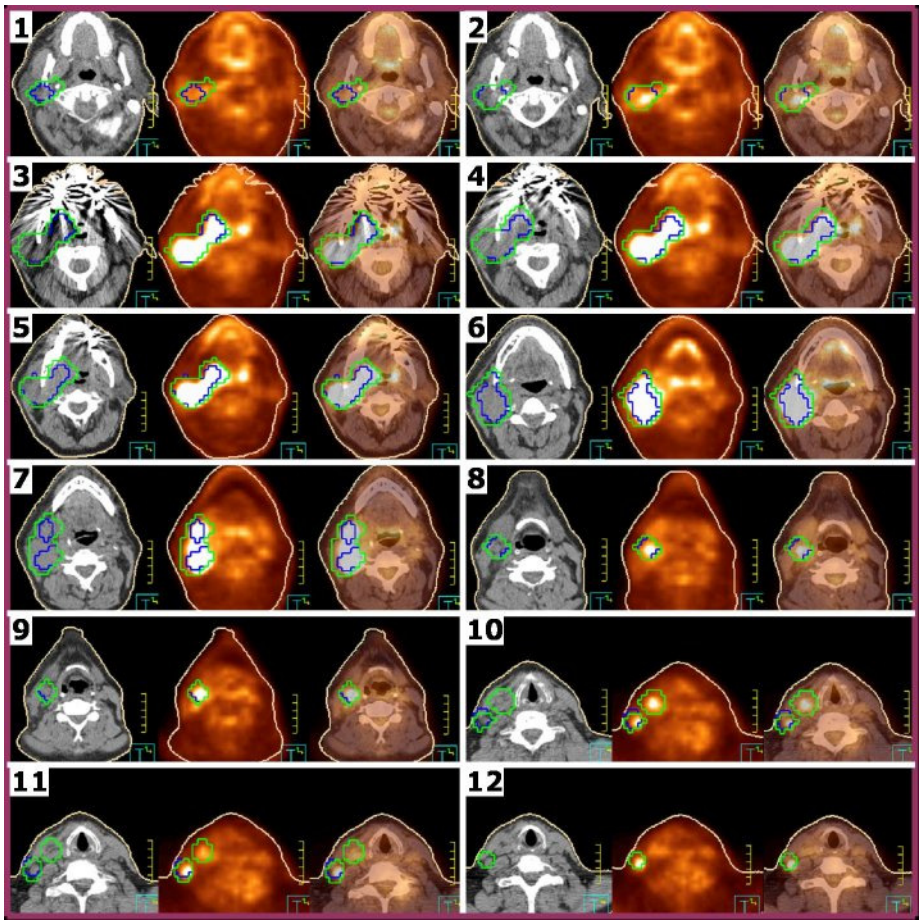

Figure 6.1: A series of CT, PET, and fused PET/CT transaxial slices for H&N case one showing the radiologist-delineation (green), the VCAT delineation (blue) and the patient's outline (light-brown). Note that because the VCAT delineation is overlapping the CAT delineation (light-blue) in all slices, it cannot be seen.

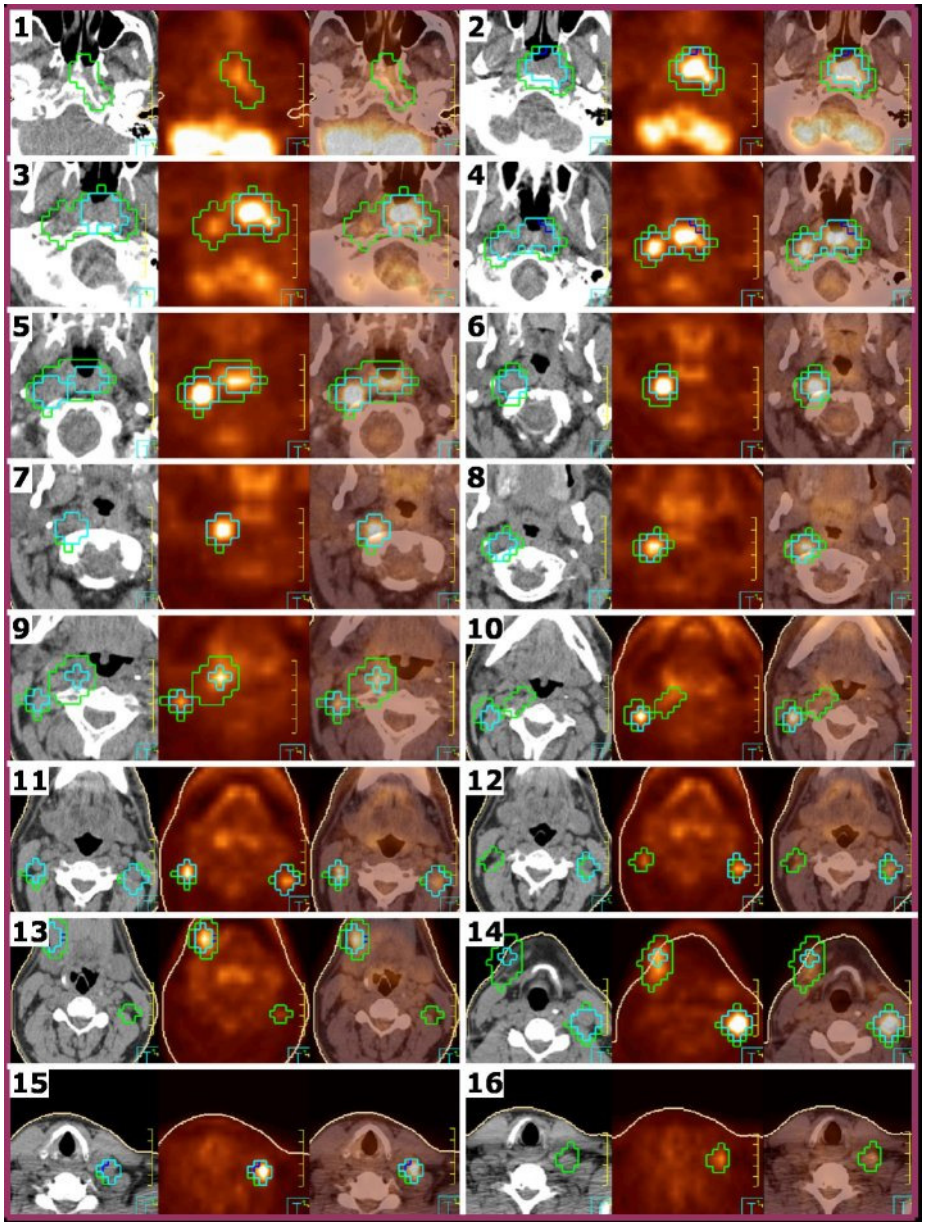

Figure 6.2: A series of CT, PET, and fused PET/CT transaxial slices for H&N case two showing the radiologist-delineation (green), the VCAT delineation (blue), the CAT delineation (light-blue) and the patient's outline (light-brown). Note that where the CAT delineation is overlapping the VCAT delineation (in most of the slices), it cannot be seen.

Figure 6.3 shows the nearest distance between the surfaces of the radiologist-delineation and the VCAT and CAT delineation. These results show that approximately 86% and 89% of the VCAT/CAT delineation overlapped the

radiologist-delineation within ±2 mm for case one and two respectively, while the corresponding values for perfect overlap are 37% and 41%

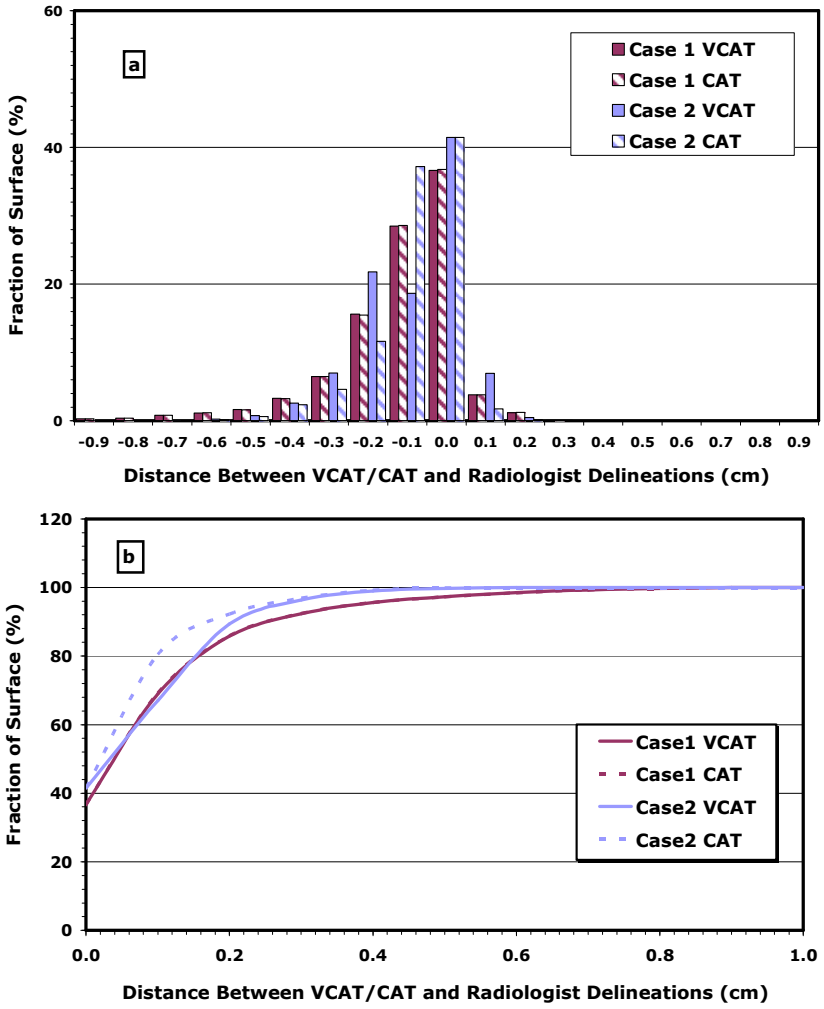

Figure 6.3: Differential (a) and cumulative (b) histograms of the nearest distance between the surface of radiologist-delineation (reference) and the VCAT and CAT delineations for H&N cases one and two using the Euclidean distance transformation.

Table 6.1 summarizes the results of comparing the radiologist-delineation versus VCAT and CAT delineations. There was very little difference between VCAT and CAT in comparison to the radiologist-delineation. There was closer agreement between VCAT/CAT and the radiologist in case one compared with case two, as evidenced by the higher values of DSC and JSC,

and smaller values of % difference. Overall, the radiologist delineations produced larger volume outlines than VCAT/CAT, being 37% in case one and 55% in case two.

H&N Patient	Radiologist-delineation (ml)	VCAT / CAT Delineations (ml)	Difference (%)	DSC	JSC
1	142.34	89.92	36.83	0.66	0.49
		89.73	36.96	0.66	0.49
2	108.00	47.95	55.60	0.40	0.25
		49.03	54.60	0.51	0.35

Table 6.1: Summary of the results of comparing the radiologist-delineation with the VCAT and CAT delineations for the two H&N patients with the Dice and Jaccard similarity coefficients.

6.3.1.2. Comparison of VCAT/CAT with oncologist outlines

Figure 6.4 and Figure 6.5 show the lesion outline comparison for H&N case one and two respectively using the oncologist-delineation (red) and the VCAT and CAT delineation. Again, the slices shown were a carefully selected subset of the full image set, chosen to show where the main differences occurred. Similarly to the radiologist-delineation, there is a good agreement in the middle slices between the oncologist-delineation and VCAT/CAT delineations. There is less agreement in the inhomogeneous neck lesion in case one where the VCAT and CAT techniques segmented a smaller lesion, seen in Figure 6.4 slices 8-10. Due to the large PET pixel size, the VCAT and CAT methods failed to follow the curvature of the anatomical structure of the mandible, as can be seen in slices 3-6.

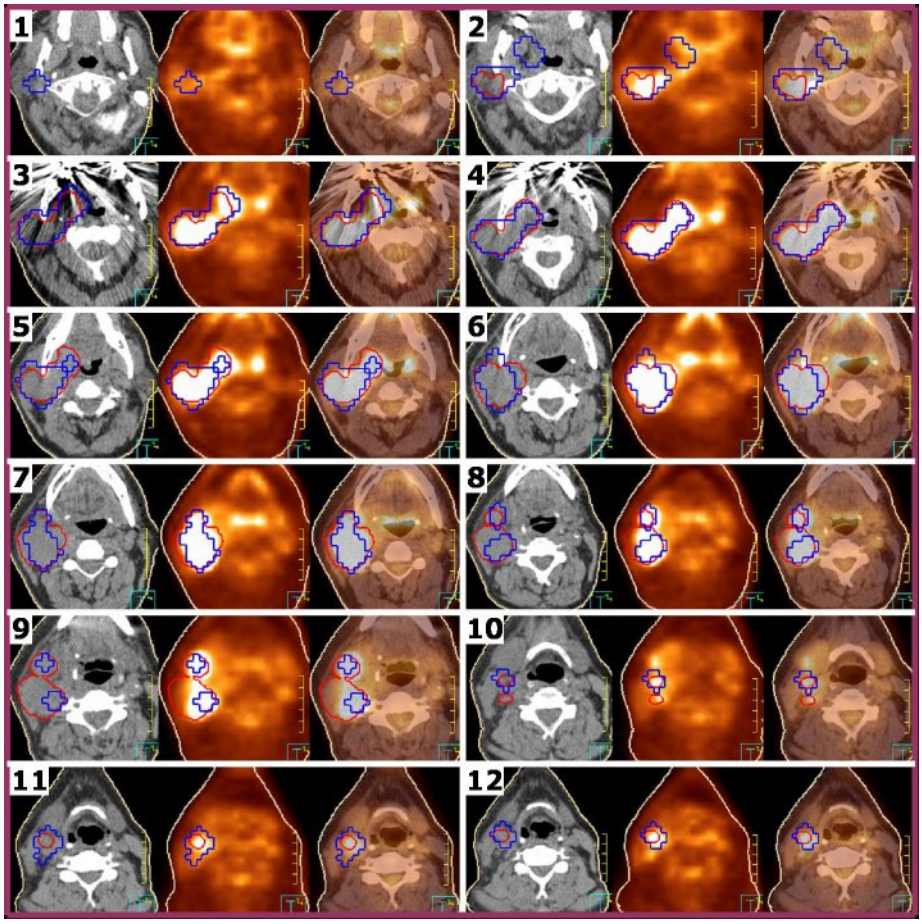

Figure 6.4: A series of CT, PET, and fused PET/CT transaxial slices for H&N case one showing the oncologist-delineation (red), the VCAT delineation (blue) and the patient's outline (light-brown). The VCAT is overlapping the CAT delineation (light-blue) in all slices therefore is not present.

In the second H&N case which is presented in Figure 6.5, both the VCAT and CAT methods failed to segment the small lesion delineated by the oncologist presented in slice 1. It is apparent from the PET image that this lesion has a low uptake, confirmed by the measured contrast, C_o, which was approximately 3. This also happened also in the small lesion on slice 3.

Case two also represents on of the expected limitations which is the patient movement between the CT and PET elements of the PETCT scan. This effect is apparent in slice 12 of Figure 6.5 where the oncologist has delineated

outlines that were not apparent on the PET images, and slice 14 where VCAT/CAT produced an outline on at the periphery of the lesion that was not apparent on the CT image. The movement appears to have been with the patient mandible having moved between the PET and CT acquisitions.

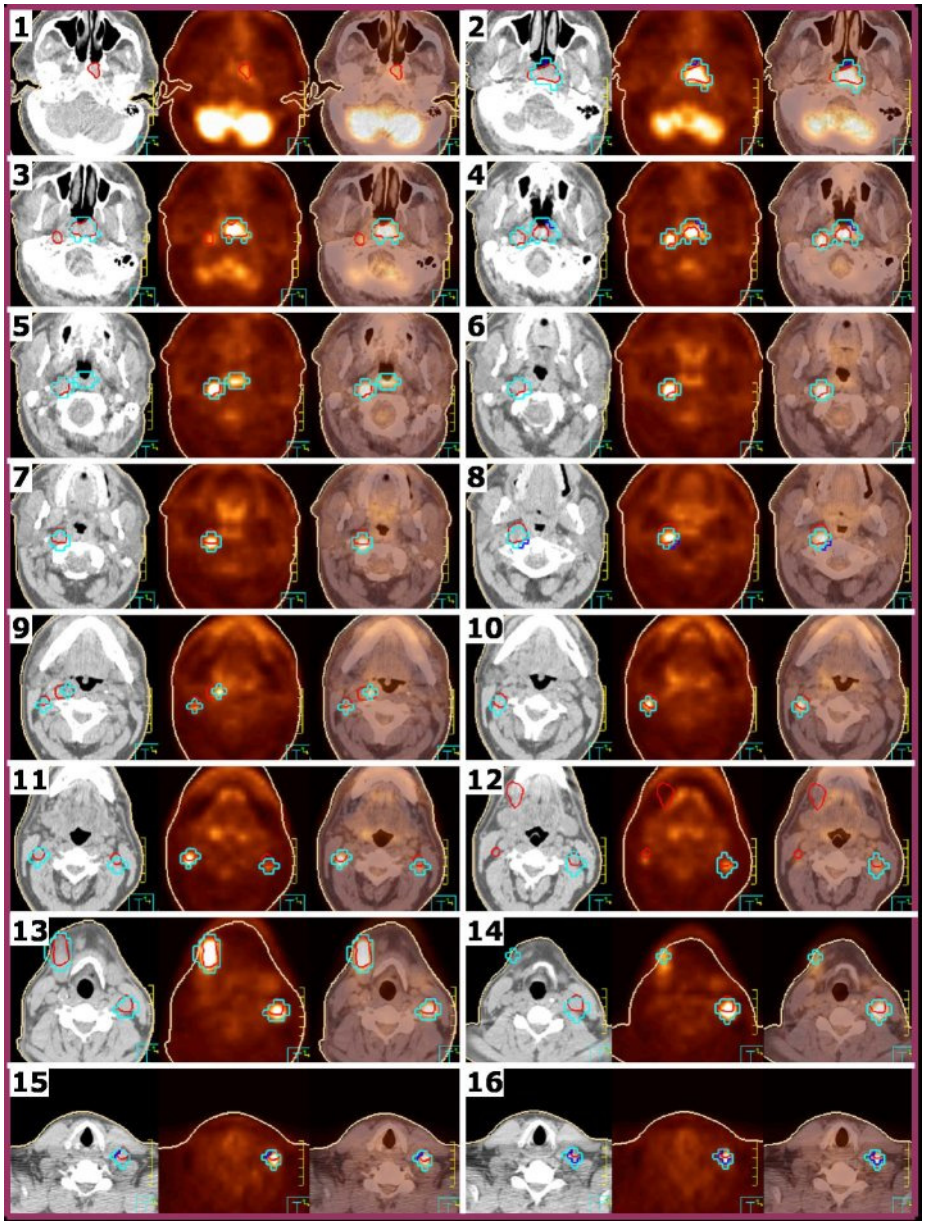

Figure 6.5: A series of CT, PET, and fused PET/CT transaxial slices for H&N case two showing the oncologist-delineation (red), the VCAT delineation (blue), the CAT delineation (light-blue) and the patient's outline (light-brown). Note that the CAT delineation is overlapping the VCAT delineation in most of slices therefore is not present.

Figure 6.6 shows histograms for the nearest distance between the surfaces of the oncologist-delineation and VCAT/CAT delineations. Although the CAT delineation in case two recorded the highest overlap with 67 % within ± 2mm, the results of case one were better than case two with 70 % within ± 2mm. Also, the results of case one were more centred on zero distance, while in case two it was more biased to the positive distance.

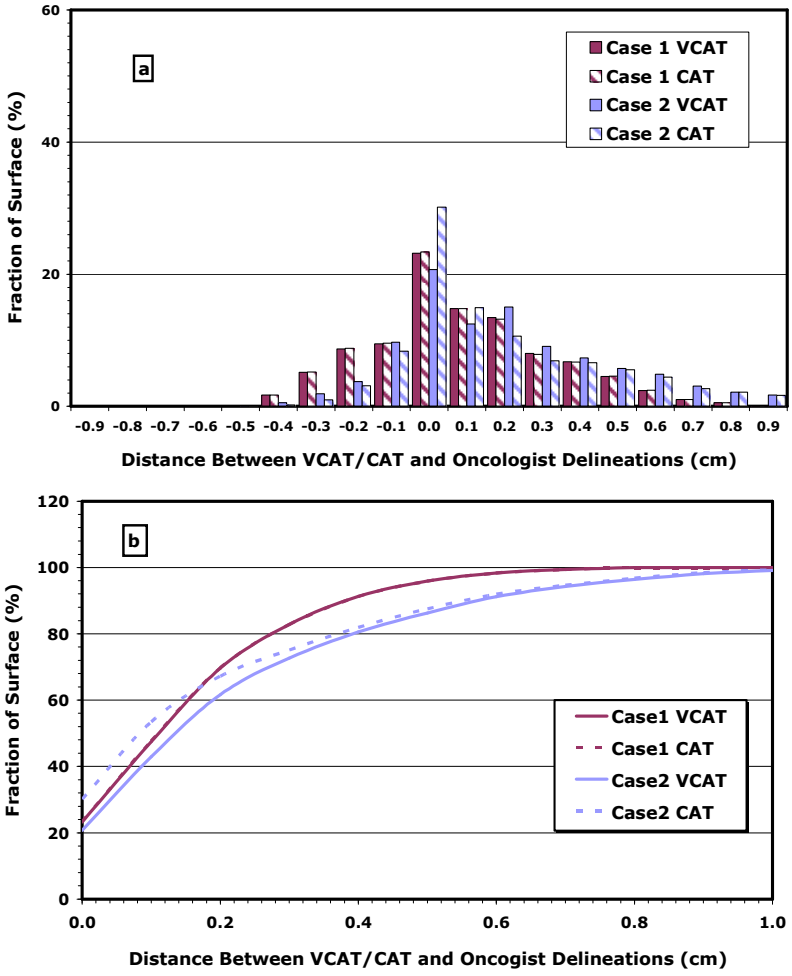

Figure 6.6: Differential (a) and cumulative (b) histograms of the nearest distance between the surface of oncologist-delineation (reference) and the VCAT and CAT delineations for H&N cases one and two using the Euclidean distance transformation.

Table 6.2 summarizes the results of comparing the oncologist-delineation versus VCAT and CAT delineations. The recorded percentage

differences in this comparison were the lowest among the previously recorded differences. It also shows that the VCAT method has produced a lower percentage difference than the CAT method in both cases. Moreover, the recorded DSC and JSC were the highest among the previous comparison. In case one, the oncologist delineation agreed extremely well with VCAT/CAT with 0 % difference in volume size; DSC = 0.76 and JSC = 0.61. However in case two the oncologist and VCAT/CAT delineations differed considerably, the former producing a volume approximately 33% smaller than VCAT/CAT.

H&N Patient	Oncologist-delineation (ml)	VCAT / CAT Delineations (ml)	Difference (%)	DSC	JSC
1	89.94	89.92	0.02	0.76	0.61
		89.73	0.23	0.76	0.61
2	36.44	47.95	31.59	0.53	0.36
		49.03	34.55	0.61	0.44

Table 6.2: Summary of the results of comparing the oncologist-delineation with the VCAT and CAT delineations for the two H&N patients with the Dice and Jaccard similarity coefficients.

6.3.1.3. Comparison of oncologist and radiologist outlines

Figure 6.7 and Figure 6.8 show the lesion outlines manually delineated on the two H&N cases by the radiologist-delineation (green) and the oncologist-delineation (red). As apparent from all slices, the radiologist-delineation was always larger than the oncologist-delineation. Although this may in part be due to the larger pixel size in PET compared with CT, the primary factor was in differences of opinion in deciding on the location and extent of tumour tissue.

The effect of movements between the CT and PET elements of the PET/CT scan is also apparent in this comparison. As apparent from slices 12, 13 and 14, there is a mismatch between the PET and CT in the mandible region. This movement did not only cause a mismatching between the two images but also a difference in lesion delineation by the radiologist and oncologist. This difference is clear in slice 12 where the oncologist delineates an outline which is not apparent in PET, and also in slice 14 where the radiologist delineates an outline which was not apparent on the CT.

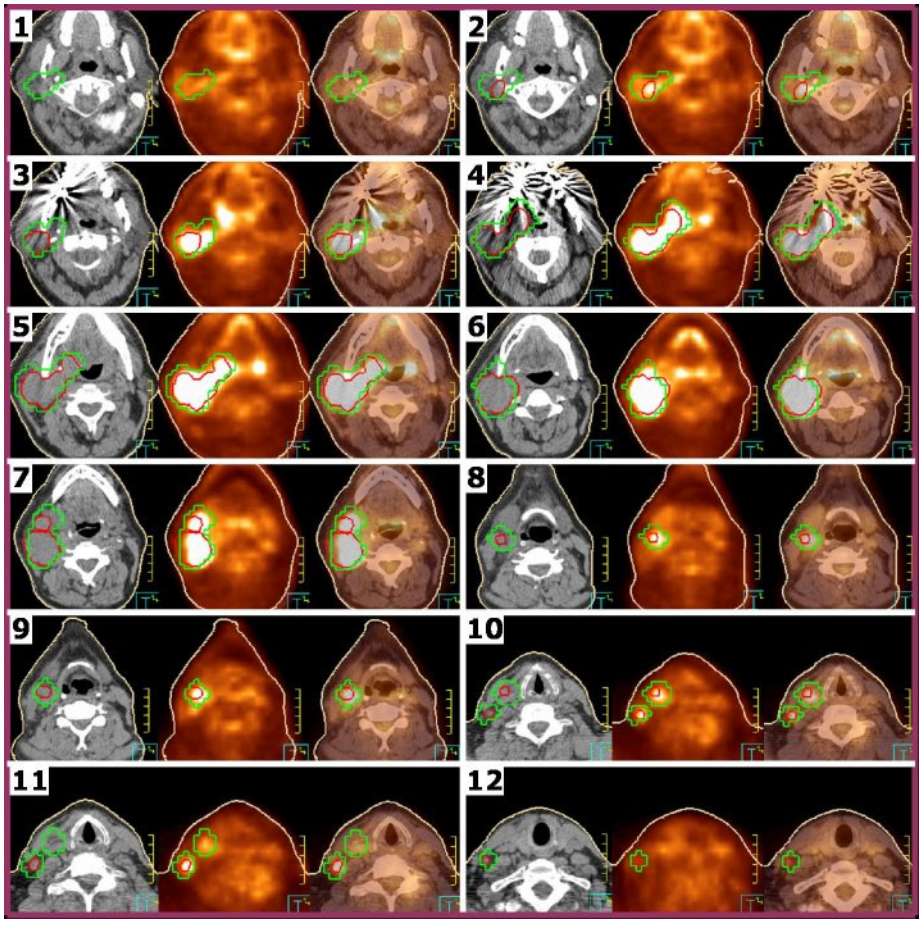

Figure 6.7: A series of CT, PET, and fused PET/CT transaxial slices for H&N case one showing the radiologist-delineation (green), oncologist-delineation (red) and the patient's outline (light-brown).

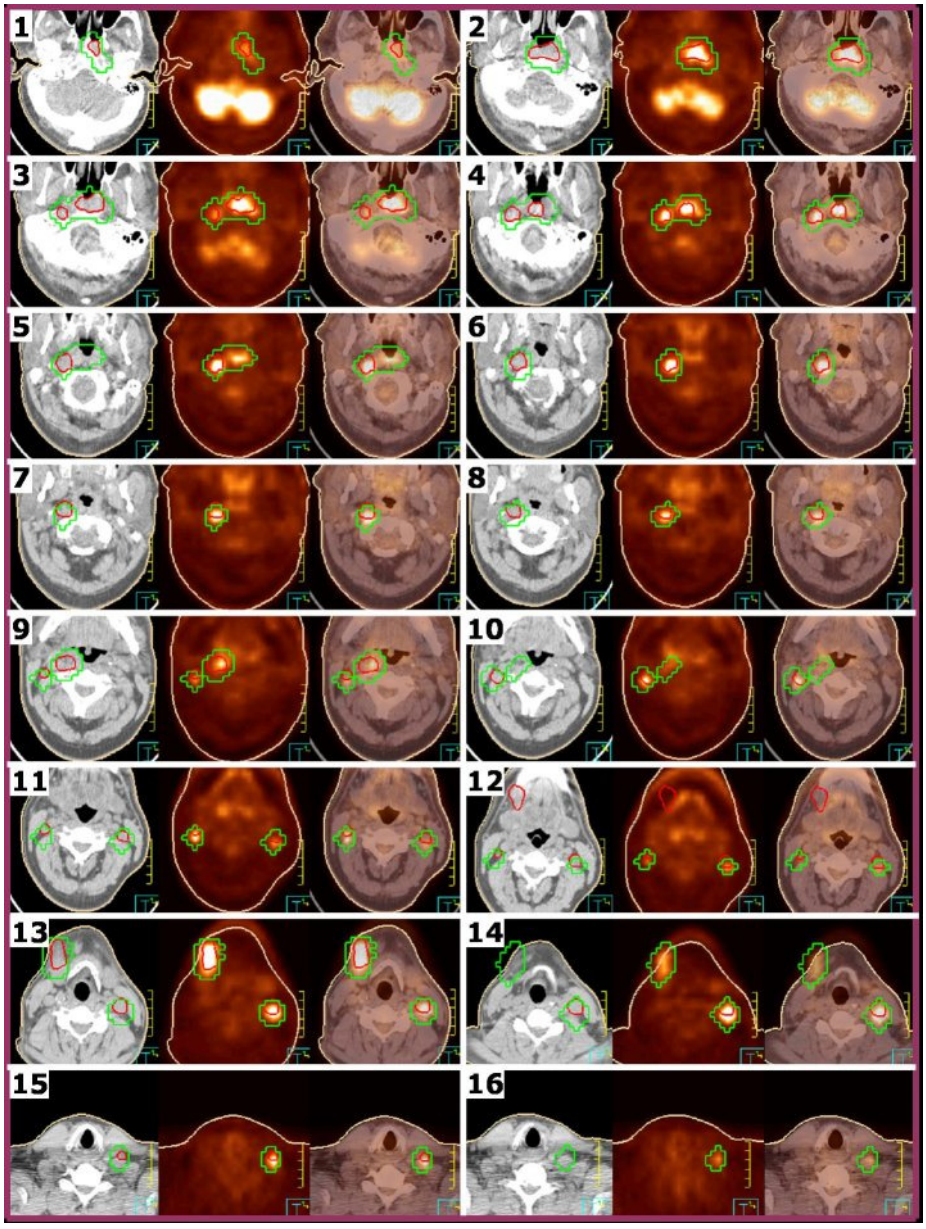

Figure 6.8: A series of CT, PET, and fused PET/CT transaxial slices for H&N case two showing the radiologist-delineation (green), oncologist-delineation (red) and the patient's outline (light-brown).

Figure 6.9 shows the nearest distance between the surfaces of the radiologist-delineation and oncologist-delineation. It can be seen that approximately 67 % and 85 % of the VCAT/CAT delineation overlapped the radiologist-delineation within ±2 mm for case one and two respectively, while the corresponding values for perfect overlap are 23% and 35%.

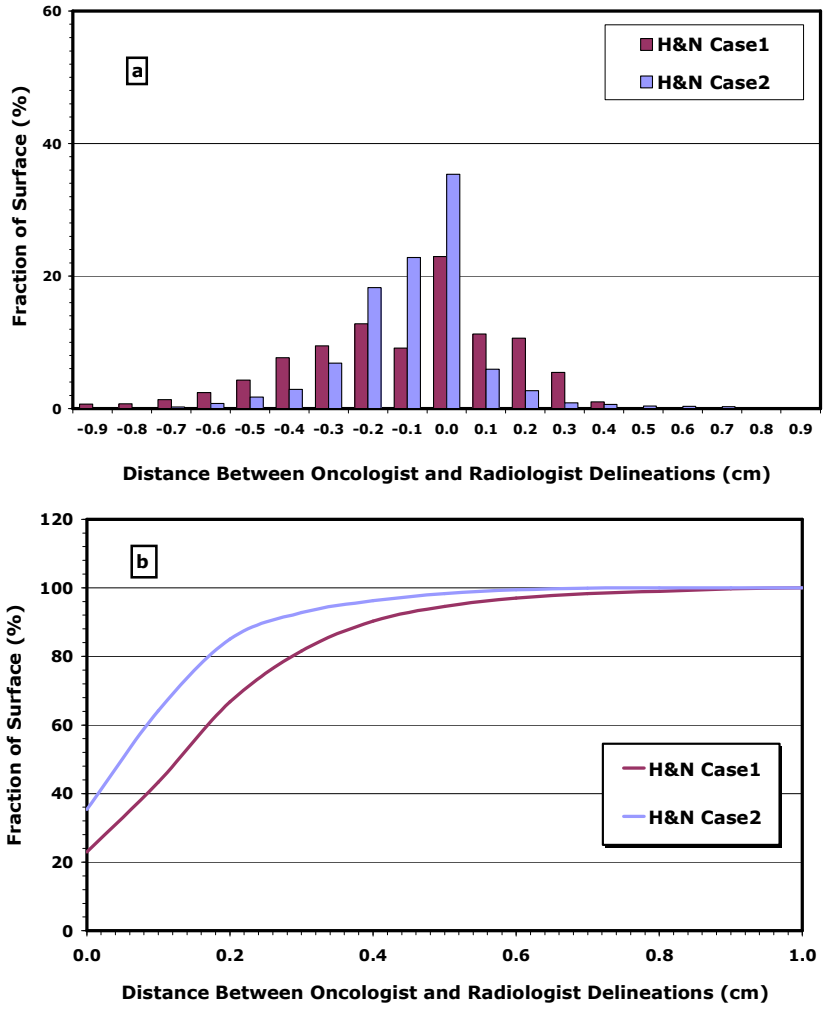

Figure 6.9: Differential (a) and cumulative (b) histograms of the nearest distance between the surface of radiologist-delineation (reference) and oncologist-delineation for H&N cases one and two using the Euclidean distance transformation.

Table 6.3 presents the results of comparing the radiologist-delineation with the oncologist-delineation. These results demonstrate that the radiologist has delineated a larger volume than the oncologist. The difference between these two volumes was increased by decreasing the oncologist-delineation. The DSC and the JSC as well as the percentage difference showed that there was a better agreement in delineating the H&N case one than case two.

H&N Patient	Radiologist-delineation (ml)	Oncologist-delineation (ml)	Difference (%)	DSC	JSC
1	142.34	89.94	36.81	0.64	0.47
2	108.00	36.44	66.26	0.48	0.32

Table 6.3: Summary of the results of comparing the radiologist-delineation with the oncologist-delineation for the two H&N patients, and the corresponding Dice and Jaccard similarity coefficients.

6.3.1.4. Impact of combining multiple regions

All the results presented in the previous comparisons were based on the same strategy used in phantoms which was using an individual loose region for each lesion and then combining the segmented volumes in a single file. However, it is common in H&N patients for there to be more than one lesion, requiring the delineation of more than one region of interest. In this section, a comparison is made of the use of VCAT/CAT in the two studied H&N patients with either a single loose region encompassing all areas of uptake, or a loose region drawn on each separate area of uptake.

The outlines for H&N case one are shown in Figure 6.10. The figure shows pairs of PET images for the same slice with the background loose region (pink), the different lesions loose regions (yellow, grey and orange), the single loose region that encompass all lesions (yellow) outlines and the corresponding VCAT delineation for each loose region method (blue and purple respectively). For the single loose region method the calculated contrast, C_o, was 18. For the multiple loose region method there were three

loose regions, with calculated contrasts of 14, 6 and 5. However, both loose region methods the VCAT and CAT outlines were identical.

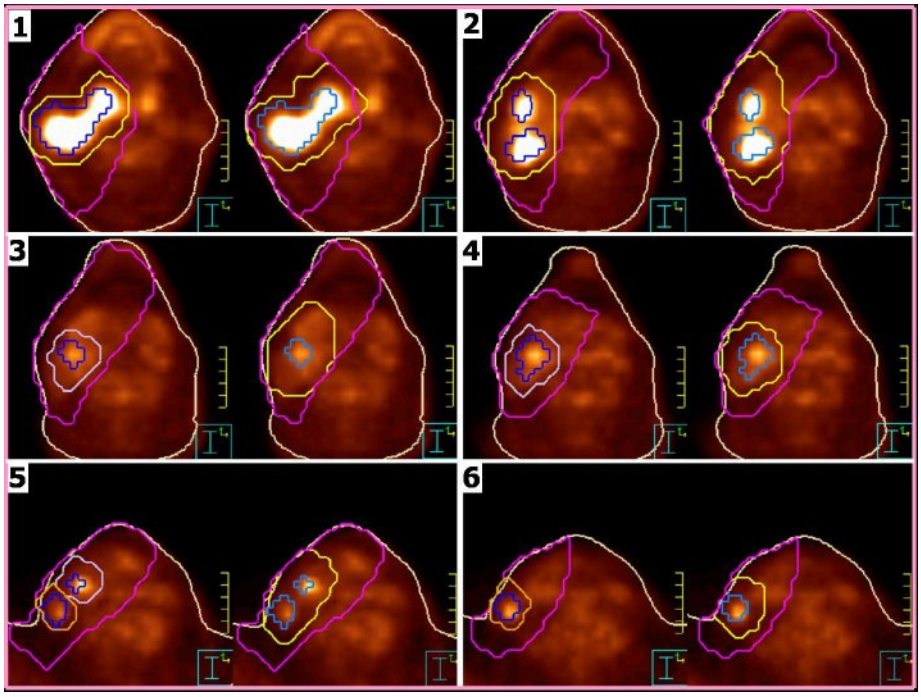

Figure 6.10: Pairs of PET images for the same slice in H&N case one showing the patient's outline (brown), the background loose region outlines (pink), the different lesions loose regions (yellow, grey and orange) in the right-hand image, the single loose region that encompass all lesions (yellow) in the left-hand image and the corresponding VCAT delineation for each loose region method (blue and purple respectively).

The outlines for H&N case two are shown in Figure 6.11. The figure shows pairs of PET images for the same slice with the background loose region (pink), the different lesions loose regions (yellow, grey and orange, green, and dark: yellow, orange, grey), the single loose region that encompass all lesions (yellow) outlines and the corresponding VCAT/CAT delineation for each loose region method (light-blue and dark-purple respectively). For the single loose region method the calculated contrast, C_o, was 11. For the multiple loose region method there were seven loose regions, with calculated contrasts of 15, 14, 14, 13, 12, 10 and 6. In this case, for the

two loose region methods the VCAT and CAT outlines were identical except for a single voxel in one of the areas of FDG uptake, as shown in a magnified view of slice 1 in Figure 6.12.

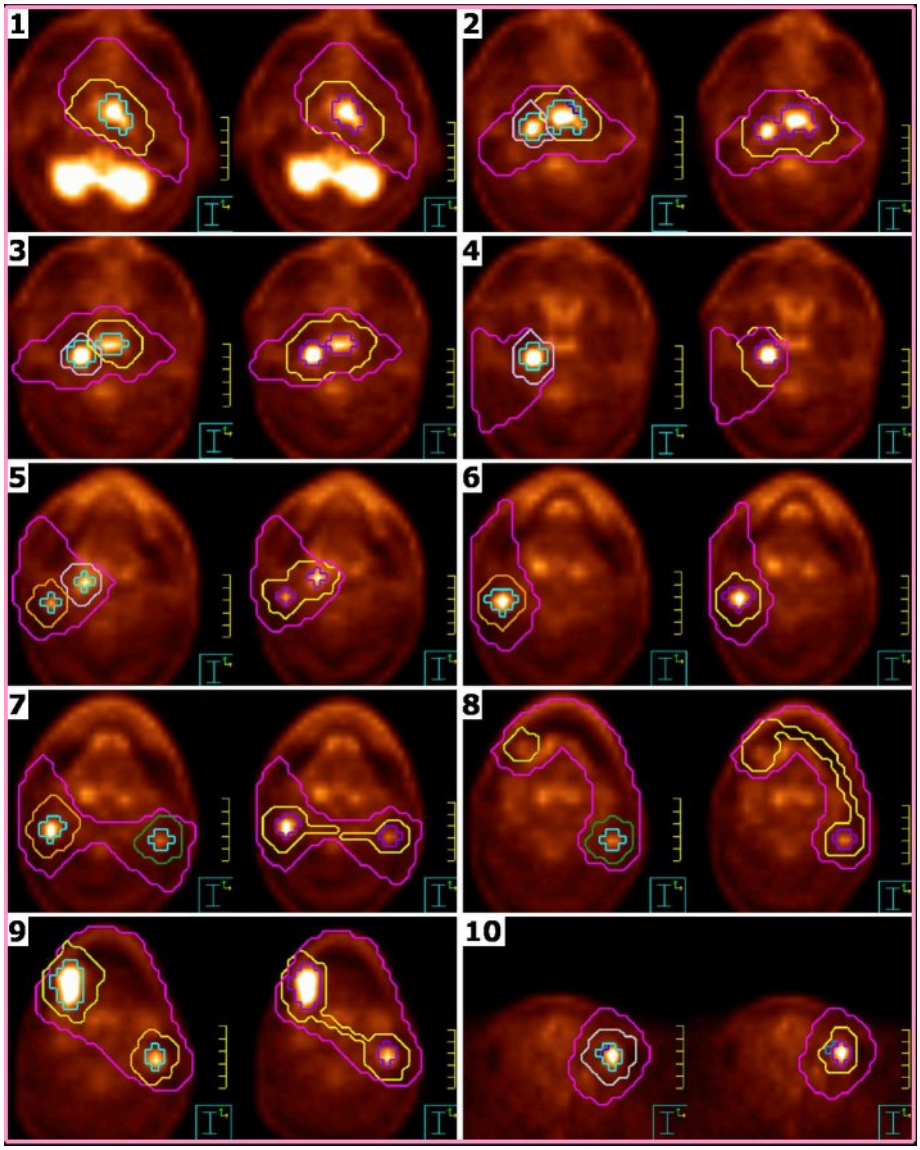

Figure 6.11: Pairs of PET images for the same slice in H&N case two showing the background loose region outlines (pink), the different lesions loose regions (yellow, grey and orange, green, and dark: yellow, orange, grey) in the right-hand image, the single loose region that encompass all lesions (yellow) in the left-hand image and the corresponding VCAT/CAT delineation for each loose region method (light-blue and dark-purple respectively).

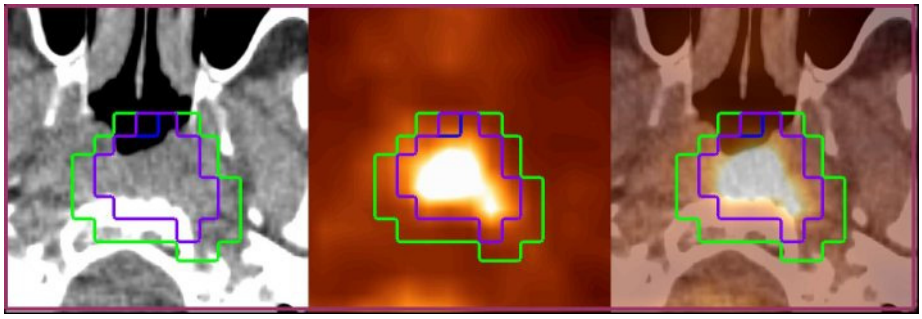

Figure 6.12: CT, PET, and PET/CT slices from the H&N case two showing a one voxel difference in the VCAT delineation using a single loose region (purple), and using individual loose regions for each area of uptake (blue) compared against the radiologist-delineation (green).

6.3.2. Non-Small Cell Lung Patients

6.3.2.1. Comparison of VCAT/CAT with radiologist outlines

Figure 6.13 and Figure 6.14 show the comparison of outlines obtained in the two NSCLC cases using the radiologist-delineation (green), VCAT (blue) and CAT (light-blue). Generally, there was better agreement between the radiologist-delineation and VCAT/CAT delineations in the central lesion slices than in the periphery as can seen in slices 11 and 12 in Figure 6.13, as well as in slices 4 and 5 in Figure 6.14. However, both the VCAT and CAT disagreed with the radiologist-delineation as seen in slices 1-3, 15 and 16 in Figure 6.13 and slices 1 and 7 in Figure 6.14. This difference can be explained as being due to respiratory movement causing blurring around the lesion's boundaries.

The effect of the respiratory movement was apparent in the two NSCLC cases. This effect caused the radiologist-delineation to be larger than the VCAT and CAT delineations because the VCAT and CAT methods did not identify the peripheral blurred area of the lesions.

The observed contrasts, C_o, for NSCLC case one and case two were 22 and 17 respectively. The resulting VCAT and CAT optimum thresholds in case one were 39.1% and 39.2% respectively while in case two they were 40.3% and 39.4% respectively.

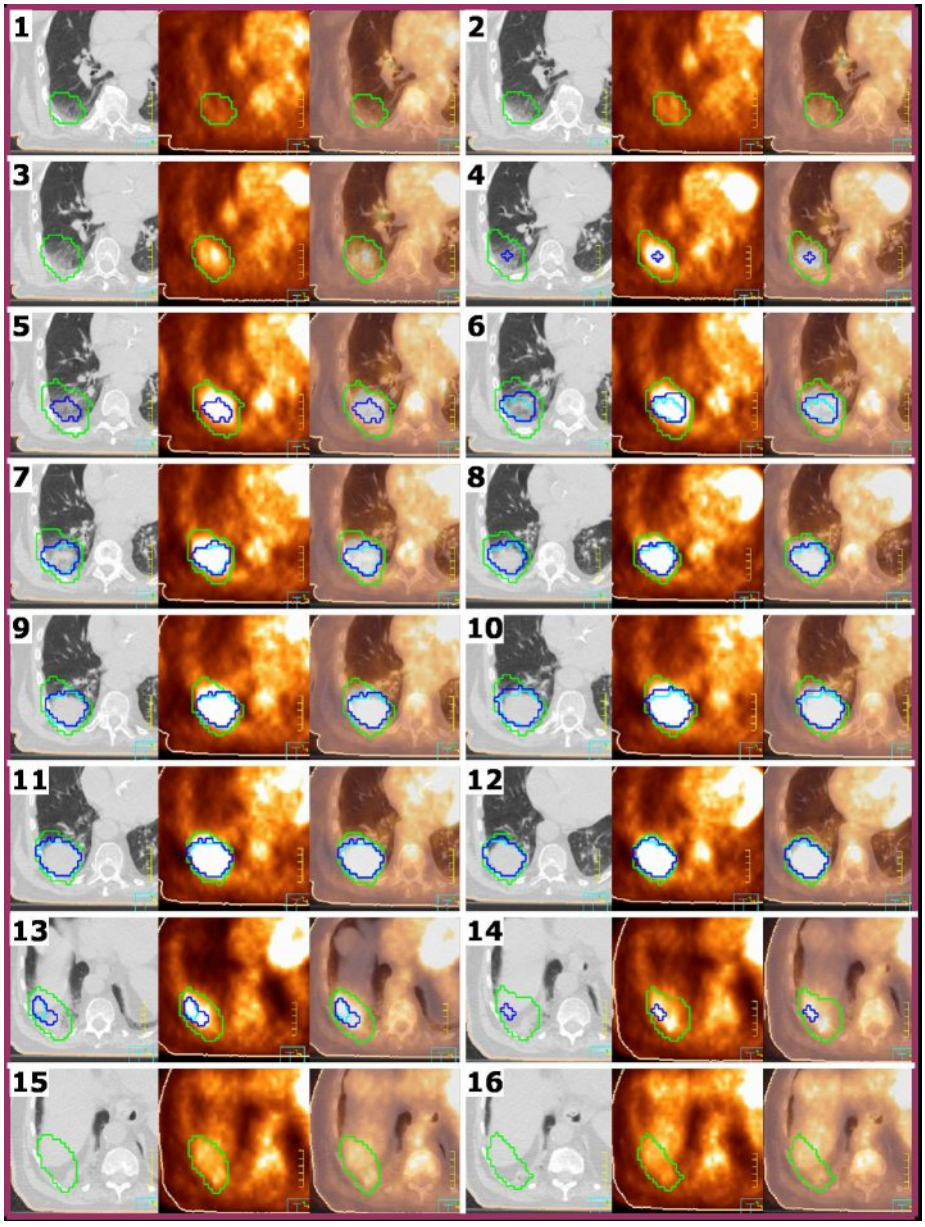

Figure 6.13: A series of CT, PET, and fused PET/CT transaxial slices for lung case one showing the radiologist-delineation (green), the VCAT delineation (blue), the CAT delineation (light-blue) and the patient's outline (light-brown). CAT overlaps the VCAT delineation in a number of slices, and therefore can not be seen.

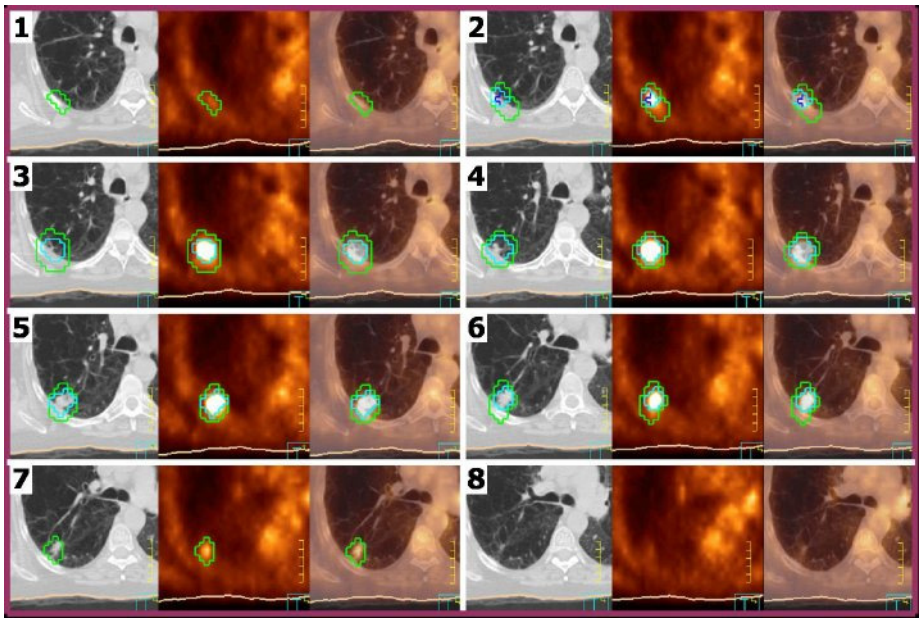

Figure 6.14: A series of CT, PET, and fused PET/CT transaxial slices for lung case two showing the radiologist-delineation (green), the VCAT delineation (blue), the CAT delineation (light-blue) and the patient's outline (light-brown). VCAT is overlapping the CAT delineation in most of slices and therefore is not seen.

Figure 6.15 presents histograms for the nearest distance between the surfaces of the radiologist-delineation and VCAT and CAT delineations for the two NSCLC patients. It is clear from the figure that both VCAT and CAT delineations were generally smaller than the radiologist-delineation without any positive values in the distance histogram. These results show agreement of approximately 40% and 99% within a difference of ±2 mm between the VCAT/CAT outlines and the radiologist-delineation for case one and two respectively, with the corresponding values for complete overlap (zero difference) being 8% and 30%.

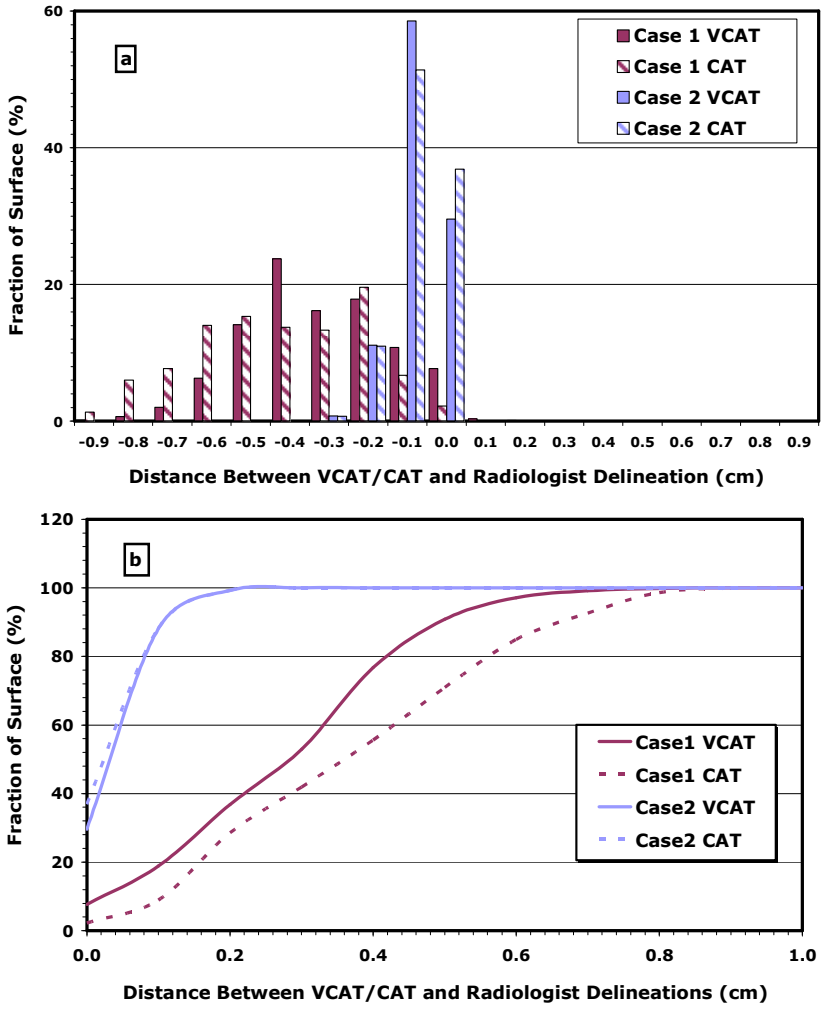

Figure 6.15: Histogram of the nearest distance between the surface of radiologist-delineation (reference) and the VCAT and CAT delineations for lung cases one and two using the Euclidean distance transformation.

Table 6.4 summarizes the results of comparing the VCAT and CAT delineations against the radiologist-delineation. Due to the lesion size for case two being considerably smaller than for case one, case two produced smaller differences in distance between VCAT/CAT and the radiologist compared to case one (as shown in Figure 6.15), whereas the percentage difference in the measured volume was similar.

NSCLC Patient	Radiologist-delineation (ml)	VCAT / CAT Delineations (ml)	Difference (%)	DSC	JSC
1	240.50	105.20	56.26	0.80	0.67
		83.56	65.26	0.78	0.64
2	21.44	7.25	66.18	0.37	0.23
		7.69	64.13	0.40	0.25

Table 6.4: Summary of the results of comparing the radiologist-delineation with the VCAT and CAT delineations for the two NSCLC patients with the Dice and Jaccard similarity coefficients.

6.3.2.2. Comparison of VCAT/CAT with oncologist outlines

Figure 6.16 and Figure 6.17 show the comparison between the oncologist-delineation and VCAT and CAT in NSCLC cases one and two respectively. It is apparent that there is a good agreement in the central slices, especially for the first case. This agreement becomes less in the peripheral slices, such as slices (1-3, 13 and 14) in Figure 6.16 and (1 and 2) in Figure 6.17, where VCAT and CAT segmented a volume which was not delineated by the oncologist; also in slices 6 and 7 in Figure 6.17 where the oncologist has delineated a volume which was not segmented by either VCAT nor CAT techniques.

It is apparent from slice 6 and 7 in Figure 6.17 that both VCAT and CAT failed to segment any voxel in these particular two slices. This is probably due to the low observed contrast in these particular areas compared to the rest of the lesion. This low observed contrast on the periphery of any lung lesion is an expected consequence of motion blurring.

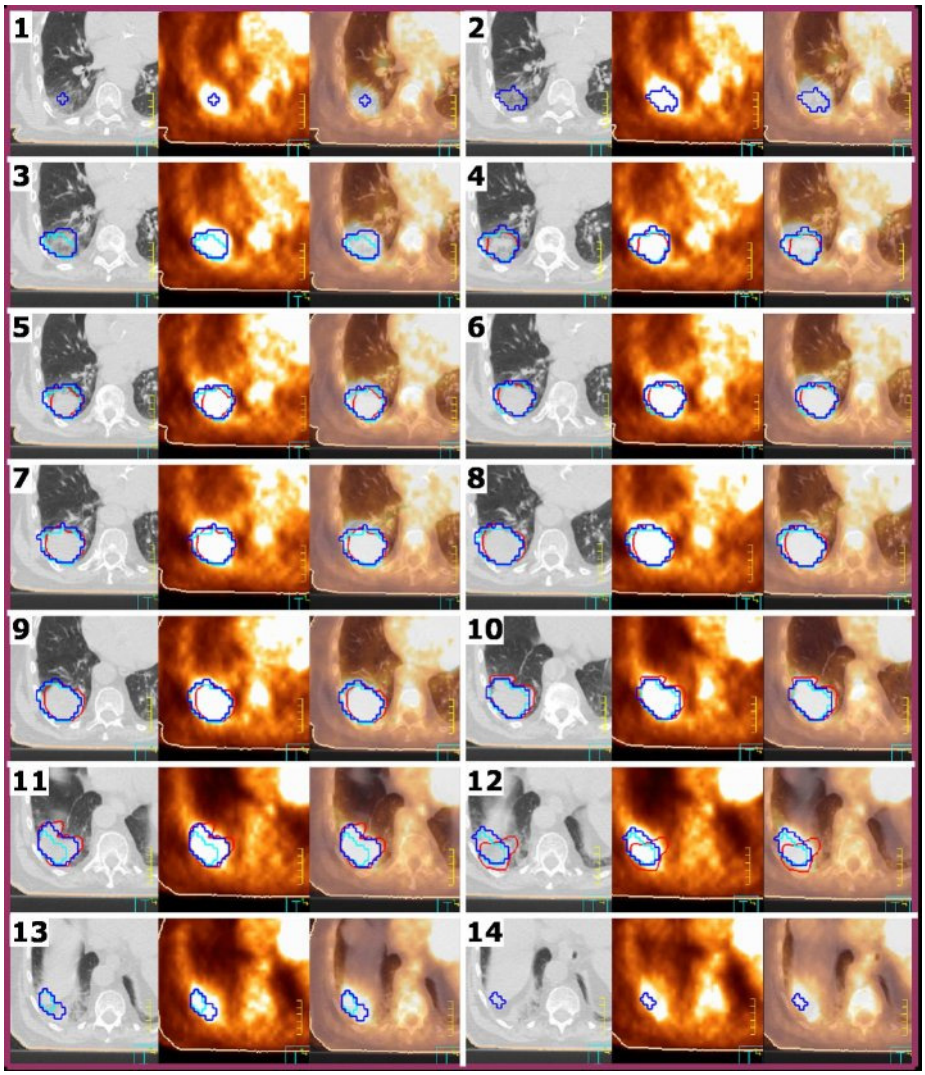

Figure 6.16: A series of CT, PET, and fused PET/CT transaxial slices for lung case one showing the oncologist-delineation (red), the VCAT delineation (blue), the CAT delineation (light-blue) and the patient's outline (light-brown). The CAT is overlapping the VCAT delineation in some slices, where it is therefore not seen.

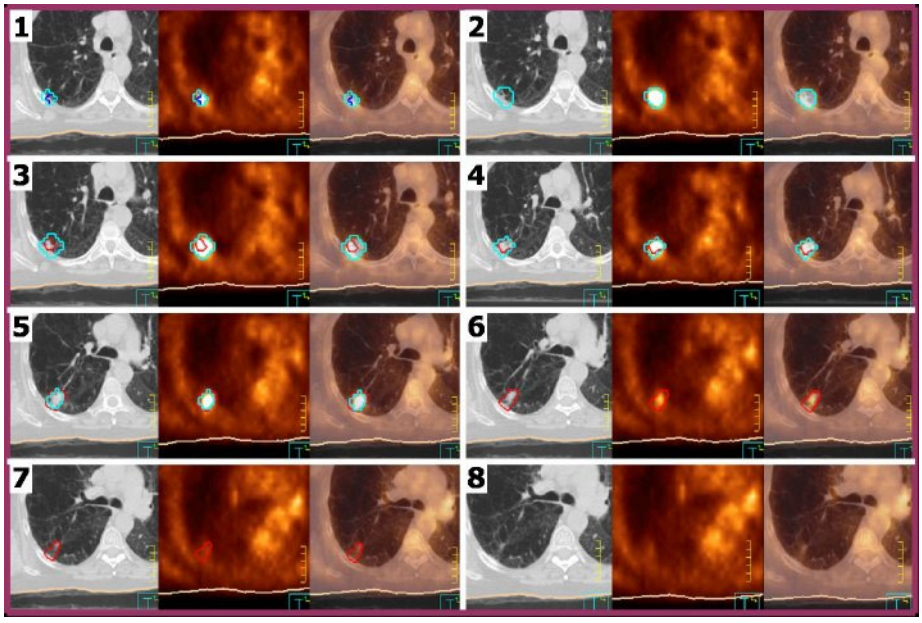

Figure 6.17: A series of CT, PET, and fused PET/CT transaxial slices for lung case two showing the oncologist-delineation (red), the VCAT delineation (blue), the CAT delineation (light-blue) and the patient's outline (light-brown). The VCAT overlaps the CAT delineation in most slices, and therefore can not be seen.

Figure 6.18 shows histograms for the nearest distances between the outlines of the oncologist-delineation and VCAT and CAT methods in the two NSCLC patients. This results show overlap of approximately 92% and 80% were within ±2 mm in cases one and two respectively between the outlines of the oncologist-delineation and VCAT/CAT, while there is approximately 38% and 26% complete overlap (zero distance difference).

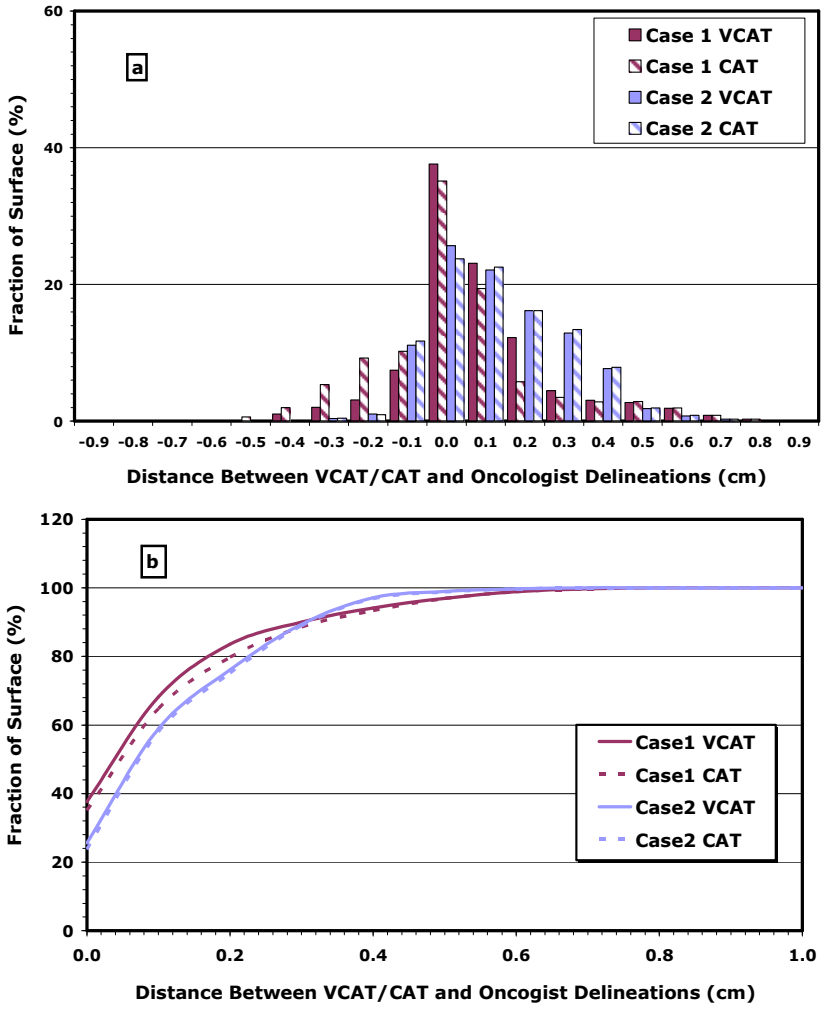

Figure 6.18: Histogram of the nearest distance between the surface of oncologist-delineation (reference) and the VCAT and CAT delineations for lung cases one and two using the Euclidean distance transformation.

Table 6.5 summarizes the results of comparing the VCAT and CAT delineations against the oncologist-delineation in the two NSCLC patients. The percentage differences and the DSC and JSC were much better than those obtained by comparing the VCAT and CAT delineations against the radiologist-delineation.

NSCLC Patient	Oncologist-delineation (ml)	VCAT / CAT Delineations (ml)	Difference (%)	DSC	JSC
1	92.70	105.20	13.48	0.61	0.44
		83.56	9.86	0.52	0.35
2	5.47	7.25	32.54	0.52	0.35
		7.69	40.59	0.54	0.37

Table 6.5: Summary of the results of comparing the oncologist-delineation with the VCAT and CAT delineations for the two NSCLC patients with the Dice and Jaccard similarity coefficients.

6.3.2.3. Comparison of oncologist and radiologist outlines

Figure 6.19 and Figure 6.20 show the comparison of lesion outlines delineated for NSCLC case one and two respectively using both the radiologist-delineation (green) and oncologist-delineation (red). It is apparent that the radiologist-delineation was larger than the oncologist-delineation in both cases, as can be seen in slice 1 in Figure 6.7 and slices 1 and 8 in Figure 6.20. These differences were more evident on the peripheral slices than the middle slices, which was due not only to the difference in opinion between the radiologist and oncologist, but also due to lesion movements from respiration.

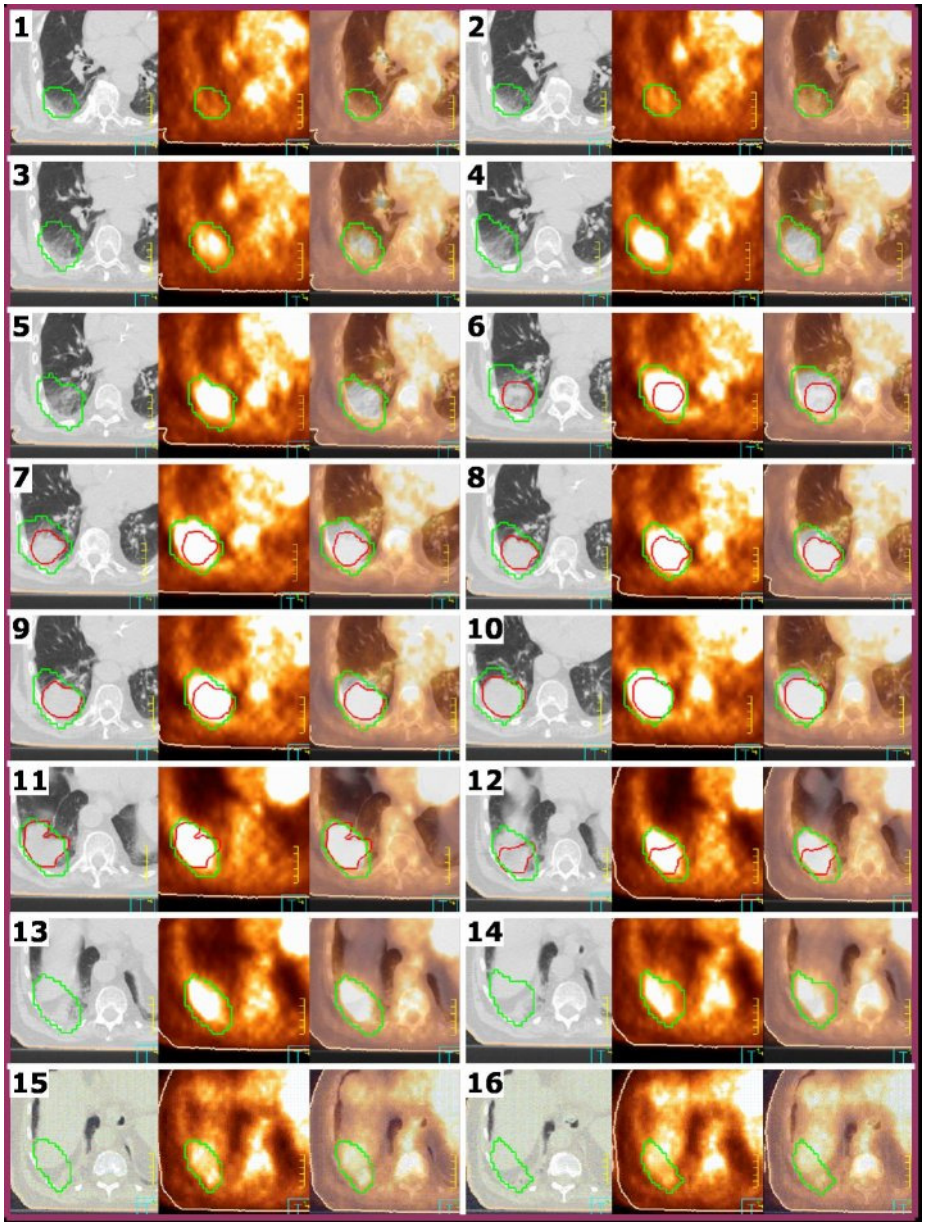

Figure 6.19: A series of CT, PET, and fused PET/CT transaxial slices for lung case one showing the radiologist-delineation (green), the oncologist-delineation (red) and the patient's outline (light-brown).

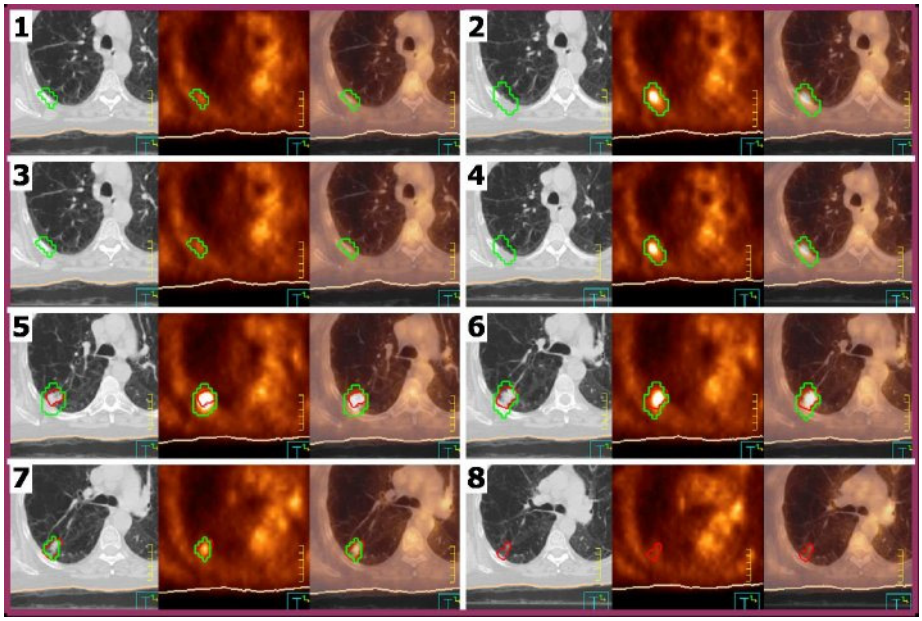

Figure 6.20: A series of CT, PET, and fused PET/CT transaxial slices for lung case two showing the radiologist-delineation (green), the oncologist-delineation (red) and the patient's outline (light-brown).

Figure 6.21 shows a histogram of the nearest distance between the radiologist-delineation and oncologist-delineations. It is apparent that the oncologist-delineation was smaller than the radiologist-delineation in case one as the nearest distances for this case was more negative. The same was true for case two, however, more positive distances were added due to the oncologist delineation in slice 8 Figure 6.20. These results show approximately 31% and 84% overlap within ±2 mm in case one and two respectively between the radiologist-delineation and oncologist-delineation, while there was only 12% and 32 % complete overlap (zero distance difference).

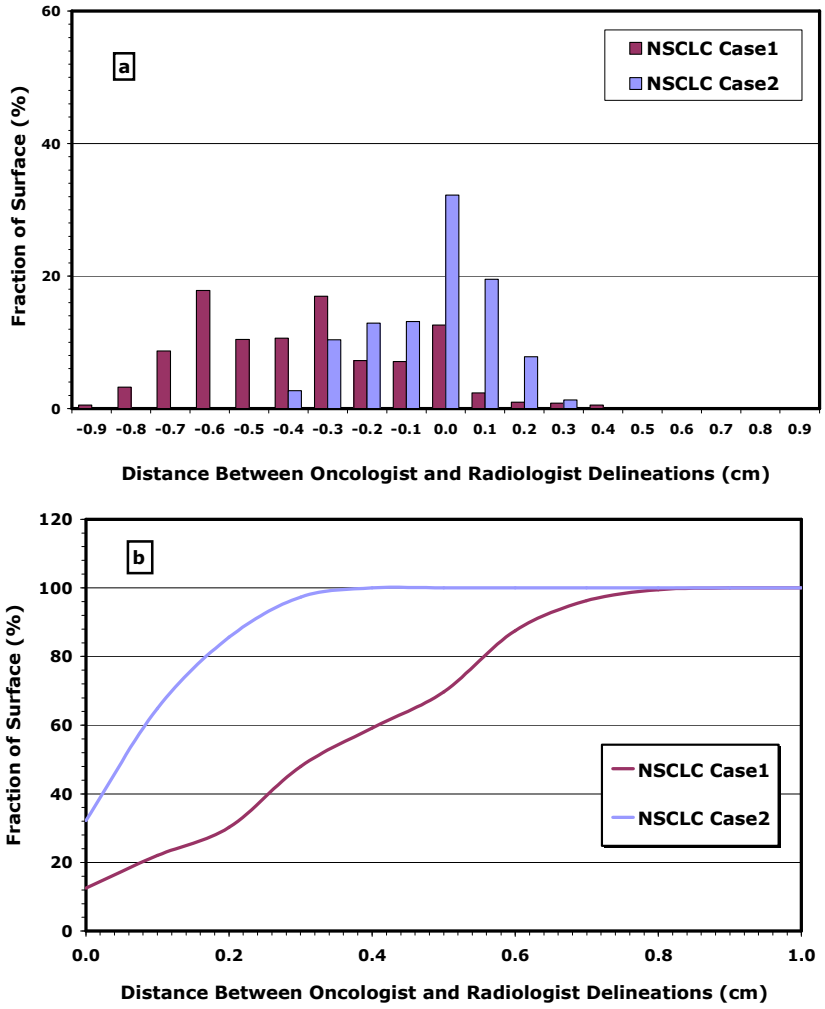

Figure 6.21: Deferential (a) and cumulative (b) histograms of the nearest distance between the surface of radiologist-delineation (reference) and oncologist-delineation for lung cases one and two using the Euclidean distance transformation.

Table 6.6 summarizes the results of comparing the radiologist-delineation versus the oncologist-delineation. These results represent a high percentage difference, even higher than those found in H&N patients. Also, a worse DSC and JSC were found in this comparison. However, the results of the percentage difference as well as the DSC and JSC suggested that there was better agreement between the radiologist and oncologist delineation in

case one than in case two. Closer correspondences were found between VCAT/CAT and each of the radiologist or oncologist delineations.

NSCLC Patient	Radiologist-delineation (ml)	Oncologist-delineation (ml)	Difference (%)	DSC	JSC
1	240.50	92.70	61.46	0.53	0.36
2	21.44	5.47	74.49	0.29	0.17

Table 6.6: Summary of the results of comparing the radiologist-delineation with the oncologist-delineation for the two NSCLC patients with the Dice and Jaccard similarity coefficients.

6.4. Discussion

A source of the error in segmenting the H&N lesions using the VCAT and CAT techniques was the variability of FDG uptake, discussed in section 1.4.1. FDG is found to normally accumulate in the brain, heart and urinary tract [126]. In head and neck, significant muscle uptake can be observed in breathing muscles with hyperventilation, in the cervical muscles with tension and in laryngeal muscles with vocalization [127]. Therefore, although these regions may show FDG uptake, they are usually considered normal. It is, therefore, important to emphasise the need for skilled definition of the loose and background regions of the VCAT and CAT segmentation techniques to avoid these normal FDG uptake areas.

Another source of error in segmenting the H&N lesions was the motion artefacts due to patient movement between the CT and PET scans [52]. Because the PET/CT study starts by acquiring the CT images and then

acquiring the PET images in a series of bed positions starting from the feet limit to the head limit, the amount of time between acquiring the CT and acquiring PET images in the H&N patients could reach up to approximately 30 minutes. This long delay may cause the patient to move especially with the absence of immobilization devices.

For the NSCLC lesions the main source of the error in using the VCAT segmentation technique was the lesion motion during respiratory movement [45, 69, 128, 129]. The CT images are usually acquired over a very short time (fractions of seconds per slice) while a single PET bed position may be acquired over 2.5 minutes. This difference in duration results in acquiring the CT images in a different respiratory phase from the PET images, and the PET images are acquired over many respiratory phases. This effect not only causes a misregistration between the CT and PET images but also causes a blurred outline for the lesion. Recently, feasible methods to correct for respiratory movement such as respiratory gated image acquisition [68, 130], image reconstruction in a specific breath phase [131] or breath-hold image acquisition [132] have been reported and are currently undergoing further clinical evaluation.

The current patient study showed clear disagreements between the radiologist-delineation and oncologist-delineation, with the oncologist delineations being larger by approximately 51% for the H&N cases and 68% for the NSCLC cases. Similar findings have been found in previous H&N studies such as [74] where the PET GTV increased by at least 25% in 17% of the studied patients and also in [133] where eight patients out of twenty-one had additional disease on PET which was not visible on CT. Also, similar findings were found in NSCLC, such as [134] where they found that the PET

GTV increased by 15 mm (expressed in terms of beam apertures) in 34% of the studied patients. The VCAT and CAT delineations proved to be in better agreement with current best practice, the radiologist-delineation, than the oncologist-delineations.

6.5. Conclusion

It has been shown that the VCAT and CAT segmentation techniques can be applied to patient images as part of the radiotherapy treatment planning process. Correct definition of the loose region at the start of VCAT/CAT was critical to avoid the inclusion of normal FDG uptake which could lead to normal tissues being included in the generated lesion outlines; therefore, it is necessary for an experienced interpreter of PET/CT to be involved.

Based on this preliminary experience, it can be concluded that VCAT/CAT produces tumour outlines in agreement with the current best practice which is the radiologist-delineation. These techniques will considerably reduce the amount of time spent by the radiologists from accurately delineate the lesion outline to just delineate the loose regions; and then the techniques proceeds automatically to determine the accurate lesion outlines, which might expect to eliminate variation between radiologists. Therefore the preferred approach for delineating tumour GTV in PET could be to use VCAT/CAT with a radiologist defining the loose region; however, further work would be necessary to fully evaluate this hypothesis.

7

Chapter 7:

SUMMARY, FUTURE WORK AND CONCLUSION

The main aim of this research was to develop the use of PET/CT images for the use in radiotherapy treatment planning with the objective of improving the accuracy of target volume delineation. This main objective has been accomplished and the key results and achievements are summarized in section 7.1 followed by suggestion for future work (section 7.2) and conclusion (section 7.3).

7.1. Summary of Key Results and Achievements

The thesis began with an introduction to the basics of both radiotherapy and positron emission tomography (Chapter 1). The chapter outlined the potential advantages of using PET in radiotherapy treatment planning and technical

issues concerning the use of PET radiotherapy target volume delineation. The delineation of tumour outlines in PET images is not straightforward due to the relatively low spatial resolution, especially for smaller tumours where it is comparable to the tumour size, which results in fuzzy edges of the lesion and gives rise to partial volume effects. Another cause of the fuzzy edges is the lesion movements during the PET image acquisition. Many previously published techniques for target volume delineation were reviewed in chapter 2, with discussion of the various advantages and disadvantages. However no single technique has yet been published that is superior to all others, or is suitable for routine and reliable application in the clinic.

7.1.1. Development of New Techniques - VCAT and CAT

Chapter 3 described the development of two novel adjusting thresholding techniques, VCAT and CAT, which accurately delineate PET/CT lesions for the purpose of radiotherapy treatment planning. These techniques are based on a one-off calibration that is specific to the scanner and data production process. The VCAT calibration curves represent the relationship between an optimum threshold value, T_{opt}, and lesion volume, V, at a given observed contrast, C_o, while the CAT calibration curves represent the correlation between T_{opt} and C_o which is applicable across all volumes except less than 1.15 ml (1.15 ml is the size of the smallest sphere in the lesion phantom used for calibration). This could be applicable for routine practice since lesions with volumes < 1.15 ml are not normally considered for RTP.

Both VCAT and CAT techniques are easy for the operator to use, making the tumour delineation more straightforward than carefully drawing around areas of uptake. The operator needs only to draw a loose region

generously around the lesion on the PET images, and a background region on all slices that contain the lesion. The loose region is then used by the computer programme to determine the lesion uptake and to constrain the segmentation. The method then proceeds automatically to calculate the observed lesion contrast and derive the lesion outline, having determined the optimum threshold for the given image.

7.1.2. Quantitative Evaluation of VCAT and CAT Accuracy

Chapters 4 and 5 presented the evaluation of VCAT and CAT accuracy in a range of different situations such as lesion shapes, noise levels, reconstruction techniques, and lesion uptake definitions. For the purpose of evaluating the accuracy of the new technique, a new concept of "acceptable error" was defined, based on an assessment of the size of error which could be tolerated in radiotherapy. The key findings were:

- The VCAT and CAT techniques are more applicable and reliable in the routine clinic than the most used previously published method. For the range of lesions that are treatable, the new techniques proved to have an accuracy which was well within the acceptable error for RTP.

- The comparison of VCAT and CAT versus the 40% fixed thresholding technique was significantly in favour to the new techniques where the fixed threshold failed to accurately segment V < 1.15ml with C_o~ 5 and all volumes having C_o~ 2 and 3.

- VCAT and CAT have limits to their applicability, which occur as lesion size and contrast approach lower levels. VCAT was able to segment lesions within the acceptable error for all contrasts down to a volume of 0.53 ml

in IT, and down to a volume of 1.15 ml for $C_o \geq 3$ in the case of FBP. The CAT method was able to segment lesions within the acceptable error down to 0.53 ml for both IT and FBP at 2.5 min t_{AC}. The CAT technique was also able to accurately segment the spherical lesions > 1.15 ml for $C_o \geq 3$ in case of IT and FBP at all t_{AC}.

- When using the simplified calibration process, with a single 60 min calibration curve, VCAT was found to give results within the acceptable error at volumes greater than 1.15 ml and contrasts greater 3 for IT reconstruction, and volumes greater than 2.57ml and contrasts greater 3 for FBP.

- Both the VCAT and CAT were successfully applied in the irregularly shaped phantom series, top-hat and crescent, with errors far less than the acceptable error.

- Overall, VCAT proved to be the more useful of the two new techniques, because it was more accurate over a wider range than CAT, being able to determine sufficiently accurate tumour outlines and volumes in small lesions and low contrast situations.

In Chapter 5 the impact of using other definitions of lesion maximum uptake were evaluated. The definition of lesion maximum uptake used initially was to find the maximum voxel value, and take the ratio of this to the background to calculate the observed contrast, C_o. However, because of the possible statistical noise in a single voxel, it was sensible to investigate a wider zone, such as using the mean of 9 and 27 voxels around the voxel with the highest intensity. Limitations were discovered in using these wider zones for the lesion maximum uptake. These limitations were mainly due to the

large volume size of the 9 (~1 ml) and 27 (~2.7 ml) voxels compared with the small lesions and the smallest spherical volume in the phantom study.

7.1.3. Clinical Evaluation of VCAT and CAT

Chapter 6 represented a preliminary evaluation of both VCAT and CAT techniques in H&N and NSCLC patients. This evaluation compared the VCAT and CAT segmented outlines with what was considered to be current best practice, the outlines delineated manually by a radiologist. Comparisons were also made with the outlines delineated manually by an oncologist.

These evaluations revealed a disagreement between the oncologist and radiologist delineations especially in NSCLC patients where the radiologist-delineations were always larger than the oncologist-delineation mainly due to three reasons:

- the difference in nature between the anatomical and physiological imaging
- movement between the CT and PET scans
- lesion movement due to the respiratory motion

The VCAT/CAT segmented outlines agreed closely with current best practice, as delineated by an experienced radiologist, as well as between VCAT/CAT segmented volumes and delineations by an oncologist. These observations were confirmed with quantitative analysis using the EDT, DSC and JSC.

An evaluation was made of the impact of defining the loose regions differently in patients with multiple lesions, i.e. primary tumour and lymph nodes. Two segmented volumes were produced: i) using one loose region that

encompassed all lesions, or ii) separate loose regions for each lesion and then combining the segmented volumes. No significant difference was found between these two approaches.

Although VCAT and CAT automatically produce tumour outlines, it may still be appropriate for the oncologist, or radiologist, to review these to ensure that they are satisfied to proceed to treatment planning. With the current implementation where the VCAT and CAT computer programme can be run on the treatment planning workstation, it is indeed possible for the oncologist to edit the VCAT/CAT outline. This is an important feature, which allows for those situations where the PET lesion is close to critical organs, or other structures which may distort the automatic outline.

7.2. Future Work

The research presented in this PhD has significantly contributed to the development of the use of PET/CT images in the use of radiotherapy treatment planning. The conclusion of this work leads to the following suggestions for future investigations.

7.2.1. Future Investigations on the VCAT and CAT Techniques

- Both VCAT and CAT techniques are based on the value of C_o obtained from the PET images. The impact of using different maximum lesion uptake definitions on the accuracies of the two techniques as well as on the calibration curves was studied. Another aspect of determining C_o is the placement of the initial loose region, since this could change the background level. Therefore, investigation is warranted of the impact on C_o of how different operators, with different expertise (e.g. radiologists and oncologists) choose to draw the loose region.

- Closely related to the above, it would be appropriate to determine by how much the inter-observer variations of the manual method employed in current clinical practice compare with the results of different operators using VCAT, which one would expect to be more consistent.

- The calibration curves for the VCAT and CAT segmentation techniques were generated for the available GE PET/CT scanner at The Christie. These calibration curves are clearly scanner dependent, so implementation on other scanner should be investigated to explore the generalisability of the new technique.

- Both VCAT and CAT techniques were evaluated using the most common PET radiotracer, FDG. Validations need to be carried out to investigate whether the new techniques are applicable with other radiotracer.

- A more extensive evaluation in a larger number of patients than that presented above is warranted. This study should be carried out on a other tumour types, and allow for investigation of inter- and intra-observer variability.

7.2.2. Future Directions for the Scan Protocol

- An accurate respiratory motion correction would be of great benefit to segment the patient's lesions especially for chest and upper abdomen regions. Such corrections should be accurate in the case of non-rigid and non-periodic motions. Whilst simple respiratory gating techniques could improve lesion outlines delineation by VCAT, more complex motion correction methods may be required in segmenting small lesions.

- It could be possible to use a scout projection PET image to identify the bed positions appropriate to the particular patient-tumour combination, which would make it possible to quickly determine the size of the lesion or tumour of interest, and also obtain a preliminary measure of the contrast. If the lesion size is below a certain volume (e.g. 1 ml) and/or the contrast is below a certain value (e.g. $C_o < 3$), then the scan time can be increased to ensure sufficiently low image noise to allow reliable operation of VCAT/CAT. Alternatively, because for different tumour types and locations, the count density varies, it could be possible to devise a way of acquiring a certain total number of counts for each disease type, in order to achieve the desirable PET image quality.

7.3. Conclusion

A new PET lesion segmentation technique has been developed which proved capable of producing tumour outlines at least as accurate as an experienced nuclear medicine specialist radiologist, and was also able to determine the tumour volume with greater accuracy over a wider range of conditions than previously published methods.

The technique automatically produces accurate 3D tumour outlines, derived by measuring the lesion contrast, from which the optimum threshold is automatically determined allowing for the size of lesion. Once the two loose regions, tumour and background, have been drawn, the technique immediately produces the final tumour outlines. The advantages are that the process is far quicker than the current practice of manual delineation, and there is no dependence on the subjective opinion of different operators.

Of the two variants of the new technique, VCAT and CAT, VCAT proved to be more accurate and effective over a wider range of lesion contrasts and volumes, and can determine lesion volumes and delineate outlines well within the errors that are acceptable in radiotherapy treatment planning for the range of tumour sizes treatable by RTP.

These results represent an important step towards discovering whether the incorporation of FDG-PET information into radiotherapy target volume delineation will impact on the local control and hence ultimately affect patient survival rates.

Appendix I

Irregular Lesions Dimensions

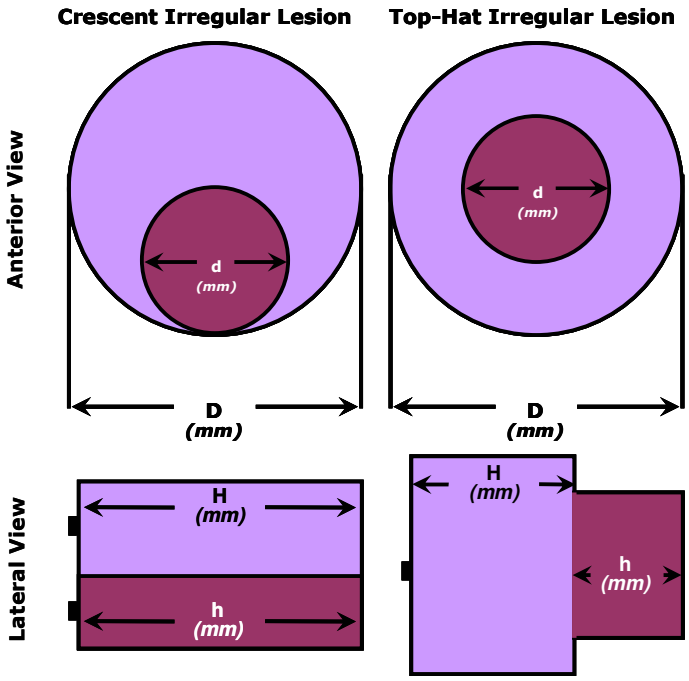

Total Volume (ml)	Crescent Irregular Lesion			
	Outer Cylinder		Inner Cylinder	
	D (mm)	H (mm)	d (mm)	h (mm)
4.89	40	9	28	9
29.1	44	25.5	20	25.5
66.8	66	25.5	30	25.5
96.1	64	40	30	40

Total Volume (ml)	Top-Hat Irregular Lesion			
	Lower Cylinder		Upper Cylinder	
	D (mm)	H (mm)	d (mm)	h (mm)
8.69	20	25.5	10	10
30.0	30	28	20	32
71.4	50	25.5	40	16
101.8	55	30	36	30

Appendix II

IDL VCAT and CAT Segmentation Procedure

The VCAT and CAT PET segmentation techniques program was written using Interactive Data Language (IDL) version 7.1. The following IDL procedure was incorporating within the Molecular Imaging Display and Analysis Software (MIDAS) which written at this Centre by Dr Peter Julyan. The program was written in a way that after defining the tumour loose and the background regions using the ROI tool available in MAIDAS, the VCAT volume using Lmax, $Lmax_9$, and $Lmax_{27}$ and the CAT volume using Lmax as well as the corresponding optimum thresholds are calculated and displayed.

Here is the complete procedure to implement the VCAT and CAT PET segmentation techniques:

```
; If a loose region is defined using the ROI tool, then
; start the following procedure to calculate the VCAT and
; CAT volumes.
IF roiVox2 GT 0 THEN BEGIN
  Cm = roiMax/MA_BG      ;The observed contrast using the maximum
  C9 = roiMean9/MA_BG    ;The observed contrast using the mean of 9 voxels
  C27= roiMean27/MA_BG   ;The observed contrast using the mean of 27 voxels
  PRINT, Cm, C9, C27
  V1=500.0               ;Initiate the volume to a very large size

;Read the reconstruction technique from the Dicom header
  CASE study.description OF
;Read the acquisition duration from the Dicom header
   'WB_3D_CTAC_FBP':CASE frameDuration OF
    60.: BEGIN           ;Calculate the T1, T9, T27
     Tm_1 = 39.35+(19.58/Cm)+(55.55/(Cm)^2)+((4.41+(23.7/Cm)+$
      (-0.04/Cm^2))/V1)+((7.66+(-33.46/Cm)+(17.35/Cm^2))/V1^2)
     T9_1 = 38.81+(42.32/C9)+(41.4/(C9)^2)+((62.02+(-55.34/C9)+$
      (9.69/C9^2))/V1)+((-1.77+(-26.96/C9)+(20.92/C9^2))/V1^2)
     T27_1= 37.69+(47.8/C27)+(39.28/(C27)^2)+((85.97+(-100.17/C27)+$
      (19.09/C27^2))/V1)+((-5.79+(-5.03/C27)+(8.95/C27^2))/V1^2)
     END

    150.: BEGIN          ;Calculate the T1, T9, T27
     Tm_1 = 38.99+(32.34/Cm)+(20.95/(Cm)^2)+((8.02+(-2.74/Cm)+$
      (36.81/Cm^2))/V1)+((4.82+(-17.64/Cm)+(-4.07/Cm^2))/V1^2)
     T9_1 = 37.54+(51.29/C9)+(13.86/(C9)^2)+((72.25+(-103.84/C9)+$
      (51.97/C9^2))/V1)+((-10.33+(15.14/C9)+(-14.21/C9^2))/V1^2)
     T27_1= 36.18+(59.32/C27)+(6.38/(C27)^2)+((96.6+(-130.68/C27)+$
      (50.97/C27^2))/V1)+((-14.54+(18.88/C27)+(-10.23/C27^2))/V1^2)
    END
```

```
 300.: BEGIN          ;Calculate the T1, T9, T27
  Tm_1 = 39.22+(42.09/Cm)+(0.9/(Cm)^2)+((7.42+(-19.13/Cm)+$
    (55.72/Cm^2))/V1)+((3.69+(0.56/Cm)+(-21.97/Cm^2))/V1^2)
  T9_1 = 38.48+(50.55/C9)+(5.1/(C9)^2)+((63.32+(-62.27/C9)+$
    (21.63/C9^2))/V1)+((-3.13+(-10.64/C9)+(5.2/C9^2))/V1^2)
  T27_1= 37.98+(50.37/C27)+(8.42/(C27)^2)+((80.92+(-79.57/C27)+$
    (22.16/C27^2))/V1)+((0.93+(-20.43/C27)+(10.45/C27^2))/V1^2)
 END

 600.: BEGIN          ;Calculate the T1, T9, T27
  Tm_1 = 40.17+(40.63/Cm)+(-4.23/(Cm)^2)+((.49+(27.50/Cm)+$
    (-8.65/Cm^2))/V1)+((5.95+(-26.55/Cm)+(17.72/Cm^2))/V1^2)
  T9_1 = 37.86+(57.88/C9)+(-17.64/(C9)^2)+((69.38+(-85.72/C9)+$
    (61.85/C9^2))/V1)+((-9.47+(5.57/C9)+(-12.83/C9^2))/V1^2)
  T27_1= 36.27+(62.99/C27)+(-18.69/(C27)^2)+((94.34+(-120.71/C27)+$
    (71.55/C27^2))/V1)+((-14.69+(18.08/C27)+(-19.43/C27^2))/V1^2)
 END

 900.: BEGIN          ;Calculate the T1, T9, T27
  Tm_1 = 38.78+(51.42/Cm)+(-17.45/(Cm)^2)+((10.31+(-33.6/Cm)+$
    (63.68/Cm^2))/V1)+((1.61+(3.68/Cm)+(-18.59/Cm^2))/V1^2)
  T9_1 = 38.13+(52.78/C9)+(-4.34/(C9)^2)+((67.35+(-65.3/C9)+$
    (22.05/C9^2))/V1)+((-6.81+(-9.32/C9)+(8.53/C9^2))/V1^2)
  T27_1= 37.42+(51.97/C27)+(0.87/(C27)^2)+((86.66+(-77.08/C27)+$
    (10.10/C27^2))/V1)+((-6.03+(-14.2/C27)+(14.36/C27^2))/V1^2)
 END

 1200.: BEGIN         ;Calculate the T1, T9, T27
  Tm_1 = 38.26+(52.67/Cm)+(-13.09/(Cm)^2)+((12.59+(-39.4/Cm)+$
    (56.56/Cm^2))/V1)+((-1.04+(12.46/Cm)+(-20.87/Cm^2))/V1^2)
  T9_1 = 37.41+(57.63/C9)+(-13.01/(C9)^2)+((71.31+(-80.13/C9)+$
    (38.72/C9^2))/V1)+((-11.63+(6.46/C9)+(-5.23/C9^2))/V1^2)
  T27_1= 34.67+(70.21/C27)+(-25.58/(C27)^2)+((100.35+(-145.93/C27)+$
    (89.59/C27^2))/V1)+((-19.22+(37.06/C27)+(-34.56/C27^2))/V1^2)
 END

 1800.: BEGIN         ;Calculate the T1, T9, T27
  Tm_1 = 38.61+(45.11/Cm)+(0.37/(Cm)^2)+((11.35+(-16.27/Cm)+$
    (17.27/Cm^2))/V1)+((1.23+(-5.57/Cm)+(2.55/Cm^2))/V1^2)
  T9_1 = 37.32+(51.15/C9)+(1.79/(C9)^2)+((72.08+(-54.01/C9)+$
    (-9.41/C9^2))/V1)+((-12.79+(-6.74/C9)+(18.47/C9^2))/V1^2)
  T27_1= 36.11+(52.57/C27)+(4.45/(C27)^2)+((92.7+(-62.49/C27)+$
    (-22.64/C27^2))/V1)+((-13.31+(-13.11/C27)+(25.91/C27^2))/V1^2)
 END

 3600.: BEGIN         ;Calculate the T1, T9, T27
  Tm_1 = 39.26+(45.68/Cm)+(-1.56/(Cm)^2)+((6.23+(-16.26/Cm)+$
    (28.06/Cm^2))/V1)+((4.48+(-5.93/Cm)+(-3.02/Cm^2))/V1^2)
  T9_1 = 37.78+(53.27/C9)+(-2.72/(C9)^2)+((68.63+(-70.61/C9)+$
    (18.54/C9^2))/V1)+((-9.18+(0.66/C9)+(3.22/C9^2))/V1^2)
  T27_1= 36.6+(56.63/C27)+(-5.38/(C27)^2)+((91.09+(-102.67/C27)+$
    (34.57/C27^2))/V1)+((-11.61+(8.97/C27)+(-4.99/C27^2))/V1^2)
 END
ENDCASE

'WB_3D_CTAC_Iterative':CASE frameDuration OF

 60.: BEGIN           ;Calculate the T1, T9, T27
```

```
 Tm_1 = 39.34+(-16.94/Cm)+(131.77/(Cm)^2)+((-3.39+(24.6/Cm)+$
  (-18.8/Cm^2))/V1)+((7.69+(-9.98/Cm)+(-10.82/Cm^2))/V1^2)
 T9_1 = 38.06+(33.98/C9)+(46.72/(C9)^2)+((65.79+(-102.84/C9)+$
  (58.47/C9^2))/V1)+((-1.15+(5.81/C9)+(-18.3/C9^2))/V1^2)
 T27_1= 36.82+(43.82/C27)+(37.58/(C27)^2)+((86.42+(-126.06/C27)+$
  (56.69/C27^2))/V1)+((-1.47+(5.78/C27)+(-14.25/C27^2))/V1^2)
END

150.: BEGIN          ;Calculate the T1, T9, T27
 Tm_1 = 38.66+(4.07/Cm)+(87.34/(Cm)^2)+((3.85+(-3.03/Cm)+$
  (-17.64/Cm^2))/V1)+((1.2+(7.03/Cm)+(-6.07/Cm^2))/V1^2)
 T9_1 = 40.45+(27.7/C9)+(47.41/(C9)^2)+((59.3+(-60.51/C9)+$
  (-11.67/C9^2))/V1)+((1.46+(-16.33/C9)+(19.61/C9^2))/V1^2)
 T27_1= 37.3+(43.57/C27)+(31.22/(C27)^2)+((95.41+(-141.71/C27)+$
  (42.13/C27^2))/V1)+((-5.14+(9.89/C27)+(-3.01/C27^2))/V1^2)
END

300.: BEGIN          ;Calculate the T1, T9, T27
 Tm_1 = 40.51+(17.12/Cm)+(46.25/(Cm)^2)+((-10.98+$(32.34/Cm)+$
  (0.12/Cm^2))/V1)+((12.18+(-27.89/Cm)+(4.49/Cm^2))/V1^2)
 T9_1 = 39.65+(20.38/C9)+(51.45/(C9)^2)+((62.44+(-2.6/C9)+$
  (-85.48/C9^2))/V1)+((-1.27+(-40.08/C9)+(52.33/C9^2))/V1^2)
 T27_1= 38.48+(26.76/C27)+(44./(C27)^2)+((84.16+(-44.2/C27)+$
  (-53.02/C27^2))/V1)+((-0.98+(-33.26/C27)+(39.95/C27^2))/V1^2)
END

600.: BEGIN          ;Calculate the T1, T9, T27
 Tm_1 = 40.06+(24.43/Cm)+(27.68/(Cm)^2)+((-4.42+(20.40/Cm)+$
  (-0.26/Cm^2))/V1)+((2.72+(-2.5/Cm)+(-7.04/Cm^2))/V1^2)
 T9_1 = 39.75+(35.68/C9)+(15.81/(C9)^2)+((66.49+(-73.98/C9)+$
  (29.57/C9^2))/V1)+((-6.44+(0.05/C9)+(-2.35/C9^2))/V1^2)
 T27_1= 38.51+(40.94/C27)+(11.38/(C27)^2)+((88.55+(-101.09/C27)+$
  (38.09/C27^2))/V1)+((-5.5+(-2.48/C27)+(-1.97/C27^2))/V1^2)
END

900.: BEGIN          ;Calculate the T1, T9, T27
 Tm_1 = 40.81+(17.97/Cm)+(43.46/(Cm)^2)+((-11.25+(65.39/Cm)+$
  (-67.78/Cm^2))/V1)+((8.85+(-33.18/Cm)+(30.92/Cm^2))/V1^2)
 T9_1 = 42.9+(14.24/C9)+(47.17/(C9)^2)+((51.75+(7.39/C9)+$
  (-70.51/C9^2))/V1)+((4.93+(-48.93/C9)+(49.25/C9^2))/V1^2)
 T27_1= 42.34+(16.41/C27)+(45./(C27)^2)+((69.6+(-9.48/C27)+$
  (-66.07/C27^2))/V1)+((8.88+(-56.12/C27)+(49.78/C27^2))/V1^2)
END

1200.: BEGIN         ;Calculate the T1, T9, T27
 Tm_1 = 39.59+(25.87/Cm)+(31.72/(Cm)^2)+((-2.59+(6.81/Cm)+$
  (3.25/Cm^2))/V1)+((3.55+(-0.83/Cm)+(-6.19/Cm^2))/V1^2)
 T9_1 = 39.75+(32.09/C9)+(22.8/(C9)^2)+((62.92+(-54.34/C9)+$
  (0.74/C9^2))/V1)+((-3.03+(-13.37/C9)+(13./C9^2))/V1^2)
 T27_1= 39.25+(32.39/C27)+(22.25/(C27)^2)+((80.45+(-63.59/C27)+$
  (-2.13/C27^2))/V1)+((1.63+(-27.13/C27)+(19.5/C27^2))/V1^2)
END

1800.: BEGIN         ;Calculate the T1, T9, T27
 Tm_1 = 39.21+(27.03/Cm)+(33.96/(Cm)^2)+((-0.46+(-7.17/Cm)+$
  (16.45/Cm^2))/V1)+((3.4+(3./Cm)+(-11.4/Cm^2))/V1^2)
 T9_1 = 36.15+(45.23/C9)+(14.72/(C9)^2)+((76.55+(-87.84/C9)+$
  (15.95/C9^2))/V1)+((-11.4+(7.78/C9)+(2.39/C9^2))/V1^2)
```

```
      T27_1= 35.58+(43.32/C27)+(20.52/(C27)^2)+((94.17+(-87.49/C27)+$
       (-8.82/C27^2))/V1)+((-7.95+(-7.08/C27)+(17.26/C27^2))/V1^2)
     END

     3600.: BEGIN          ;Calculate the T1, T9, T27
      Tm_1 = 39.08+(33.88/Cm)+(24.95/(Cm)^2)+((2.63+(-26.32/Cm)+$
       (25.62/Cm^2))/V1)+((.58+(17.33/Cm)+(-19.09/Cm^2))/V1^2)
      T9_1 = 39.74+(25.01/C9)+(38.75/(C9)^2)+((70.16+(-48.36/C9)+$
       (-35.9/C9^2))/V1)+((-10.75+(-2.27/C9)+(19.66/C9^2))/V1^2)
      T27_1= 38.62+(27.04/C27)+(38.42/(C27)^2)+((92.86+(-71.76/C27)+$
       (-34.14/C27^2))/V1)+((-11.97+(-0.92/C27)+(19.53/C27^2))/V1^2)
     END
    ENDCASE
   ENDCASE

   PRINT, "Tmax(1)=", Tm_1, "T9(1)=", T9_1, "T27(1)=", T27_1

   FOR I= 0, 100 DO BEGIN
    N= N_ELEMENTS (WHERE(imageSet(WHERE(imROIdrawn EQ 255)) GE $
             (Tm_1*roiMax/100.0)))
    Vm_2= N*voxVol        ;The volume size that corresponds to T1
;Read the reconstruction technique from the Dicom header
    CASE study.description OF
;Read the acquisition duration from the Dicom header
     'WB_3D_CTAC_FBP':CASE frameDuration OF  ;Calculate T2 using the maximum
      60.: Tm_2 = 39.35 + (19.58/Cm) + (55.55/(Cm)^2)+ ((4.41+(23.7/Cm)+$
       (-0.04/Cm^2))/Vm_2)+((7.66+(-33.46/Cm)+(17.35/Cm^2))/Vm_2^2)

      50.: Tm_2 = 38.99+(32.34/Cm)+(20.95/(Cm)^2)+((8.02+(-2.74/Cm)+$
       (36.81/Cm^2))/Vm_2)+((4.82+(-17.64/Cm)+(-4.07/Cm^2))/Vm_2^2)

      300.: Tm_2 = 39.22+(42.09/Cm)+(0.9/(Cm)^2)+((7.42+(-19.13/Cm)+$
       (55.72/Cm^2))/Vm_2)+((3.69+(0.56/Cm)+(-21.97/Cm^2))/Vm_2^2)

      600.: Tm_2 = 40.17+(40.63/Cm)+(-4.23/(Cm)^2)+((.49+(27.50/Cm)+$
       (-8.65/Cm^2))/Vm_2)+((5.95+(-26.55/Cm)+(17.72/Cm^2))/Vm_2^2)
      900.: Tm_2 = 38.78+(51.42/Cm)+(-17.45/(Cm)^2)+((10.31+(-33.6/Cm)+$
       (63.68/Cm^2))/Vm_2)+((1.61+(3.68/Cm)+(-18.59/Cm^2))/Vm_2^2)

      1200.: Tm_2 = 38.26+(52.67/Cm)+(-13.09/(Cm)^2)+((12.59+(-39.4/Cm)+$
       $(56.56/Cm^2))/Vm_2)+((-1.04+(12.46/Cm)+(-20.87/Cm^2))/Vm_2^2)

      1800.: Tm_2 = 38.61+(45.11/Cm)+(0.37/(Cm)^2)+((11.35+(-16.27/Cm)+$
       (17.27/Cm^2))/Vm_2)+((1.23+(-5.57/Cm)+(2.55/Cm^2))/Vm_2^2)

      3600.: Tm_2 = 39.26+(45.68/Cm)+(-1.56/(Cm)^2)+((6.23+(-16.26/Cm)+$
       (28.06/Cm^2))/Vm_2)+((4.48+(-5.93/Cm)+(-3.02/Cm^2))/Vm_2^2)
     ENDCASE

     'WB_3D_CTAC_Iterative':CASE frameDuration OF
      60.: Tm_2 = 39.34+(-16.94/Cm)+(131.77/(Cm)^2)+((-3.39+(24.6/Cm)+$
       -18.8/Cm^2))/Vm_2)+((7.69+(-9.98/Cm)+(-10.82/Cm^2))/Vm_2^2)

      150.: Tm_2 = 38.66+(4.07/Cm)+(87.34/(Cm)^2)+((3.85+(-3.03/Cm)+$
       -17.64/Cm^2))/Vm_2)+((1.2+(7.03/Cm)+(-6.07/Cm^2))/Vm_2^2)

      300.: Tm_2 = 40.51+(17.12/Cm)+(46.25/(Cm)^2)+((-10.98+(32.34/Cm)+$
       (0.12/Cm^2))/Vm_2)+((12.18+(-27.89/Cm)+(4.49/Cm^2))/Vm_2^2)
```

```
      600.: Tm_2 = 40.06+(24.43/Cm)+(27.68/(Cm)^2)+((-4.42+(20.40/Cm)+$
       (-0.26/Cm^2))/Vm_2)+((2.72+(-2.5/Cm)+(-7.04/Cm^2))/Vm_2^2)

      900.: Tm_2 = 40.81+(17.97/Cm)+(43.46/(Cm)^2)+((-11.25+(65.39/Cm)+$
       (-67.78/Cm^2))/Vm_2)+((8.85+(-33.18/Cm)+(30.92/Cm^2))/Vm_2^2)

      1200.: Tm_2 = 39.59+(25.87/Cm)+(31.72/(Cm)^2)+((-2.59+(6.81/Cm)+$
       (3.25/Cm^2))/Vm_2)+((3.55+(-0.83/Cm)+(-6.19/Cm^2))/Vm_2^2)

      1800.: Tm_2 = 39.21+(27.03/Cm)+(33.96/(Cm)^2)+((-0.46+(-7.17/Cm)+$
       (16.45/Cm^2))/Vm_2)+((3.4+(3./Cm)+(-11.4/Cm^2))/Vm_2^2)

      3600.: Tm_2 = 39.08+(33.88/Cm)+(24.95/(Cm)^2)+((2.63+(-26.32/Cm)+$
       (25.62/Cm^2))/Vm_2)+((.58+(17.33/Cm)+(-19.09/Cm^2))/Vm_2^2)
      ENDCASE
    ENDCASE

    Diff_m= ABS(Tm_1 - Tm_2) ;Calculate the difference between T1 and T2
    IF Diff_m LE 0.001 THEN BEGIN
      WIDGET_CONTROL, MAVm, SET_VALUE=STRTRIM(Vm_2, 2)
      WIDGET_CONTROL, MATm, SET_VALUE=STRTRIM((Tm_2*roiMax/100.), 2)
      BREAK
    ENDIF ELSE BEGIN
     IF V1 GT Vm_2 THEN BEGIN
       V1= Vm_2          ;volume size using the VCAT technique
       T = Tm_1
     ENDIF ELSE BEGIN
       WIDGET_CONTROL, MAVm, SET_VALUE=STRTRIM(V1, 2)
       WIDGET_CONTROL, MATm, SET_VALUE=STRTRIM((T*roiMax/100.), 2)
       BREAK
     ENDELSE
     Tm_1= Tm_2
    ENDELSE
   ENDFOR
   PRINT, I, Tm_2

   V1 = 500.0
   FOR I= 0, 100 DO BEGIN
     N= N_ELEMENTS (WHERE(imageSet(WHERE(imROIdrawn EQ 255)) GE $
              (T9_1*roiMean9/100.0)))
     V9_2= N*voxVol
;Read the reconstruction technique from the Dicom header
     CASE study.description OF
;Read the acquisition duration from the Dicom header
      'WB_3D_CTAC_FBP':CASE frameDuration OF ;Calculate T2 using mean of 9
       60.: T9_2 = 38.81+(42.32/C9)+(41.4/(C9)^2)+((62.02+(-55.34/C9)+$
       (9.69/C9^2))/V9_2)+((-1.77+(-26.96/C9)+(20.92/C9^2))/V9_2^2)

       150.: T9_2 = 37.54+(51.29/C9)+(13.86/(C9)^2)+((72.25+(-103.84/C9)+$
       (51.97/C9^2))/V9_2)+((-10.33+(15.14/C9)+(-14.21/C9^2))/V9_2^2)

       300.: T9_2 = 38.48+(50.55/C9)+(5.1/(C9)^2)+((63.32+(-62.27/C9)+$
       (21.63/C9^2))/V9_2)+((-3.13+(-10.64/C9)+(5.2/C9^2))/V9_2^2)

       600.: T9_2 = 37.86+(57.88/C9)+(-17.64/(C9)^2)+((69.38+(-85.72/C9)+$
       (61.85/C9^2))/V9_2)+((-9.47+(5.57/C9)+(-12.83/C9^2))/V9_2^2)
```

```
    900.: T9_2 = 38.13+(52.78/C9)+(-4.34/(C9)^2)+((67.35+(-65.3/C9)+$
    (22.05/C9^2))/V9_2)+((-6.81+(-9.32/C9)+(8.53/C9^2))/V9_2^2)

    1200.: T9_2 = 37.41+(57.63/C9)+(-13.01/(C9)^2)+((71.31+(-80.13/C9)+$
    (38.72/C9^2))/V9_2)+((-11.63+(6.46/C9)+(-5.23/C9^2))/V9_2^2)

    1800.: T9_2 = 37.32+(51.15/C9)+(1.79/(C9)^2)+((72.08+(-54.01/C9)+$
    (-9.41/C9^2))/V9_2)+((-12.79+(-6.74/C9)+(18.47/C9^2))/V9_2^2)

    3600.: T9_2 = 37.78+(53.27/C9)+(-2.72/(C9)^2)+((68.63+(-70.61/C9)+$
    (18.54/C9^2))/V9_2)+((-9.18+(0.66/C9)+(3.22/C9^2))/V9_2^2)
   ENDCASE

   'WB_3D_CTAC_Iterative':CASE frameDuration OF
    60.: T9_2 = 38.06+(33.98/C9)+(46.72/(C9)^2)+((65.79+(-102.84/C9)+$
    (58.47/C9^2))/V9_2)+((-1.15+(5.81/C9)+(-18.3/C9^2))/V9_2^2)

    150.: T9_2 = 40.45+(27.7/C9)+(47.41/(C9)^2)+((59.3+(-60.51/C9)+$
    (-11.67/C9^2))/V9_2)+((1.46+(-16.33/C9)+(19.61/C9^2))/V9_2^2)

    300.: T9_2 = 39.65+(20.38/C9)+(51.45/(C9)^2)+((62.44+(-2.6/C9)+$
    (-85.48/C9^2))/V9_2)+((-1.27+(-40.08/C9)+(52.33/C9^2))/V9_2^2)

    600.: T9_2 = 39.75+(35.68/C9)+(15.81/(C9)^2)+((66.49+(-73.98/C9)+$
    (29.57/C9^2))/V9_2)+((-6.44+(0.05/C9)+(-2.35/C9^2))/V9_2^2)

    900.: T9_2 = 42.9+(14.24/C9)+(47.17/(C9)^2)+((51.75+(7.39/C9)+$
    (-70.51/C9^2))/V9_2)+((4.93+(-48.93/C9)+(49.25/C9^2))/V9_2^2)

    1200.: T9_2 = 39.75+(32.09/C9)+(22.8/(C9)^2)+((62.92+(-54.34/C9)+$
    (0.74/C9^2))/V9_2)+((-3.03+(-13.37/C9)+(13./C9^2))/V9_2^2)

    1800.: T9_2 = 36.15+(45.23/C9)+(14.72/(C9)^2)+((76.55+(-87.84/C9)+$
    (15.95/C9^2))/V9_2)+((-11.4+(7.78/C9)+(2.39/C9^2))/V9_2^2)

    3600.: T9_2 = 39.74+(25.01/C9)+(38.75/(C9)^2)+((70.16+(-48.36/C9)+$
    (-35.9/C9^2))/V9_2)+((-10.75+(-2.27/C9)+(19.66/C9^2))/V9_2^2)
   ENDCASE
  ENDCASE

 Diff_9= ABS(T9_1 - T9_2)  ;Calculate the difference between T1 and T2
 IF Diff_9 LE 0.001 THEN BEGIN
     WIDGET_CONTROL, MAV9, SET_VALUE=STRTRIM(V9_2, 2)
     WIDGET_CONTROL, MAT9, SET_VALUE=STRTRIM((T9_1*roiMean9/100.), 2)
   BREAK
 ENDIF ELSE BEGIN
  IF V1 GT V9_2 THEN BEGIN
    V1= V9_2          ;volume size using the VCAT technique of 9
    T = T9_1
  ENDIF ELSE BEGIN
    WIDGET_CONTROL, MAV9, SET_VALUE=STRTRIM(V1, 2)
    WIDGET_CONTROL, MAT9, SET_VALUE=STRTRIM((T*roiMean9/100.), 2)
    BREAK
  ENDELSE
  T9_1= T9_2
 ENDELSE
 ENDFOR
PRINT, I, T9_2
```

```
  V1 = 500.0
  FOR I= 0, 100 DO BEGIN
   N= N_ELEMENTS (WHERE(imageSet(WHERE(imROIdrawn EQ 255)) GE $
            T27_1*roiMean27/100.0)))
   V27_2= N*voxVol
;Read the reconstruction technique from the Dicom header
   CASE study.description OF
;Read the acquisition duration from the Dicom header
    'WB_3D_CTAC_FBP':CASE frameDuration OF ;Calculate T2 using mean of 27
     60.: T27_2= 37.69+(47.8/C27)+(39.28/(C27)^2)+((85.97+(-100.17/C27)+$
      (19.09/C27^2))/V27_2)+((-5.79+(-5.03/C27)+(9.95/C27^2))/V27_2^2)

     150.: T27_2= 36.18+(59.32/C27)+(6.38/(C27)^2)+((96.6+(-130.68/C27)+$
      (50.97/C27^2))/V27_2)+((-14.54+(18.88/C27)+(-10.23/C27^2))/V27_2^2)

     300.: T27_2= 37.98+(50.37/C27)+(8.42/(C27)^2)+((80.92+(-79.57/C27)+$
      (22.16/C27^2))/V27_2)+((0.93+(-20.43/C27)+(10.45/C27^2))/V27_2^2)

     600.: T27_2= 36.27+(62.99/C27)+(-18.69/(C27)^2)+((94.34+(-
120.71/C27)+$
      (71.55/C27^2))/V27_2)+((-14.69+(18.08/C27)+(-19.43/C27^2))/V27_2^2)

     900.: T27_2= 37.42+(51.97/C27)+(0.87/(C27)^2)+((86.66+(-77.08/C27)+$
      (10.10/C27^2))/V27_2)+((-6.03+(-14.2/C27)+(14.36/C27^2))/V27_2^2)

     1200.: T27_2= 34.67+(70.21/C27)+(-25.58/(C27)^2)+((100.35+(-
145.93/C27)+$
      (89.59/C27^2))/V27_2)+((-19.22+(37.06/C27)+(-34.56/C27^2))/V27_2^2)

     1800.: T27_2= 36.11+(52.57/C27)+(4.45/(C27)^2)+((92.7+(-62.49/C27)+$
      (-22.64/C27^2))/V27_2)+((-13.31+(-13.11/C27)+(25.91/C27^2))/V27_2^2)

     3600.: T27_2= 36.6+(56.63/C27)+(-5.38/(C27)^2)+((91.09+(-102.67/C27)+$
      (34.57/C27^2))/V27_2)+((-11.61+(8.97/C27)+(-4.99/C27^2))/V27_2^2)
    ENDCASE

    'WB_3D_CTAC_Iterative':CASE frameDuration OF
     60.: T27_2= 36.82+(43.82/C27)+(37.58/(C27)^2)+((86.42+(-126.06/C27)+$
      (56.69/C27^2))/V27_2)+((-1.47+(5.78/C27)+(-14.25/C27^2))/V27_2^2)

     150.: T27_2= 37.3+(43.57/C27)+(31.22/(C27)^2)+((95.41+(-141.71/C27)+$
      (42.13/C27^2))/V27_2)+((-5.14+(9.89/C27)+(-3.01/C27^2))/V27_2^2)

     300.: T27_2= 38.48+(26.76/C27)+(44./(C27)^2)+((84.16+(-44.2/C27)+$
      (-53.02/C27^2))/V27_2)+((-0.98+(-33.26/C27)+(39.95/C27^2))/V27_2^2)

     600.: T27_2= 38.51+(40.94/C27)+(11.38/(C27)^2)+((88.55+(-101.09/C27)+$
      (38.09/C27^2))/V27_2)+((-5.5+(-2.48/C27)+(-1.97/C27^2))/V27_2^2)

     900.: T27_2= 42.34+(16.41/C27)+(45./(C27)^2)+((69.6+(-9.48/C27)+$
      (-66.07/C27^2))/V27_2)+((8.88+(-56.12/C27)+(49.78/C27^2))/V27_2^2)

     1200.: T27_2= 39.25+(32.39/C27)+(22.25/(C27)^2)+((80.45+(-63.59/C27)+$
      (-2.13/C27^2))/V27_2)+((1.63+(-27.13/C27)+(19.5/C27^2))/V27_2^2)

     1800.: T27_2= 35.58+(43.32/C27)+(20.52/(C27)^2)+((94.17+(-87.49/C27)+$
      (-8.82/C27^2))/V27_2)+((-7.95+(-7.08/C27)+(17.26/C27^2))/V27_2^2)
```

```
      3600.: T27_2= 38.62+(27.04/C27)+(38.42/(C27)^2)+((92.86+(-71.76/C27)+$
       (-34.14/C27^2))/V27_2)+((-11.97+(-0.92/C27)+(19.53/C27^2))/V27_2^2)
     ENDCASE
    ENDCASE

    Diff_27= ABS(T27_1 - T27_2) Calculate the difference between T1 and T2
    IF Diff_27 LE 0.001 THEN BEGIN
        WIDGET_CONTROL, MAV27, SET_VALUE=STRTRIM(V27_2, 2)
        WIDGET_CONTROL, MAT27, SET_VALUE=STRTRIM((T27_2*roiMean27/100.), 2)
      BREAK
    ENDIF ELSE BEGIN
     IF V1 GT V27_2 THEN BEGIN
       V1= V27_2          ;volume size using the VCAT technique of 27
       T = T27_1
     ENDIF ELSE BEGIN
       WIDGET_CONTROL, MAV27, SET_VALUE=STRTRIM(V1, 2)
       WIDGET_CONTROL, MAT27, SET_VALUE=STRTRIM((T*roiMean27/100.), 2)
       BREAK
     ENDELSE
     T27_1= T27_2
    ENDELSE
   ENDFOR
   PRINT, I, T27_2

;    CAT Technique
;Read the reconstruction technique from the Dicom header
    CASE study.description OF
;Read the acquisition duration from the Dicom header
      'WB_3D_CTAC_FBP':CASE frameDuration OF
       60.   : Tc_m = 40.7 + (7.32/Cm) + (110.2/Cm^2)
       150.  : Tc_m = 40.7 + (19.2/Cm) + (58.1/Cm^2)
       300.  : Tc_m = 40.8 + (33.1/Cm) + (21.7/Cm^2)
       600.  : Tc_m = 40.4 + (38.3/Cm) + (7.43/Cm^2)
       900.  : Tc_m = 40.3 + (44.5/Cm) + (-3.73/Cm^2)
       1200.: Tc_m = 39.2 + (49.4/Cm) + (-5.48/Cm^2)
       1800.: Tc_m = 40.2 + (43.1/Cm) + (3.05/Cm^2)
       3600.: Tc_m = 40.6 + (37.2/Cm) + (12.5/Cm^2)
      ENDCASE
     'WB_3D_CTAC_Iterative':CASE frameDuration OF
       60.   : Tc_m = 38.6 + (-9.76/Cm) + (122.3/Cm^2)
       150.  : Tc_m = 38.2 + (18.4/Cm) + (58.5/Cm^2)
       300.  : Tc_m = 38.1 + (31.7/Cm) + (28.7/Cm^2)
       600.  : Tc_m = 37.8 + (43.7/Cm) + (1.08/Cm^2)
       900.  : Tc_m = 37.8 + (39.0/Cm) + (14.8/Cm^2)
       1200.: Tc_m = 39.5 + (28.5/Cm) + (23.4/Cm^2)
       1800.: Tc_m = 38.0 + (37.2/Cm) + (18.7/Cm^2)
       3600.: Tc_m = 38.2 + (36.6/Cm) + (21.8/Cm^2)
     ENDCASE
   ENDCASE
   N= N_ELEMENTS (WHERE(imageSet(WHERE(imROIdrawn EQ 255)) GE $
             (Tc_m*roiMax/100.0)))
   Vc= N*voxVol           ;volume size using the CAT technique
   WIDGET_CONTROL, MAVc, SET_VALUE=STRTRIM(Vc, 2)
   WIDGET_CONTROL, MATc, SET_VALUE=STRTRIM((Tc_m*roiMax/100.), 2)
ENDIF
```

Appendix III

Publications and Abstracts of Presentations

The publications listed in this appendix relate to the work which the author has carried out or contribute to during the course of his PhD studies.

Publications

D.L. Hastings, **M.M. Aly**, P.J. Julyan, C.G. Rowbottom, B.k. Yap, M.A. Harris (2009) A novel method for automated tumour delineation on PET/CT for radiotherapy treatment planning. Nuklearmedizin 48: A146

M. Aly, P. Julyan, C. Rowbottom, B. Yap, M. Harris, D. Hastings (2010) PET/CT lesion delineation for RTP using a novel Volume and Contrast Adjusted Thresholding (VCAT) method. Radiotherapy and Oncology 94: S37

Abstracts of Presentations

Moamen M. Aly, Peter J. Julyan, Carl G. Rowbottom, Beng K. Yap, Margaret A. Harris and David L. Hastings (2010) A new semi-automated method for FDG-PET lesion delineation for radiotherapy treatment planning. Uses of PET in Radiotherapy, Institute of Physics and Engineering in Medicine, London.

References

1. International Commission on Radiation Units and Measurements, *ICRU(50): Prescribing, Recording, and Reporting Photon Beam Therapy*. 1993: Bethesda, MD.
2. International Commission on Radiation Units and Measurements, *ICRU(62): Prescribing, Recording, and Reporting Photon Beam Therapy*. 1999: Bethesda, MD.
3. C. Clifton Ling, John Humm, Steven Larson, Howard Amols, Zvi Fuks, Steven Leibel, and Jason A. Koutcher, *Towards multidimensional radiotherapy (MD-CRT): biological imaging and biological conformality.* International Journal of Radiation Oncology*Biology*Physics, 2000. **47**(3): p. 551-560.
4. S. Levin and Edward J. Hoffman Craig, *Calculation of positron range and its effect on the fundamental limit of positron emission tomography system spatial resolution.* Physics in Medicine and Biology, 1999. **44**(3): p. 781.
5. Otto Warburg, *On the Origin of Cancer Cells.* Science, 1956. **123**(3191): p. 309-314.
6. Ashley M. Groves, Thida Win, Simona Ben Haim, and Peter J. Ell, *Non-[18F]FDG PET in clinical oncology.* The Lancet Oncology, 2007. **8**(9): p. 822-830.
7. DJ. Schlyer, *PET Tracers and Radiochemistry.* Ann. Acad. Med. Singapore, 2004. **33**: p. 146–154.
8. M. A. Pantaleo, M. Nannini, A. Maleddu, S. Fanti, V. Ambrosini, C. Nanni, S. Boschi, and G. Biasco, *Conventional and novel PET tracers for imaging in oncology in the era of molecular therapy.* Cancer Treatment Reviews, 2008. **34**(2): p. 103-121.
9. Ronald Nutt, *The History of Positron Emission Tomography.* Molecular Imaging & Biology, 2002. **4**(1): p. 11-26.
10. Simon R. Cherry, Magnus Dahlbom, Michael E. Phelps, Simon Cherry, and Magnus Dahlbom, *PET: Physics, Instrumentation, and Scanners*, in *PET*. 2006, Springer New York. p. 1-117.
11. M. E. Casey and R. Nutt, *A Multicrystal Two Dimensional BGO Detector System for Positron Emission Tomography.* Nuclear Science, IEEE Transactions on, 1986. **33**(1): p. 460-463.
12. H. Kume, S. Suzuki, Junichi Takeuchi, and Koichiro Oba, *Newly Developed Photomultiplier Tubes with Position Sensitivity Capability.* Nuclear Science, IEEE Transactions on, 1985. **32**(1): p. 448-452.
13. W. W. Moses, *Time of flight in PET revisited.* Nuclear Science, IEEE Transactions on, 2003. **50**(5): p. 1325-1330.

14. S. Surti, S. Karp, L. M. Popescu, E. Daube-Witherspoon, and M. Werner, *Investigation of time-of-flight benefit for fully 3-DPET.* Medical Imaging, IEEE Transactions on, 2006. **25**(5): p. 529-538.
15. Roger Lecomte, *Novel detector technology for clinical PET.* European Journal of Nuclear Medicine and Molecular Imaging, 2009. **36**(0): p. 69-85.
16. Simon R. Cherry, Steven R. Meikle, and Edward J. Hoffman, *Correction and Characterization of Scattered Events in Three-Dimensional PET Using Scanners with Retractable Septa.* J Nucl Med, 1993. **34**(4): p. 671-678.
17. L. Shao, R. Freifelder, and J. S. Karp. *Triple energy window scatter correction technique in PET*. in *Nuclear Science Symposium and Medical Imaging Conference, 1992., Conference Record of the 1992 IEEE*. 1992.
18. S. Grootoonk, T. J. Spinks, D. Sashin, N. M. Spyrou, and T. Jones, *Correction for scatter in 3D brain PET using a dual energy window method.* Physics in Medicine and Biology, 1996. **41**(12): p. 2757.
19. D. L. Bailey and S R Meikle, *A convolution-subtraction scatter correction method for 3D PET.* Physics in Medicine and Biology, 1994. **39**(3): p. 411.
20. M. Bentourkia, P. Msaki, J. Cadorette, and R. Lecomte, *Assessment of Scatter Components in High-Resolution PET: Correction by Nonstationary Convolution Subtraction.* J Nucl Med, 1995. **36**(1): p. 121-130.
21. M. Ollinger John, *Model-based scatter correction for fully 3D PET.* Physics in Medicine and Biology, 1996. **41**(1): p. 153.
22. C. C. Watson, *New, faster, image-based scatter correction for 3D PET.* Nuclear Science, IEEE Transactions on, 2000. **47**(4): p. 1587-1594.
23. M. Macmanus, U. Nestle, K. E. Rosenzweig, I. Carrio, C. Messa, O. Belohlavek, M. Danna, T. Inoue, E. Deniaud-Alexandre, S. Schipani, N. Watanabe, M. Dondi, and B. Jeremic, *Use of PET and PET/CT for Radiation Therapy Planning: IAEA expert report 2006-2007.* Radiother Oncol., 2009. **91**(1): p. 85-94. Epub 2008 Dec 25.
24. Yusuf E. Erdi, Kenneth Rosenzweig, Alev K. Erdi, Homer A. Macapinlac, Yu-Chi Hu, Louise E. Braban, John L. Humm, Olivia D. Squire, Chen-Shou Chui, Steven M. Larson, and Ellen D. Yorke, *Radiotherapy treatment planning for patients with non-small cell lung cancer using positron emission tomography (PET).* Radiotherapy and Oncology, 2002. **62**(1): p. 51-60.
25. M. P. Mac Manus, R. J. Hicks, J. P. Matthews, A. McKenzie, D. Rischin, E. K. Salminen, and D. L. Ball, *Positron emission tomography is superior to computed tomography scanning for response-assessment after radical radiotherapy or chemoradiotherapy in patients with non-small-cell lung cancer.* J Clin Oncol., 2003. **21**(7): p. 1285-92.

26. Jeffrey D. Bradley, Carlos A. Perez, Farrokh Dehdashti, and Barry A. Siegel, *Implementing Biologic Target Volumes in Radiation Treatment Planning for Non-Small Cell Lung Cancer.* J Nucl Med, 2004. **45**(90010): p. 96S-101.
27. Konstantin Lavrenkov, Mike Partridge, Gary Cook, and Michael Brada, *Positron emission tomography for target volume definition in the treatment of non-small cell lung cancer.* Radiotherapy and Oncology, 2005. **77**(1): p. 1-4.
28. Seong-Young Kwon, Hee-Seung Bom, Jung-Joon Min, Young-Soon Seo, Ho-Chun Song, Seong-Bom Hong, Kook-Joo Na, Chan Choi, and Young-Chul Kim, *PET/CT improves accuracy of mediastinal nodal staging by reducing false positivity of calcified lymph nodes regardless of histologic type of non-small cell lung cancer.* J. NUCL. Med. MEETING ABSTRACTS, 2006. **47**(suppl_1): p. 168P-b-.
29. Slobodan Devic, Nada Tomic, Sergio Faria, Geoffrey Dean, Robert Lisbona, William Parker, Chris Kaufman, and Ervin B. Podgorsak, *Impact of 18FDG-PET/CT on biological target volume (BTV) definition for treatment planning for non-small cell lung cancer patients.* Nuclear Instruments and Methods in Physics Research Section A: Accelerators, Spectrometers, Detectors and Associated Equipment, 2007. **571**(1-2): p. 89-92.
30. M. Feng, F. M. Kong, M. Gross, S. Fernando, J. A. Hayman, and R. K. Ten Haken, *Using fluorodeoxyglucose positron emission tomography to assess tumor volume during radiotherapy for non-small-cell lung cancer and its potential impact on adaptive dose escalation and normal tissue sparing.* Int J Radiat Oncol Biol Phys., 2009. **73**(4): p. 1228-34.
31. H. A. Macapinlac, *FDG-PET in head and neck, and thyroid cancer.* Chang Gung Med J., 2005. **28**(5): p. 284-95.
32. E. C. Ford, P. E. Kinahan, L. Hanlon, A. Alessio, J. Rajendran, D. L. Schwartz, and M. Phillips, *Tumor delineation using PET in head and neck cancers: threshold contouring and lesion volumes.* Med Phys., 2006. **33**(11): p. 4280-8.
33. Mazen El-Bassiouni, I. Frank Ciernik, J. Bernard Davis, Inas El-Attar, Beatrice Reiner, Cyrill Burger, Gerhard W. Goerres, and Gabriela M. Studer, *[18FDG] PET-CT-Based Intensity-Modulated Radiotherapy Treatment Planning of Head and Neck Cancer.* International Journal of Radiation Oncology*Biology*Physics, 2007. **69**(1): p. 286-293.
34. L. Deantonio, D. Beldi, G. Gambaro, G. Loi, M. Brambilla, E. Inglese, and M. Krengli, *FDG-PET/CT imaging for staging and radiotherapy treatment planning of head and neck carcinoma.* Radiat Oncol., 2008. **3**: p. 29.
35. A. Guido, L. Fuccio, B. Rombi, P. Castellucci, A. Cecconi, F. Bunkheila, C. Fuccio, E. Spezi, A. L. Angelini, and E. Barbieri, *Combined 18F-FDG-PET/CT imaging in radiotherapy target delineation for head-and-neck cancer.* Int J Radiat Oncol Biol Phys., 2009. **73**(3): p. 759-63.

36. Hyun Hoon Chung, Hoenil Jo, Won Jun Kang, Jae Weon Kim, Noh-Hyun Park, Yong-Sang Song, June-Key Chung, Soon-Beom Kang, and Hyo-Pyo Lee, *Clinical impact of integrated PET/CT on the management of suspected cervical cancer recurrence.* Gynecologic Oncology, 2007. **104**(3): p. 529-534.
37. Y. Yildirim, S. Sehirali, M. E. Avci, C. Yilmaz, K. Ertopcu, S. Tinar, Y. Duman, and S. Sayhan, *Integrated PET/CT for the evaluation of para-aortic nodal metastasis in locally advanced cervical cancer patients with negative conventional CT findings.* Gynecol Oncol., 2008. **108**(1): p. 154-9. Epub 2007 Oct 22.
38. H. Dolezelova, P. Slampa, B. Ondrova, J. Gombosova, S. Sovadinova, T. Novotny, K. Bolcak, J. Ruzickova, L. Hynkova, and M. Forbelska, *The impact of PET with 18FDG in radiotherapy treatment planning and in the prediction in patients with cervix carcinoma: results of pilot study.* Neoplasma, 2008. **55**(5): p. 437-41.
39. T. Leong, C. Everitt, K. Yuen, S. Condron, A. Hui, S. Y. Ngan, A. Pitman, E. W. Lau, M. MacManus, D. Binns, T. Ackerly, and R. J. Hicks, *A prospective study to evaluate the impact of FDG-PET on CT-based radiotherapy treatment planning for oesophageal cancer.* Radiother Oncol., 2006. **78**(3): p. 254-61. Epub 2006 Mar 20.
40. H. A. Jacene, R. Filice, W. Kasecamp, and R. L. Wahl, *18F-FDG PET/CT for monitoring the response of lymphoma to radioimmunotherapy.* J Nucl Med., 2009. **50**(1): p. 8-17. Epub 2008 Dec 17.
41. D. Vriens, L. F. de Geus-Oei, W. T. van der Graaf, and W. J. Oyen, *Tailoring therapy in colorectal cancer by PET-CT.* Q J Nucl Med Mol Imaging., 2009. **53**(2): p. 224-44.
42. Dirk Pauleit, Gabriele Stoffels, Frank Floeth, Hans Herzog, Lutz Tellmann, Kurt Hamacher, Heinz Coenen, and Karl Langen, *Double-tracer PET with FET and FDG in cerebral gliomas.* J. NUCL. Med. MEETING ABSTRACTS, 2006. **47**(suppl_1): p. 290P-.
43. Vincent Gregoire, Karin Haustermans, Xavier Geets, Sarah Roels, and Max Lonneux, *PET-Based Treatment Planning in Radiotherapy: A New Standard?* J Nucl Med, 2007. **48**(1_suppl): p. 68S-77.
44. Jana L. Fox, Ramesh Rengan, William O'Meara, Ellen Yorke, Yusuf Erdi, Sadek Nehmeh, Steven A. Leibel, and Kenneth E. Rosenzweig, *Does registration of PET and planning CT images decrease interobserver and intraobserver variation in delineating tumor volumes for non-small-cell lung cancer?* International Journal of Radiation Oncology*Biology*Physics, 2005. **62**(1): p. 70-75.
45. Abdelhamid Saoudi, Amir Pourmoghadas, Philippe St.Laurent, Francois Raymond, Libni Eapen, and Joanna E Cygler, *Effect of motion and medium heterogeneity on PET tracer quantification and target volume delineation in*

radiotherapy treatment planning. J. NUCL. Med. MEETING ABSTRACTS, 2006. **47**(suppl_1): p. 447P-b-.

46. D. Visvikis and P. J. Ell, *Impact of technology on the utilisation of positron emission tomography in lymphoma: current and future perspectives.* Eur J Nucl Med Mol Imaging., 2003. **30 Suppl 1**: p. S106-16. Epub 2003 May 13.
47. Hans Herzog, Lutz Tellmann, Roger Fulton, Isabelle Stangier, Elena Rota Kops, Kay Bente, Christian Boy, Rene Hurlemann, and Uwe Pietrzyk, *Motion Artifact Reduction on Parametric PET Images of Neuroreceptor Binding.* J Nucl Med, 2005. **46**(6): p. 1059-1065.
48. Curtis B. Caldwell, Katherine Mah, Matthew Skinner, and Cyril E. Danjoux, *Can PET provide the 3D extent of tumor motion for individualized internal target volumes? A phantom study of the limitations of CT and the promise of PET.* International Journal of Radiation Oncology*Biology*Physics, 2003. **55**(5): p. 1381-1393.
49. M. Okubo, Y. Nishimura, K. Nakamatsu, M. Okumura, T. Shibata, S. Kanamori, K. Hanaoka, and M. Hosono, *Static and moving phantom studies for radiation treatment planning in a positron emission tomography and computed tomography (PET/CT) system.* Ann Nucl Med., 2008. **22**(7): p. 579-86. Epub 2008 Aug 29.
50. Andreas K. Buck and Sven N. Reske, *Cellular Origin and Molecular Mechanisms of 18F-FDG Uptake: Is There a Contribution of the Endothelium?* J Nucl Med, 2004. **45**(3): p. 461-463.
51. Simone Maschauer, Olaf Prante, Markus Hoffmann, J. Thiess Deichen, and Torsten Kuwert, *Characterization of 18F-FDG Uptake in Human Endothelial Cells In Vitro.* J Nucl Med, 2004. **45**(3): p. 455-460.
52. Mohei M. Abouzied, Elpida S. Crawford, and Hani Abdel Nabi, *18F-FDG Imaging: Pitfalls and Artifacts.* J Nucl Med Technol, 2005. **33**(3): p. 145-155.
53. Kazuo Kubota, Taiju Matsuzawa, Takehiko Fujiwara, Masatoshi Ito, Jun Hatazawa, Kiichi Ishiwata, Ren Iwata, and Tatsuo Ido, *Differential Diagnosis of Lung Tumor with Positron Emission Tomography: A Prospective Study.* J Nucl Med, 1990. **31**(12): p. 1927-1932.
54. Siema M. B. Bakheet, John Powe, Adnan Ezzat, and Assem Rostom, *F-18-FDG Uptake in Tuberculosis.* Clinical Nuclear Medicine, 1998. **23**(11): p. 739-742.
55. Seiei Yasuda, Akira Shohtsu, Michiru Ide, Shigeharu Takagi, Junnichi Ogawa, Toshio Mitomi, and Yutaka Suzuki, *High Fluorine-18 Labeled Deoxyglucose Uptake in Sarcoidosis.* Clinical Nuclear Medicine, 1996. **21**(12): p. 983-984.
56. Yen-Kung Chen and Yen-Ling Chen, *Elevated F-18 FDG Uptake in the Thymus in Graves' Disease.* Clinical Nuclear Medicine, 2003. **28**(2): p. 142-143.
57. Waheeda Sureshbabu and Osama Mawlawi, *PET/CT Imaging Artifacts.* J Nucl Med Technol, 2005. **33**(3): p. 156-161.

58. E. M. Kamel, C. Burger, A. Buck, G. K. von Schulthess, and G. W. Goerres, *Impact of metallic dental implants on CT-based attenuation correction in a combined PET/CT scanner.* European Radiology, 2003. **13**(4): p. 5.
59. Paul E. Kinahan, Bruce H. Hasegawa, and Thomas Beyer, *X-ray-based attenuation correction for positron emission tomography/computed tomography scanners.* Seminars in Nuclear Medicine, 2003. **33**(3): p. 166-179.
60. Thomas Beyer, Andreas Bockisch, Hilmar Kuhl, and Maria-Jose Martinez, *Whole-Body 18F-FDG PET/CT in the Presence of Truncation Artifacts.* J Nucl Med, 2006. **47**(1): p. 91-99.
61. Siroos Mirzaei, Michel Guerchaft, Christopher Bonnier, Peter Knoll, Michel Doat, and Peter Braeutigam, *Use of segmented CT transmission map to avoid metal artifacts in PET images by a PET-CT device.* BMC Nuclear Medicine, 2005. **5**(1): p. 3.
62. J. Nuyts and S. Stroobants. *Reduction of attenuation correction artifacts in PET-CT*. in *Nuclear Science Symposium Conference Record, 2005 IEEE*. 2005.
63. Catherine Lemmens and Johan Nuyts. *Metals in PET/CT: Causes and reduction of artifacts in PET images*. in *Nuclear Science Symposium Conference Record, 2008. NSS '08. IEEE*. 2008.
64. C. Bai, K. M. Brown, L. Shao, A. J. Da Silva, and Z. Zhao, *A new technique for CT truncation compensation in combined CT/PET imaging.* (Abstract) J Nucl Med, 2003. **44**: p. 270.
65. K. Sourbelle, M. Kachelriess, and W. A. Kalender, *Reconstruction from truncated projections in CT using adaptive detruncation.* European Radiology, 2005. **15**(5): p. 1008-1014.
66. Osama Mawlawi, Jeremy J. Erasmus, Tinsu Pan, Dianna D. Cody, Rachelle Campbell, Albert H. Lonn, Steve Kohlmyer, Homer A. Macapinlac, and Donald A. Podoloff, *Truncation Artifact on PET/CT: Impact on Measurements of Activity Concentration and Assessment of a Correction Algorithm.* Am. J. Roentgenol., 2006. **186**(5): p. 1458-1467.
67. Sadek A. Nehmeh, Yusuf E. Erdi, Clifton C. Ling, Kenneth E. Rosenzweig, Heiko Schoder, Steve M. Larson, Homer A. Macapinlac, Olivia D. Squire, and John L. Humm, *Effect of Respiratory Gating on Quantifying PET Images of Lung Cancer* J Nucl Med, 2002. **43**(7): p. 876-881.
68. Paul Kinahan, Hubert Vesselle, Lawrence Macdonald, Adam Alessio, Steven Kohlmyer, and Thomas Lewellen, *Whole-body respiratory gated PET/CT.* J. NUCL. Med. MEETING ABSTRACTS, 2006. **47**(suppl_1): p. 187P-a-.
69. Valentino Bettinardi, Stefano Schipani, Maria Picchio, Mauro Cattaneo, Massimo Danna, Nadia Di Muzio, Claudio Landoni, Pasquale Tamborra, Pietro Mancosu, and Ferruccio Fazio, *4D-PET/CT for volume target definition in the radiotherapy*

of lung cancer. J. NUCL. Med. MEETING ABSTRACTS, 2006. **47**(suppl_1): p. 234P-b-.

70. Olivier G. Rousset, Yilong Ma, and Alan C. Evans, *Correction for Partial Volume Effects in PET: Principle and Validation.* J Nucl Med, 1998. **39**(5): p. 904-911.
71. JAD Aston, VJ Cunningham, and RN Gunn. *Statistical Based PET Partial Volume Correction*. in *Joint Statistical Meetings*. 2002. New York: the American Statistical Association.
72. M. Leahy Richard and Qi Jinyi, *Statistical approaches in quantitative positron emission tomography.* Statistics and Computing, 2000. **10**(2): p. 147-165.
73. T. D. Pham. *Image segmentation using probabilistic fuzzy c-means clustering*. in *Image Processing, 2001. Proceedings. 2001 International Conference on*. 2001.
74. I. Frank Ciernik, Elena Dizendorf, Brigitta G. Baumert, Beatrice Reiner, Cyrill Burger, J. Bernard Davis, Urs M. Lutolf, Hans C. Steinert, and Gustav K. Von Schulthess, *Radiation treatment planning with an integrated positron emission and computer tomography (PET/CT): a feasibility study.* International Journal of Radiation Oncology*Biology*Physics, 2003. **57**(3): p. 853-863.
75. Takeshi Nishioka, Tohru Shiga, Hiroki Shirato, Eriko Tsukamoto, Kazuhiko Tsuchiya M.D, Takashi Kato, Keiichi Ohmori, Akira Yamazaki, Hidefumi Aoyama, Seiko Hashimoto, Ta-Chen Chang, and Kazuo Miyasaka, *Image fusion between 18FDG-PET and MRI/CT for radiotherapy planning of oropharyngeal and nasopharyngeal carcinomas.* International Journal of Radiation Oncology*Biology*Physics, 2002. **53**(4): p. 1051-1057.
76. Yusuf E. Erdi, Barry W. Wessels, Murray H. Loew, and Alev K. Erdi, *Threshold Estimation in Single Photon Emission Computed Tomography and Planar Imaging for Clinical Radioimmunotherapy.* Cancer Res, 1995. **55**(23_Supplement): p. 5823s-5826.
77. Nobuyuki Otsu, *A Threshold Selection Method from Gray-Level Histograms.* Systems, Man and Cybernetics, IEEE Transactions on, 1979. **9**(1): p. 62-66.
78. David T. Long, Michael A. King, and John and Sheehan, *Comparative evaluation of image segmentation methods for volume quantitation in SPECT.* Medical Physics, 1992. **19**(2): p. 483-489.
79. Kenneth J. Biehl, Feng-Ming Kong, Farrokh Dehdashti, Jian-Yue Jin, Sasa Mutic, Issam El Naqa, Barry A. Siegel, and Jeffrey D. Bradley, *18F-FDG PET Definition of Gross Tumor Volume for Radiotherapy of Non-Small Cell Lung Cancer: Is a Single Standardized Uptake Value Threshold Approach Appropriate?* J Nucl Med, 2006. **47**(11): p. 1808-1812.
80. Yusuf E. Erdi, O. Mawlawi, Steven M. Larson, M. Imbriaco, H. Yeung, R. Finn, and John L. Humm, *Segmentation of lung lesion volume by adaptive positron emission tomography image thresholding.* Cancer, 1997. **80**(S12): p. 2505-2509.

81. Jean-Francois Daisne, Merence Sibomana, Anne Bol, Thomas Doumont, Max Lonneux, and Vincent Gregoire, *Tri-dimensional automatic segmentation of PET volumes based on measured source-to-background ratios: influence of reconstruction algorithms.* Radiotherapy and Oncology, 2003. **69**(3): p. 247-250.
82. Walter Jentzen, Lutz Freudenberg, Ernst G. Eising, Melanie Heinze, Wolfgang Brandau, and Andreas Bockisch, *Segmentation of PET Volumes by Iterative Image Thresholding.* J Nucl Med, 2007. **48**(1): p. 108-114.
83. I. Sobel, and Feldman,G., *A 3x3 isotropic gradient operator for image processing*, in *Pattern Classification and Scene Analysis*, R. and Hart Duda, P., Editor. 1973, John Wiley and Sons. p. 271-2.
84. D. Marr and E. Hildreth, *Theory of Edge Detection.* Proceedings of the Royal Society of London. Series B. Biological Sciences, 1980. **207**(1167): p. 187-217.
85. Xavier Geets, John Lee, Anne Bol, Max Lonneux, and Vincent Grégoire, *A gradient-based method for segmenting FDG-PET images: methodology and validation.* European Journal of Nuclear Medicine and Molecular Imaging, 2007. **34**(9): p. 1427-1438.
86. S.L. Horowitz and T. Pavlidis. *Picture Segmentation by a Directed Split and Merge Procedure*. in *ICPR 74*. 1974. Denmark.
87. Ellen Day, James Betler, David Parda, Bodo Reitz, Alexander Kirichenko, Seyed Mohammadi, and Moyed Miften, *A region growing method for tumor volume segmentation on PET images for rectal and anal cancer patients.* Medical Physics, 2009. **36**(10): p. 4349-4358.
88. H. Digabel and C. Lantuejoul. *Iterative algorithms*. in *2nd Europ. Symp. Quantitative Anal. Microstructures Mater. Sci.* 1977: Biol. Med.
89. C. Riddell, P. Brigger, R. E. Carson, and S. L. Bacharach, *The watershed algorithm: a method to segment noisy PET transmission images.* Nuclear Science, IEEE Transactions on, 1999. **46**(3): p. 713-719.
90. P. Tylski, G. Bonniaud, E. Decenciere, J. Stawiaski, J. Coulot, D. Lefkopoulos, and M. Ricard. *18F-FDG PET images segmentation using morphological watershed: a phantom study*. in *Nuclear Science Symposium Conference Record, 2006. IEEE*. 2006.
91. Demetri Terzopoulos, Andrew Witkin, and Michael Kass, *Symmetry-seeking models and 3D object reconstruction.* International Journal of Computer Vision, 1988. **1**(3): p. 211-221.
92. Michael Kass, Andrew Witkin, and Demetri Terzopoulos, *Snakes: Active contour models.* International Journal of Computer Vision, 1988. **1**(4): p. 321-331.
93. Wei-Chung Lin, Shiuh-Yung Chen, and Chin-Tu Chen, *A new surface interpolation technique for reconstructing 3D objects from serial cross-sections.* Computer Vision, Graphics, and Image Processing, 1989. **48**(1): p. 124-143.

94. Demetri Terzopoulos, Andrew Witkin, and Michael Kass, *Constraints on deformable models:Recovering 3D shape and nonrigid motion.* Artificial Intelligence, 1988. **36**(1): p. 91-123.
95. I. El Naqa, D. Yang, A. Apte, D. Khullar, S. Mutic, J. Zheng, J. D. Bradley, P. Grigsby, and J. O. Deasy, *Concurrent multimodality image segmentation by active contours for radiotherapy treatment planning.* Med Phys., 2007. **34**(12): p. 4738-49.
96. J. C. Dunn, *A Fuzzy Relative of the ISODATA Process and Its Use in Detecting Compact Well-Separated Clusters.* Journal of Cybernetics, 1973. **3**(3): p. 32 - 57.
97. C. Bezdek James, *Pattern Recognition with Fuzzy Objective Function Algorithms*. 1981: Kluwer Academic Publishers. 256.
98. Li Yanling and Shen Yi. *Robust Image Segmentation Algorithm Using Fuzzy Clustering Based on Kernel-Induced Distance Measure*. in *Computer Science and Software Engineering, 2008 International Conference on*. 2008.
99. Dzung L. Pham and Jerry L. Prince, *An adaptive fuzzy C-means algorithm for image segmentation in the presence of intensity inhomogeneities.* Pattern Recognition Letters, 1999. **20**(1): p. 57-68.
100. M. Hatt, C. Cheze le Rest, A. Turzo, C. Roux, and D. Visvikis, *A Fuzzy Locally Adaptive Bayesian Segmentation Approach for Volume Determination in PET.* Medical Imaging, IEEE Transactions on, 2009. **28**(6): p. 881-893.
101. Mathieu Hatt, Catherine Cheze le Rest, Patrice Descourt, André Dekker, Dirk De Ruysscher, Michel Oellers, Philippe Lambin, Olivier Pradier, and Dimitris Visvikis, *Accurate Automatic Delineation of Heterogeneous Functional Volumes in Positron Emission Tomography for Oncology Applications.* International Journal of Radiation Oncology*Biology*Physics, 2010. **77**(1): p. 301-308.
102. P. Jaccard, *Étude comparative de la distribution orale dans une portion des Alpes et des Jura.* Bulletin del la Société Vaudoise des Sciences Naturelles, 1901. **37**: p. 547-579.
103. Lee R. Dice, *Measures of the Amount of Ecologic Association Between Species.* Ecology, 1945. **26**(3): p. 297-302.
104. Aditya Bharatha, Masanori Hirose, Nobuhiko Hata, Simon K. Warfield, Matthieu Ferrant, Kelly H. Zou, Eduardo Suarez-Santana, Juan Ruiz-Alzola, Anthony D'Amico, Robert A. Cormack, Ron Kikinis, Ferenc A. Jolesz, and Clare M. C. Tempany, *Evaluation of three-dimensional finite element-based deformable registration of pre- and intraoperative prostate imaging.* Medical Physics, 2001. **28**(12): p. 2551-2560.
105. Tiezhi Zhang, Yuwei Chi, Elisa Meldolesi, and Di Yan, *Automatic Delineation of On-Line Head-And-Neck Computed Tomography Images: Toward On-Line*

Adaptive Radiotherapy. International Journal of Radiation Oncology*Biology*Physics, 2007. **68**(2): p. 522-530.

106. A. Rosenfeld and J.L. Pfaltz, *Distance Functions on Digital Pictures.* Patern Recognition, 1967. **1**: p. 33-61.
107. F. Y. Shih and Wu Yi-Ta, *The efficient algorithms for achieving Euclidean distance transformation.* IEEE Transactions on Image Processing, 2004. **13**(8): p. 1078-1091.
108. Roel J. H. M. Steenbakkers, Joop C. Duppen, Isabelle Fitton, Kirsten E. I. Deurloo, Lambert J. Zijp, Emile F. I. Comans, Apollonia L. J. Uitterhoeve, Patrick T. R. Rodrigus, Gijsbert W. P. Kramer, Johan Bussink, Katrien De Jaeger, José S. A. Belderbos, Peter J. C. M. Nowak, Marcel van Herk, and Coen R. N. Rasch, *Reduction of observer variation using matched CT-PET for lung cancer delineation: A three-dimensional analysis.* International Journal of Radiation Oncology*Biology*Physics, 2006. **64**(2): p. 435-448.
109. Habib Zaidi and Issam El Naqa, *PET-guided delineation of radiation therapy treatment volumes: a survey of image segmentation techniques.* European Journal of Nuclear Medicine and Molecular Imaging, 2010. **37**(11): p. 2165-2187.
110. Laura A. Drever, Wilson Roa, Alexander McEwan, and Don Robinson, *Comparison of three image segmentation techniques for target volume delineation in positron emission tomography.* J Appl Clin Med Phys, 2007. **8**(2): p. 93-109.
111. M. Teräs, T. Tolvanen, J. Johansson, J. Williams, and J. Knuuti, *Performance of the new generation of whole-body PET/CT scanners: Discovery STE and Discovery VCT.* European Journal of Nuclear Medicine and Molecular Imaging, 2007. **34**(10): p. 1683-1692.
112. *National Electrical Manufacturers Association, NEMA standards publication No. NU 2–1994: performance measurements of positron emission tomography,*. 1994, National Electrical Manufacturers Association: Washington, DC.
113. *National Electrical Manufacturers Association, NEMA standards publication No. NU 2–2001: performance measurements of positron emission tomography,*. 2001, National Electrical Manufacturers Association: Rosslyn, VA.
114. P. E. Kinahan and J. G. Rogers, *Analytic 3D image reconstruction using all detected events.* Nuclear Science, IEEE Transactions on, 1989. **36**(1): p. 964-968.
115. R. M. Manjeshwar, S. G. Ross, M. Iatrou, T. W. Deller, and C. W. Stearns. *Fully 3D PET Iterative Reconstruction Using Distance-Driven Projectors and Native Scanner Geometry*. in *Nuclear Science Symposium Conference Record, 2006. IEEE*. 2006.
116. Heiko Schoder, Yusuf E. Erdi, Kenneth Chao, Mithat Gonen, Steven M. Larson, and Henry W. D. Yeung, *Clinical Implications of Different Image Reconstruction*

Parameters for Interpretation of Whole-Body PET Studies in Cancer Patients. J Nucl Med, 2004. **45**(4): p. 559-566.

117. Friedman Milton, *The Use of Ranks to Avoid the Assumption of Normality Implicit in the Analysis of Variance.* Journal of the American Statistical Association, 1937. **32**(200): p. 675-701.
118. L. J. Vanuytsel, J. F. Vansteenkiste, S. G. Stroobants, P. R. De Leyn, W. De Wever, E. K. Verbeken, G. G. Gatti, D. P. Huyskens, and G. J. Kutcher, *The impact of (18)F-fluoro-2-deoxy-D-glucose positron emission tomography (FDG-PET) lymph node staging on the radiation treatment volumes in patients with non-small cell lung cancer.* Radiother Oncol., 2000. **55**(3): p. 317-24.
119. J. Bradley, W. L. Thorstad, S. Mutic, T. R. Miller, F. Dehdashti, B. A. Siegel, W. Bosch, and R. J. Bertrand, *Impact of FDG-PET on radiation therapy volume delineation in non-small-cell lung cancer.* Int J Radiat Oncol Biol Phys., 2004. **59**(1): p. 78-86.
120. Hani Ashamalla, Sameer Rafla, Kapila Parikh, Bahaa Mokhtar, Ganesh Goswami, Shravan Kambam, Hussain Abdel-Dayem, Adel Guirguis, Pamela Ross, and Alex Evola, *The contribution of integrated PET/CT to the evolving definition of treatment volumes in radiation treatment planning in lung cancer.* International Journal of Radiation Oncology*Biology*Physics, 2005. **63**(4): p. 1016-1023.
121. Inga S. Grills, Di Yan, Quinten C. Black, Ching-Yee O. Wong, Alvaro A. Martinez, and Larry L. Kestin, *Clinical implications of defining the gross tumor volume with combination of CT and 18FDG-positron emission tomography in non-small-cell lung cancer.* International Journal of Radiation Oncology*Biology*Physics, 2007. **67**(3): p. 709-719.
122. Vinai Gondi, Kristin Bradley, Minesh Mehta, Andy Howard, Deepak Khuntia, Mark Ritter, and Wolfgang Tome, *Impact of hybrid fluorodeoxyglucose positron-emission tomography/computed tomography on radiotherapy planning in esophageal and non-small-cell lung cancer.* International Journal of Radiation Oncology*Biology*Physics, 2007. **67**(1): p. 187-195.
123. Arnold C. Paulino, Mary Koshy, Rebecca Howell, David Schuster, and Lawrence W. Davis, *Comparison of CT- and FDG-PET-defined gross tumor volume in intensity-modulated radiotherapy for head-and-neck cancer.* International Journal of Radiation Oncology*Biology*Physics, 2005. **61**(5): p. 1385-1392.
124. Hani Ashamalla, Adel Guirgius, Ewa Bieniek, Sameer Rafla, Alex Evola, Ganesh Goswami, Randall Oldroyd, Bahaa Mokhtar, and Kapila Parikh, *The Impact of Positron Emission Tomography/Computed Tomography in Edge Delineation of Gross Tumor Volume for Head and Neck Cancers.* International Journal of Radiation Oncology*Biology*Physics, 2007. **68**(2): p. 388-395.
125. *The Role of PET/CT in Radiation Treatment Planning for Cancer Patient Treatment*. 2008, International Atomic Energy Agency (IAEA): Austria. p. 40.

126. Lale Kostakoglu, Ruth Hardoff, Rosna Mirtcheva, and Stanley J. Goldsmith, *PET-CT Fusion Imaging in Differentiating Physiologic from Pathologic FDG Uptake.* Radiographics, 2004. **24**(5): p. 1411-1431.
127. Arnold C. Paulino, Bin S. Teh, and E. Brian Butler, *Head and Neck*, in *PET-CT in Radiotherapy Treatment Planning*, Arnold C. Paulino and Bin S. Teh, Editor. 2008, SAUNDERS ELSEVIER: Philadelphia. p. 93-107.
128. Medhat M. Osman, Christian Cohade, Yuji Nakamoto, Laura T. Marshall, Jeff P. Leal, and Richard L. Wahl, *Clinically Significant Inaccurate Localization of Lesions with PET/CT: Frequency in 300 Patients.* J Nucl Med, 2003. **44**(2): p. 240-243.
129. J. Vansteenkiste and C. Dooms, *Positron emission tomography in nonsmall cell lung cancer.* Curr Opin Oncol., 2007. **19**(2): p. 78-83.
130. Sang-Keun Woo, Joon Choi, Yong Choi, Kyung-Han Lee, and Byung-Tae Kim, *Motion correction of PET images with respiratory-gated CT images in PET/CT studies.* J. NUCL. Med. MEETING ABSTRACTS, 2006. **47**(suppl_1): p. 388P-a-.
131. Sadek A. Nehmeh, Yusuf E. Erdi, Kenneth E. Rosenzweig, Heiko Schoder, Steve M. Larson, Olivia D. Squire, and John L. Humm, *Reduction of Respiratory Motion Artifacts in PET Imaging of Lung Cancer by Respiratory Correlated Dynamic PET: Methodology and Comparison with Respiratory Gated PET.* J Nucl Med, 2003. **44**(10): p. 1644-1648.
132. S. A. Nehmeh, Y. E. Erdi, G. S. Meirelles, O. Squire, S. M. Larson, J. L. Humm, and H. Schoder, *Deep-inspiration breath-hold PET/CT of the thorax.* J Nucl Med., 2007. **48**(1): p. 22-6.
133. D. E. Heron, R. S. Andrade, J. Flickinger, J. Johnson, S. S. Agarwala, A. Wu, S. Kalnicki, and N. Avril, *Hybrid PET-CT simulation for radiation treatment planning in head-and-neck cancers: a brief technical report.* Int J Radiat Oncol Biol Phys., 2004. **60**(5): p. 1419-24.
134. Michael T. Munley, Lawrence B. Marks, Christopher Scarfone, Gregory S. Sibley, Edward F. PatzJr., Timothy G. Turkington, Ronald J. Jaszczak, David R. Gilland, Mitchell S. Anscher, and R. Edward Coleman, *Multimodality nuclear medicine imaging in three-dimensional radiation treatment planning for lung cancer: challenges and prospects.* Lung Cancer, 1999. **23**(2): p. 105-114.